Forschungsberichte

IPEK
Institut für Produktentwicklung
am Karlsruher Institut für Technologie

J. Jochen Hauschild

Entwicklung einer Vorgehensweise zur Bestimmung und Verifikation von Wärmeübergangsparametern aus CFD Simulationen von Trockenkupplungssytemen

Development of an Estimation and Verification Approach for Heat Transfer Parameters of Dry Clutch Systems obtained from CFD Simulations

Band 91

Systeme ▪ Methoden ▪ Prozesse

Hrsg.: Prof. Dr.-Ing. Dr. h.c. A. Albers

IPEK
Institut für Produktentwicklung
am Karlsruher Institut für Technologie

Forschungsberichte

J. Jochen Hauschild

Entwicklung einer Vorgehensweise zur Bestimmung und Verifikation von Wärmeübergangsparametern aus CFD Simulationen von Trockenkupplungssystemen

Development of an Estimation and Verification Approach for Heat Transfer Parameters of Dry Clutch Systems Obtained from CFD Simulations

Band 91

Herausgeber: Prof. Dr.-Ing. Dr. h.c. A. Albers

Druck: Stolzenberger Druck und Werbung GmbH & Co. KG, Leimen
06224-7697915

ISSN 1615-8113

Entwicklung einer Vorgehensweise zur Bestimmung und Verifikation von Wärmeübergangsparametern aus CFD Simulationen von Trockenkupplungssystemen

Zur Erlangung des akademischen Grades
Doktor der Ingenieurwissenschaften
der Fakultät für Maschinenbau
Karlsruher Institut für Technologie (KIT)

genehmigte
Dissertation

von

Dipl.-Ing. J. Jochen Hauschild
aus Bad Soden am Taunus

Tag der mündlichen Prüfung: 16. Dezember 2015
Hauptreferent: Prof. Dr.-Ing. Dr. h.c. A. Albers
Korreferent: Prof. Dr.-Ing. T. Vietor

Vorwort des Herausgebers

Wissen ist einer der entscheidenden Faktoren in den Volkswirtschaften unserer Zeit. Der Unternehmenserfolg wird in der Zukunft mehr denn je davon abhängen, wie schnell ein Unternehmen neues Wissen aufnehmen, zugänglich machen und verwerten kann. Die Aufgabe eines Universitätsinstitutes ist es, hier einen wesentlichen Beitrag zu leisten. In den Forschungsarbeiten wird ständig Wissen generiert. Dieses kann aber nur wirksam und für die Gemeinschaft nutzbar werden, wenn es in geeigneter Form kommuniziert wird. Diese Schriftenreihe dient als eine Plattform zum Transfer und macht damit das Wissenspotenzial aus aktuellen Forschungsarbeiten am IPEK - Institut für Produktentwicklung Karlsruhe[1] am Karlsruher Institut für Technologie (KIT) verfügbar.

Die Forschungsfelder des Institutes sind die methodische Entwicklung und das Entwicklungsmanagement, die rechnergestützte Optimierung von Strukturen und Systemen, die Antriebstechnik mit einem Schwerpunkt auf den Gebieten Antriebsstrang-Engineering und Tribologie und Monitoring von Lager- und Funktionsreibsystemen, die NVH mit dem Fokus auf Schwingungen und Akustik an Komponenten und am Gesamtfahrzeug, die Mikrosystemtechnik mit dem Fokus auf die zugehörigen Entwicklungsprozesse sowie die Mechatronik. Die Forschungsberichte werden aus allen diesen Gebieten Beiträge zur wissenschaftlichen Fortentwicklung des Wissens und der zugehörigen Anwendung – sowohl den auf diesen Gebieten tätigen Forschern als auch ganz besonders der anwendenden Industrie – zur Verfügung stellen. Ziel ist es, qualifizierte Beiträge zum Produktentwicklungsprozess zu leisten.

Albert Albers

[1] Eh.: Institut für Maschinenkonstruktionslehre und Kraftfahrzeugbau, Universität Karlsruhe (TH)

Vorwort zu Band 91

In der Fahrzeugantriebstechnik werden unterschiedliche Konzepte zur Anpassung der Charakteristik des Verbrennungsmotors an die Lastcharakteristik des Fahrzeuges gewählt. Im Allgemeinen werden Getriebe mit unterschiedlichen Gangstufen, oder auch stufenlose Getriebe, zwischen Motor und Antriebsrädern eingebracht, um so eine geeignete Anpassung der Charakteristiken von Kraft- und Arbeitsmaschine zu erreichen. Um einen Gangwechsel zu ermöglichen, ist normalerweise eine Umschaltung des Drehmomentflusses notwendig. Im einfachsten Fall, bei manuellen Antriebssträngen, wird der Motor zum Gangwechsel vom Getriebe getrennt. Dazu sind Kupplungssysteme erforderlich. Diese Kupplungssysteme haben zusätzlich die Aufgabe, die Drehzahllücke beim Anfahren zwischen der Drehzahl des Motors und den sich zunächst nicht drehenden Antriebsrädern auszugleichen. Für die Erfüllung dieser Grundfunktionen werden unterschiedliche Konzepte verwendet. Prinzipiell wird hierbei der Wirkmechanismus des Reibkraftschlusses genutzt. Eines der am weitesten verbreiteten Grundkonzepte ist dabei die sogenannte trockene Kupplung. Bei diesem Konzept werden die funktionserfüllenden Wirkflächenpaare jeweils aus einem Wirkkontakt zwischen Friktionsmaterial und einer geeigneten metallischen Oberfläche gebildet. Die einfachste Bauform ist dabei die Einscheiben-Trockenkupplung, bei der zwei Friktionselemente auf einer Kupplungsscheibe angeordnet sind. Diese werden zwischen der Wirkfläche des Schwungrades und der Wirkfläche der Anpressplatte im Kupplungssystem verspannt. Zur Verspannung wird im Allgemeinen eine Tellerfeder eingesetzt. Die Herausforderung beim Design von Kupplungssystemen ist nun zum einen, eine geeignete Modulation zu erreichen, so dass, insbesondere bei manuell betätigten Kupplungen der Fahrer den Anfahrvorgang komfortabel umsetzen kann. Gleichzeitig entsteht natürlich bei jedem Kupplungsvorgang, also der Angleichung der Wirkflächengeschwindigkeiten Schwungrad/ Kupplungsdruckplatte – Kupplungsscheibe, eine erhebliche Wärme im Kupplungssystem selbst, da die Differenzdrehzahl zwischen beiden Systemen nur über Reibung mit Relativgeschwindigkeit – also Gleitreibung - überwunden werden kann. Die so im Kupplungssystem entstehende Wärme ist ein entscheidender Designparameter, der die Leistungsfähigkeit von Kupplungen wesentlich bestimmt. Ziel muss es dabei sein, die Erwärmung des Kupplungssystems unter allen Randbedingungen so zu beherrschen, dass das Reibungs- und Verschleißverhalten des Wirkflächenpaares zwischen Friktionsmaterial und den Gegenwirkflächen den Ansprüchen genügt und eine ausreichende Gebrauchsdauer im Normalfahrbetrieb erreicht wird. Erschwerend kommt hinzu, dass durch die zunehmende Leistungsdichte die Bauräume für die Komponenten eng begrenzt sind. Der Wärmetransport von den Wirkflächenpaaren in die Umgebung ist damit eine Herausforderung. Nur durch ein gezieltes Design dieser

Wärmetransportprozesse können Hochleistungskupplungen sicher dimensioniert werden. Die Beschreibung des Wärmehaushaltes ist dabei bereits seit vielen Jahren Gegenstand verschiedener wissenschaftlicher Arbeiten. Die nun vorliegenden neuen numerischen Methoden und auch die Leistungsfähigkeit moderner Rechneranlagen erlaubt es, hier weiter vorzudringen und eine verbesserte Modellbildung zu realisieren. An dieser Stelle setzt die Arbeit von Herrn Dr.-Ing. Jochen Hauschild an. Er hat sich zum Ziel gesetzt, durch die Nutzung der CFD Simulation der Umströmung des Kupplungssystems und einer experimentell validierten Bedatung mit den notwendigen thermodynamischen Kenngrößen eine neue Möglichkeit zur Simulation des Wärmehaushaltes in Kupplungssystemen zu realisieren. Die Arbeit leistet so einen wesentlichen Beitrag für die Konstruktion moderner Antriebssysteme im Fahrzeugbau.

November, 2015 Albert Albers

Preface to Volume 91

In the field of vehicle drivetrain technology different concepts for the adaption of the characteristics of the combustion engine and the load characteristics of the vehicle are chosen. Commonly transmissions with different gear steps, or seamless transmissions, are placed between engine and the driving wheels to adapt the characteristics of force and work machine. A switching of the torque flow is normally necessary to realize are gear change. In the simplest case, with manual drive trains, the engine is disconnected from the transmission for a gear change. For this clutch systems are necessary. These clutch systems have the additional task of compensating the rotational speed gap between the engine and the initially not rotating driving wheels. For the fulfillment of these basic functions different concepts are used. In principle the mechanism of action used here is based on frictional traction. The most common basic concept is the so called dry clutch. In this concept the function fulfilling Working Surface Pairs are formed respectively of one working contact between the friction material and a suitable metallic counter surface. The simplest design is the single disc dry clutch, where two friction elements are located on one clutch disc. These elements are tensioned inside the clutch system between the working surface of the flywheel and the working surface of the pressure plate. For the tensioning a diaphragm spring is utilized in general. The challenge with the design of a clutch system is now the achievement of a suitable modulation, so that the driver can, in particular with manually operated clutch systems, realize a comfortable vehicle launch. Simultaneously with every coupling operation, in other words the adaption of rotational speeds of the working surfaces of the flywheel/ pressure plate – clutch disc, a significant heat amount is generated inside the clutch system itself, as the differential speed between both systems can only be overcome by friction with relative movement – sliding friction. The hereby generated heat inside the clutch system is therefore a crucial design parameter which essentially determines the performance of clutch systems. The aim must be to control the heating inside the clutch system under every boundary condition, so that the frictional and wear behavior of the Working Surface Pairs of friction material and the counter faces masters the requirements and supplies a sufficient life time in normal driving operation. This is aggravated by the fact, that by the increase of the power density the packaging space for these components is very limited. Heat transport from the Working Surface Pairs to the ambient is therefore a challenge. Only with specific design of these heat transport processes high performance clutch systems can be safely designed. The description of the heat transfer processes has been object of different scientific studies over many years. The now available numerical methods and the performance of modern computer systems permits a further advance and an improved model building. The work of Dr.-Ing. Jochen

Hauschild takes this as staring point. With the usage of CFD simulations of the flow around the clutch system and experimentally validated data of the necessary thermodynamic parameters he targets to realize a new possibility to simulate the heat balance of clutch systems. The work provides an essential contribution to the construction of modern powertrain systems in vehicle manufacturing.

November, 2015 Albert Albers

Kurzfassung

Mit steigenden Anforderungen an Qualität und Haltbarkeit wird es in der Antriebsstrangentwicklung fortlaufend wichtiger in frühen Phasen detaillierte Informationen in Bezug auf Systemverhalten zu Verfügung zu stellen. Diese Daten können entweder durch Tests oder durch Simulation erhalten werden, wobei die Simulation wegen der Vorteile in Zeit und Ressourcen bevorzugt wird.

Die Dimensionierung einer Kupplung für manuelle Schaltgetriebe wird hauptsächlich auf zwei Ebenen durchgeführt: Thermische Kapazität und Verschleißverhalten. Beide Zustände sind stark von den Temperaturen, die im Friktionskontakt erzeugt werden, abhängig. Die thermische Kapazität einer Kupplung ist durch die thermische Masse, welche direkt im Kontakt mit dem Friktionskontakt ist, gegeben. Das Langzeit Verschleißverhalten ist durch den Wärmetransport an die Umgebung und durch das Lastprofil charakterisiert.

Das richtige Verständnis für die Einstufung der Wärmeübertragungsmechanismen und der Randbedingungen ist eine Schlüsselstelle in der effizienten Ermittlung der Kupplungsgröße. In diesem Forschungsfeld bietet die zusammengesetzte Wärmeübergangssimulation mittels einer CFD Software ein großes Potential die Wärmeübergangscharakteristik im Hinblick auf die Entwicklung vereinfachter thermischer Modelle von Kupplungssystemen zu bestimmen.

Diese Arbeit widmet sich der Charakterisierung des Wärmeübergangs von trocken laufenden Kupplungssystemen für manuelle Schaltgetriebe, dem Prozess der Ergebnisvereinfachung und der Validierung der Ergebnisse, die von einer CFD Simulation generiert wurden.

Abstract

With rising demand in quality and durability it is more and more important to provide detailed information on system performance in the early stages of powertrain development. This information can either be provided by tests or simulative methods. The latter approach is preferred for efficient use of time and resources.

The dimensioning of a clutch system for manual transmissions is mainly performed in two stages: thermal capacity and wear performance. Both conditions are strongly dependent on the temperatures induced at the frictional interface. The capacity of a clutch is primarily influenced by the thermal masses which are directly introduced to the frictional heating. Long term wear performance depends on the heat transfer properties and also on the load profile.

Correct understanding and characterization of heat transfer mechanisms and boundary conditions is a key point to the efficient determination of clutch size. In this field the conjugate heat transfer analysis in a Computational Fluid Dynamics (CFD) software analysis offers a great potential to determine heat transfer characteristics in order to develop simplified approaches for the simulation of clutch systems.

This paper deals with the heat transfer characterization of dry clutch systems for manual transmissions, the simplification process and the verification of results generated from CFD clutch models.

Danksagung

Diese Arbeit entstand während meiner Zeit in der Getriebe- und Kupplungsvorentwicklung der Ford Motor Company in Zusammenarbeit mit dem Institut für Produktentwicklung Karlsruhe des Karlsruhe Institute of Technology.

Zuerst möchte ich o. Prof. Dr.-Ing. Dr. h.c. Albert Albers für die Betreuung der Arbeit, die konstruktiven Diskussionen und die Möglichkeit diese Arbeit am Institut für Produktentwicklung in Karlsruhe durchführen zu können, danken. Mein Dank gilt ebenfalls Herrn Prof. Dr.-Ing. Thomas Vietor für die Übernahme des Koreferats.

Für die konstruktiven Gesprächen, die Unterstützung in der Planung, Ideenfindung und Betreuung möchte ich Pat Kelly, Andreas Tissot und Torsten Sude danken. Insbesondere möchte ich Christian Meyer für seine kontinuierliche Unterstützung und sein Vertrauen danken. Insgesamt war es eine Freude in so einer kollegialen Umgebung zu arbeiten.

Von der Ford Versuchsabteilung möchte ich Dirk Beisman und Erwin Kallies mit ihren Teams für die durchgehende und effektive Unterstützung bei den Messungen, welche in Merkenich durchgeführt worden sind, danken. Der lokalen CAE Gruppe gilt ebenfalls mein Dank für die vielen Diskussionen und Gespräche. Für die Unterstützung bei der CAD-Rekonstruktion möchte ich Markus Reisch danken.

Vom Institut für Produktentwicklung Karlsruhe möchte ich Johannes Bernhard und Philipp Merkel für die Betreuung, Christian Denda und Christian Koch für die durchgeführten PIV Messungen, danken.

Zuletzt möchte ich einen großen Dank meiner eigenen Familie und meinen Eltern aussprechen. Danke für die großartige Unterstützung.

Karlsruhe, 10.07.2015

J. Jochen Hauschild

Inhalt

List of Abbreviations

A	mm² / -	Area / Surface Area / System Matrix / Calibration Constant
A_c	-	Constant
a	m²/s / m/s²	Thermal Diffusity / Acceleration Rate
B	-	Control Input Matrix / Calibration Constant
b_1	-	Correction Factor
b_2	-	Correction Factor
C	-	Measurement Matrix
C^+	-	Dimensionless Wall Friction Constant
C_{12}	-	Net Radiation Factor
c_f	-	Friction Factor
c_p	J/(kgK)	Thermal Capacity
d_1	-	Engine Speed Drop Factor
d_2	-	Driver Factor
f_{tyre}	-	Tyre Friction
g	m/s²	Gravity
H	-	Measurement Matrix
h	-	Scaling Parameter
h_{av}	W/(m²K)	Augmented Heat Transfer Coefficient
h_{glob}	W/(m²K)	Global Heat Transfer Coefficient
h_{loc}	W/(m²K)	Local Heat Transfer Coefficient
$h_{loc,y+}$	W/(m²K)	Specified Y+ Heat Transfer Coefficient
i	-	Gear Ratio
J_{red}	kgm²	Reduced Enertia
J_{rest}	kgm²	Inertia of Transmission and Shafts

K	-	Kalman Gain Matrix
k	-	Surface Layer Element Number
K_1	-	Constant for Nusselt Number Calculation
K_V	-	Shape Factor of the Velocity Profile
k_x	N	Sum of External Forces on a Volume Element in X-Direction
k_y	N	Sum of External Forces on a Volume Element in Y-Direction
k_z	N	Sum of External Forces on a Volume Element in Z-Direction
L_{av}	W/K	Augmented Heat Conductance
L_{conv}	W/K	Convection Heat Conductance
L_{cond}	W/K	Conduction Heat Conductance
l	m	Length / Conduction Length
M	Nm	Torque
m	kg / -	Mass / Nusselt Number Constant
M_{res}	Nm	Load Torque
n	-	Time Step Number / Number of Parameters
n^*	-	Exponent of the Power Law Profile of the Temperature Head
n_P	-	Exponent for Nusselt Number Calculation
n_R	-	Exponent for Nusselt Number Calculation
Nu	-	Nusselt Number
P	- / W	Turbulence Function of the Turbulent Dimensionless Temperature Profile / Power Input into the Clutch System
p	bar	Pressure
$\overline{p}$	bar	Time Averaged Pressure

p'	bar	Pressure Fluctuation
p_i	-	Parameter Value
Pr	-	Prandtl Number
Pr_t	-	Turbulent Prandtl Number
P_t	-	State Covariance Matrix
P_{t+1}	-	Updated State Covariance Matrix
P_{xy}	-	Cross Covaraiance Matrix
P_y	-	Measurement Covariance
Q	- / W	System Noise Covariance Matrix / Electrical Power
$\dot{Q}$	W	Heat Flux
$\dot{Q}_{conv}$	W	Convection Heat Flux
$\dot{Q}_{rad}$	W	Radiation Heat Flux
$\dot{q}_s$	W/m²	External, Specific Heat Flux into a Volume Element
$\dot{q}_w$	W/m²	Specific Wall Heat Flux
R	J/(kgK) / m / Ω	General Gas Constant / Radius / Resistance
r_a	m	Outer Radius of the Disk
r_{dyn}	m	Dynamic Tyre Radius
Re_Ω	-	Reynoldsnumber Based on the Outer Radius of the Disk
R_e	-	Reynolds Number
S_R	Ω/K	Anemometer Sensitivity
T	K	Temperature
$\overline{T}$	K	Time Averaged Temperature
T''	K	Temperature Fluctuation
T_∞	K	Free Stream Temperature

T^+	K	Dimensionless Temperature
t	s	Time
T_{amb}	K	Ambient Temperature
$T_{fl,loc}$	K	Near Wall Local Fluid Temperature
$T_{fl,y+}$	K	Fluid Temperature at a Specified Y+
T_{ref}	K	Reference Temperature
t_s	s	Slip Time
T_w	K	Wall Temperature
u	m/s	Fluid Velocity in X-Direction
$\tilde{u}$	m/s	Time Averaged Velocity in X-Direction
u''	m/s	Velocity Fluctuation in X-Direction
u_∞	m/s	Free Stream Velocity
u^+	-	Dimensionless Wall Velocity
U_b	V	Bridge Voltage
u_τ	m/s	Shear Velocity
u_t	-	Control Vector
$\vec{v}$	m/s	Velocity Vector
v	m/s	Fluid Velocity in Y-Direction
$\tilde{v}$	m/s	Time Averaged Velocity in Y-Direction
v''	m/s	Velocity Fluctuation in X-Direction
v_t	-	Measurement Noise
w	m/s	Fluid Velocity in Z-Direction
$\tilde{w}$	m/s	Time Averaged Velocity in Z-Direction
w''	m/s	Velocity Fluctuation in X-Direction
w_i	-	Wheighting Factor

w_t	-	System Noise
x_c	m	Critical Distance
x_t	-	State Vector
$\hat{x}_{t+1}$	-	Current Prediction of the State Vector
y^+	-	Dimensionless Wall Coordinate
$\hat{y}_{t+1}$	-	Current Prediction of the Measurement Vector
y_m	-	Measurement Vector

Greek Letters

α	-	Wall Value of the Flow Tangent Swirl / Temperature Coefficient / Constant for Sigma Point Selection
δ	m	Boundary Layer Thickness
δ_t	m	Thermal Boundary Layer Thickness
δy	m	Position Offset Parameter
ε	-	Emission Rate
η_{PT}	-	Powertrain Efficiency
Φ	m²/s³	Dissipation Rate
κ	-	Von Karaman Constant / Constant for Sigma Point Selection
λ	W/(mK) / -	Thermal Conductivity/ Constant for Sigma Point Selection
μ	kg/(ms)	Dynamic Viscosity
ν	m²/s	Kinematic Viscosity
ρ	kg/m³	Density
$\overline{\rho}$	kg/m³	Time Averaged Density
ρ'	kg/m³	Density Fluctuation
σ		Bolzman Constant

τ	MPa	Shear Stress
τ_w	MPa	Wall Shear Stress
φ	°	Gradient Angle
χ	-	Sigma Point
ω	rpm	Rotation Rate

Indices

Amb	Ambient
BH	Bell Housing
CAE	Computer Aided Engineering
CC	Clutch Cover
CCD	Charged-Coupled-Device
CFD	Computational Fluid Dynamics
COV	Cover
DMF	Dual Mass Flywheel
DS	Diaphragm Spring
eff	Effective
FW	Flywheel
HTC	Heat Transfer Coefficient
LS	Lift Spring
PP	Pressure Plate
Riv	Rivets
SR	Sense Ring
SS	Sense Spring

1 Introduction

Before a vehicle program can be brought to market it has to pass numerous verification tests. One of the tests is the general durability cycle, which simulates the load condition on a vehicle over its lifetime. This cycle is built up by different sections to cover acquired customer usage data and the manufacturer's technical standards. Each section can apply to various boundary conditions (e.g. road surface or environmental conditions), specific vehicle components (e.g. body, powertrain or auxiliary systems) or driving maneuvers (e.g. hill start, high speed, handling). The design of the tests is done in regard of the technical standards of the manufacturer, customer data, locally available track properties and best usage of the test track. Figure 1 shows an aerial view of the different vehicle proving grounds of Ford Motor Company. Each of these proving grounds is used to evaluate a vehicle for one specific market. It can easily be derived that due to test track complexity in Figure 1 the individual test procedures vary.

Figure 1: Aerial View on Selected Ford Motor Company Proving Grounds

Aim of the individual durability cycle is either to prove that the vehicle components work together as a system and can meet the market based assigned lifetime targets or to reveal possible sources of reduced lifetime. The obtained data can be used to provide valuable feedback to the vehicle development process and can be seen as reasonable input to the verification phase.

The efficiency of an overall development process can be measured by the strictness of the designated targets, the customer feedback and how much resources are needed

to fulfill the designated targets. Since expenses in the product verification phase of a vehicle program increase with the duration, the running distance in the durability cycle is reduced. The cycle events are arranged in a certain order, so that the reduced running distance best simulates the designated vehicle life.

Independent from the section of the test cycle, the powertrain of the vehicle is involved almost every time. Therefore the heavily loaded powertrain components require more detailed examination. In a vehicle equipped with a dry clutch system the temperature of the frictional interfaces is a major design criteria. The event order, load per event and how the clutch is operated have a great influence on resulting temperatures and thus on wear mechanisms.

There are many influences on the wear and temperature behavior of dry clutch systems, especially for vehicles equipped with manual transmissions. It is therefore extremely important to obtain detailed information on the performance of a clutch system in an early stage of the development process. A very helpful tool in this area can be a design selection tool, calculating the heat transfer and temperature of a clutch system based on simplified assumptions for the clutch parts, geometry and heat transfer.

2 State of Research

2.1 Structure of Common Vehicle Powertrains

Due to increasing technical complexity and performance, modern vehicle powertrains face rising demand in efficiency, packaging and overall functionality. The basic powertrain components of a modern mid-size vehicle are shown in Figure 2. Main task of the powertrain is to supply, transform and transfer the demanded energy used for propulsion of the vehicle to the wheels.[2]

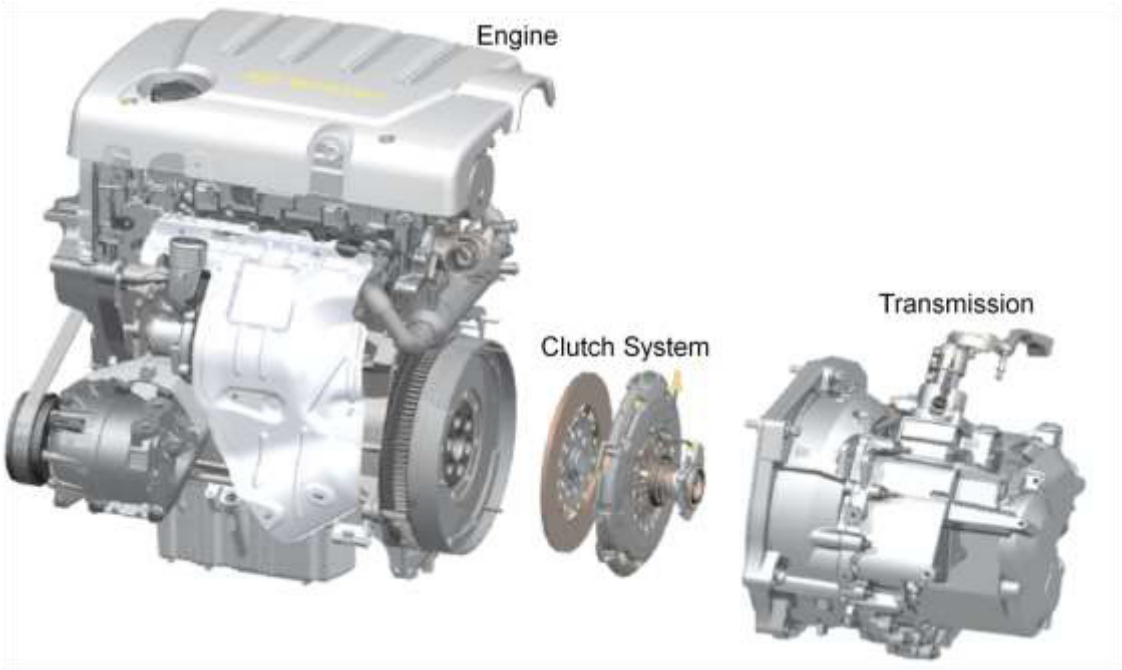

Figure 2: Basic Powertrain Components of a Mid-Size Vehicle[3]

For the energy supply there exist several concepts. The largest market share is represented by conventional thermal combustion engines. All of these systems are operated in a circular process in which a fuel air mixture is compressed, ignited (with or without additional energy input) and expanded rapidly. Most common fuel types in Europe are petrol, gasoline, natural or liquefied petroleum gas. In South America also ethanol is largely used as energy source. Due to tightening environmental regulations an uprising concept is to use electrical energy for propulsion. Electrical vehicle concepts have the advantage of a high effectiveness because the energy carrier can be directly transformed into propulsion energy at the wheel compared with combustion engines where the energy has to be transformed with the help of a gearbox. A large

[2] Kirchner 2007, P.1ff.
[3] Kirchner 2007, P.7

disadvantage is the range compared to a combustion system due to the battery capacity. Still, these systems can be used efficiently in urban regions. To overcome the range restrictions of electrical vehicles and to reduce to CO_2 emissions of combustion engines hybrid concepts are becoming more and more important. In serial hybrid powertrains the combustion engine is operated in a fuel efficient manner powering a generator which supplies the electrical energy used for propulsion of the vehicle. In parallel concepts both, the combustion and the electrical engine, can be used for energy supply towards the wheels. With parallel and serial concepts it is possible to regain energy, normally dissipated during braking, by recuperation.[4]

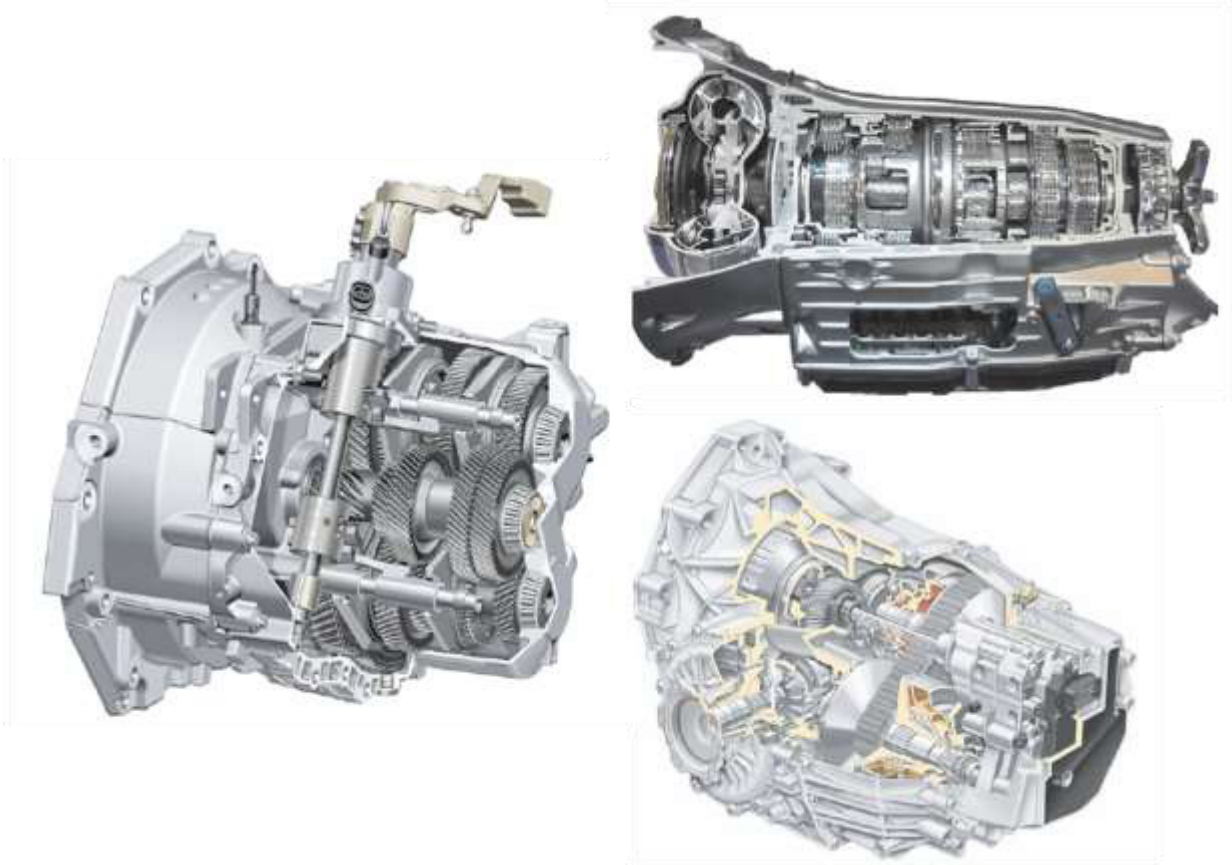

Figure 3: Examples of Vehicle Transmissions: Manual (left), Torque Converter Automatic (top right), Continuous Variable Transmission (bottom right)[5]

Since most combustion engines supply different torque levels at different engine speeds the transmission has the main objective to transform the propulsive power supplied by the engine to efficiently cover the current power demanded by road, driving and loading conditions.

The main types of transmissions are:[6]

[4] Stan 2005, P1ff., Wallentowitz & Reif 2006, P5ff.
[5] Kirchner 2007, P.36 / P.53 / P.58
[6] Lechner & Naunheimer 2007, P.11ff.

- Manual Transmission (MT)
- Automated Manual Transmission (AMT)
- Automatic Transmission (AT)
- Double Clutch Transmission (DCT)
- Continuously Variable Transmission (CVT)

In Europe the largest market share have manual transmissions, with automatic transmissions on a rise. Automatic transmissions have in North America the highest market share. In regards of fuel efficiency automatic transmissions have the disadvantage that additional energy is needed for the control of the transmission and additional losses are possible based on the selection of the coupling technology of engine and transmission. All transmission types are available for front, rear and all-wheel drive configurations.[7]

The coupling and decoupling of engine and transmission is performed by the clutch system, which can be segmented into the following:

- Dry Clutch
- Wet Clutch
- Double Dry Clutch
- Double Wet Clutch
- Torque Converter

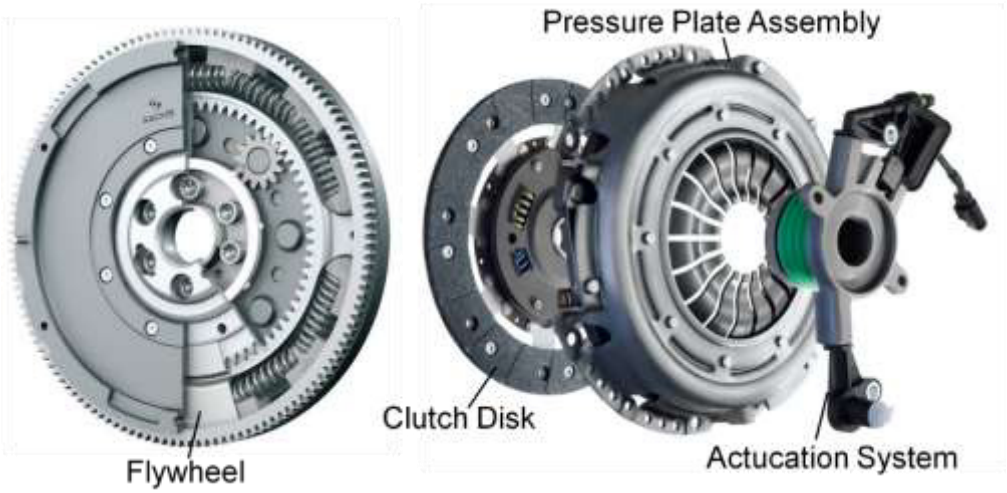

Figure 4: Basic Components of a Manual Transmission Clutch System[8]

Apart from the coupling and decoupling the clutch system in modern vehicles has also the target of vibration damping, supply a flexible coupling between the crankshaft and the transmission input shaft and to compensate misalignments. [9]

[7] Wallentowitz & Reif 2006, P.29ff.
[8] http://www.zf.com/brands/content/de/sachs/products_sx/pc_sx/products_pc.html
[9] http://www.zf.com/brands/content/de/sachs/products_sx/pc_sx/products_pc.html

The basic components of a clutch system for manual transmissions are shown in Figure 4. The flywheel which is connected directly to the crankshaft of the engine system can be executed as solid single or dual mass flywheel. The clutch disk is located between the pressure plate assembly and the flywheel. It is directly connected to the transmission input shaft and is the carrier of the lining material. The pressure plate assembly's main components are the pressure plate, diaphragm spring, clutch cover and the lift springs. For a self-adjusting system (SAC) the main components are shown in Figure 5.

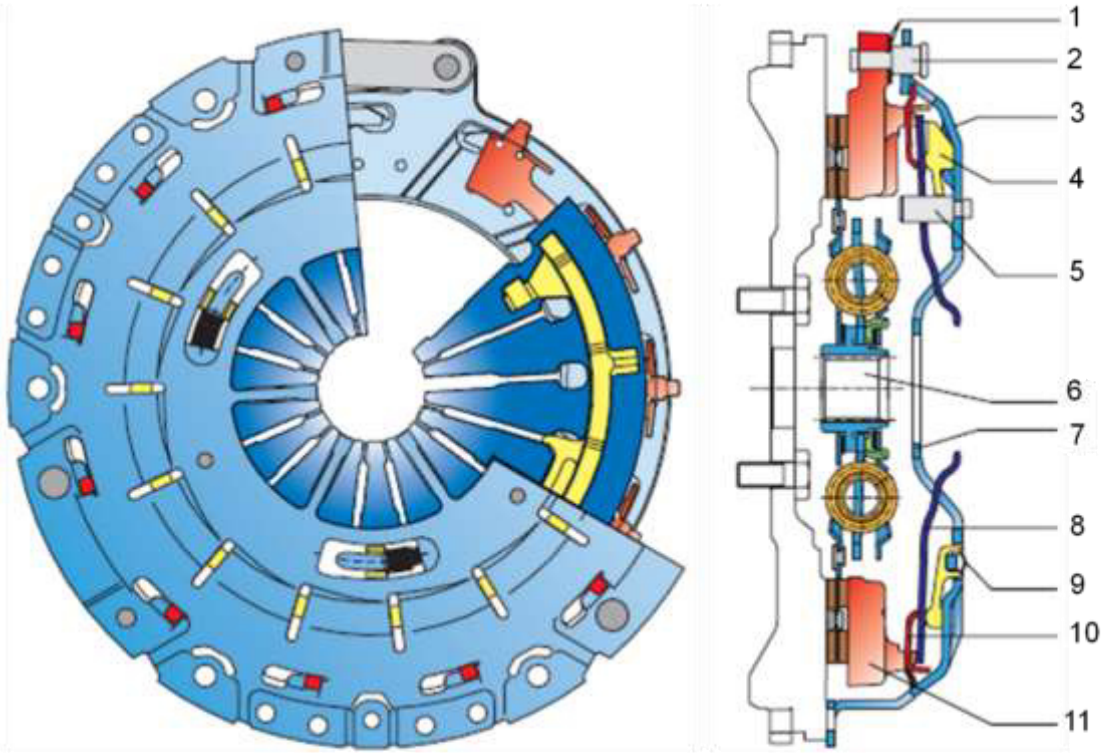

1: Leaf Spring
2: Bolt
3: Clutch Cover
4: Ramp Ring
5: Bolt
6: Clutch Disk
7: Endstop
8: Diaphragm Spring
9: Ramp Spring
10: Sensor Spring
11: Pressure Plate

Figure 5: Structure of a Pressure Plate Assembly of a SAC System[10]

Main task of the pressure plate assembly is to supply sufficient clamping force for the frictional torque transfer between the engine and the transmission. The clutch cover is usually mounted to the flywheel with screws. By applying a force to the inner area of the diaphragm spring the clamping force of the pressure plate and therefore the torque

[10] LUK Brochure 2015

capacity reduces. Clutch actuation can be executed mechanically, hydraulically or electrically. Most common systems for actuation are concentric slave cylinders (CSC) or leverages.[11]

In Figure 6 the packaging of a clutch system in a Fiesta ST MK06 is shown. The clutch system is surrounded by the bell housing which is a part of the transmission casing.

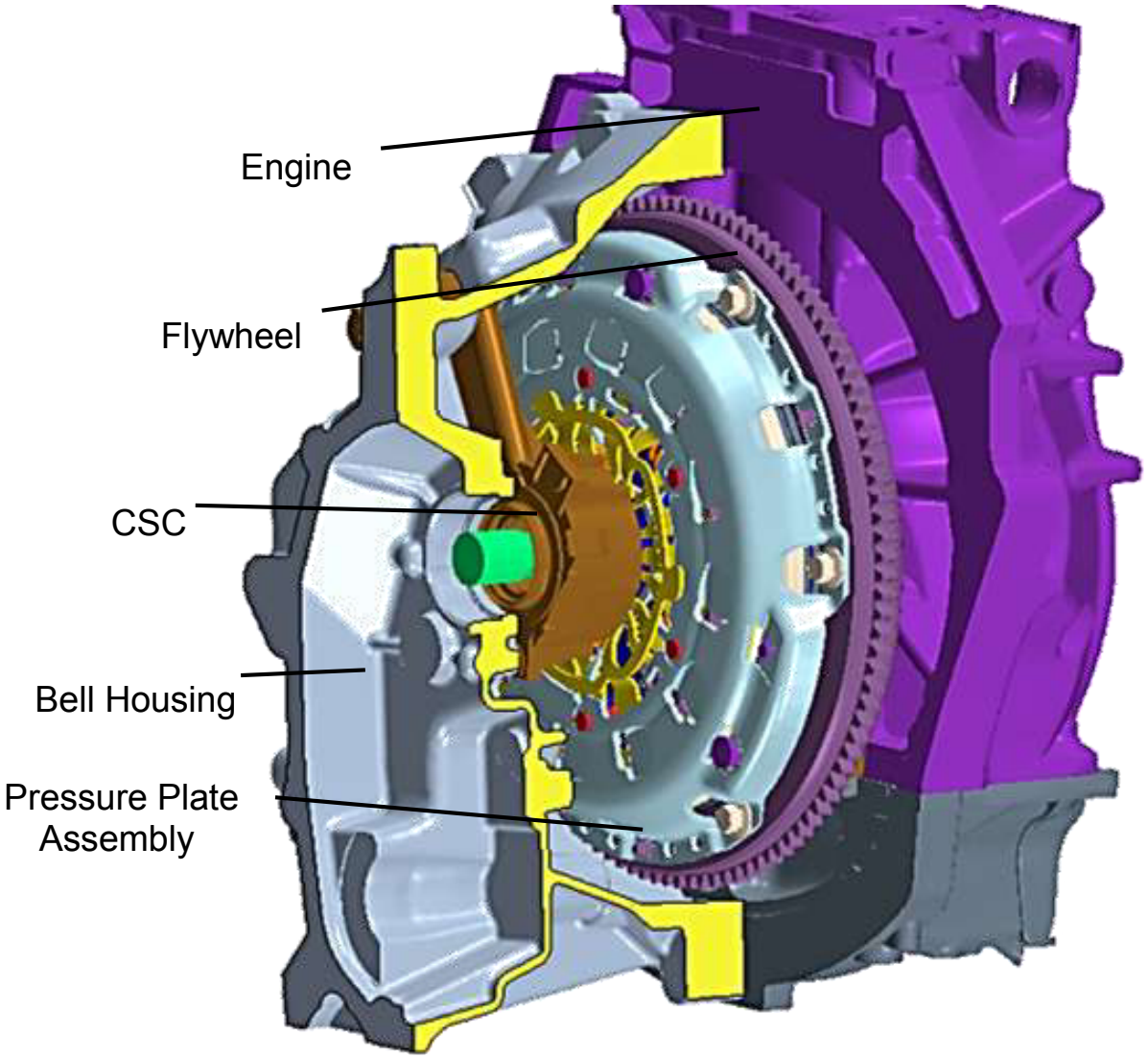

Figure 6: Structure of a Clutch System of a Fiesta ST MK06

The durability of a clutch system is highly dependent on wear of the frictionally loaded lining surface of the clutch disk. Wear rates of a clutch lining are mainly influenced by the surface temperature of the lining, slip time, transferred torque and speed difference between engine and transmission input shaft. Transferred torque, speed difference and slip time are highly affected by vehicle loading and the driving situation. The main influence on the temperature of a clutch is the frequency of engagements and energy

[11] LUK Brochure 2015

input into the system. A low power input and a high frequency can for example lead to equivalent temperatures as obtained by a low frequency and high power input. Important for lining wear is the temperature at which the slip energy is transferred into the system. Figure 7 shows an example for a wear rate diagram from a typical dry clutch lining.

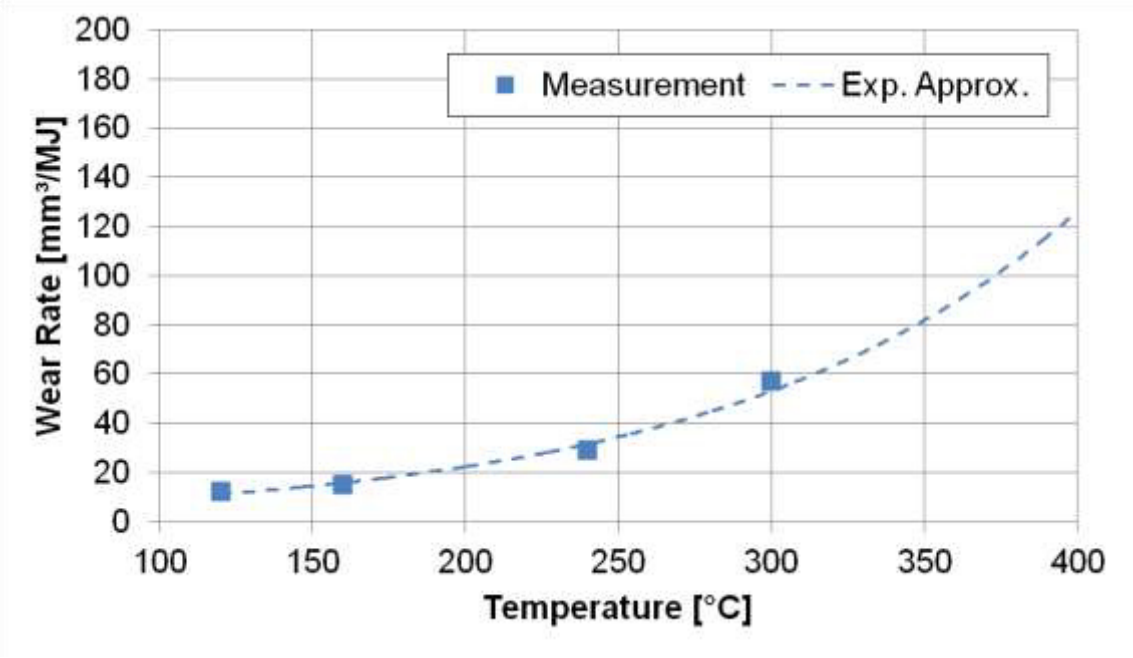

Figure 7: Wear rate of an organic lining[12]

The wear rate of clutch linings is measured in volume per energy and is obtained by running defined rig tests. In the example shown in Figure 7 it can be derived that an increase of 100 °K to 250°C results in duplication of the wear rate. The temperature dependence results from the fact, that linings are commonly compositions of different materials. The main components are fibrous reinforcements (strength contributors), matrix resin binders, lubricators, friction modifiers, heat sinks or dissipators and mating member conditioners. Each ingredient has different objectives to fulfill and influences the overall behavior of a lining. Wear behavior is primarily influenced by the temperature dependent properties of the matrix resin and the bonding between matrix and fibrous reinforcements.[13] In case a temperature level above a lining specific limit is reached during an engagement, the matrix resin loses its strength and fading will occur. Fading describes a temperature dependent drop of the friction coefficient μ and therefore a reduced torque capacity of the system. This phenomenon can be accompanied with burning of the frictional surface (structural damage of several

[12] Schaeffler Friction Products GmbH Moorbach, Clutch facing material B-8080 S, Data Sheet
[13] Albers et al 2009 a

surface layers) and decomposition of the friction surface which will result in smoke and smell development.[14]

Apart from conventional organic lining materials, new designs with innovative high performance materials are currently under development. The use of ceramic as friction material can bring advantages of wear behavior and high friction values.[15]

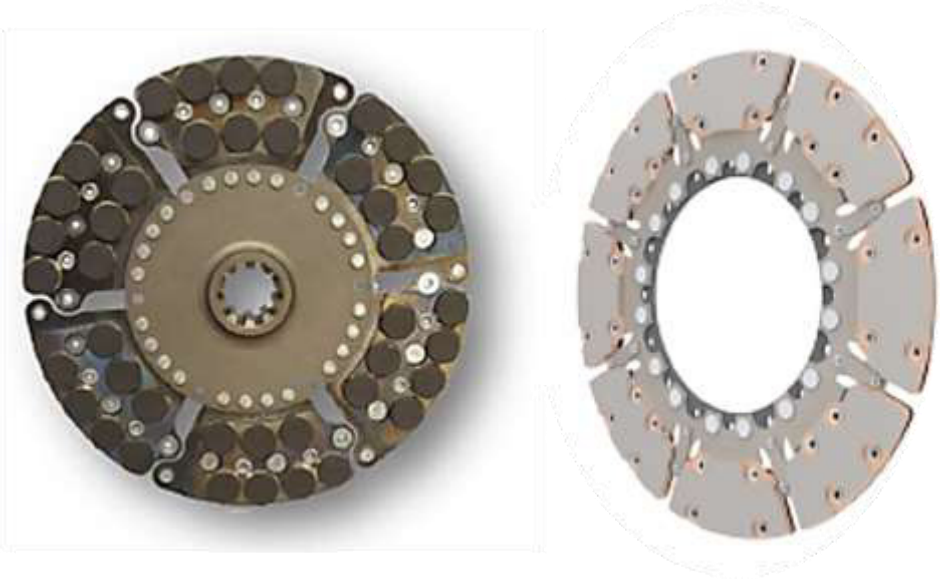

Figure 8: Clutch Disk with Ceramic Lining[16]

A disadvantage of clutch systems with ceramic lining elements is that the overall comfort of the entire clutch system is reduced. As shown in [17] these disadvantages can be reduced with automated clutch actuation systems with adaptable engagement characteristics.

2.2 Heat Transfer Mechanisms

The highest influence on the temperature levels reached during an engagement is the thermal mass located next to the heat source.[18]

Organic materials have a very low thermal conductivity compared to cast iron materials. This means that nearly all of the heat generated in the frictional interface is transmitted to the casting materials. During an engagement the temperature level reached is dependent on the power input into the system and the starting temperature.

[14] Albers et al 2006 a, P.351
[15] Albers et al 2015 a, Albers et al 2010 a
[16] Albers et al 2015 a, Albers et al 2011 a
[17] Albers et al 2010 b
[18] Beitler 2008, P.123ff.

Therefore knowledge of the temperature levels a clutch system is exposed to is dependent on the heat dissipation characteristics of the overall system.

2.2.1 Radiation

Heat transfer by radiation is mainly evoked by energy transport by electromagnetic waves. This form of heat transfer has no need of a direct material connection to transfer heat from one part to another. The fluid between the two parts considered can also be involved in the heat transfer, or have a negligible influence (air in most cases).[19]

To display the highest influencing factors on radiation, the simplified cases found in [20] will be taken as examples. For the amount of heat transfer by radiation between two grey and parallel bodies equation 2.1 can be evaluated.

$$\dot{Q} = C_{12} \cdot A \cdot \left(T_1^4 - T_2^4\right) \tag{2.1}$$

The surface A in equation 2.1 is the resulting visible area between the two bodies if a vertical observer is placed on one of the bodies. The constant C_{12} in equation 2.1 is referred to as net radiation factor, which is determined by geometry and the emission rates. For the simple case of two parallel surfaces equation 2.2 determines the constant C_{12}. Equation 2.3 evaluates the constant C_{12} for the heat transfer between an outer pipe and a shaft located in the center of rotation.

$$C_{12} = \frac{\sigma}{\frac{1}{\varepsilon_1} + \frac{1}{\varepsilon_2} - 1} \tag{2.2}$$

$$C_{12} = \frac{\sigma}{\frac{1}{\varepsilon_1} + \frac{A_{inner}}{A_{outer}}\left(\frac{1}{\varepsilon_2} - 1\right)} \tag{2.3}$$

For surfaces that are not parallel, the projected surface has to be evaluated to obtain the heat transfer by radiation. [21]

A high energy transport by radiation is therefore only possible with high emission rates, a large temperature difference and a high visible area between the components involved.

With regards to clutch systems [22] proposed a procedure how to measure the needed heat transfer coefficients by radiation explicitly.

---

[19] Marek & Nitsche 2007, P.238ff.
[20] VDI Wärmeatlas 2006, Ka1-Ka11
[21] VDI Wärmeatlas 2006, Ka1-Ka11
[22] Beitler 2008, P.136ff.

2.2.2 Conduction

Heat conduction is mainly dependent on the heat conduction parameters of the materials involved. The amount of heat transferred from one side of a random body to another is mainly dependent on the temperature gradient in that direction. For a simplified case of a one dimensional and stationary heat transfer inside a wall, the conductional heat transfer can be characterized by equation 2.4.

$$\dot{Q} = -\lambda \cdot A \cdot \frac{dT}{dx} \tag{2.4}$$

As can be derived from equation 2.4, the heat conducted through a body can be maximized by high thermal conductivities, high connection areas, or high temperature gradients. [23]

In the case of instationary heat transfer, the thermal mass of the material involved becomes relevant and the gradients inside a component can change over time. For this case several simplified solution strategies exist. The most interesting in case of thermal networks with conjugate heat transfer is the lumped capacitance method. The method is based on the assumption, that a body can be treated as one thermal mass, if the resistance for heat transfer out of the body is much higher than the resistance for heat transfer inside the body. This means that the resistance for heat transfer out of the body becomes the main influencing factor. This method, as shown by Beitler [24], can be applied to clutch systems and effectively reduces the simulation effort to estimate the temperature inside a clutch system. The basic model structure is shown in Figure 9.

[23] Marek & Nitsche 2007, P.20

[24] Beitler 2008, P.194ff.

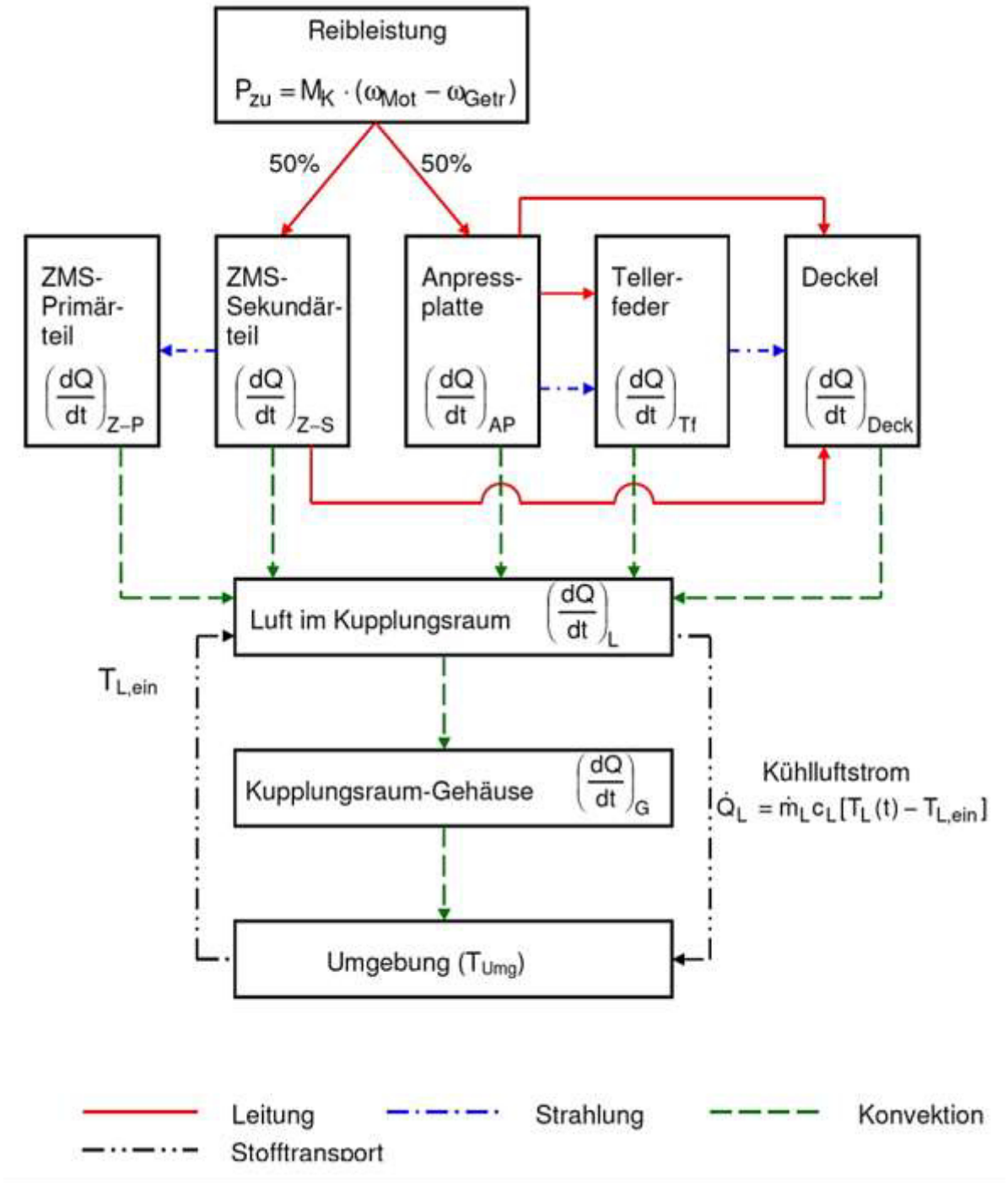

Figure 9: Model Structure of Beitler [25]

Assuming the validity of the application of the lumped capacitance method to clutch systems, one remaining question for conductional heat transfer between two parts is which effective area and conduction length to consider. A hint on how to treat this can be found in the definition of the finite volume method used in many computational fluid dynamics software programs.

[25] Beitler 2008, P.195

The finite volume method is based on the assumption, that the integrals of the integral form of the energy conservation equations of a control volume can be approximated by the fluxes through its boundary surfaces.

Between two cells, the conductional heat transfer is determined by the connection surface and the distance between the center of masses and the center of the connection surface. Now assuming that a component inside a clutch system, which can be represented as one thermal mass, represents one cell in the finite volume method, the effective conduction surface between the two parts is equal to the touching surface.

The conduction length can be determined analytically according to Figure 10, which is based on the assumptions proposed in [26].

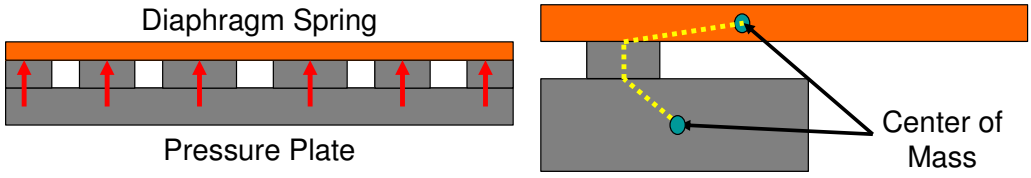

Figure 10: Simplified Model for Determining the Heat Conduction Resistances

The connection length is defined as distance between the center of mass of the two components. The distance is to be chosen as the shortest connection between the surfaces of the so called cooling elements.

As the example for the connection between the pressure plate and diaphragm spring in Figure 10 shows, symmetry conditions can also be used to determine the resulting connection length. Neglecting the connection points to the lift springs and the fingers of the diaphragm spring, the connection between the pressure plate and the diaphragm spring can be assumed as two ring elements connected via 15 supports.

$$\left(\frac{\lambda \cdot A}{l}\right)_{tot} = \left(\left(\frac{l}{\lambda \cdot A}\right)_1 + ... + \left(\frac{l}{\lambda \cdot A}\right)_n\right)^{-1} \tag{2.5}$$

Dividing the two plates into 15 sections with a support located in the middle, the total heat transfer between the two parts can then be interpreted as parallel circuit of 15 serial resistances. The overall resistance can then be evaluated by equation 2.5. It can be derived easily from equation 2.5 that if the connection length of the 15 connections is equal, it is sufficient to evaluate the connection length for one element as displayed in Figure 10. The connection area is equal to the overall touching area in this case. This approach is based on the electrical analogy approach displayed in [27].

[26] Oedekoven 1989
[27] Marek & Nitsche 2007, P.25ff.

2.2.3 Convection

Convectional heat transfer describes the heat transfer between a solid component and a fluid. Dependent on the source of the fluid flow, one can divide the convectional heat transfer into free convection and forced convection.[28]

In free convection flow results from temperature induced density distributions in the fluid surrounding the heated component. The differences in fluid density lead to a buoyancy flow. The relative speed between the solid structure and the fluid is rather small. At the surface of the solid component air is heated up. With a rising temperature the density of the fluid is decreased causing an exchange with fluid regions with a lower temperature. For a clutch system, free convection has only a large influence in the field of cooling down simulations if the engine is turned off.[29]

The more relevant area of convectional heat transfer related to clutch systems is the forced convection. The amount of heat exchange is in this case mainly dependent on flow field and the temperature difference to the fluid. Also the flow structure is of high importance. The heat transferred from a surface can be higher if the flow structure is turbulent.[30]

To display the influencing factors, the flow system around and the closely coupled heat transfer from a flat plate will be taken as example. Before doing this, it is necessary to firstly present the mathematical and physical basics on how fluid flow systems can be described in general.

2.2.3.1 Mathematical Models for the Description of Fluid Flow Systems

Fluid flow systems can in general be described by three main conservation laws: the mass conservation- the impulse conservation- and the energy conservation law.

The continuity equations, based on the mass conservation law, are derived from the assumption, that inside a control volume no mass is lost. The time dependent change in the mass inside a control volume is equal to the sum of all mass flow into and out of a control volume. For a compressible fluid this leads to equation (2.6). [31]

$$\frac{\partial \rho}{\partial t} + \frac{\partial(\rho \cdot u)}{\partial x} + \frac{\partial(\rho \cdot v)}{\partial y} + \frac{\partial(\rho \cdot w)}{\partial z} = 0 \tag{2.6}$$

The impulse conservation or Navier-Stokes equations for a laminar fluid flow system (eq. 2.7 to 2.9) consider a control volume based impulse balance. A time dependent

[28] Marek & Nitsche 2007, P.185ff.
[29] VDI Wärmeatlas 2006, Fa1-Fa6
[30] VDI Wärmeatlas 2006, Ga1-Ga9
[31] Oertel et al 2006, P.204ff.; Zierep & Bühler 1991, P.9ff.

change rate of the impulse of a volume element is equal to an addition of the difference between the impulse streams into and out of the volume element, the sum of shear forces and normal forces on the volume element and the sum of forces acting on the mass of the volume element (e.g. acceleration forces).

$$\rho\cdot\left(\frac{\partial u}{\partial t}+u\cdot\frac{\partial u}{\partial x}+v\cdot\frac{\partial u}{\partial y}+w\cdot\frac{\partial u}{\partial z}\right)=k_x-\frac{\partial p}{\partial x}+\frac{\partial}{\partial x}\left[\mu\cdot\left(2\cdot\frac{\partial u}{\partial x}-\frac{2}{3}\cdot\left(\nabla\cdot\vec{v}\right)\right)\right]+\frac{\partial}{\partial y}\left[\mu\cdot\left(\frac{\partial u}{\partial y}+\frac{\partial v}{\partial x}\right)\right]+\frac{\partial}{\partial z}\left[\mu\cdot\left(\frac{\partial w}{\partial x}+\frac{\partial u}{\partial z}\right)\right] \tag{2.7}$$

$$\rho\cdot\left(\frac{\partial v}{\partial t}+u\cdot\frac{\partial v}{\partial x}+v\cdot\frac{\partial v}{\partial y}+w\cdot\frac{\partial v}{\partial z}\right)=k_y-\frac{\partial p}{\partial y}+\frac{\partial}{\partial y}\left[\mu\cdot\left(2\cdot\frac{\partial v}{\partial y}-\frac{2}{3}\cdot\left(\nabla\cdot\vec{v}\right)\right)\right]+\frac{\partial}{\partial x}\left[\mu\cdot\left(\frac{\partial u}{\partial y}+\frac{\partial v}{\partial x}\right)\right]+\frac{\partial}{\partial z}\left[\mu\cdot\left(\frac{\partial v}{\partial z}+\frac{\partial w}{\partial y}\right)\right] \tag{2.8}$$

$$\rho\cdot\left(\frac{\partial w}{\partial t}+u\cdot\frac{\partial w}{\partial x}+v\cdot\frac{\partial w}{\partial y}+w\cdot\frac{\partial w}{\partial z}\right)=k_z-\frac{\partial p}{\partial z}+\frac{\partial}{\partial z}\left[\mu\cdot\left(2\cdot\frac{\partial w}{\partial z}-\frac{2}{3}\cdot\left(\nabla\cdot\vec{v}\right)\right)\right]+\frac{\partial}{\partial x}\left[\mu\cdot\left(\frac{\partial w}{\partial x}+\frac{\partial u}{\partial z}\right)\right]+\frac{\partial}{\partial y}\left[\mu\cdot\left(\frac{\partial v}{\partial z}+\frac{\partial w}{\partial y}\right)\right] \tag{2.9}$$

The energy conservation equation is the last equation needed to close the system of equations. A time dependent change of the inner energy and kinetic energy is here equal to the sum of energy streams into and out of the volume element by convection and conduction, the energy input rate caused by pressure, normal or shear forces, external energy input and the energy input caused by volume forces (equation 2.10).

$$\rho\cdot c_p\cdot\left(\frac{\partial T}{\partial t}+u\cdot\frac{\partial T}{\partial x}+v\cdot\frac{\partial T}{\partial y}+w\cdot\frac{\partial T}{\partial z}\right)=\left(\frac{\partial p}{\partial t}+u\cdot\frac{\partial p}{\partial x}+v\cdot\frac{\partial p}{\partial y}+w\cdot\frac{\partial p}{\partial z}\right)+\left(\frac{\partial}{\partial x}\left[\lambda\cdot\frac{\partial T}{\partial x}\right]+\frac{\partial}{\partial y}\left[\lambda\cdot\frac{\partial T}{\partial y}\right]+\frac{\partial}{\partial z}\left[\lambda\cdot\frac{\partial T}{\partial z}\right]\right)+\rho\cdot\dot{q}_s+\mu\cdot\Phi \tag{2.10}$$

$$\Phi = 2\cdot\left[\left(\frac{\partial u}{\partial x}\right)^2+\left(\frac{\partial v}{\partial y}\right)^2+\left(\frac{\partial w}{\partial z}\right)^2\right] + \left(\frac{\partial v}{\partial x}+\frac{\partial u}{\partial y}\right)^2+\left(\frac{\partial w}{\partial y}+\frac{\partial v}{\partial z}\right)^2+\left(\frac{\partial u}{\partial z}+\frac{\partial w}{\partial x}\right)^2 - \frac{2}{3}\cdot\left(\frac{\partial u}{\partial x}+\frac{\partial v}{\partial y}+\frac{\partial w}{\partial z}\right)^2 \tag{2.11}$$

In equation 2.10 Φ is the dissipation term (eq. 2.11), which represents frictional energy beeing transferred into heat energy. This process is irreversible.

The displayed equations are only valid for laminar fluid flow. When turbulent effects become more influenting, additional equations and mathematical methods become neccessary to discribe fluid flow. In turbulent flows the generation and decay of vortices provides an additional fluctuation of the flow quantities.

To describe turbulent flow a common and well established approach is to use mass or time averaged quantities and additional fluctiation quantities to describe the flow quantities. This approach is usually refered to as Reynolds averaging process.[32]

$$\begin{aligned} \rho &= \overline{\rho}+\rho',\ u = \tilde{u}+u'' \\ p &= \overline{p}+p',\ v = \tilde{v}+v'' \\ T &= \overline{T}+T'',\ w = \tilde{w}+w'' \end{aligned} \tag{2.12}$$

Equations 2.12 show how some flow quantities are described. For the first coordinate in the Navier-Stokes equations the resulting equation with additional terms due to turbulence based fluctuations which have to be considered is displayed in equation 2.13.

$$\begin{aligned} &\frac{\partial(\overline{\rho}\cdot\tilde{u})}{\partial t}+\frac{\partial(\overline{\rho}\cdot\tilde{u}^2)}{\partial x}+\frac{\partial(\overline{\rho}\cdot\tilde{u}\cdot\tilde{v})}{\partial y}+\frac{\partial(\overline{\rho}\cdot\tilde{u}\cdot\tilde{w})}{\partial z}=\tilde{k}_z-\frac{\partial\overline{p}}{\partial x} \\ &+\mu\cdot\frac{\partial}{\partial x}\left[2\cdot\frac{\partial\tilde{u}}{\partial x}-\frac{2}{3}\cdot\left(\nabla\cdot\tilde{\vec{v}}\right)+\left(2\cdot\frac{\partial\overline{u''}}{\partial x}-\frac{2}{3}\cdot\left(\nabla\cdot\overline{\vec{v}''}\right)\right)\right] \\ &+\mu\cdot\frac{\partial}{\partial y}\left(\frac{\partial\tilde{v}}{\partial x}+\frac{\partial\tilde{u}}{\partial v}+\frac{\partial\overline{v''}}{\partial x}+\frac{\partial\overline{u''}}{\partial v}\right)+\mu\cdot\frac{\partial}{\partial z}\left(\frac{\partial\tilde{w}}{\partial x}+\frac{\partial\tilde{u}}{\partial z}+\frac{\partial\overline{w''}}{\partial x}+\frac{\partial\overline{u''}}{\partial z}\right) \\ &-\left(\frac{\partial\overline{(\rho\cdot u''^2)}}{\partial x}+\frac{\partial\overline{(\rho\cdot u''\cdot v'')}}{\partial y}+\frac{\partial\overline{(\rho\cdot u''\cdot w'')}}{\partial z}\right) \end{aligned} \tag{2.13}$$

[32] Oertel et al 2006, P.216ff.

To close the system of equations it is necessary to introduce modeling approaches to describe the fluctuation quantities.

2.2.3.2 Modeling Procedures for Turbulent Quantities

For the modeling of the turbulent quantities different models exist:[33]

- Direct Numerical Simulation (DNS)
- Large Eddy Simulation (LES)
- Reynolds Averaged Navier Stokes (RANS)
- Hybrid Methods

The direct numerical simulation is the most accurate simulation method of turbulent flow behavior. In this method all Navier-Stokes equations are solved without any averaging or approximation process involved. The method is in need of a very detailed discretisized mesh, which increases the computational effort, making this method not efficiently applicable to complex engineering problems. A simplified method of the direct numerical simulation is the large eddy simulation. In this method large eddies are treated more accurate than small eddies, which reduces the complexity, but also the accuracy. Compared to other simulation methods it is still coupled to high computational effort. For most engineering problems the direct numerical simulation methods are way too complex to obtain the desired quantities (e.g. forces, heat transfer coefficients, etc.). Based on the equations of chapter 2.2.3.1, in which the instationary effects are modeled as part of the turbulence, different approaches can be considered. These Approaches can be summarized under Reynolds averaged Navier-Stokes approaches (RANS).[34]

Two widely applied examples of the RANS model family are the k-ε and the k-ω model. Both models use the turbulent energy as one variable to describe the turbulent behavior. In the k-ε model the second quantity used is the turbulent dissipation rate. The k-ω model uses the energy dissipation frequency as model variable. In regards to clutch systems the realizable k-ε model has the advantage of being more accurate for swirling flows. A detailed comparison of available RANS turbulence modeling procedures and models can be found in[35].

2.2.3.3 Fluid Flow and Heat Transfer over a Flat Plate

The flow field of a fluid flowing around a solid body can be roughly divided into two main regions. In the first region near the surface of the body the fluid velocity tends towards the bodies velocity with decreasing normal distance to the surface due to frictional forces. This region, where frictional forces have a notable effect, is referred

[33] Ferzinger & Peric 2008, P.315ff.
[34] Ferzinger & Peric 2008, P.344ff.
[35] Zhai, Zhang & Chen 2007

to in literature as boundary layer. Figure 11 shows the velocity and temperature field for a fluid flowing over a flat plate.

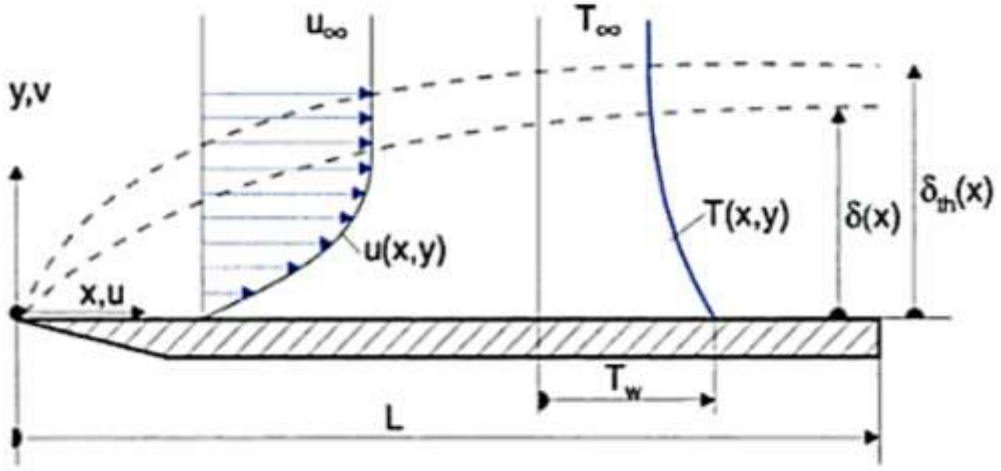

Figure 11: Temperature and Velocity Field of a Fluid Flowing over a Flat Plate[36]

From the onset of the plate, the boundary layer thickness δ(x) increases. As displayed, the velocity rises with increasing distance from the plate surface. The boundary layer thickness is usually defined as distance from the surface, where the fluid velocity has reached 99% of the free stream velocity. With increasing distance from the plates onset or with a rising free stream velocity it becomes necessary to further divide the boundary layer due to additional turbulent effects.[37]

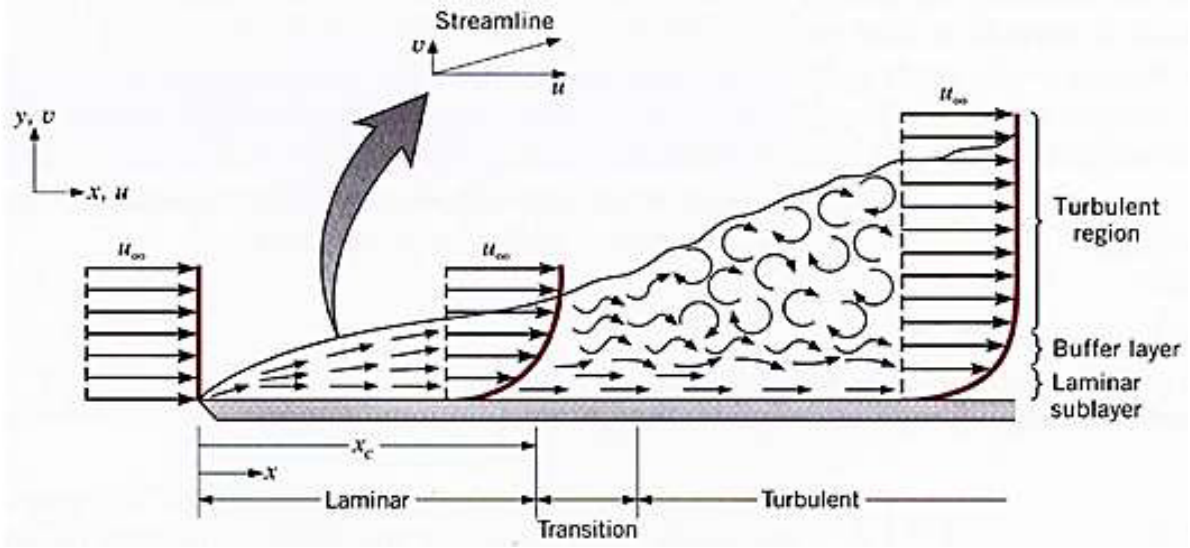

Figure 12: Flow Structure of a Boundary Layer over a Flat Plate[38]

[36] Kopitz & Polifke 2009, P.210
[37] http://me-lrt.de/warme-stoff-transport-grenzschichten-temperatur-geschwindigkeit
[38] http://me-lrt.de/warme-stoff-transport-grenzschichten-temperatur-geschwindigkeit

Over the length of the plate the boundary layer can be divided into three individual, but dependent zones (Figure 12). In the laminar zone, the fluid flow is considered to have one main flow direction and the flow system has an organized character. In the turbulent zone the flow structure in surface normal direction can again be divided into three main layers. Near the surface the fluid flow has almost laminar character. This region is defined as laminar sublayer. In this region, as in the earlier defined laminar zone of the boundary layer, forces are mainly transferred by viscosity based shear. In the turbulent layer, fluid forces are mainly transferred by turbulent mixing. The transition region from the laminar sublayer to the turbulent outer layer is referred to in literature as buffer or transition layer. In this zone both diffusion and turbulent mixing are of same order of magnitude.[39]

To describe the velocity inside the boundary layer, a well-established approach is to use wall laws. The approach is based on the following main assumptions[40]:

1. The flow field inside the boundary layer is mainly one dimensional
2. The pressure gradient in flow direction is small
3. Inside the viscous sublayer viscosity based shear forces are larger than turbulence based shear forces
4. In the turbulent layer viscous forces have negligible effect

With these assumptions eq. 2.14 (valid in the viscous sublayer) and eq. 2.15 (valid in the turbulent layer) can be derived from the boundary layer equations.[41]

$$u^+ = y^+ = \frac{y \cdot u_\tau}{\upsilon} \tag{2.14}$$

$$u^+ = \frac{1}{\kappa} \cdot \ln\left(y^+\right) + C^+ \tag{2.15}$$

$$u_\tau = \sqrt{\frac{\tau_w}{\rho}} \tag{2.16}$$

These wall laws have universal character and are offered and used in mostly all CFD-codes.

[39] Oertel et al 2006, P.254ff.
[40] Schlichting & Gertsen 2005, P.27ff.
[41] Schlichting & Gertsen 2005, P.145ff.

The heat transfer from a flat plate is closely coupled to the flow field. For most flow systems this coupling can be described by the Prandtl-Number.

$$h_{loc} = \frac{\dot{q}_w}{\left(T_w - T_{fl,loc}\right)} = \frac{\rho \cdot c_p \cdot u_\tau}{T^+} \tag{2.17}$$

$$T^+ = Pr \cdot u^+ \tag{2.18}$$

$$T^+ = Pr_t \cdot \left(u^+ + P\right) \tag{2.19}$$

$$P = f\left(Pr, Pr_t\right) \text{ with } Pr = 0.7 \text{ and } Pr_t = 0.85 \text{ for air} \tag{2.20}$$

As can be seen from equations 2.17 to 2.20 the temperature field and therefore the overall heat transfer by convection is closely coupled to the flow field around the body of interest.[42]

A high convectional heat transfer can therefore be obtained by a high density or thermal capacity of the fluid, high frictional forces at the surface and a high temperature gradient between the fluid and the solid body.

2.2.3.4 Heat Transfer Coefficient Definitions

For the description of the heat transfer coefficients inside the clutch system, three main possibilities exist: [43]

1. Local heat transfer coefficient together with the local wall temperature and the temperature in the cell next to the wall (eq. 2.21)

2. Local heat transfer coefficient together with a fluid reference temperature at a specified y+ value (eq. 2.22), generally known as the “specified wall y+ heat transfer coefficient”

3. Heat transfer coefficient based on a global reference temperature (eq. 2.23)

For both the first and second option it is necessary to evaluate the temperature distribution around the body of interest and the local heat transfer coefficient. This approach would increase the complexity of a simplified thermal clutch model, because it would be additionally necessary to model the wall temperature and the temperature field of the air inside the bell housing.

The third option offered by the simulation software is to use a heat transfer coefficient based on a global reference temperature (equation 2.23). The reference temperature is mainly chosen in dependence of the flow system. For pipe flows for instance the inlet

---

[42] Schlichting & Gertsen 2005, P.235ff.

[43] Star-CCM+ User Manual 2010

or outlet temperature of the flow can be chosen. For the closely related research field of mixing vessel flow systems the average temperature of air mainly is chosen as reference temperature.

$$h_{loc} = \frac{q_w}{\left(T_{wall} - T_{fl,cell}\right)} \tag{2.21}$$

$$h_{loc,y+} = \frac{q_w}{\left(T_{wall} - T_{fl,y+}\right)} \tag{2.22}$$

$$h_{gobal} = \frac{q_w}{\left(T_{wall} - T_{ref.}\right)} \tag{2.23}$$

Another possibility to describe the convective heat transfer is the adiabatic heat transfer coefficient.[44] This method applies when the temperature field is facing large variations (e.g. cooling of circuit board components). The adiabatic heat transfer coefficient is then defined by eq. 2.24.

$$h_{ad} = \frac{q_w}{\left(T_{wall} - T_{wall,adiabatic}\right)} \tag{2.24}$$

Apart from the other definitions presented earlier, this heat transfer coefficient uses the adiabatic wall temperature as reference temperature, which can be obtained with the help of CFD simulation and setting the boundary heat flux to zero. The resulting heat transfer coefficient is only dependent on geometrical and fluid flow boundary conditions. For clutch systems the temperature field is in general relatively stable, with regards to the heating source, making the additional simulation effort to obtain the adiabatic wall temperature and evaluating the heat transfer coefficient a not very effective approach.

2.2.3.5 Similarity Analysis

Since the flow field inside the bell housing is mainly caused by frictional and displacement effects, the analogy theorems can be a useful baseline for considerations on the transferability of heat transfer laws from one clutch system to another.

Reynolds was the first to discover the close relation between the impulse and energy equations. The heat flux at a wall is proportional to the temperature profile which in itself is proportional to the fluid velocity gradient. This coupling is generally described by equation 2.25 for flow systems with a Prandtl-Number close to or equal to one.[45]

[44] Moffat 2010; Li, Zhou & Aung 2009; Rhee 2006

[45] Pischinger et al 2009, P.17

$$c_f \cdot \frac{Re}{2} = Nu \tag{2.25}$$

$$c_f \cdot \frac{Re}{2} \cdot Pr^{\frac{1}{3}} = Nu \tag{2.26}$$

For other values of the Prandtl-Number (Prandtl-Number for air: 0.71) equation 2.26 can be used. It is the modified analogy of Chilton-Colburn[46]. In both equations the remaining task is to identify the dependence of surface friction coefficients on the rotation rate. In rotating systems, for example, the Reynolds number can be described by equation 2.27 and the Nusselt number can be described by equation 2.28 of chapter 2.2.3.6.

2.2.3.6 Rotating Disk in Free Air

In Figure 13 the flow field in the simplest case of a rotating disk system is shown. Fluid is being pumped towards the center of the disk and then is accelerated in circumferential direction. Due to centrifugal forces, the fluid moves towards the outer radius of the disk. As displayed in Figure 13 force transmission by shear stress also causes movement in a small distance above the surface of the disk. It can be observed, that the overall flow structure is three dimensional. Theodor v. Karman was the first to investigate and present a solution to this boundary layer problem with regards to the flow system.[47]

[46] Kopitz & Polifke 2009, P.275ff.

[47] Schlichting & Gertsen 2005, P.120ff.

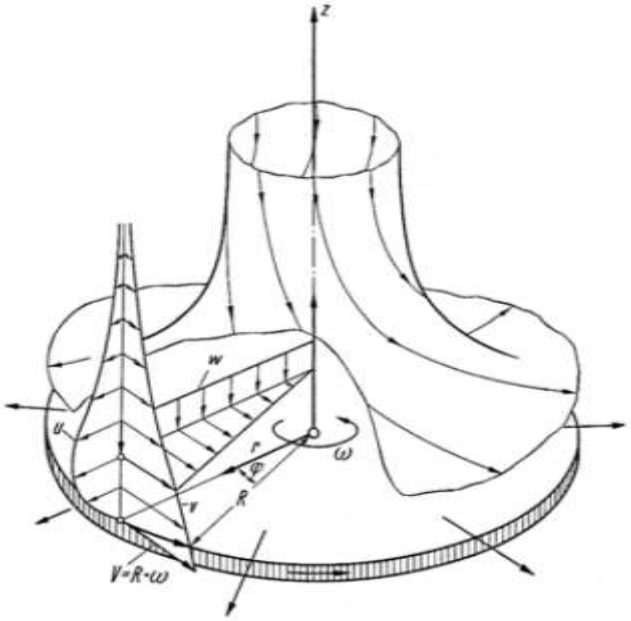

Figure 13: Flow Field around a Rotating Disk[48]

A detailed and extensive review on Heat transfer from rotating disk systems was performed by Shevchuck.[49] He summarized the work of different authors and found that for laminar flow of an isothermally heated disk rotating in free air, heat transfer can most generally be described by equation (2.28) with a good match to experimental data. The Nusselt number displayed in equation (2.28) represents the relation between convectional and conductional heat transfer normal to a boundary layer with the Reynolds number for rotating systems defined by equation (2.29).

$$Nu = K_1 \cdot Re^{n_R} \; ; n_R = 0.5 \text{ and } K_1 = 0.32...0.34 \tag{2.28}$$

$$Re_\Omega = \frac{\omega \cdot r_a^2}{v} \tag{2.29}$$

For the laminar and isothermal case, the heat transferred is therefore dependent on the viscosity, engine speed and the disks dimensions.

In case of a turbulent flow condition the constant K_1 changes and the exponent n_R approaches 0.8. Since on a rotating disk both laminar and turbulent regions can be found, Shevchuck introduced an approach using a new relation for the velocity and temperature profiles to solve the flow and energy equations inside the boundary layer and obtain a solution valid for the entire disk.

$$K_1 = A_c \cdot (1+\alpha^2)^{\frac{1}{2}} \cdot Pr \cdot \left(\frac{4+m}{2+m+n^*} \cdot K_V \cdot b_2 + (1-K_V)^{n_P} \cdot b_1 \right)^{-1} \tag{2.30}$$

[48] Schlichting & Gertsen 2005, P.121

[49] Shevchuk 2009

The relation for the constant K_1 from this novel approach is displayed in equation 2.30. From this equation it can be derived, that the heat transfer on a rotating disk in free air is not only dependent on the viscosity, rotation rate and size of the disk, but also on the temperature distribution on the disk (n*), the vorticity of the flow and the surface roughness. It can be easily seen that even in this simplified case it is difficult to obtain the correct heat transfer characteristics from an analytical equation.[50]

Application examples of modeling procedures and measurements on heat transfer from rotating disks can be found in [51].

2.2.3.7 Enclosed Rotating Disk

For an enclosed rotating disk, the physical considerations from the disk rotating in free air are still active. Since the fluid in this case is not taken from an unlimited reservoir as in the free air case, the flow structure and the heat transfer will be slightly different. The friction torque necessary to maintain the rotation rate of the rotating disk can be less than in the free air case, since part of the kinetic energy transferred to the air inside the enclosure can be retained.[52]

2.2.3.8 Rotating Disk with Stationary Wall / Co-Rotating Disks

If simplified, the phenomena of two co-rotating disks and a rotating disk with a stationary wall can be discussed together. The only difference between the two cases is the relation of the rotation rate.

[50] Shevchuck 2009, P.33ff.

[51] Kreith et al 1958; Wagner 1948; Lavalle & Rahman 2010; Cardone et al 1996; Adair & Tucker 1997

[52] Zierep & Bühler 1991, P.110ff.

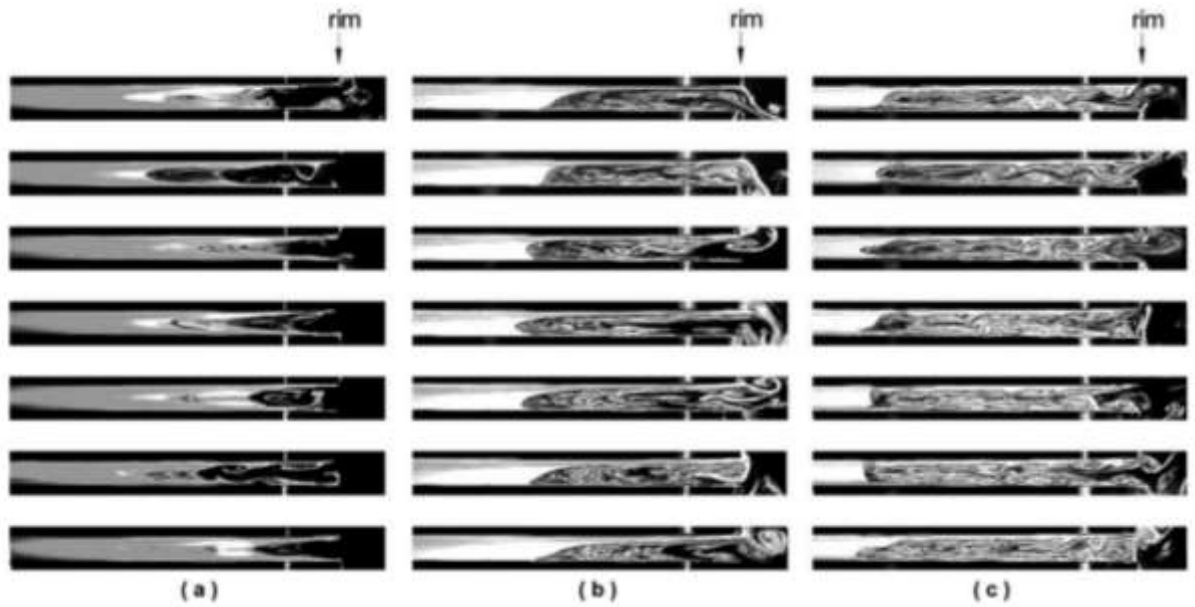

Figure 14: Flow Structure of Rotating Disks with: (a): Co-Rotation; (b) Rotor / Stator; (c) Counter Rotation

In Figure 14 the different configurations of the flow structure of two in parallel rotating disks is shown [53]. While in the case of co-rotation, there exists nearly no exchange with the ambient air for air located near the center of rotation, the situation changes if there exists a relative rotation rate difference.

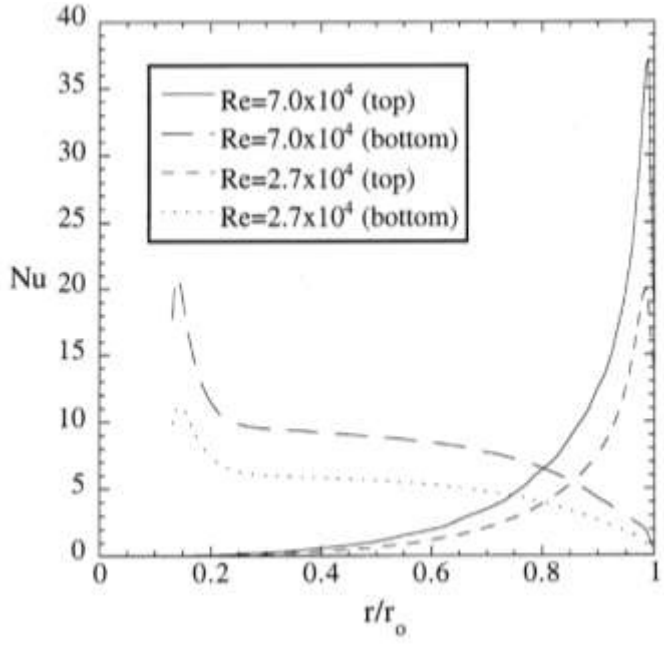

Figure 15: Nusselt Numbers for a Stationary and a Rotating Disk[54]

[53] Soong et al 2003
[54] Hill & Ball 1999

As can be concluded from Figure 14, turbulence and also flow exchange with ambient air increases with increasing speed difference between the two disks.

Figure 15 shows the Nusselt numbers for two disks arranged one above the other in a rotor-stator case. It can be seen, that for the rotating disk (labeled top in Figure 15) the heat transfer increases progressively towards the outer radius due to a large velocity gradient.

2.2.3.9 Rotating Cavity with Radial Outflow

Figure 16 shows two examples of the flow field of rotating cavities with radial outflow.

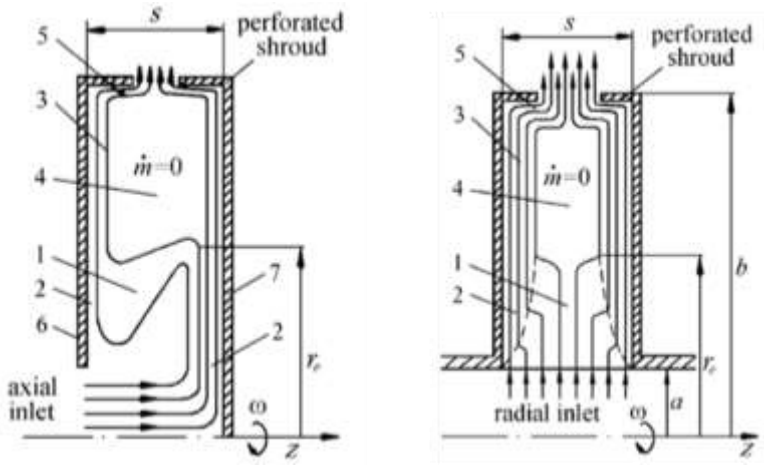

Figure 16: Examples of Streamlines for Rotating Cavities with Radial Outflow[55]

Air enters the rotating cavity and is forced towards the outer radius of the cavity by centrifugal forces. A unique difference to the earlier presented flow systems is, that in both configurations an area, which has no mass exchange with the rest of the flow field, forms. This area can be assumed rotating as solid mass. The amount of heat transferred from the rotating cavity is dependent on the size of the cavity inlets and outlets and also on the distance between the axial restrictions.[56]

2.2.3.10 Enclosed Rotating Cylinder

The flow structure of a cylinder rotating inside a closed housing is quite similar to the flow system of an enclosed rotating disk. If the cylinder radius is considered small against the cylinder length, the flow system displayed in Figure 17 will develop.

[55] Shevchuck 2009, P.149

[56] Shevchuck 2009, P.147ff.

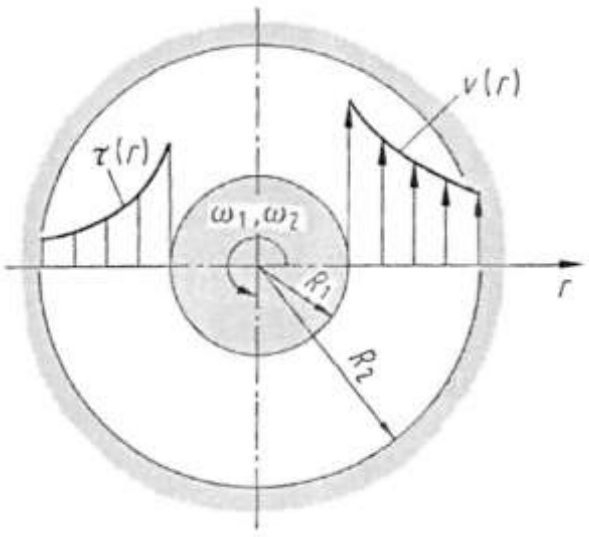

Figure 17: Flow Structure of an Enclosed Rotating Cylinder[57]

In Figure 17 the outer enclosure also rotates with a constant rotation rate. If the rotation rate is set to zero, the flow system and therefore the heat transfer will be comparable to that of a Couette flow.

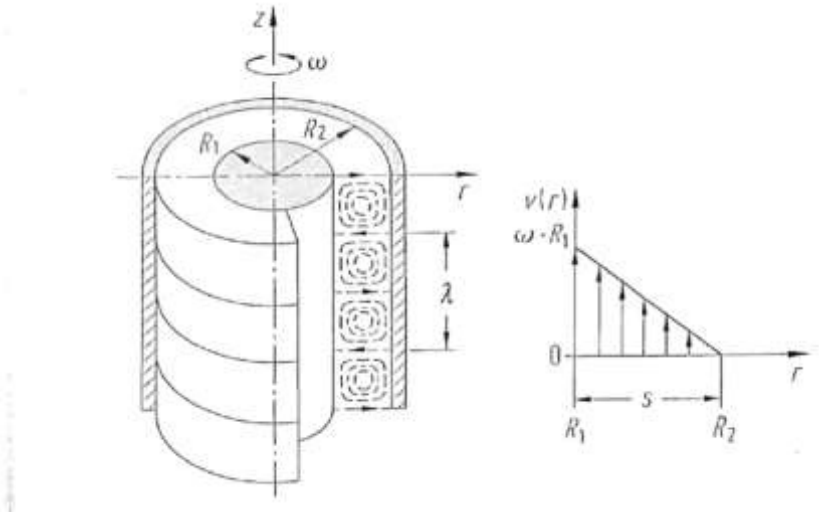

Figure 18: Taylor Swirls of an Enclosed Rotating Cylinder[58]

With an increasing rotation rate of the cylinder it is possible, that instabilities of the flow field, known as Taylor swirls occur (Figure 18). These turbulent swirls lead to an increased impulse exchange and an increased frictional torque (equal to an increase in the heat transfer coefficient).[59]

[57] Zierep & Bühler 1991, P.52
[58] Zierep & Bühler 1991, P.60
[59] Zierep & Bühler 1991, P.51ff.

2.2.3.11 Simulation Methods for Rotating Systems

For the modeling of the rotational movement of a clutch system, three main concepts exist. The first concept is to simply apply a velocity boundary condition to the surface with a pre-defined reference rotation axis. In this simple approach no additional acceleration terms are added to the equations of movement. This proceeding can be applied if the modeled rotating geometry has no (or very few negligible) faces spanned in the axial and radial direction in a cylindrical coordinate system based on the rotation axis. If many surfaces are oriented in the explained way, the modeling approach can result in high inaccuracies, because displacement effects are not considered.[60]

In the second and most widely applied concept, the modeled system is divided into individual regions, in best case connected by conformal interfaces. Each region is then assigned to a pre-defined coordinate system and a rotation rate around a selected axis can be set. This approach is called “moving reference frame” (MRF)[61]. The main concept of this approach is that the flow inside the rotating region is treated and solved under stationary conditions. To obtain the stationary conditions additional acceleration terms are added to the impulse equations. These terms represent the coriolis and centrifugal forces present when describing the movement of a rotating system from a stationary observing point. When the MRF region is surrounded with a stationary region, two main concepts for coupling these regions exist. In the first concept the regions are coupled directly. This results in the often confusing fact, that the flow through the stationary part of the flow system is only valid for the current angular position of the clutch system. The second approach to this problem is to provide an averaging algorithm in circumferential direction on the coupling surface. This approach is often referred to as “mixing plane”[62]. The solution for the exchange between the stationary and rotating region is therefore blurred. Application examples of moving reference frame can be found in [63].

The most accurate reproduction of a flow system for a rotating geometry can be obtained by applying the third concept, the sliding mesh method. In this method, the mesh is divided into two different meshing regions, a rotating and a stationary region with a conformal interface between them. After the solution for one relative position between these two meshes is obtained, the rotating region is rotated one step ahead, so that each cell on the interface is connected to the next partner. This procedure is then repeated until a stopping criteria (rotation angle or simulation time) is reached. Of

[60] Fluent 2001, Chapter 9
[61] Wesseling 2009, P.47
[62] Wu et al, 2013
[63] Tamm 2002; Schütz 2009; Zadravec 2007; Thuresson 2014; Gullberg et al 2009, Hopf & Gauch 2000

all the presented methods, this method requires the highest computational resources due to the transient structure of the method.[64]

2.2.3.12 CFD Simulations and Flow Analysis on Clutch Systems

Wittig et al[65] studied the influence of positioning different orifices or fans on a clutch system to increase the heat transfer. They used a rotating reference frame method coupled with stationary boundary conditions on an abstracted geometry to solve the flow field. Due to periodical symmetry of the clutch system they only simulated a reduced pie section. As thermal boundary condition, the hot parts, e.g. pressure plate, were set to 200 °C and all other parts to 100 °C.

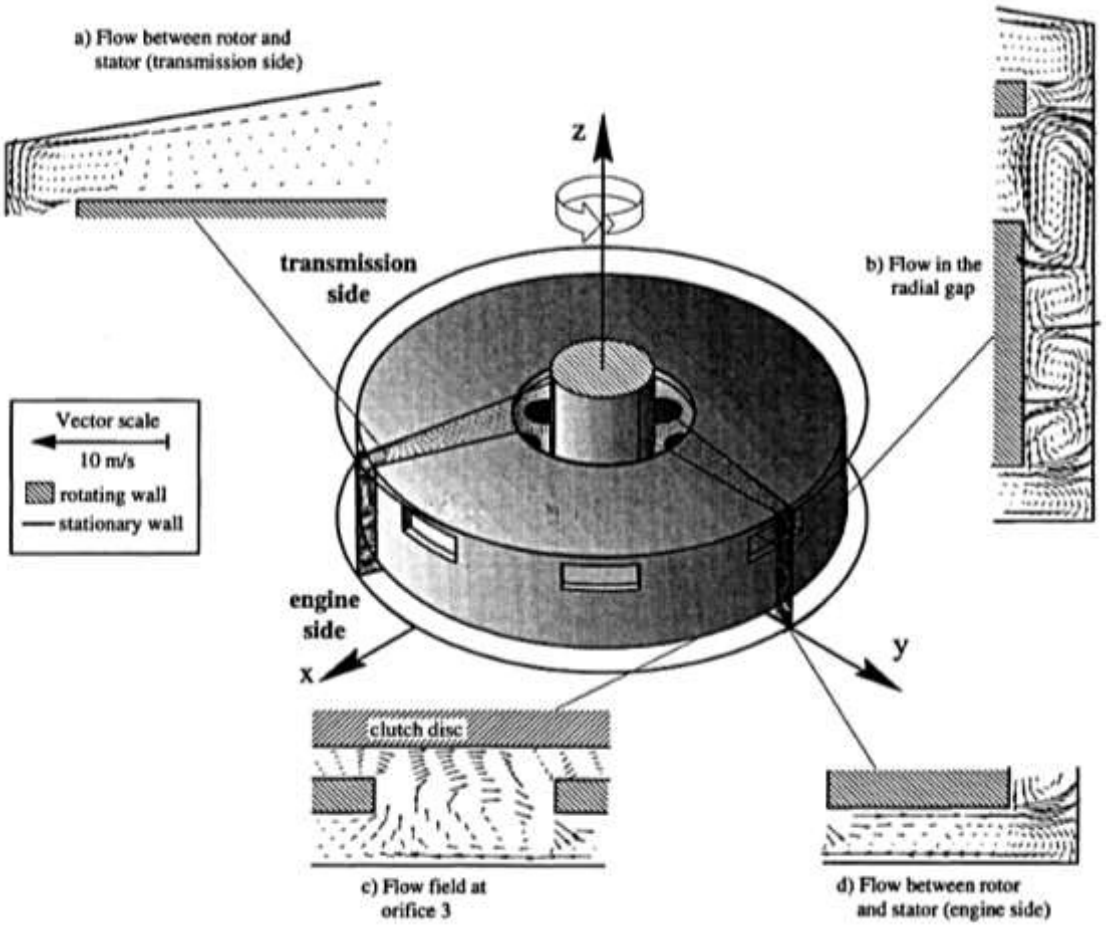

Figure 19: Results for the Flow Field of [66]

Figure 19 shows the flow field results from the investigation. At the engine and transmission side of the clutch system, air is being accelerated towards the outer diameter. At the transmission or engine wall air recirculates back to the inner diameter of the clutch system. This is closely related to a disk rotating close to a stationary wall.

[64] Ferrer 2015; Schwarze 2013; Benkreira 1996
[65] Wittig et al 1998
[66] Wittig et al 1998

They concluded that through intelligent positioning of fans or orifices, heat transfer can be increased. They also pointed out that CFD-simulations are highly important for optimization purposes and precise heat transfer determination of high speed rotating components.

Lee and Cho[67] used a CFD-simulation model to predict the heat transfer characteristics of a clutch system and implemented the results into a finite element code to predict the temperatures of a clutch system during a cyclic event. They also chose to simulate only a section of the total geometry to save computational complexity. As thermal boundary conditions, they set the pressure plate and flywheel temperature at a constant temperature.

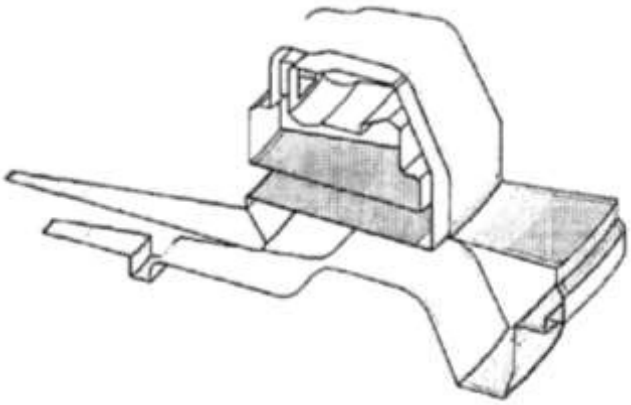

Figure 20: CFD-Modeling Geometry of [68]

A difference to the simulations from Wittig et al is that Lee and Cho did not use a rotating reference method, but set the rotating velocity property at the surface. As explained in chapter 2.2.3.11 this approach does not consider any displacement effects from surfaces oriented in the axial-radial direction inside the clutch system. Still the comparison with measurement data showed that the simulations were within an error of ± 5 °C.

Pryzbilla et al[69] used a simplified conjugate heat transfer CFD-model of a clutch system to gain information of the heat transfer characteristics inside the clutch system, to be used as boundary conditions for a clutch size determination tool. Their model used the rotating reference frame method and a constant heat input rate of 260 W per frictional interface. Their result for the pressure plate temperature for an engine speed of 2500 rpm can be seen in Figure 21.

[67] Lee & Cho 2006
[68] Lee & Cho 2006
[69] Pryzbilla et al 2011

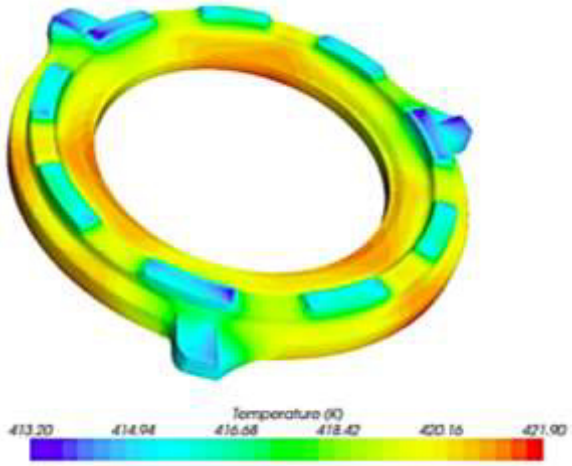

Figure 21: Simulated Temperature Distribution in the Pressure Plate[70]

The Authors focus on the temperatures and the heat transfer coefficients, but give no information on the flow structure and on the validity of the CFD simulation. They conclude that the CFD analysis is a powerful tool in the design selection process and can give valuable information on how the heat is transferred inside the bell housing.

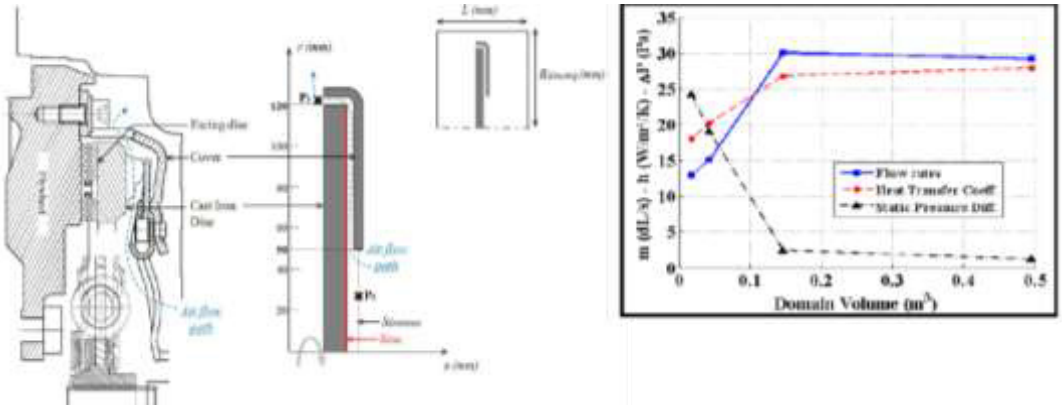

Figure 22: Simulation Domain and Results of [71]

In [72] the general influence of housing size was investigated. The main result of this work is that until a specific size of the surrounding domain is reached heat transfer and flow rates increase. With increasing domain size the system tends to behave like a system rotating in free air.

The influence of an active cooling concept for commercial vehicles is displayed in [73]. According to the authors, the efficiency of a heavy duty vehicle can be increased by 6 to 41 %.

[70] Pryzbilla et al 2011
[71] Levillan et al 2015
[72] Levillan et al 2015
[73] Neumann & Stürmer 2007

A summary of possibilities and current state of research on dry clutch cooling concepts can be found in [74].

2.3 Flow Measurement Principles

A detailed and extensive summary of possible procedures and devices for measuring physical flow properties can be found in [75], on which this section is mainly based. To classify the different measurement techniques in regards of this study and their functional principle they were segmented as displayed in Figure 23.

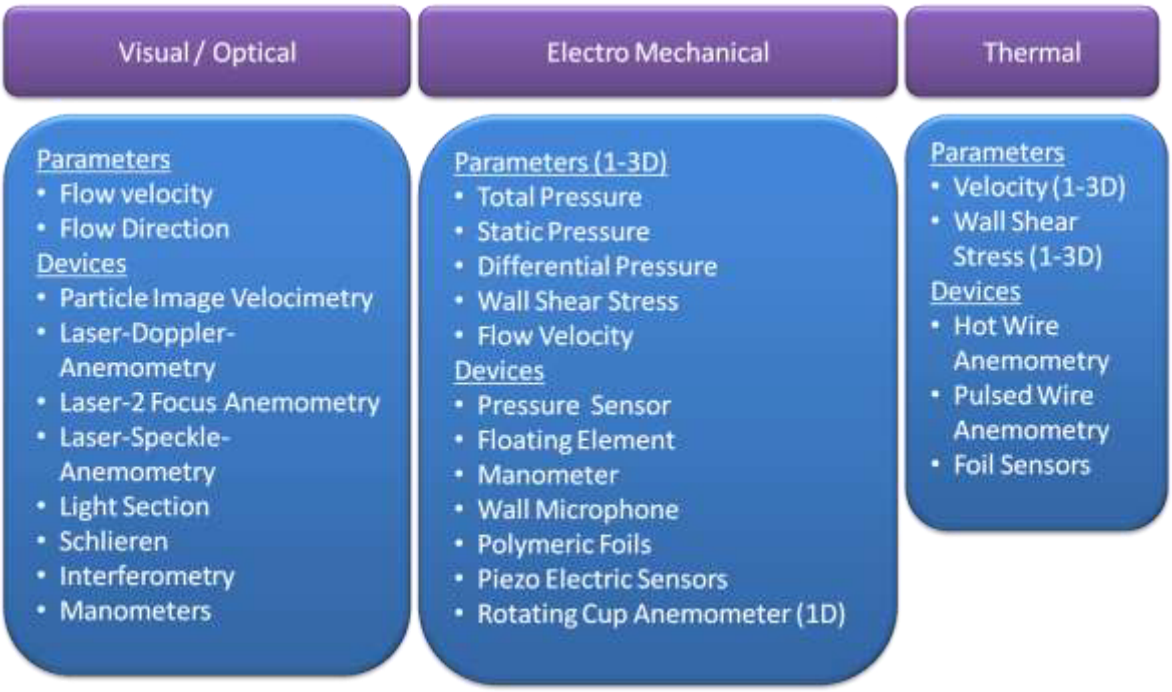

Figure 23: Segmentation of Available Measurement Techniques

2.3.1 Visual / Optical Measurement Techniques

Nearly all visual flow measurement techniques use particles which are added to the fluid for flow visualization. Most important properties of the particles (tracers) are that they have a good following behavior and have approximately the same density as the fluid observed. If the tracer particles are too large or have a high mass, the fluid flow will not be captured correctly due to inertia forces. The tracers are made visible by adding a light source, which is most commonly a laser. A selection of different visualization techniques is presented in Figure 24.

[74] Beitler 2008, P.44ff.
[75] Nitsche & Brunn 2006

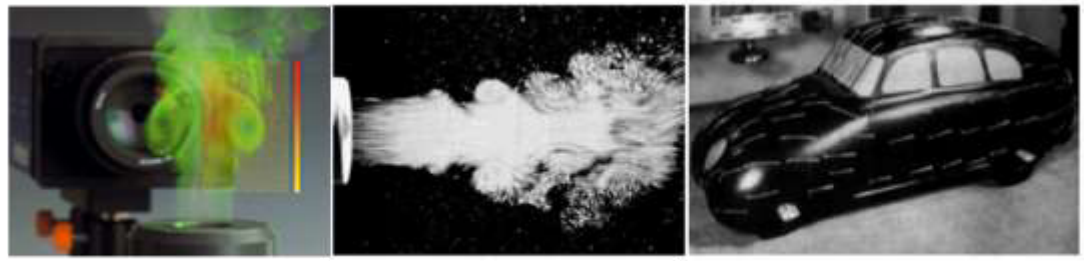

Figure 24: Flow Visualization Techniques[76]

The obtained visible particles can then be used to obtain a qualitative image of the flow field, or to quantify the velocity vector field through particle image velocimetry (PIV). The PIV technique uses a high speed CCD-camera to take two consecutive pictures of the luminous particles in the flow field. With a tracking algorithm the movement of individual groups of particles can then be identified.

A technique without the need of adding particles is the interferometry technique. It uses the refraction properties of the fluid under investigation. Density distributions cause a refraction of a light beam subjected to the fluid. The refraction angle can be used to correlate the fluid velocity.

Manometers are also categorized as visual measurement technique. In the simplest case the fluid pressure of a fluid of interest is directly subjected to a fluid inside a manometer. The different pressures at the two ends of the fluid in a glass tube cause the fluid to rise or fall, making it possible to directly correlate the fluid pressure.

For rotating flow systems with a high packaging, visualization techniques such as adding wool strings to the surface or adding color to the fluid cannot be applied due to packaging. Another difficulty of visualization techniques with regards to a clutch system is the need of visual access to the flow field of interest. The visual measurement techniques can therefore be efficiently used for measurements outside of the clutch system. Measurements inside the clutch system can only be performed with additional significant effort and resources as parts of the following examples show.

In literature visual measurement principles have been applied to similar problems. Kunisaki et al[77] for example used particle image velocimetry to measure the flow field inside a torque converter. To get visual access to the inside they constructed one cover side out of Plexiglas as shown on the left side of Figure 25.

[76] Nitsche & Brunn 2006, P.155 & P.161; La Vision Homepage www.lavision.de
[77] Kunisaki et al 2001

Figure 25: Modified Torque Converter[78]

Kuboti et al[79] studied in a similar manner the influences of the flow behavior of the working fluid on the lock up operation of a torque converter.

The tightly coupled flow behavior of rotating disk systems has been studied by several authors. Wu[80] used the particle image velocimetry and laser section to measure and visualize the flow field in between two co-rotating disks. He indicated that the flow field between the disks is three dimensional, but can be characterized by a two dimensional measurement technique. Moisy et al performed measurements on counter rotating disks in [81]. They conclude that 2D measurements are possible if a certain ratio between the disk distance and disks outer radius is adhered. At higher ratios the fluid flow becomes more unstable and the three dimensional proportions of the flow increase.

Albers et al.[82] present the potential of PIV measurements to aid the verification of CFD simulations on the example of a wet clutch. They highlight that by the use of a PIV system the verification process can be enhanced by the measurement of inner variables (e.g. velocity vector). Usual verification processes use external variables such as drag torque which result from the flow field inside the considered system. They show that their CFD simulation model and the PIV measurements are in good accordance, but local differences in the flow field exist.

Another broad application of PIV in flow field studies of rotating machinery can be found in the field of turbomachinery research. A good overview on activities in this topic can be found in[83]. Main interest in these measurements is the flow behavior around the turbine blades regarding optimization potentials.

It can be concluded from literature, that flow measurements inside and outside of rotating systems can be performed and aid the understanding and verification of

[78] Kunisaki et al 2001
[79] Kubota et al 2003
[80] Wu 2009
[81] Moisy et al 2003
[82] Albers et al 2012 b
[83] Wosetschläger & Göttlich 2008

rotating flow systems. Compared to other measurement techniques the particle image velocimetry has the advantage of delivering the highest amount of information by measuring flow planes. The positioning of the measurement planes in the flow field of interest has to be performed based on all prior knowledge available. Three dimensional influences, flow instabilities and transient effects can influence the measurement results. This technique can be efficiently used for flow problems with good visual access. With decreasing visual accessibility (e.g. flow inside a clutch system) the complexity of the measurement problem rises due to additional measures to gain visual access.

2.3.2 Electro / Mechanical Measurement Techniques

Electro / Mechanical measurement techniques are based on transforming fluid forces acting onto a specified surface of the measurement probe into translational forces. A good example is the floating element device.

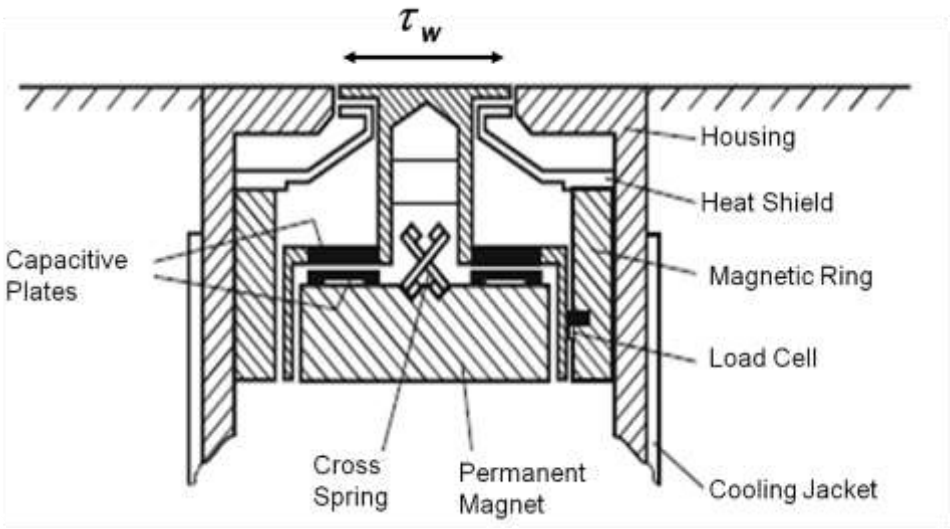

Figure 26: Floating Element Wall Shear Stress Sensor; adapted from[84]

With a floating element device, the wall shear stress can be directly calculated by measuring the offset of the floating element under flow conditions with an inductive displacement sensor and the elasticity of the support springs. Figure 26 shows an example of such a floating element sensor. For a rotating cup measurement device the fluid forces acting on the impeller of the probe cause it to turn. The kinetic energy of the impeller is then transformed into electrical energy.

Pressure sensing techniques are nearly all based on a pressure based deformation of a diaphragm. The deformation is then transformed by piezo-quartz elements or strain

[84] Nitsche & Brunn 2006, P.85

gages into an electric signal to determine the local pressure. A selection of measurement principles is shown in Figure 27.

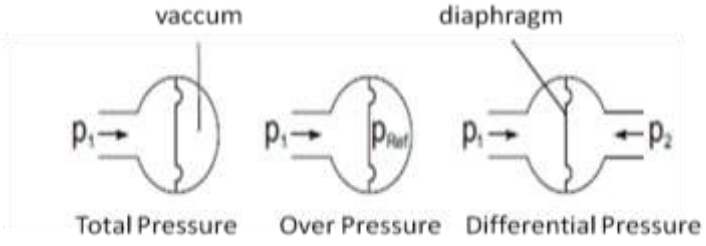

Figure 27: Pressure Sensing Principles[85]

Pressure sensors can also be used for wall shear stress measurements. A widely used technique is the Preston-Tube Method. Main advantage is that Preston tubes are relatively simple to handle. The method uses the unsymmetrical velocity profile to correlate the wall shear stress and has to be calibrated according to the boundary conditions of the measurement problem. An enhancement of the procedure is the Computer-Aided-Preston-Tube-Method (CPM). The method consists of iteratively correcting the wall shear stress value to adjust the velocity profile based on the wall laws. An extension of this method is the CPM3 method. In this method three Preston tubes with different diameters are used to measure the local effective velocity. The wall shear stress of all tubes is then adjusted iteratively to fit the velocity profile until the calculated wall shear stress of all tubes is equal.

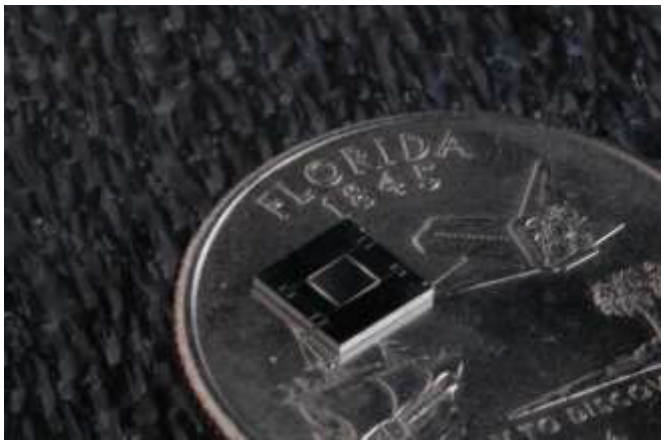

Figure 28: MEMS Wall Shear Stress Sensor[86]

If only small packaging space is available, the group of Micro-Electro-Mechanical Systems (MEMS) offers a great potential. The technology of silicon based integrated

[85] Nitsche & Brunn 2006, P.25

[86] http://www.nasa.gov/topics/aeronautics/features/shear_stress_prt.htm

circuit micromachining makes it possible to construct sensors, actuators and microsystems with high performance and a low requirement on packaging space.[87] Figure 28 shows the size of a recently developed MEMS floating element sensor for wall shear stress measurements.

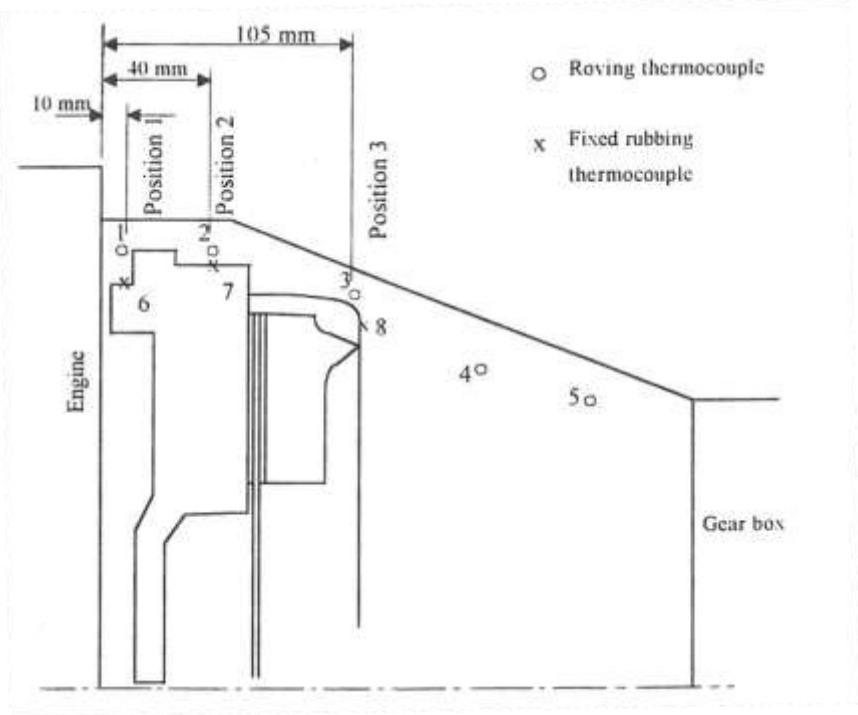

Figure 29: Measurement Positions of [88]

One example of applying an electro mechanical measurement technique to a clutch related problem can be found in [89]. Pitot tubes with a built in temperature sensor are used to measure the pressure and temperature distributions at several specific positions around the clutch system. The pressure was then transformed into a velocity value by using the Bernoulli equation. The Nusselt-Reynolds correlation was then used to find a relation between the velocity and heat transfer coefficient, which was not successful. The difficulties were related to the assumptions made and additional influences from radiation. Figure 29 shows the measurement positions.

For the measurements inside a rotating clutch system the displayed devices are rated as not suitable. The most critical aspects are the packaging of the sensor and the acceleration forces acting on the sensor due to the rotation of the clutch. Electro mechanical measurement techniques are most suitable for measurements under stationary conditions. For the measurements of fluid velocities and pressures of the flow outside of the clutch system, the displayed techniques are most suitable. The

[87] Naughton & Sheplak 2002
[88] Ford Report REP 1485 P.63
[89] Ford Report REP 1485

measurement technique can also be used to aid calibration of other sensors as will be shown later.

2.3.3 Thermal Measurement Techniques

Thermal measurement techniques use tight coupling between the flow field and the temperature field. The two most widely used techniques are the hot wire anemometry and the pulsed wire anemometry. The latter technique operates by the transmitter / receiver principle. An element is used to generate a short heat pulse in the fluid, while other elements in direct neighborhood act as receivers. The time delay between the emission of the heat pulse and the detection by the receiver elements can then be used to calculate the flow velocity. A typical sensor probe is shown in Figure 30.

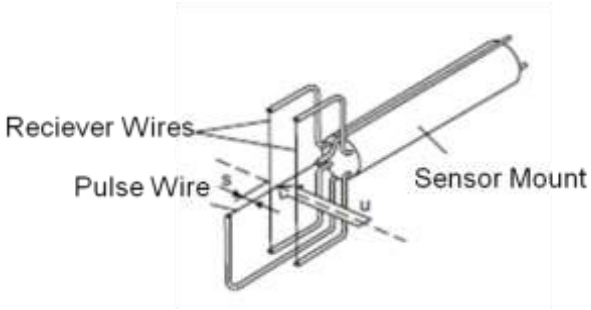

Figure 30: Pulsed Wire Probe, adapted from [90]

Hot wire anemometry is based on measuring the heat dissipation of the sensor. Like resistance thermometers, the electrical resistance of the sensing element is used to calculate its temperature (equation 2.31). The author of [91] also differentiates sensors between passive mode (negligible self-heating - only applicable for temperature measurements) and active mode (strong self-heating – heat transfer / wall shear stress / flow velocity measurements). Operation of a sensor in active mode is also referred to in literature as constant temperature anemometry (CTA).

$$R(T) = R_0 \cdot [1 + \alpha(T - T_r)] \tag{2.31}$$

When subjected to a fluid with a specific flow velocity, the temperature of the sensing element will decrease due to the increase in convectional cooling (free and forced convection now active). In active mode the sensor voltage has to be increased to obtain the same temperature as under the fluid-at-rest condition. This increase can then be used efficiently as quantifier for fluid velocity.

[90] Nitsche & Brunn 2006, P.56
[91] Mocikat & Herwig 2009

The sensitivity of a hot wire anemometer sensor to temperature can be described according to by equation 2.32.[92]

$$S_R = \frac{\partial R(T)}{\partial T} = R_0 \cdot \alpha \tag{2.32}$$

The overall and stationary heat balance without radiation from the sensing element of the sensor is displayed in equation 2.33 and 2.34. If the ambient temperature (usual value 20°C) is considered as reference temperature, the sensor sensitivity can be reformulated by integrating equation 2.35 into 2.31 and differentiating the resulting equation with respect to the convectional conductance.

$$\dot{Q}_{in} = \dot{Q}_{out} \tag{2.33}$$

$$\dot{Q}_{out} = \frac{\lambda \cdot A_{cond}}{l_{cond}} \cdot (T - T_{amb}) + h \cdot A_{conv} \cdot (T - T_{amb}) \tag{2.34}$$

$$(T - T_{amb}) = \frac{\dot{Q}_{out}}{L_{cond} + L_{conv}} \tag{2.35}$$

$$R(L_{conv}) = R_0 \cdot \left(\left[1 + \alpha \cdot \frac{\dot{Q}_{in}}{L_{cond} + L_{conv}} \right] \right) \tag{2.36}$$

$$S_R = \frac{\partial R(L_{conv})}{\partial L_{conv}} = \frac{-R_0 \cdot \alpha \cdot \dot{Q}_{in}}{(L_{cond} + L_{conv})^2} \tag{2.37}$$

The sensitivity towards convection (eq. 2.37) can therefore be maximized by enhancing the heat generated in the sensing element, minimizing the conduction losses to the support material and a high sensor coefficient (reference resistance multiplied with the specific temperature coefficient). These considerations can be utilized as design and mounting guidelines for foil sensors. With optimized parameters it is possible to measure turbulence related fluctuation quantities with these sensors.

As pointed out in [93] hot wire anemometry probes for one dimensional flow measurements are also sensitive towards flow direction due to sensor geometry. Dependent on the flow angle relative to the sensing element the shape and size of the thermal boundary layer and therefore the heat transfer will be different. Therefore a measurement of a fluid flow with one dominant flow direction with unknown flow angle will always require two sensors. Typical hot wire anemometry sensor heads are

[92] Mocikat & Herwig 2009

[93] Nitsche & Brunn 2006, Chapter 3

displayed in Figure 31. The more sensing elements the sensor has, the more dimensions can be measured.

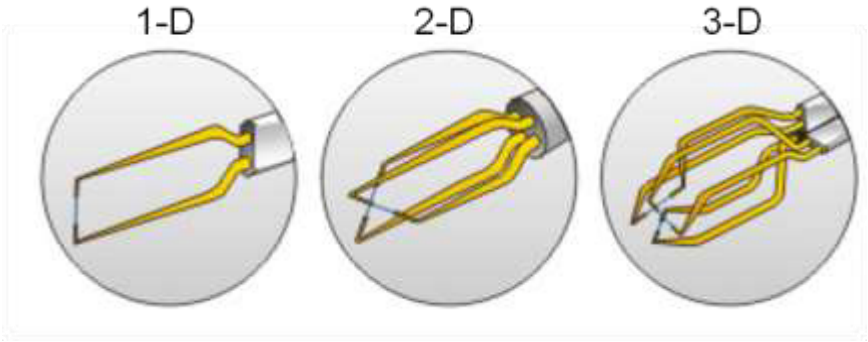

Figure 31: CTA Hot Wire Sensor Heads[94]

Since the calibration of the sensors is also very resistance dependent, the probes are usually calibrated in total (sensor head and mounting tube).

In principle all measurements performed with electro / mechanical techniques can also be performed with thermal measurement techniques without high additional effort. As a specific example Elkins uses in [95] several hot wire anemometers to measure temperature, velocity and heat flux quantities around a heated rotating disk system. With a hot wire sensor in passive mode (referred to as cold wire anemometry) he measures the turbulent temperature variations in the flow. He also points out the importance of using temperature dependent calibrations for thermal sensors to compensate any changes in fluid temperature.

A group of sensors which require small packaging space are foil sensors. The sensing element for this group of sensors is directly placed on a carrier material and can be directly mounted onto the geometry of interest.

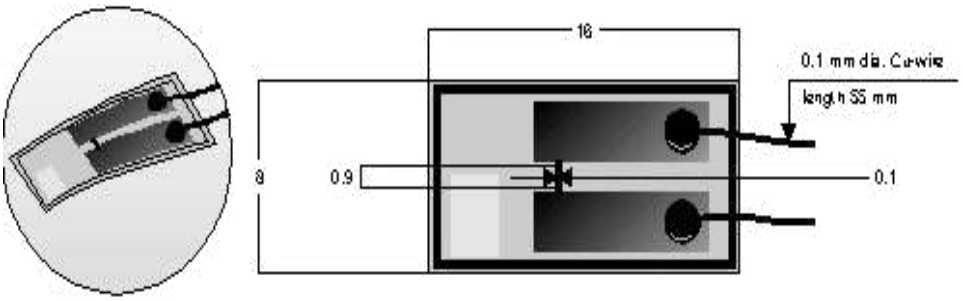

Figure 32: Foil Sensor 55R47[96]

[94] Dantec Dynamics Homepage www.dantecdynamics.com
[95] Elkins 1997
[96] Dantec Dynamics Homepage www.dantecdynamics.com

The possibility to flush mount the sensors on the surface minimizes the influence of the sensor on the ambient fluid flow. These sensors can be used for measuring wall temperature, heat flux, flow velocity, wall shear stress and transition detection.

An interesting and detailed review of design considerations for foil sensor optimization can be found in [97]. By placing and operating another sensor of equal design below the sensor used for flow measurements the author minimizes the losses due to conduction. The sensors are usually manufactured on and to customer demand to match the specific measurement task. Figure 32 shows the geometry of a commercially available foil sensor. The sensing element made of Nickel has a size of 0.1 x 0.9 mm and is connected to gold-plated lead areas which are deposited on a 50 µm KaptonT foil. According to the manufacturer as well as general literature on foil sensors it is always recommended to calibrate the sensors under mounting conditions.

The most commonly used calibration formulas for foil sensors are all of the type of equation 2.38.[98]

$$(\tau_w)^{\frac{1}{n}} = A + B \cdot \left(U_B^2 - U_{B,0}^2\right) \tag{2.38}$$

$$\frac{Q_{el} - Q_0}{\Delta T} = A + B \cdot (\rho \cdot \mu \cdot \tau_w)^{\frac{1}{3}} \tag{2.39}$$

Equation (2.39) proposed by Kreplin and Höhler for foil sensor calibration has the advantage, that it also incorporates temperature dependent coefficients. Both equations (2.38) and (2.39) can be simplified to equation 2.40.

$$(\tau_w)^{\frac{1}{3}} = A(T) + B(T) \cdot \left(U_B^2 - U_{B,0}^2\right) \tag{2.40}$$

The group of thermal measurement techniques shows a wider range of applicability to a clutch system compared to electro / mechanical and visual measurement techniques. For measurements outside of the clutch system the technique has no disadvantage compared to the electro / mechanical techniques. Both require a flow temperature dependent correction of the calibration curve. Properties like low influence on the fluid flow, small packaging and low influence of centrifugal forces make foil sensors also attractive for measuring flow quantities inside the clutch system. Main advantage is that the sensors can be applied directly to the surface of the part of interest and do not need additional sensor mounts.

---

[97] Mocikat & Herwig 2009

[98] Nitsche & Brunn 2006, P.88ff.

2.4 Basis for the Thermal Clutch Temperature Model

The clutch temperature simulation method presented Beitler[99] is used as basis for the clutch size selection tool presented later in this work. Therefore the overall procedure and base equations used will be detailed in this section.

Beitler proposed in his publication, that clutch systems can in general be treated as interconnected multiple thermal mass models. He simulated the clutch temperature based on one partial differential equation per considered part. He considered for the clutch system the flywheel with primary and secondary side, pressure plate, diaphragm spring and clutch cover.

Additionally he simulated the air inside the bell housing and the bell housing each as a thermal mass. The clutch components are thermally coupled by radiation and conduction heat transfer. Between the air inside the bell housing and the clutch system or bell housing the heat is transferred by convection. At the outer surface a convection heat transfer coefficient can be set with a constant ambient air temperature. To consider the influence of a forced cooling, he also considered an additional cooling air mass flow having a direct effect on the air temperature inside the bell housing.

[99] Beitler 2008

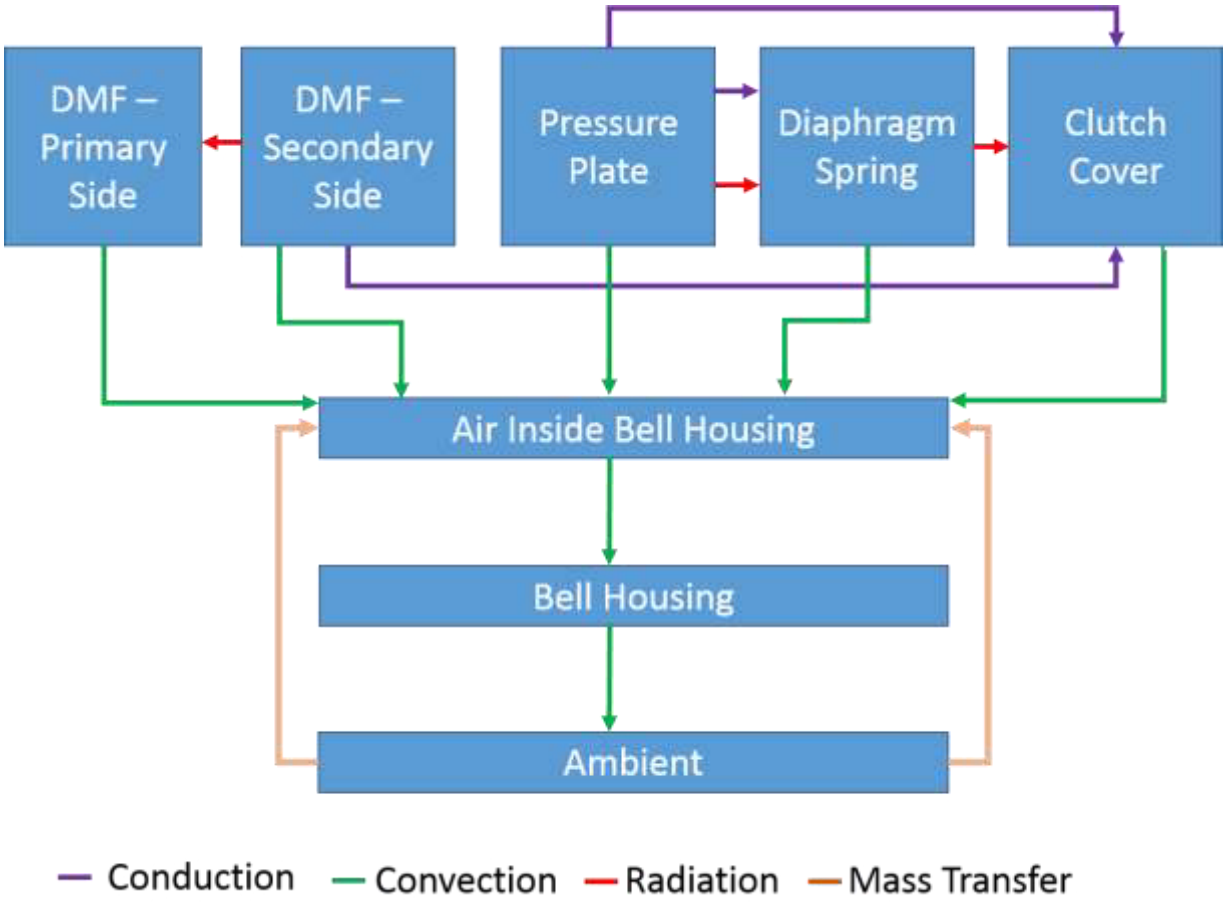

Figure 33: Clutch Temperature Simulation Model Structure derived from [100]

To determine the radiation and convection heat transfer coefficients between the individual parts, Beitler conducted a series of tests. He firstly determined the radiation heat transfer parameters by measuring the emission rate experimentally. The more important convective heat transfer coefficients were determined in a two stage experiment. Firstly the individual volume flows through the different channels inside the clutch system where determined on a centrifuge test stand. This was accomplished by closing, or blocking individual channels while leaving others open and additionally varying the rotation rate. After the volume flow rates were determined in dependence of the rotation rate, he conducted cooling down experiments. The tested components were heated up in an oven and then subjected to a defined air flow according to the prior measurements.

With the obtained convection and rotation coefficients he derived the remaining conduction coefficients between the parts iteratively to match a measured temperature profile.

[100] Beitler 2008, P.195

2.4.1 Simplified Friction Energy Calculation

A simplified established idealized procedure to describe the rotational speed behavior during synchronization is displayed in Figure 34. During synchronization the primary side (engine) is decelerated, while the secondary side is accelerated until the speed difference between primary and secondary side is zero.[101]

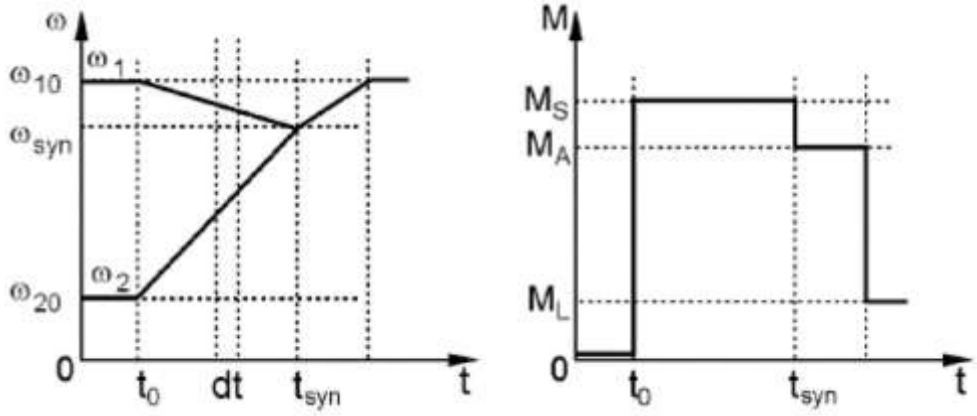

Figure 34: Idealized Engine Speed and Torque Behavior during Vehicle Launch[102]

In case of a vehicle launch with constant acceleration forces (constant load torque) the clutch synchronization time can be calculated by equation 2.41 which is based on a simple torque balance around the primary and secondary side of the clutch system.[103]

$$t_s = \frac{J_{engine} \cdot J_{red} \cdot \left(\omega_{eng}(t=0) - \omega_{trans}(t=0)\right)}{J_{engine} \cdot \left(M_{Cl} - M_{res}\right) + J_{red} \cdot \left(M_{Cl} - M_{Eng}\right)} \tag{2.41}$$

$$J_{red} = \frac{J_{rest} + \left(m_{vehicle} + m_{trailer}\right) \cdot r_{dyn}^2}{i_{first\,gear}^2} \tag{2.42}$$

$$M_{res} = \frac{\left(f_{tyre} \cdot \cos(\varphi) + \sin(\varphi)\right) \cdot \left(m_{vehicle} + m_{trailer}\right) \cdot g \cdot r_{dyn}}{\eta_{PT} \cdot i_{firstgear}} \tag{2.43}$$

The reduced inertia of the secondary side in equation 2.41 (wheel / brakes / transmission / etc.) is calculated according to 2.42, the resistance torque by equation 2.43.[104]

With a given clutch torque or a given synchronization time it is then possible to calculate the friction energy via equation 2.44.[105]

$$P(t) = M_{cl} \cdot \left(\omega_{eng}(t) - \omega_{trans}(t)\right) \tag{2.44}$$

---

[101] Albers et al 2006 a, P.334
[102] Albers et al 2006 a, P.334
[103] Albers et al 2006, P.335
[104] Gauterin & Unrau 2008
[105] Albers et al 2006, P.337ff.

2.4.2 Numerical Methods for Differential Equations

As solver for the iterative temperature estimation, there are explicit and implicit methods available. Explicit methods have an advantage, that the temperatures are predicted based on the knowledge of the temperatures from the last time increment. An example for the basic structure of a discrete temperature estimation problem to solve with an explicit method is shown in equation 2.45. For a one dimensional finite difference method the main type of equation to solve is displayed if equation 2.46.[106]

$$x^{k+1} = A \cdot x^{k} \tag{2.45}$$

$$x_i^{k+1} = M \cdot x_{i-1}^{k} + (1 - 2 \cdot M) \cdot x_i^{k} + M \cdot x_{i+1}^{k} \tag{2.46}$$

$$M := \frac{a \cdot \Delta t}{\Delta s^2} \leq 0.5 \tag{2.47}$$

Explicit methods can be solved directly, but require the user to define a time increment for the selected simulation task, which does not cause stability problems (eq. 2.47). The explicit methods are therefore restricted.[107]

Implicit methods can be used to predict the system temperatures without limitations to the time step used inside the simulation code. An example for the structure of an implicitly discretisized finite difference problem is shown in equation 2.48. The difference to the structure of the explicit method is that an inverse operation is now necessary to solve.

$$A \cdot x^{n+1} = b \tag{2.48}$$

Numerous concepts for the solution equations of this type exist. A good overview of possible methods and mathematical background can be found in [108].

When regarding temperature dependent material properties for the heat capacity and thermal conductance the temperature problem becomes nonlinear (eq. 2.49).

$$\begin{aligned} \frac{dT_{PP}}{dt} = \frac{1}{m_{PP} \cdot c_p(T_{pp})} \cdot [&\lambda_{PP-DS}(T) \cdot (T_{DS} - T_{PP}) + \lambda_{PP-CC}(T) \cdot (T_{CC} - T_{PP}) \\ &+ \lambda_{PP}(T) \cdot (T_{PP\,k-1} - T_{PP}) + \alpha_{PP} \cdot (T_{Air\,BH} - T_{PP})] \end{aligned} \tag{2.49}$$

An approach to this type of equations is to use iterative solvers. A simple method is shown in equation (2.48) and (2.50), which is an iterative Gauß-Seidel solution scheme adapted from [109].

---

[106] Baer & Stephan 2010, P.156ff.
[107] Baer & Stephan 2010, P.215
[108] Ferzinger & Peric 2008
[109] Müllges et al 2004, P.234ff.

$$x_i^{n+1} = \frac{b_i}{a_{ii}} - \sum_{j=i+1}^{I} \frac{a_{ij}}{a_{ii}} \cdot x_j^n + \sum_{j=1}^{i-1} \frac{a_{ij}}{a_{ii}} \cdot x_j^{n+1} \tag{2.50}$$

In this method the temperatures of the future time step are estimated iteratively with starting temperatures of the iteration procedure set to the temperatures of the current state and a_{ii} and b_i representing the coefficients of the matrices A and b.

2.5 Parameter Identification with Kalman Filtering

The Kalman filter algorithm was developed by R. Kalman in the 1960's and belongs to the class of recursive algorithms. Originally the filter was developed for linear systems. Main idea behind the filter is to use available measurement data and statistical information on the system to improve an estimate for the currently predicted system state. The recursive operating procedure also makes it possible to use the algorithm for real time estimation problems.[110]

In literature different formulations of the Kalman filter can be found. The algorithm can be directly applied to the differential equation of interest (Continuous Time Kalman Filters) without further discretization.[111]

Another possibility is to apply the filtering algorithm to the discretized state and measurement equations. This technique is called discrete time Kalman filtering. Due to the similarity to the modeling equations of the simplified thermal model and ease of application the focus is on discrete time filters.

2.5.1 Discrete Time Linear Kalman Filter

A linear system can be described by the discrete time state space equations 2.51 and 2.52.

$$\hat{x}_{t+1} = A \cdot x_t + B \cdot u_t + w_t \tag{2.51}$$

$$\hat{y}_{t+1} = C \cdot x_{t+1} + v_t \tag{2.52}$$

In this representation A is the state transition matrix, B the control-input matrix, C the measurement matrix, $\hat{x}$ the current prediction of the state vector and u the control vector. w and v are the system- and measurement noise vectors usually described by zero mean time invariant Gaussian White Noise processed with variance σ. Based on the prediction of the system state performed in equation 2.51, the main objective is now to find a better estimate for the system state based on a performed measurement.

[110] Kalman 1960

[111] Prokhorov 1979

In a Kalman filter this is performed by using equation 2.53 with the Kalman gain matrix K.

$$x_{t+1} = \hat{x}_{t+1} + K \cdot (y_m - \hat{y}_{t+1}) \tag{2.53}$$

The Kalman gain can be interpreted as trust factor. As an example of a scalar case, if K would be less than 0.5, the trust in the measurement would be lower. If K would exceed 0.5, the confidence in the system model would be lower. The question that remains is how to select the Kalman gain for a higher dimensional case.

A comprehensive and detailed derivation on how to optimally select the Kalman gain matrix can be found in [112] and is presented in equation 2.54 for an additive noise case.

$$K = \frac{P_{xy}}{P_y + R} \tag{2.54}$$

$$P_{xy} = P_{t+1} \cdot C^T \;;\; P_y = C \cdot P_{t+1} \cdot C^T \;;\; P_{t+1} = A \cdot P_t \cdot A^T + Q \tag{2.55}$$

In equation 2.55 P_{xy} is the cross covariance between the measurements and the current state, P_y represents the measurement covariance, R is the measurement error covariance, P is the updated covariance matrix of the system state and Q is the system error covariance.

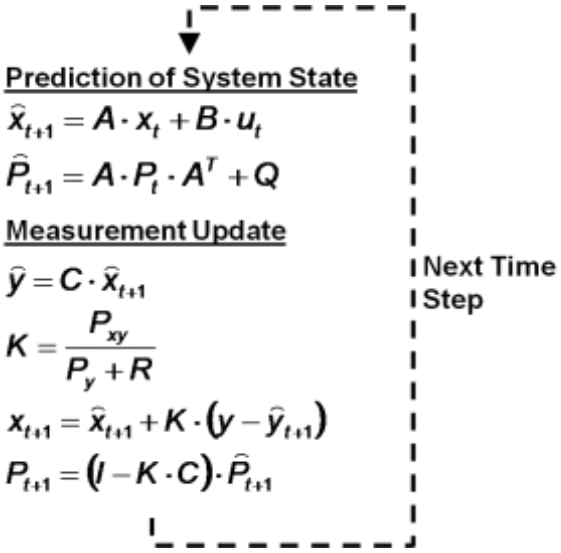

Figure 35: Kalman Filter Process for a Linear System with Additive Noise

The Kalman filter process displayed in Figure 35 can be described as iterative alternation of statistical prediction and correction procedures.

[112] Biering 2001, P.15ff.

2.5.2 Extensions to Non-Linear Cases

For identification tasks that involve non-linear system or measurement update equations the linear update equations (eq. 2.51 and 2.52) can no longer be applied. Nonlinearities can be caused by non-linear functions or multiplicative combinations of state variables in the measurement update or state prediction equation. For the application of the filter to nonlinear problems additional linearization is necessary. In literature different algorithms can be found to treat this non-linearity.

The Extended Kalman Filter (EKF) is a direct extension of the linear Kalman filter to the non-linear case by linearizing the non-linear terms of the system and/or measurement equations around an operation point with the help of Jacobian matrices. The system transition matrix and/or the measurement update matrix are then replaced by its linearization.

$$\hat{x}_{t+1} = f(x_t, u_t, w_t) \tag{2.56}$$

$$F_{ij,t} = \left.\frac{\partial f_i}{\partial x_j}\right|_{x_t, u_t} \tag{2.57}$$

For a system with non-linear state equation (eq. 2.56) the derived linearized state transition matrix from equation 2.57 can be straight forward implemented into the linear algorithm of Figure 35.[113]

Another recently developed algorithm is the Unscented Kalman Filter (UKF) which was developed by Julier and Uhlmann [114] and belongs to the class of sigma point filters. In this filter the system and/or measurement equations remain untouched. By selecting a set of so called sigma points described by the statistical properties of the system the nonlinearities can be efficiently treated without having to calculate Jacobian matrices at every time step.

$$\chi_0 = \bar{x} \tag{2.58}$$

$$\chi_i = \bar{x} + \left(\sqrt{(n+\lambda)\cdot P}\right)_i \qquad 1 \le i \le n \tag{2.59}$$

$$\chi_{i+n} = \bar{x} - \left(\sqrt{(n+\lambda)\cdot P}\right)_i \qquad n+1 \le i \le 2\cdot n \tag{2.60}$$

$$\lambda = \alpha^2 \cdot (n+\kappa) - n \tag{2.61}$$

The crucial point of the algorithm is to select the sigma points. The selection has similarities to Monte-Carlo type Methods, with the difference that the points are selected by a certain procedure and not randomly drawn. For an unscented Kalman

[113] Ribeiro 2004

[114] Julier & Uhlmann 1997

filter the selection procedure for the sigma points is shown in equations 2.58 to 2.61. The factors in equation 2.61 are selected to represent the statistical properties of the regarded problem. For Gaussian random variables, alpha is usually selected a small positive number, κ usually zero and n is the number of state variables. The obtained sigma points are then propagated through the state transition or measurement update equation. After this, the covariances needed for the algorithm can be calculated from the propagated sigma points.[115]

Another filter belonging to the class of sigma point filters is the Central Difference Kalman Filter (CDKF). The main difference to the UKF is in the selection of sigma points and weights. While in the UKF several factors are necessary to calculate the samples and weights, in the CDKF only one factor is necessary. The sigma point selection scheme is shown in Figure 36 for a simple two dimensional case.[116]

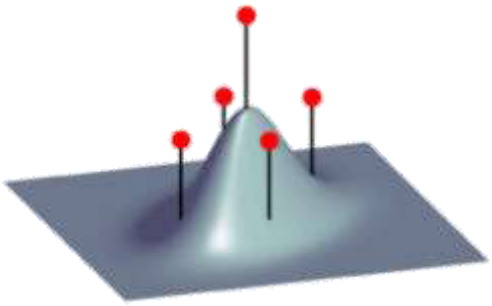

Figure 36: Principle of Sigma Point Selection for a Two Dimensional Case[117]

The overall process of a Central Difference Kalman Filter with additive noises and nonlinearities in the system and measurement model is shown in Figure 37.

[115] Julier & Uhlmann 1997
[116] Merwe 2004, P.62ff.
[117] Merwe 2004, P.52

Sigma Point Generation for State Update

$$\chi_0 = \bar{x}$$

$$\chi_i = \bar{x} + h \cdot \left(\sqrt{P}\right)_i \qquad 1 \le i \le n$$

$$\chi_{i+n} = \bar{x} - h \cdot \left(\sqrt{P}\right)_i \qquad n+1 \le i \le 2 \cdot n$$

Weights

$$w_0^{(m)} = \frac{h^2 - n}{h^2}$$

$$w_i^{(m)} = \frac{1}{2 \cdot h^2} \qquad 1 \le i \le 2 \cdot n$$

$$w_i^{(c1)} = \frac{1}{4 \cdot h^2} \qquad 1 \le i \le 2 \cdot n$$

$$w_i^{(c2)} = \frac{h^2 - 1}{4 \cdot h^2} \qquad 1 \le i \le 2 \cdot n$$

Time Update Equations

$$\chi_i^{t+1} = f\left(\chi_i^t, u^t\right) \qquad 0 \le i \le 2 \cdot n$$

$$\hat{x}^{t+1} = \sum_{i=0}^{2n} w_i^{(m)} \cdot \chi_i^{t+1}$$

$$\hat{P} = \sum_{i=1}^{L} \left[w_i^{(c1)} \cdot \left(\chi_i^{t+1} - \chi_{n+i}^{t+1}\right)^2 + w_i^{(c2)} \cdot \left(\chi_i^{t+1} + \chi_{n+i}^{t+1} - 2 \cdot \chi_0^{t+1}\right)^2 \right] + Q$$

Sigma Point Generation for Measurement Update

$$\chi_{0,m} = \hat{x}^{t+1}$$

$$\chi_{i,m} = \hat{x}^{t+1} + h \cdot \left(\sqrt{\hat{P}}\right)_i \qquad 1 \le i \le n$$

$$\chi_{i+n,m} = \hat{x}^{t+1} - h \cdot \left(\sqrt{\hat{P}}\right)_i \qquad n+1 \le i \le 2 \cdot n$$

Measurement Update Equations

$$y_i^{t+1} = h\left(\chi_{i,m}^{t+1}\right) \qquad 0 \le i \le 2 \cdot n$$

$$\hat{y}^{t+1} = \sum_{i=0}^{2n} w_i^{(m)} \cdot y_i^{t+1}$$

$$P_y = \sum_{i=1}^{L} \left[w_i^{(c1)} \cdot \left(y_i^{t+1} - y_{n+i}^{t+1}\right)^2 + w_i^{(c2)} \cdot \left(y_i^{t+1} + y_{n+i}^{t+1} - 2 \cdot y_0^{t+1}\right)^2 \right] + R$$

Cross-Covariance and Kalman Gain

$$P_{xy} = \sqrt{w_1^{(c1)}} \cdot \left[y_i^{t+1} - y_{n+i}^{t+1} \right]^T$$

$$K = \frac{P_{xy}}{P_y}$$

State and Covariance Correction

$$\bar{x} = \hat{x}^{t+1} + K \cdot \left(y_m - \hat{y}^{t+1}\right)$$

$$P = P - K \cdot P_y \cdot K^T$$

Figure 37: Central Difference Kalman Filter Procedure According to [118]

[118] Merwe 2004, P.71ff.

2.5.3 Extensions to the UKF

Based on the work of Julier and Uhlmann, Merwe expanded the algorithm of the UKF and provided with his work a framework for parameter and state estimation. Most of this sub-section is based on his work.[119]

A large problem of the UKF and CDKF algorithms is that with increasing accuracy of the estimated states or parameters, the algorithm can become unstable. This is caused by small round-off errors, due to the limited accuracy of computer calculations, leading to negative diagonal entries in the covariance matrices. To circumvent these difficulties a square root algorithm can be applied. In this algorithm the square root of the covariance is propagated and updated. With this extension the covariance matrices can never contain negative values on the main diagonal.

Parameter and state estimation can be performed by applying a dual or joint filtering algorithm. In the dual algorithm two filters, one for the system states and one for the system parameters, are operated alternatively. In the state filter the parameters are taken as known constants and in the parameter filter the states are assumed as known. Due to the reduction of the order of the matrices the filter requires less computational resources than the following joint form. It is in this case also possible to use two different types of filters if the non-linearities are restricted only to the state or parameter equations.

A joint approach for state and parameter estimation is based on an augmented state vector. The augmented vector contains both the state and parameter value. With the augmented state vector, the normal UKF or CDKF algorithm is run. A slight disadvantage of this alternative is that the matrices order becomes very large. Still this variant of combined state and parameter estimation is regarded superior, because it does not except possible interaction between the states and parameters as in the dual version.

The determination of physically meaningful parameters requires additional mathematical considerations to limit the parameters to the positive domain. One way to treat this setback is to incorporate the parameter limitations (usually inequality equations) into the measurement equations. Another way of treating the constraints is to use a moving horizon strategy. The best and most adequate way of limiting the parameters to a certain domain is to use the concept found in [120]. The parameters can be limited to a certain domain by not directly estimating them. They are calculated by an equation similar to equation 2.62. The estimated parameters are the x_i's in the hyperbolical tangent function.

---

[119] Merwe 2004

[120] Merwe 2004, P.227ff.

$$p_i = p_{i,0} \cdot (1 + s \cdot \tanh(x_i)) \tag{2.62}$$

With the use of a pre-factor $p_{i,0}$ (selected as best guess of the parameter) and a scaling factor s the values of the parameter estimates are limited to the domain shown in Figure 38.

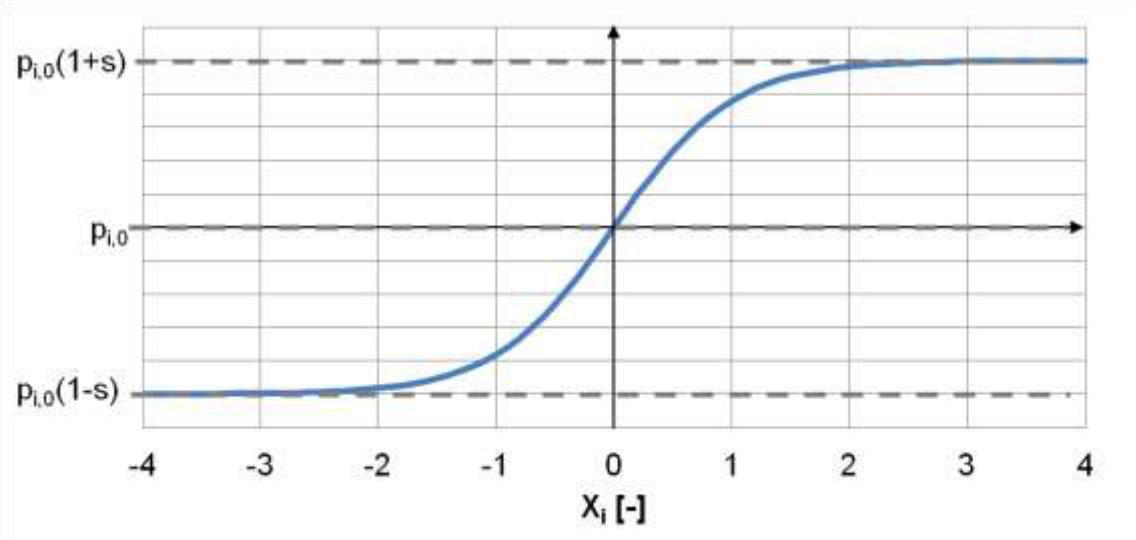

Figure 38: Resulting Parameter Limitation based on [121]

When choosing values for $p_{i,0}$ and s the operator has to grant, that the finally estimated parameters are in the restricted range. Otherwise the incorrect setting will lead to bad estimates or cause divergence.

2.6 The Integrated Product Engineering Model (IPeM)

The IPeM was developed at the Institute of Product Development at the Karlsruhe Institute of Technology and represents a problem oriented approach to the product development process. Main target of this model is to standardize the different product development processes of different engineering domains into one single framework.

[121] Merwe 2004, P.228

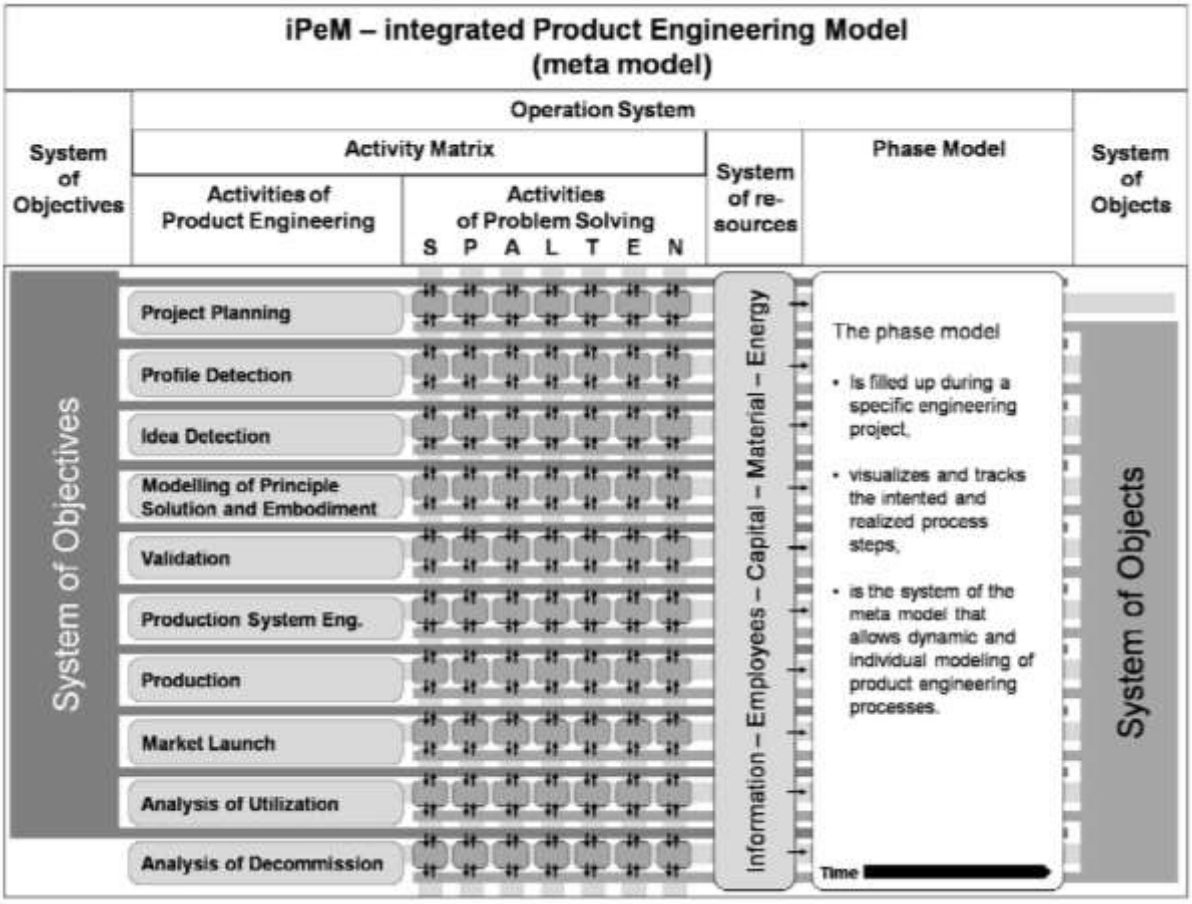

Figure 39: Integrated Product Engineering Model (IPeM)

IPeM itself is a meta-model, which means the process itself can be used as general approach to form a unique process for the specific development task (e.g. new design, redesign, market pull…). The general structure of the model is presented in Figure 39.[122]

Main target of the IPeM is to provide a guideline to transfer the system of objectives via the operation system into the system of objects. In this approach the main focus is on the operation system. The operation system can be divided into four main areas.

The activities of product engineering form the first area and represent a list of relevant operations for the developer in the product development process. The activities in this section of the operation system involve from the project planning in the beginning to the analysis of decomission all relevant steps in the product development process. The steps inside this section can not be seen as choronological step by step procedure but as separate engineering activities throughout the process.

The next cluster inside the operation system is formed by the activities of problem solving. The transformation of the system of objectives into the system of objects inside

[122] Albers 2010 c

the activity matrix is performed by the SPALTEN process. This process can be understood as sequential and universal problem solving method. The general process steps are displayed in Figure 40.[123]

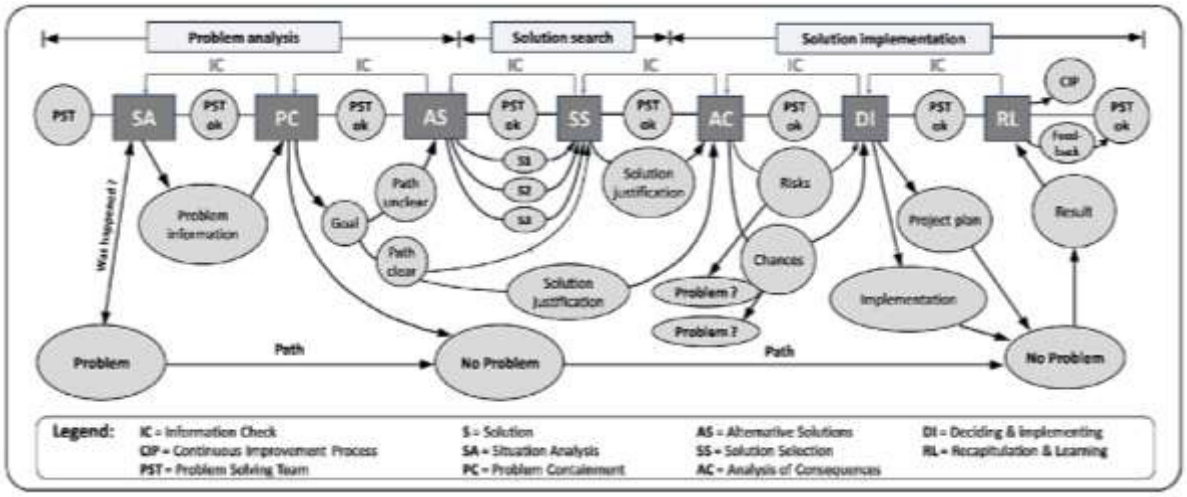

Figure 40: SPALTEN Process of the IPeM

The main activities inside the SPALTEN process are:

- Situation Analysis
- Problem Containment
- Alternative Solutions
- Solution Selection
- Analysis of Consequences
- Deciding and Implementing
- Recapitulation and Learning

The SPALTEN process can fundamentally be interpreted as fractal process, which means that all steps inside the process can be SPALTEN processes themselves.

Resources are a very important field inside the operation system, as they define the amount of available manpower, methods, materials, capital, information, etc. available to process the steps inside the activity matrix.[124]

The last field inside the operation system is formed by the phase model. The phase model can in the simplest case be defined by plotting different activities on a timeline. It can be interpreted as visualization technique and kind of agenda of the product

[123] Albers 2011 b
[124] Albers 2012 a

development process, which simplifies the project processing for the engineer and the control and monitoring.[125]

2.7 System Analysis via C&C²-A

For the simplified description of technical products, systems or processes the contact and channel method (C&CM) can be applied. Basic elements of the original method[126] are the Working Surface Pairs (WSP), which carry out functions, and the Channel and Support Structures (CSS), which connect the WSPs. Main advantage of this method is that coherences in complex structures can be displayed on a very abstract level and influencing conditions can be monitored easily.[127]

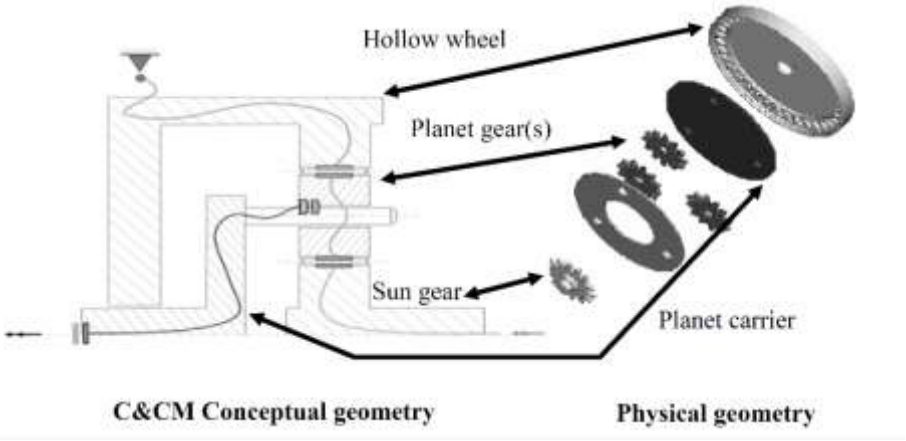

Figure 41: Example of a System Discription by C&CM[128]

The working surface pair is defined as a pair-wise interface between a component and another component or a boundary surface towards its environment which can be a liquid, gas or a field permanently or occasionally in contact. Energy, information or material exchange takes place at the working surface pairs. It inherits the actual functional contact. The channel and support structure is defined as physical component or volume of material in different condition of aggregation which directly connects exactly two WSPs. Apart from energy-, material- or information transfer the CSSs can also store these system variables. Figure 41 shows an example on how a planetary gear set can be described with the help of C&CM.[129]

[125] Albers 2013 a
[126] Albers 2002
[127] Albers 2005 a
[128] Albers 2009 b
[129] Albers 2009 b

Additionally to these two basic elements Albers[130] introduced connectors inside the contact and channel connector method (C&C²-A). Connectors represent an abstraction of the functionally relevant description of the surrounding system environment. Connectors are not inside the regarded system and integrate the influencing properties which are outside of the system boundaries into the considered system and therefore completes the method.

For the basic definitions of all elements inside the C&C²-A method a good summary can be found in [131].

[130] Albers 2013 b

[131] Albers 2013 c, P29ff.

3 Scientific Delta

Starting point of this work was to develop a temperature determination method for clutch system selection. Since it is not always possible or convenient to completely determine the heat transfer by measurements or using theoretical considerations on heat transfer the possibility to determine the heat transfer coefficients via a CFD-based conjugate heat transfer analysis will be taken into considerations.

On the overall validity of the flow system calculated by a CFD model inside a clutch system there exists, to the knowledge of the author, no method or verification procedure. It is therefore necessary to perform a categorization analysis on possible flow measurement techniques regarding the flow system and packaging conditions of clutch systems.

Regarding the product development process it is also necessary to find a possibility to integrate the CFD-analysis and therefore a large part of this work into the product development process.

The main targets regarding the CFD analysis can be categorized into the following steps:

- Derivation of the heat transfer parameters with the help of a CFD simulation model for the entire range of engine speeds for a selected clutch system
- Development of a synthesis and verification process
- Integration of the CFD analysis in the product development process

After the CFD simulation results have been generated, they will be used as basis for the clutch temperature determination model. For this, it is necessary to develop a simplification procedure, which can be used as guideline for future clutch systems. Since the clutch systems are not all the same it is also necessary to find a procedure on how to treat several clutch systems in one simulation environment.

The main targets regarding the simplified thermal clutch model are:

- Development of a thermal clutch simulation tool capable of calculating the heat distribution inside the clutch system for different powertrain combinations and load situations based on the considerations of Beitler[132]
- Determination of a simplification process for future clutch systems
- Verification of the flow and heat transfer results created by the CFD model by flow and heat transfer measurements

[132] Beitler 2008

4 Thermal Clutch Simulation Model

In this chapter general considerations on thermal modeling of clutch systems are displayed. In addition the influence of the driver is presented. In the middle of this chapter the modeling procedure is presented. The simplification process as basis for the generalization of clutch systems is displayed in the end of this chapter.

4.1 Influence of Vehicle Verification Procedures on Clutch System Life

Prior to the synthesis of the thermal clutch simulation tool, common durability test procedures at Ford Motor Company were analyzed to gain knowledge on basic influencing factors of clutch life. As indicated in chapter 1 test procedures can vary according to boundary conditions from market targets, available testing facilities and resources.

Vehicle loading, for instance, has a high effect on wear behavior. Dependent on the mixture of the loading procedure throughout the durability cycle, the temperature of the clutch system can vary. Figure 42 shows a vehicle load condition over the completion of the cycle for different vehicle durability tests.

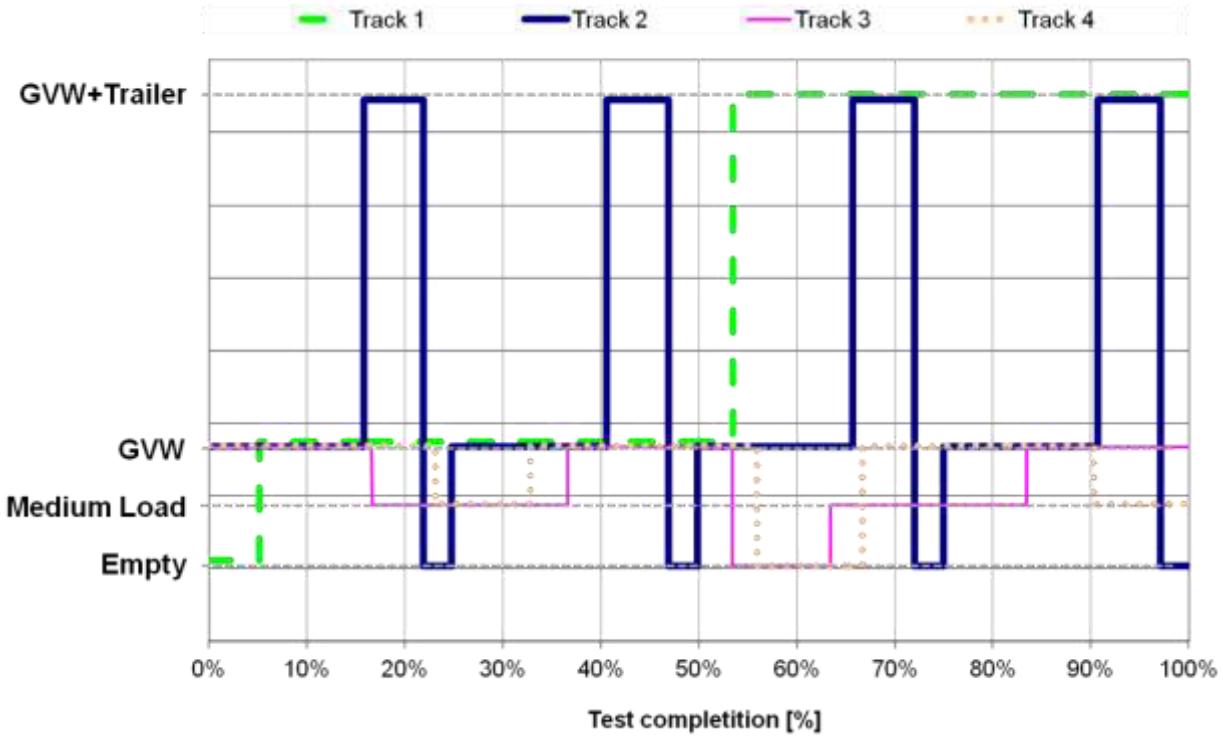

Figure 42: Vehicle Loading Distribution

It can easily be derived, that for test cycles with a repeating structure clutch wear will be more evenly distributed over the entire durability cycle. In test cycles with a structure

according to track 1 in Figure 42 the continuous high loading at the second half of the cycle can lead to thermal problems and increased clutch wear compared to track 2 where a possibility for the clutch system to recover exists.

The ambient air also has effect on the temperature of the clutch system. Figure 43 displays the temperature throughout a year on the testing locations mentioned in Figure 1 are shown.

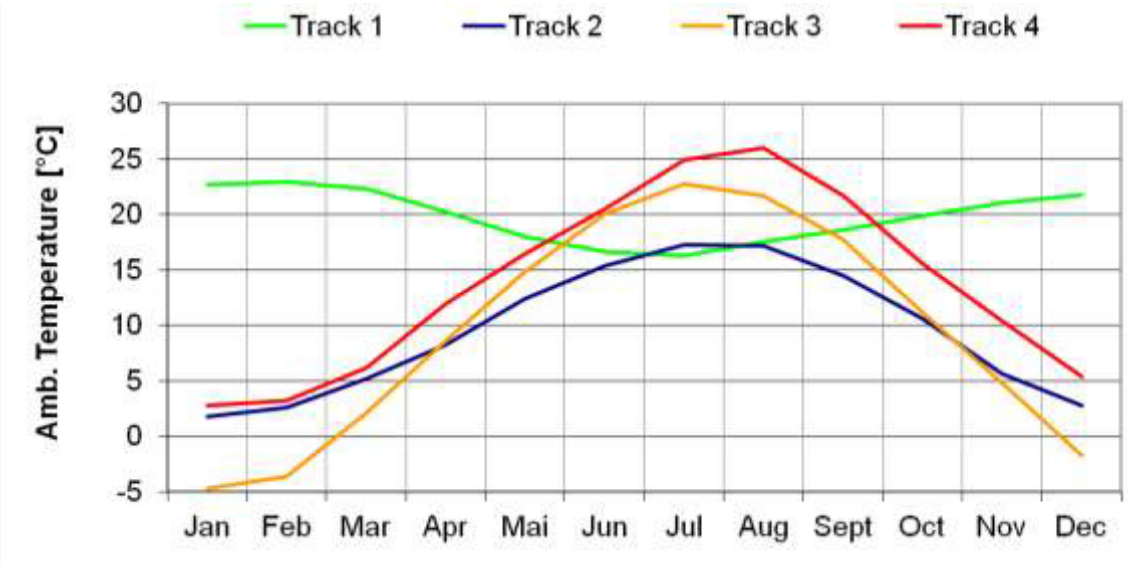

Figure 43: Ambient Temperature Variation of Different Test Tracks

Dependent on the starting date of the test cycle, the ambient temperatures can be significantly different, resulting in a lower wear rate due to a lower average temperature of the clutch system.

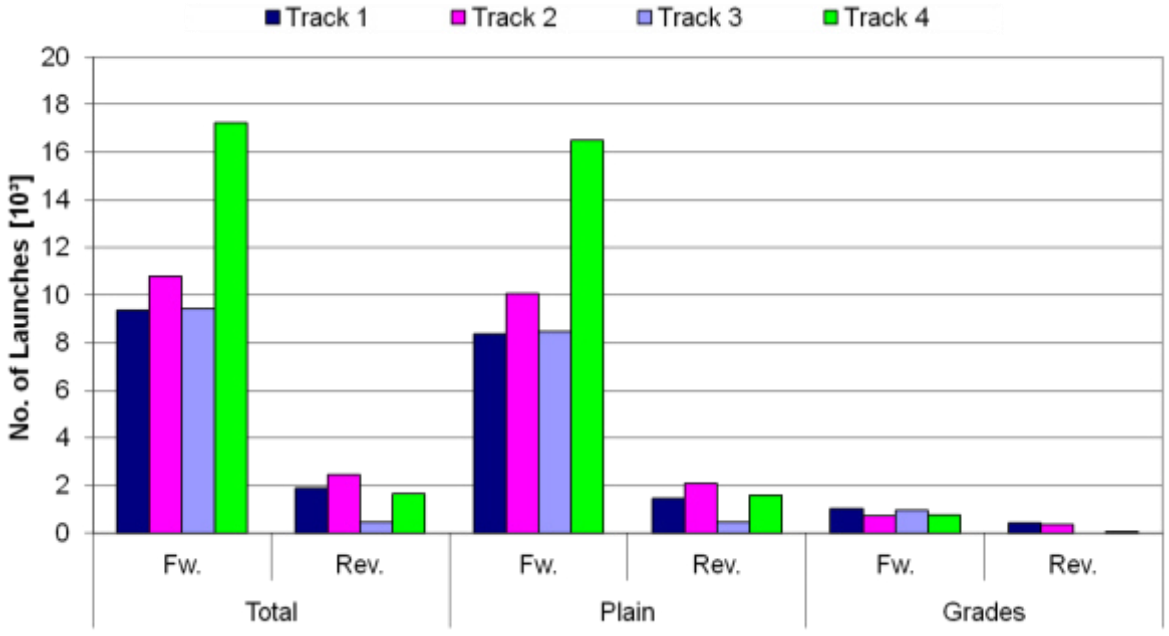

Figure 44: Launch Events in Test Procedures

Clutch wear mainly occurs during launch events due to the high energy input in a short amount of time. Another criterion to judge the severeness of a durability cycle is therefore the amount of launches performed. The difference in total amount of launch events can be derived from Figure 44. It is obvious that different wear results will occur. Comparing the amount of launches in plane to the amount on grades leads to the conclusion that not only hill launches have to be observed when designing a clutch.

Next to the loading of a vehicle and the number of launch events, the driver is highly impacting the energy input of a clutch system. In automatic transmissions the variety of shift and launch events is reduced because the operation is partially software and partly driver controlled. However vehicles equipped with a manual transmission need special attention regarding the operation of the clutch and accelerator pedal.

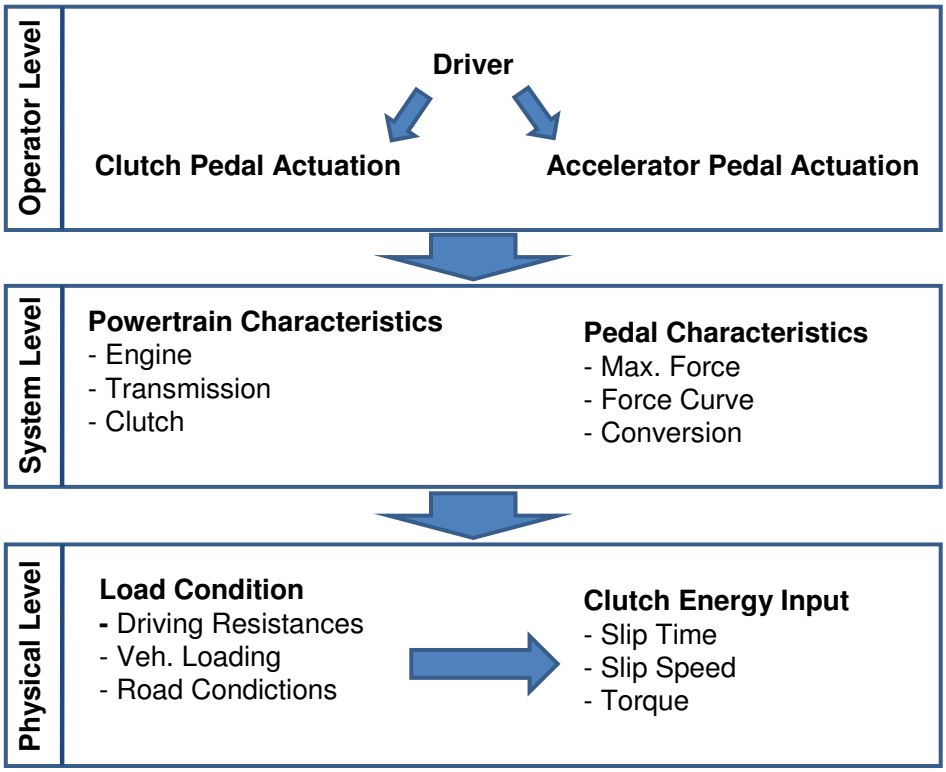

Figure 45: System Levels of Vehicle Operation

Manual actuation of both, clutch and accelerator pedal, increases the variation because the driver has to focus on two pedals which are usually operated dependent on each other. The operation is influenced by the drivers' expertise. Figure 45 shows a typical example of vehicle operation system levels related to the launching or shifting process and their interaction. This schematic indicates that a different clutch or accelerator pedal operation can lead to varying energies. As an example of driver variation the launch energy variation vs. the accelerator pedal position is displayed in Figure 46.

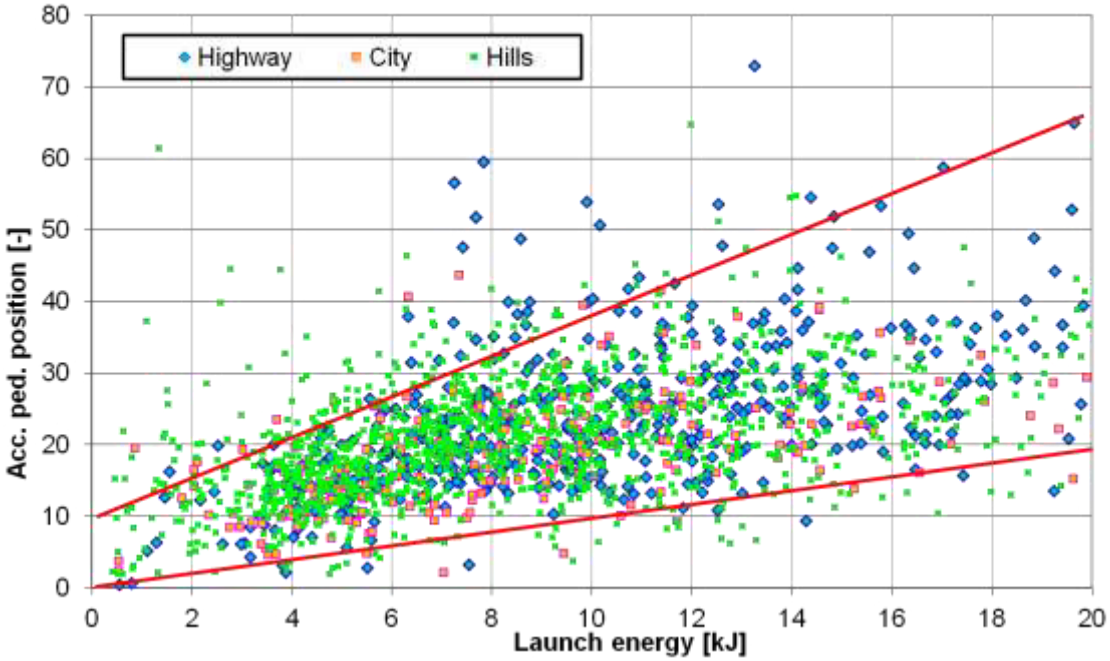

Figure 46: Launch Energy Variation in Dependence of Accelerator Pedal Position

In Figure 47 a measured energy distribution recorded on a test track is displayed for launch events on flat road. The profile shown is skewed with a solid boundary in the origin and a large spread. This distribution is an indicator that the recorded profile is not only influenced by statistical effects, but by another "noise factor". This is an indicator that a major uncertainty in clutch size selection is the driver.

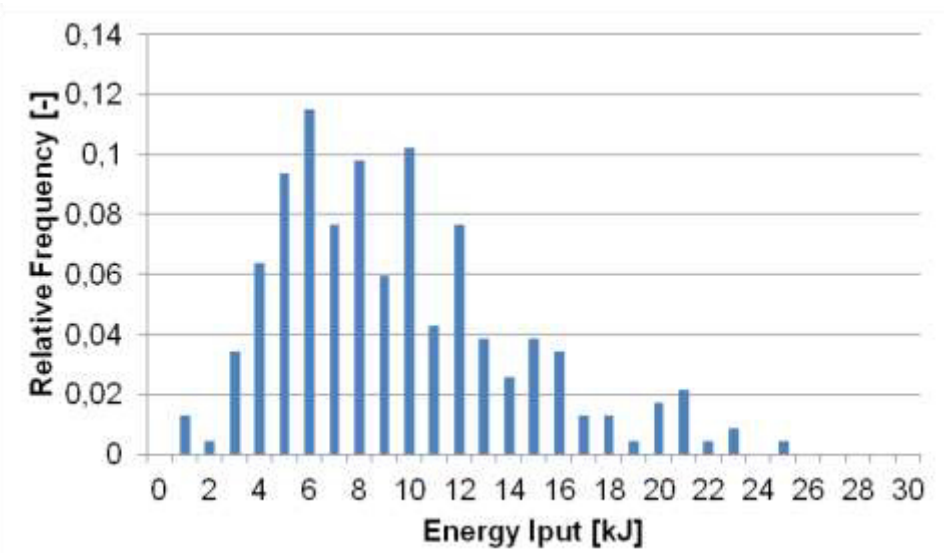

Figure 47: Variation of Energy Input for Plane Launch Events

The knowledge of the overall vehicle system and the subsystems interaction is also very important. System knowledge can be acquired by a “learning by doing” process or by understanding the interaction between the different subsystems of a vehicle. Figure 48 shows a scheme on how system knowledge can be acquired.

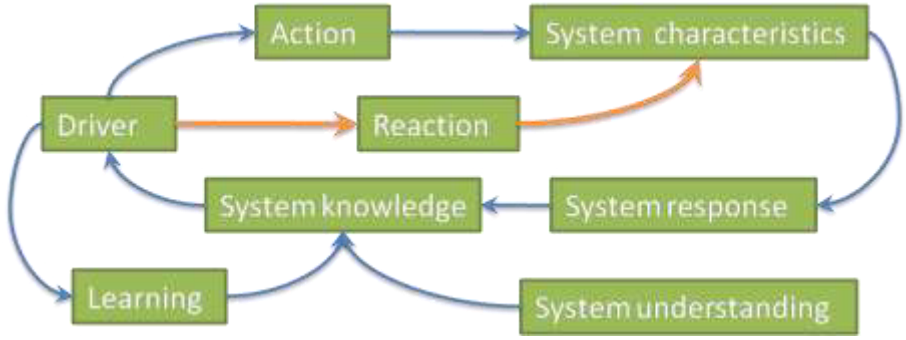

Figure 48: System Knowledge Build-Up Scheme

The driver's performance is dependent on his skill to adapt, which is mainly influenced by the accumulated experience.

As an example of system knowledge the shifting behavior obtained from different test tracks is shown in Figure 49. It can be seen that launch events have a higher impact on energy input into the clutch system than shift events. Apart from normal shifting behavior also abusive shifting behaviors were recorded on all test cycles.

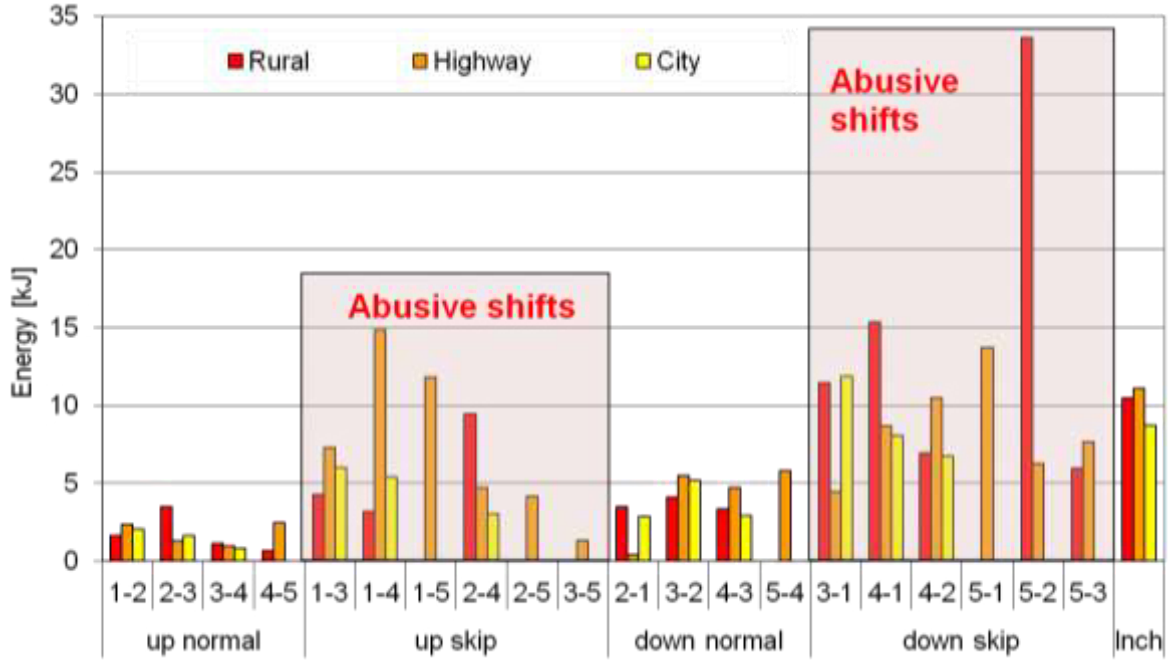

Figure 49: Monitored Shifting Behavior on Different Test Tracks

Abusive shifting can be produced by skipping gears or constant depression on the clutch pedal in acceleration phases. These events are not part of the driving event procedure and are totally accounted to the driver's influence.

From the performed test track analysis it can be concluded, that the driver behavior is a highly influencing factor on clutch performance and durability. A clutch size selection tool is therefore in need of factors characterizing the driver behavior based on statistically evaluated measures.

4.2 Heat Transfer Analysis

Before starting the actual analysis of the heat transfer from a clutch system to ambient a comparison of heat transfer mechanisms on a simplified experimental setup was performed.

4.2.1 Comparison of Heat Transfer Mechanisms

For the heat transfer to the ambient all types of heat transfer (convection / conduction / radiation) are involved in a dry clutch system. To estimate the influence of the individual heat transfer mechanism, measurements were performed for the heat exchange between the diaphragm spring and the pressure plate of a clutch system. Figure 50 shows schematically the experimental setup.

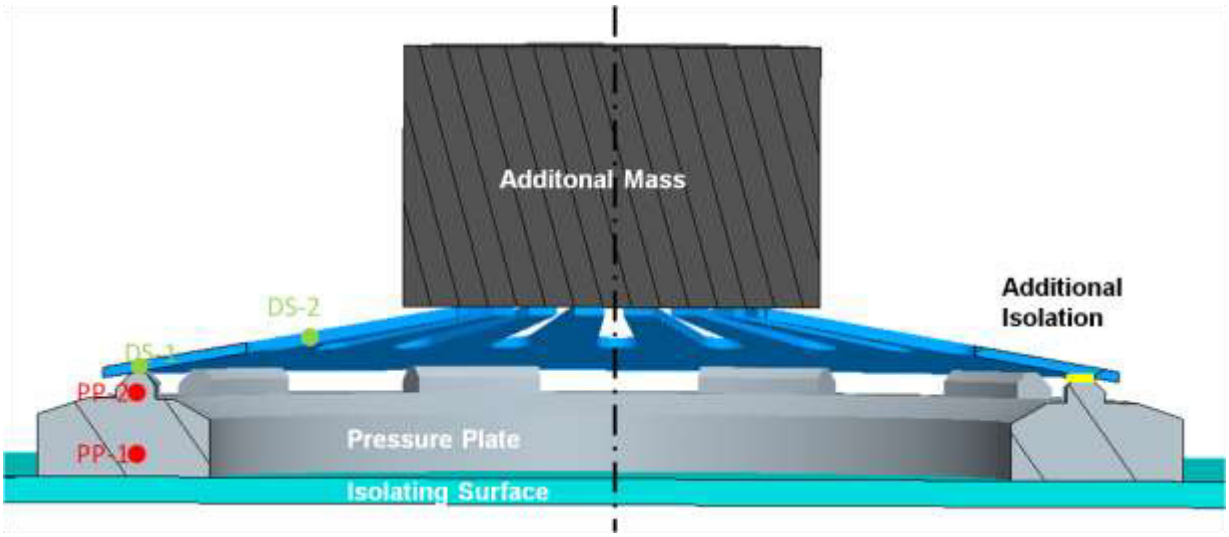

Figure 50: Schematic of the Experimental Setup

The pressure plate was heated up in an oven. After the heat up process the pressure plate was placed on an isolating surface. When a temperature of 100 °C was reached, the diaphragm spring was put onto the pressure plate. To judge the influence of radiation, small isolators were put between the pressure plate and the diaphragm spring in one of the performed experiments.

Figure 51 shows the result of the measurements for the isolated (top), placed on diaphragm spring with no additional mass (middle) and placed on diaphragm spring with 10 Kg additional mass. Comparing the energy exchange of the isolated and the case with no additional mass on the diaphragm spring, it can easily be seen, that the energy loss due to radiation is neglectable against the energy loss due to conduction. Compared to the case with an additional mass of 10 Kg, the temperature rise of the diaphragm spring without additional mass is slightly slower. This is due to the increased contact surface between the parts due to the additional mass.

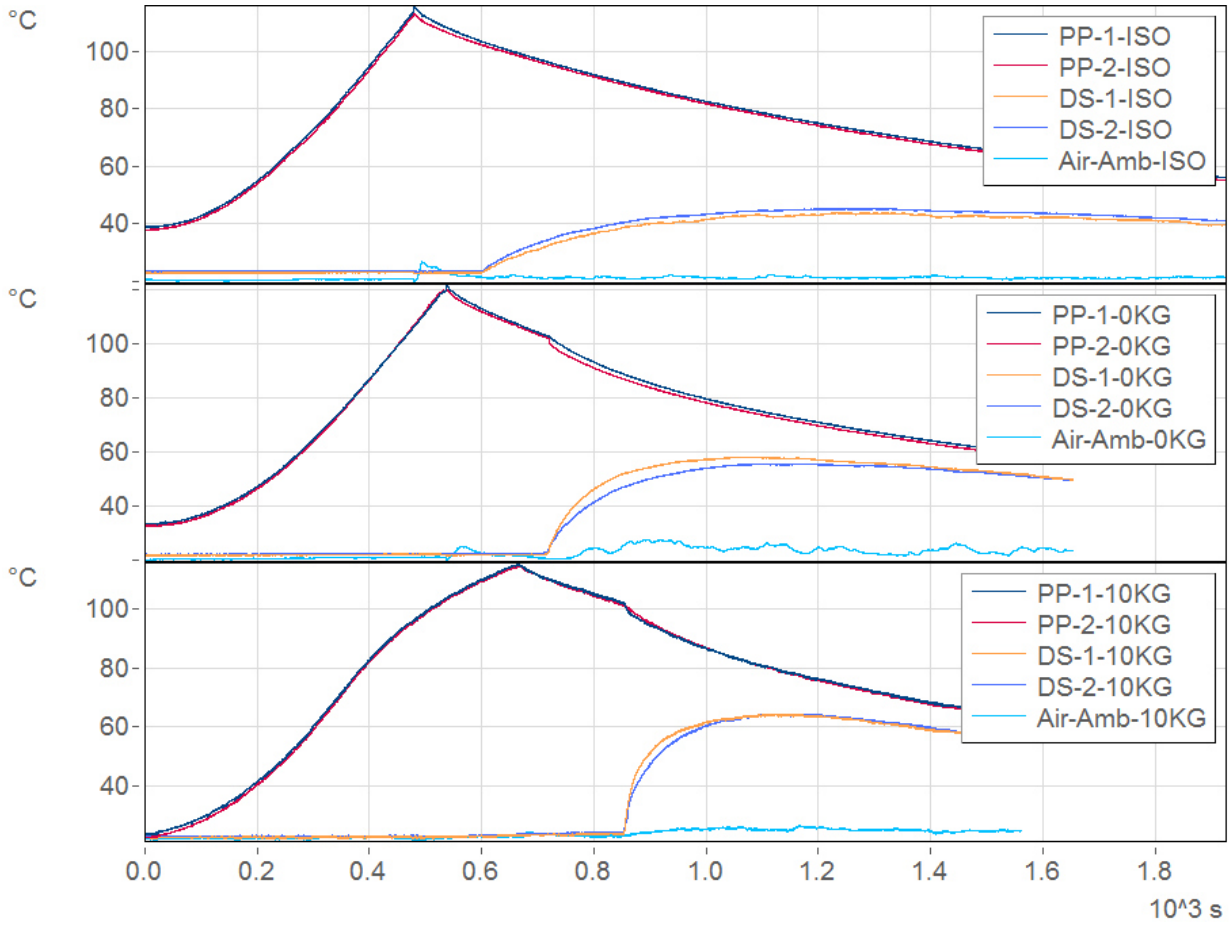

Figure 51: Temperature Trace of Pressure Plate and Diaphragm Spring

In this simplified test the heat exchange between the pressure plate and diaphragm spring is a combined process of radiation and free convection. Under operating conditions the convectional effects will increase due to forced convection. Therefore in this study heat transfer by radiation can and will be neglected.

4.2.2 Heat Transfer Circuits

A simplified overall heat flow path is displayed in Figure 52. The heat generated in the clutch system is transferred to the ambient mainly by convection. Dependent on the engine speed and vehicle speed the amount can vary. Conduction to the transmission is only possible through the actuation system or by the transmission input shaft. Both are only indirectly coupled with the heat source and therefore this path can be neglected.

From Figure 52 it can also be seen, that the air inside the bell housing has a central position in heat transfer. Heat from the clutch system has to be transported to the bell housing via air before it can be transferred to the ambient. Convectional heat transfer rates inside the bell housing depend on the engine speed, while the rates on the outer ring in Figure 52 depend on the vehicle speed.

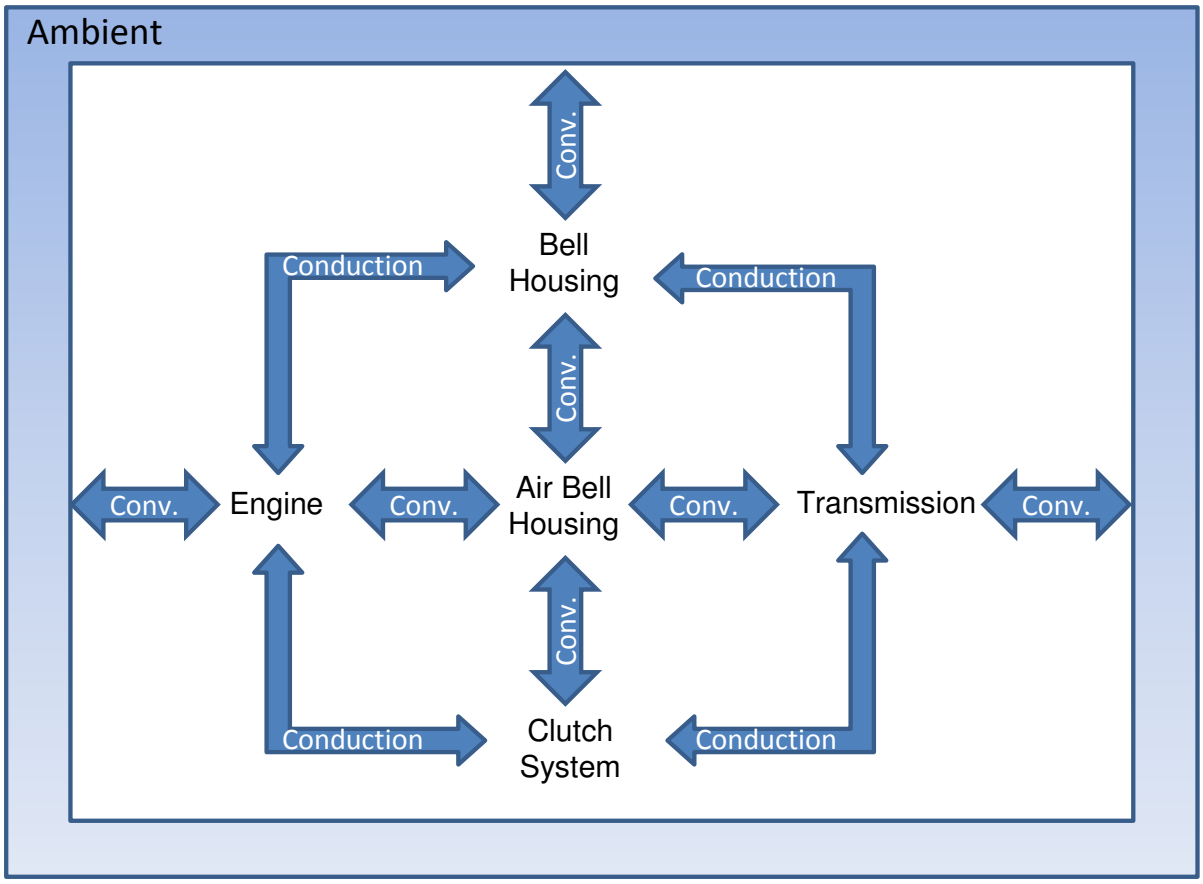

Figure 52: Overview Heat Transfer in a Powertrain System

For the heat-up of air inside the bell housing and an almost stationary culmination level (operating condition of the vehicle), the engine temperature is the most important factor. It also influences the temperature of the bell housing and the transmission.

4.2.2.1 Inner Circuit

Heat transfer from a clutch system can be divided into three different phases:

1. Heating Phase
2. Compensation Phase
3. Cooling Phase

In the heating phase the energy input, resulting from the torque transmission of the clutch system and the rotational speed difference between the engine and the transmission input shaft, causes the components connected to the frictional interfaces to heat up. During this phase, high temperature gradients inside the clutch exist and the main heat transfer mechanism is heat conduction. The temperature of the components next to the frictional interface is highly affected by their thermal mass. The pressure plate of the clutch system will, due to its lower mass, always face higher temperatures compared to the flywheel.

After the clutch system is closed, the high temperature gradients in the components of the clutch system are compensated. As in the heating phase, the main heat transfer mechanism is heat conduction. High influence on the temperatures in this phase is the connectivity to other parts inside the clutch system. The stored heat inside the pressure plate for instance can be transferred faster, if the coupling to the diaphragm spring or the cover is good.

In both, the heating phase and the compensation phase, the convectional heat transfer can be neglected. The amount of heat transferred by convection or conduction depends on the temperature difference between the thermal masses, on the thermal conductance and the distance from the heat source to the surface or interface to another part.

After the temperature gradients inside the system have been compensated, the cooling of the clutch components begins. The heat transfer from the clutch system to the air inside the bell housing is closely coupled to the flow conditions inside the clutch system and outside the clutch system.

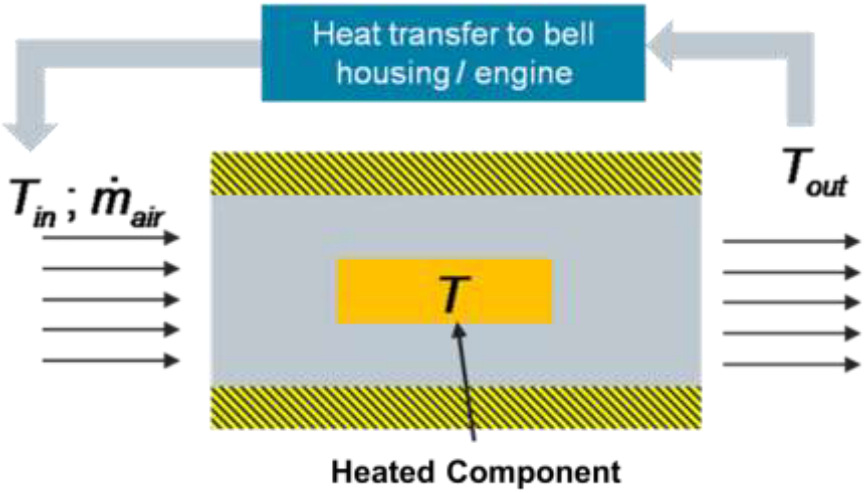

Figure 53: Simplified Heat Transfer from the Clutch System

Figure 53 shows a simplified model of the conditions inside the bell housing. The air flowing into the clutch system passes the heated components and absorbs a mass flow dependent amount of heat. After leaving the clutch system, the absorbed heat is transferred to the bell housing or engine.

The amount of air flowing through the clutch system is dependent on the friction levels and the flow structures inside the clutch system. To obtain an overview on the influencing factors on heat transfer and the general flow structure, the chosen approach in a first step was to divide the flow field inside the bell housing into analogous flow fields found in literature (chapter 2.2.3.6 to 2.2.3.10).

The flow field inside the bell housing is closely related to the research area of rotating disk systems. In Figure 54 a simplified division of the flow field inside the bell housing is given.

Starting from the engine side, the flow field between the flywheel and the engine sided wall can be best described by a rotating disk near a stationary wall. Inside the clutch system, the flow field can be divided into two main areas. The region close to the input shaft, where the disk, the diaphragm spring and the flywheel are located can be interpreted as co-rotating disks.

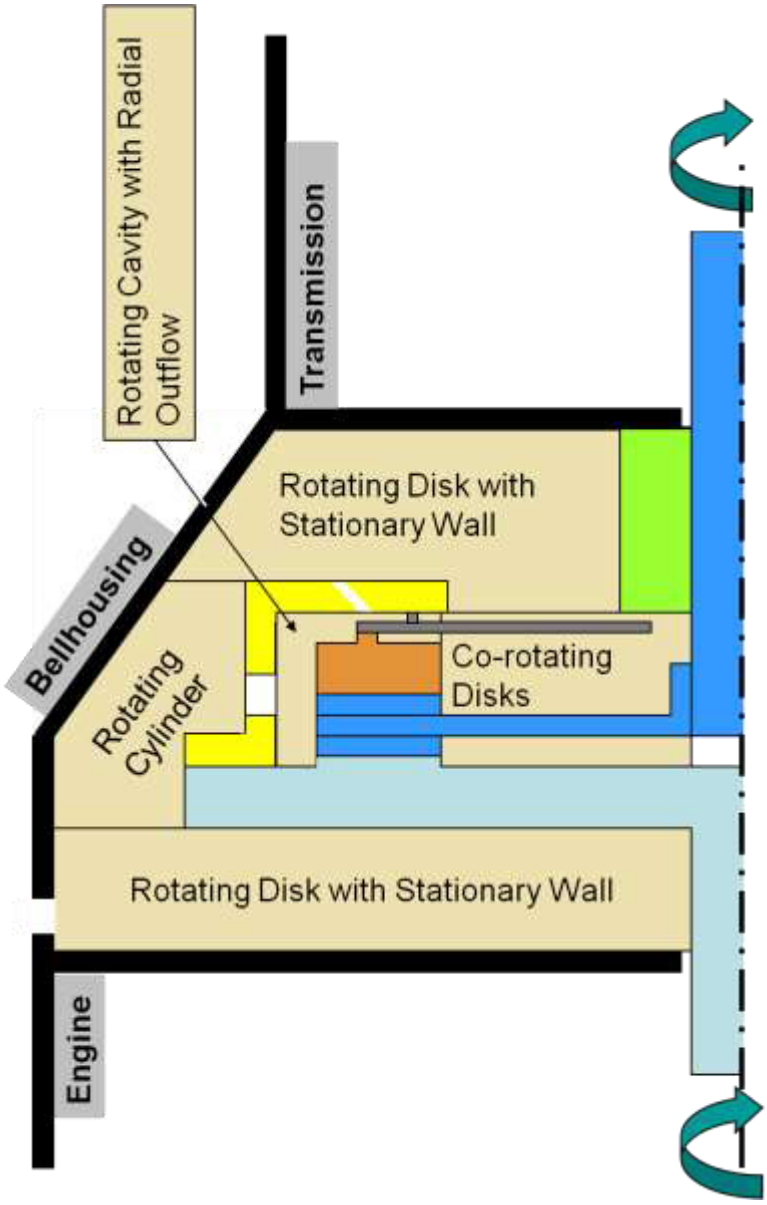

Figure 54: Division of the Flow System inside the Bell Housing

Towards the outer diameter of the clutch system the region formed by the clutch cover, pressure plate, lining and top part of the diaphragm spring is assumed to be highly related to a rotating cavity with radial outflow. The outside of the clutch cover and the bell housing form additional two regions. At the transmission side of the bell housing

the region is again closely related to a rotating disk with stationary wall. The last region of this division is the region limited by the bell housing and the circumferential area of the clutch cover. The fluid flow inside this region is closely related to an enclosed rotating cylinder.

4.2.2.2 Outer Circuit

The heat transferred from the powertrain to the ambient air is dependent on the flow conditions inside the engine compartment and the vehicle velocity. Figure 55 shows the average heat transfer coefficient of the bell housing obtained from an underhood CFD (CFD: Computational Fluid Dynamics) simulation for a front traversal mounting of the powertrain obtained from an internal study of the local TASE Group of Ford Motor Company. Compared to data from literature for common geometries it can be seen that the behavior at higher speeds is between a rectangle and a hexagon in crossflow.[133]

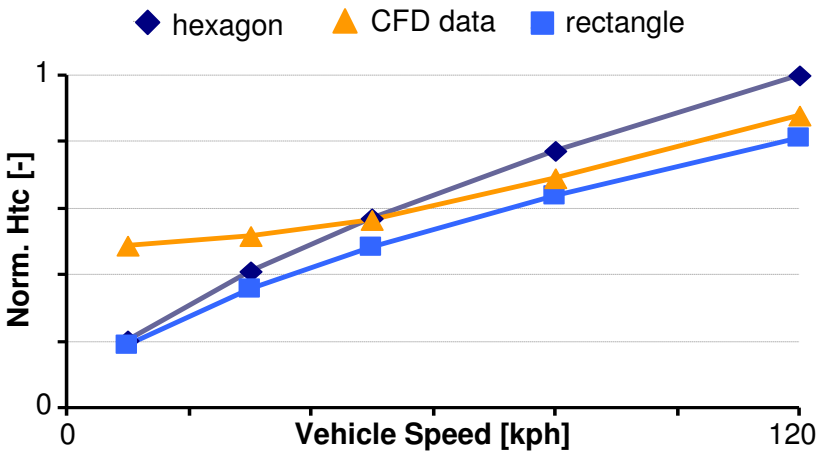

Figure 55: Vehicle Speed Influence on the Normalized Average Heat Transfer Coefficient (Htc) of the Bell Housing

The influence of the cooling fan for this vehicle can be seen at lower velocities. The heat transfer coefficient there is higher caused by the additional air flow of the cooling fan.

In Figure 56 the heat transfer coefficient distribution for a vehicle speed of 80 kph is displayed which was also supplied by the local TASE department. Areas which are oriented towards the rear of the vehicle show small heat transfer coefficients. Areas which are exposed to direct air impingement show higher values of the heat transfer coefficient.

[133] Marek & Nitsche 2007, P.188

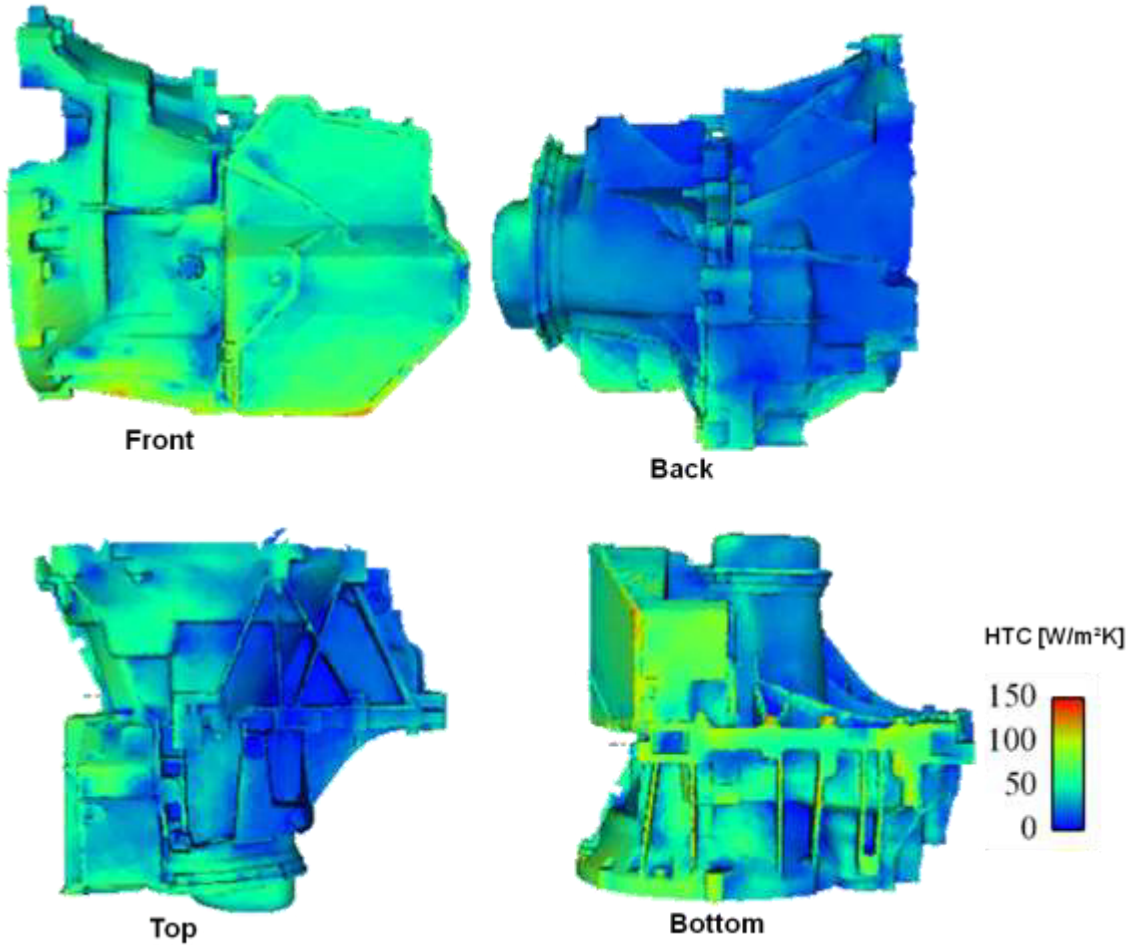

Figure 56: Heat Transfer Coefficient of a Transmission Assembly

4.2.3 Material Data

Material parameters in a simulation model can be treated as constant or temperature dependent. Temperature dependent material parameters have the disadvantage, that inside the simulation model the parameters are not treated as constants and have to be updated with temperature and time. The material parameters are therefore directly influencing the choice of simulation method.

Material characteristics like heat conductivity, thermal capacity and density are in general temperature dependent material parameters. The density of solid materials can be treated as constant. For gases or liquids, the assumption of a constant density is not always valid. For most gases the density is dependent on its current pressure and temperature. The relation can be most generally described by equation 4.1.[134]

$$\rho(p,T) = \frac{p}{R \cdot T} \tag{4.1}$$

[134] Siekmann & Thamsen 2008, P.106

If compressibility effects are neglected and the air pressure is assumed constant (equal to ambient pressure), the density of air inside the bell housing can be assumed only to be temperature dependent.

From the cold condition when the engine is started, the mass of air inside the bell housing is heated up and therefore decreases through openings to ambient (e.g. drainage holes, misalignments, etc.) until stationary temperatures inside the bell housing are obtained. In case of a slip event, the temperature of the air inside the bell housing increases, the air mass again decreases. As displayed in Figure 57, a temperature increase of 100 °K can lead to a 20% decrease of the air mass inside the bell housing.

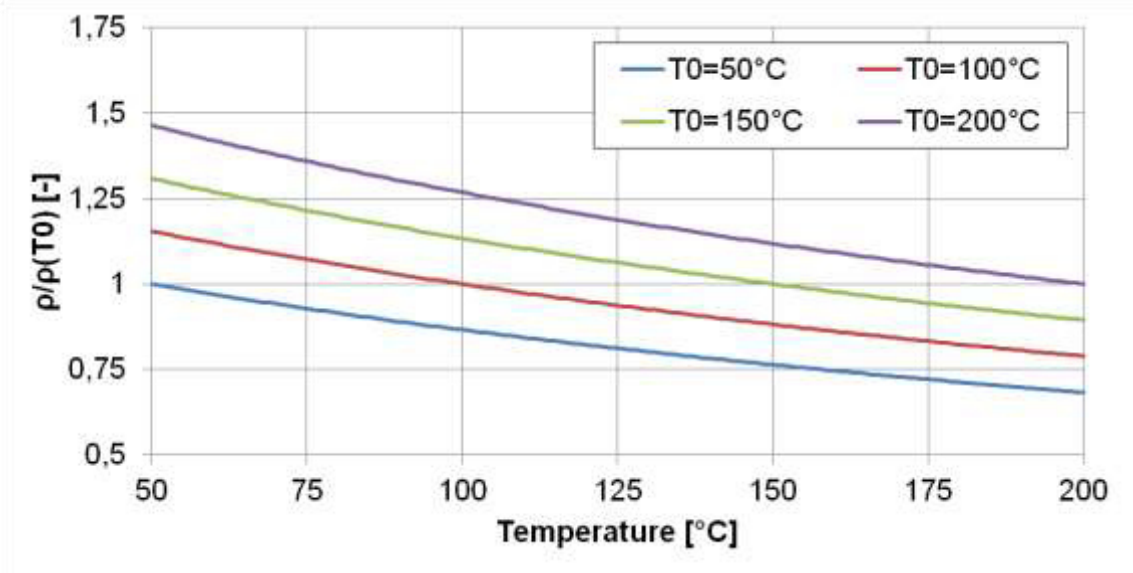

Figure 57: Relative Temperature Dependency of Air Density

It is therefore necessary in a simulation model for a clutch system to consider the changes in the thermal mass of air.

To judge the temperature dependence of the clutch material parameters, material measurements were performed. Target of the measurements was the determination of the temperature dependent thermal capacity and conductivity. The measurements were performed by NETZSCH Gerätebau GmbH with a NETZSCH LFA 447 NanoFlash (DIN EN 821 / ASTM E-1461).

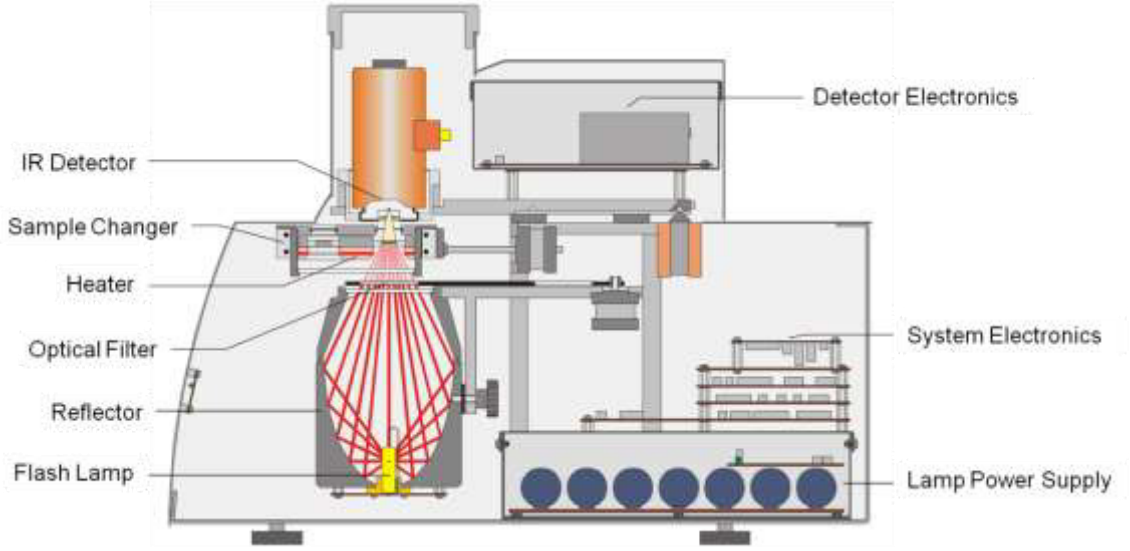

Figure 58: NETZSCH LFAQ 447 NanoFlash Operating Principle[135]

The operating principle of the NanoFlash is presented in Figure 58. A flash lamp located on one side of the material probe is used to create a thermal pulse. The flash intensity and duration can be adjusted in the system electronics. An IR detector is used to measure the temperature response on the opposite side of the probe. The resulting time dependent temperature function is then used to correlate the thermal diffusity. The thermal conductivity can finally be derived from formula 4.2.

$$\lambda(T) = \rho(T) \cdot c_p(T) \cdot a(T) \tag{4.2}$$

The determination of the density was obtained by using the hydrostatic balance method at room temperature. The thermal capacity was determined by the comparison method after ASTM-E 1461-2007 with a pure iron probe as reference.

To characterize the thermal material properties at different temperatures, the device in Figure 58 also contains an oven to pre-heat the material sample. All material probes were measured in new condition at 20 °C / 50 °C / 100 °C / 200 °C. At each temperature 5 measurements were performed and the average was applied. The overall maximum standard variance of the performed measurements was below 2% for each temperature. Figure 59 shows an example of the sample preparation.

A measurement of the material properties at different mileages to consider aging effects in the materials was not performed due to time constraints. The effect of the mileage on the material properties is recommended to be characterized in an additional study.

[135] Product Brochure: Netzsch LFA 447 NanoFlash

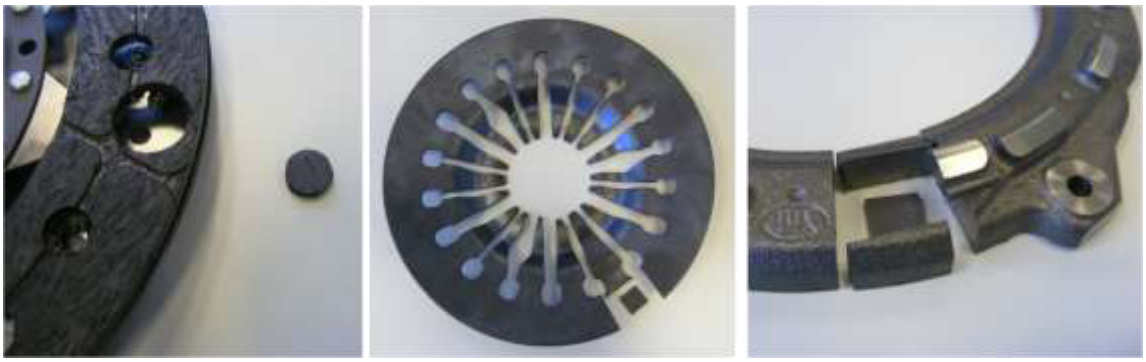

Figure 59: Sample Preparation: left: Lining; middle: Diaphragm Spring; right: Pressure Plate

A clear advantage of this method is that also compound materials can be measured. This makes it possible to also characterize the thermal properties of the lining material, which is usually a mixture of numerous materials. All clutch related materials can therefore be characterized by using the same method, which increases the profitability of this procedure.

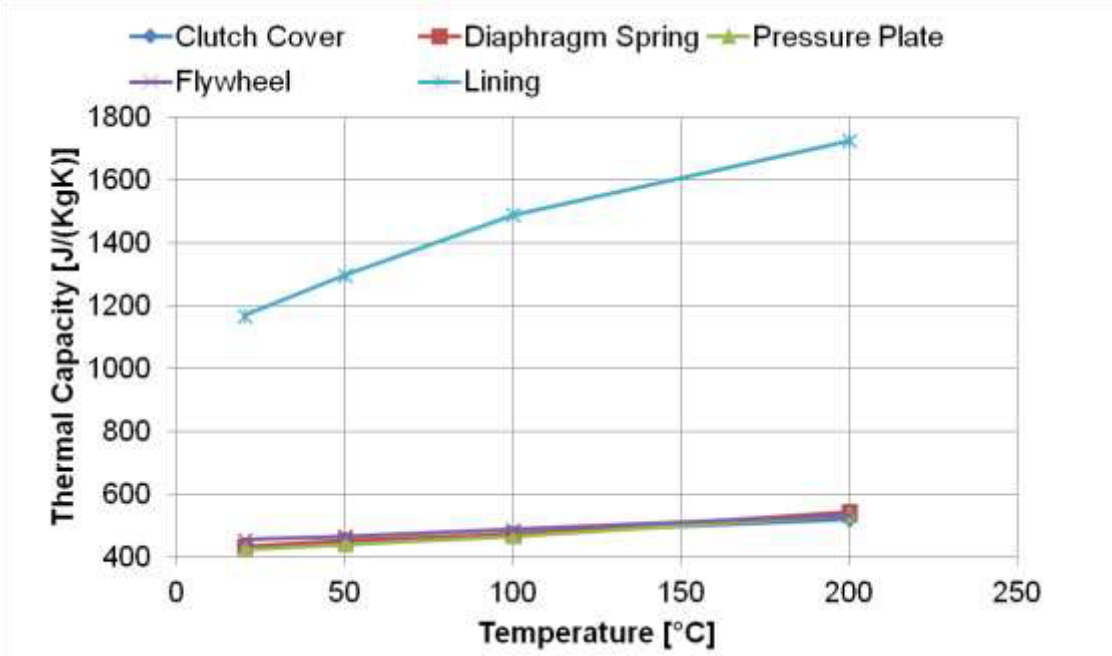

Figure 60: Temperature Dependence Thermal Capacity of Clutch System Materials

In Figure 60 the results of the thermal capacity measurements for the main clutch parts are displayed. All materials show similar behavior. From the normal operating condition of approximately 100 °C, an increase of 100 K results in a 12% increase of the thermal capacity. For the lining material, the thermal capacity is approximately 3 times higher than for the steel components.

For the thermal conductivity, the behavior is different. In Figure 61 the thermal conductivity dependences are displayed. While the thermal conductivity of the pressure plate and the diaphragm spring increases moderately with a temperature

increase, the thermal conductivity drops moderately for the flywheel and the clutch cover.

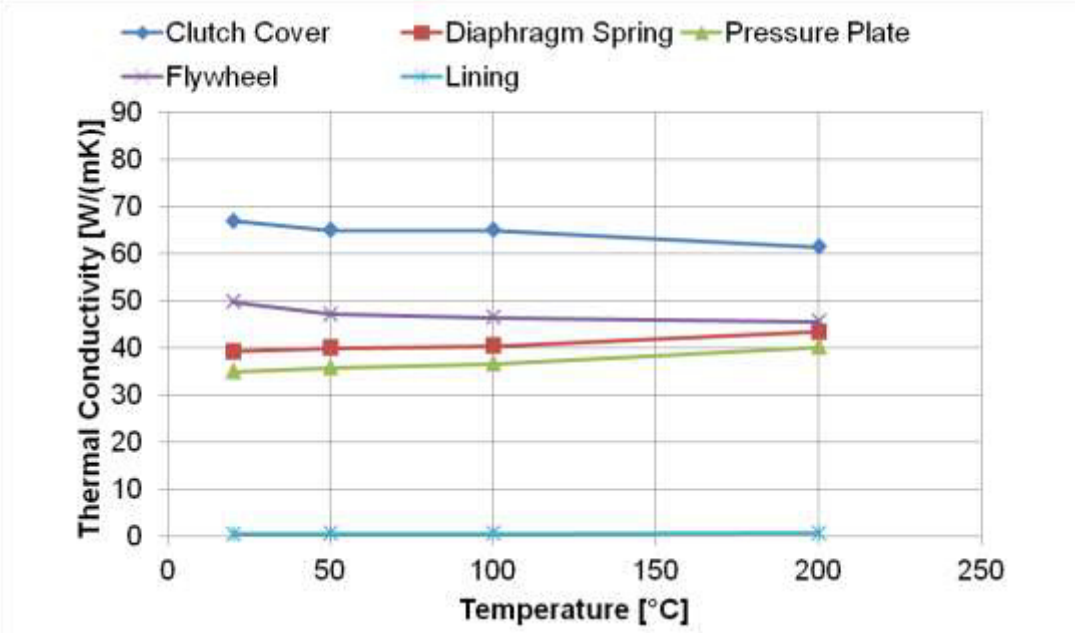

Figure 61: Temperature Dependence Thermal Conductivity of Clutch System Materials

The level of the thermal conductivity for the individual clutch parts is also different. The highest conductivity was measured for the clutch cover. The average increase / decrease from an operating condition of 100 °C and a temperature rise of 100 K is approximately 8%. As expected, the lining material has the lowest thermal conductivity.

From the results of the material measurements it can be quickly derived, that a correct knowledge of the material parameters of the clutch system components is of high importance. To display the effects of using constant instead of temperature dependent material parameters, a simplified example for heat conduction between the flywheel and the clutch cover will be applied.

The simplified heat balance for the conductional heat transfer between the flywheel and the clutch cover with negligible heat transfer by convection and radiation can be described by equation 4.3.

$$\frac{dT_{FW}}{dt} = \frac{\lambda_{eff} \cdot A}{l \cdot m_{FW} \cdot c_{p,FW}} \cdot \left(T_{Cov} - T_{FW}\right) \tag{4.3}$$

Now assuming that in one case the material parameters are constant and in another case they are temperature dependent, with a temperature difference of 100 K between both cases, the relation between the temperature changes at each time step can be described by equation 4.4.

$$\frac{\left(\frac{dT_{FW}}{dt}\right)_{const}}{\left(\frac{dT_{FW}}{dt}\right)_{temp.dep.}} = \frac{\left(\frac{\lambda_{eff} \cdot A}{l \cdot m_{FW} \cdot c_{p,FW}} \cdot (T_{Cov} - T_{FW})\right)_{const}}{\left(\frac{\lambda_{eff} \cdot A}{l \cdot m_{FW} \cdot c_{p,FW}} \cdot (T_{Cov} - T_{FW})\right)_{temp.dep.}} \tag{4.4}$$

Assuming that the masses and geometrical parameters are constant together with the assumption that the thermal capacity of the flywheel rises by 8% and the thermal conductivity of both parts drops by 8% at a temperature increase of 100 K, equation 4.4 simplifies to equation 4.5.

$$\frac{\left(\frac{dT_{FW}}{dt}\right)_{const}}{\left(\frac{dT_{FW}}{dt}\right)_{temp.dep.}} = 1.17 \cdot \frac{(T_{Cov} - T_{FW})_{const}}{(T_{Cov} - T_{FW})_{temp.dep.}} \tag{4.5}$$

This means that in this simplified case there exists already an offset of 17% if constant material parameters are assumed. It is therefore recommended to use temperature dependent material parameters.

4.2.4 Conclusion

For the heat transfer from clutch to ambient convection and conductional heat transfer play a major role for the heat transfer. As shown, heat transfer by radiation can be neglected. For convectional heat transfer it can be seen, that correlations found in literature for the Nusselt-Number are very problem specific and dependent on many geometrical and physical parameters. The problem with describing a flow or heat transfer for a clutch system with the theory of rotating disk systems is not only that the geometry is heavily abstracted, but also that the solution for one area is the starting condition for the next area in the flow system. This means, that small errors in one region are propagated through the system and make it less likely to obtain a correct solution in other regions. All correlations for the flow and heat transfer of rotating disk systems were obtained under constant, homogenous or idealized boundary conditions, which do not exist for the flow inside the bell housing. It is therefore seen impractical to correlate heat transfer quantities inside a clutch system by using literature data of simplified rotating disk cases.

Overall, CFD simulations in chapter 2.2.3.12 seem to offer a good way of determining the heat transfer characteristics. The possibility of calculating the heat transfer characteristics with geometrical and physical boundary conditions close to reality is seen as highest potential of obtaining the correct heat transfer characteristics of a clutch system.

As displayed in last part of this chapter thermal material parameters have to be modeled temperature dependent, which increases the model complexity.

4.3 Clutch Thermal Model

The first step in the development of a simulation tool, capable of simulating different clutch systems, is to perform a screening analysis on the general structure and the components of clutch systems. Main parts of a clutch system for an automotive application are (see chapter 2.1):

- Pressure Plate
- Flywheel
- Diaphragm Spring
- Clutch Disk (with Lining)
- Clutch Cover

Dependent on the functionality additional components can be present in a clutch system. For instance a self-adjusting clutch system (Figure 5) additionally has components that compensate the lining wear in order to obtain constant leaver relations and therefore a constant engagement force behavior of the clutch system. The additional components on one side enhance the thermal capacity and on the other side provide additional heat conduction paths through the pressure plate assembly.

Another difficulty arises, when a closer look is taken on the flywheel. With higher demands on vibration damping, it becomes necessary to apply dual mass flywheels. Dual mass flywheels consist of a primary and a secondary mass, which are connected via springs. These springs between the two masses are, for lubrication purposes, running in a grease or oil filling.

In both cases, for the self-adjusting clutch system and the dual mass flywheel, the additional parts would have to be treated as individual thermal masses. It would therefore be necessary to implement different clutch systems into the simulation tool to be able to reflect the differences in part numbers. Since it cannot be foreseen, what the future holds, it would be more convenient to find a way to treat all clutch systems with the same amount of thermal masses.

The main components presented earlier are always present for all clutch systems. It was hence decided to choose these components as main model parameters. The procedure how to still account for the additional components will be shown in chapter 4.4.

4.3.1 Model Structure

The principle model structure is shown in Figure 62 and is an adapted form of the model structure used in Figure 33 from [136]. The model was derived based on initial C&CM analysis with the help of the methods presented in chapter 2.7. Additionally to the thermal masses the model also includes the engine, transmission and clutch lining.

[136] Beitler 2008

Convectional interfaces are shown in orange, conductional interfaces in black and the frictional interface in blue. All parts in Figure 62 are treated as single thermal masses, except for the parts in direct contact with the frictional interfaces. For these parts, additional surface layers (green) are simulated to obtain a proper correlation towards the surface temperature. A total of three boundary layers per part was selected as standard.

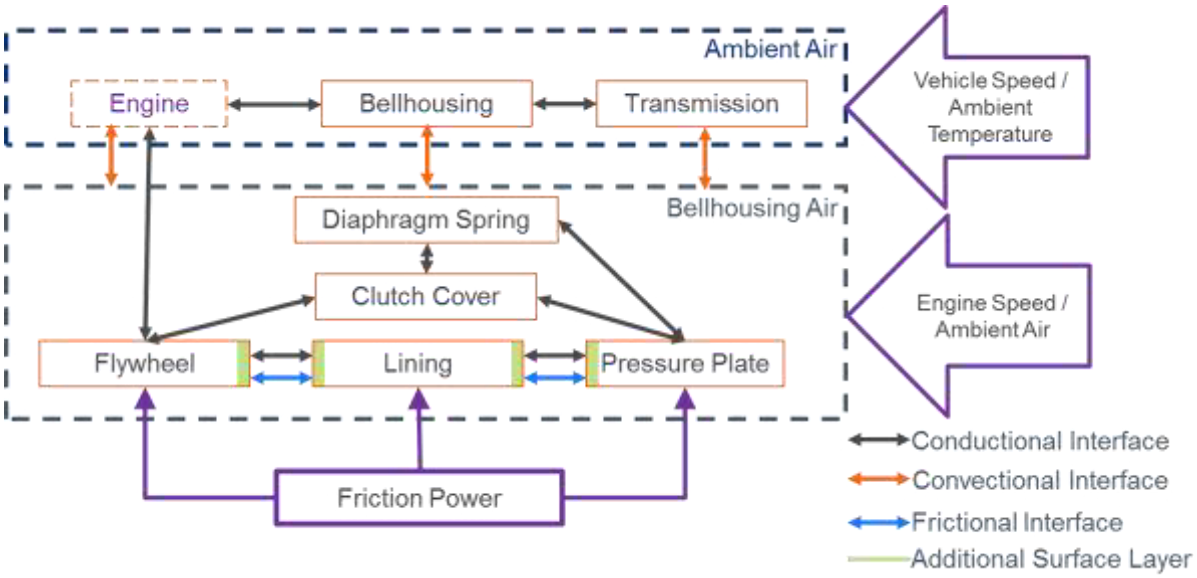

Figure 62: Boundary Diagram of Clutch Temperature Model based on initial C&CM Analysis

The engine temperature can be chosen as constant value, or be defined as input parameter together with the ambient temperature, vehicle speed and engine speed in the input file. Due to this, the convectional boundary is shown in a dashed line.

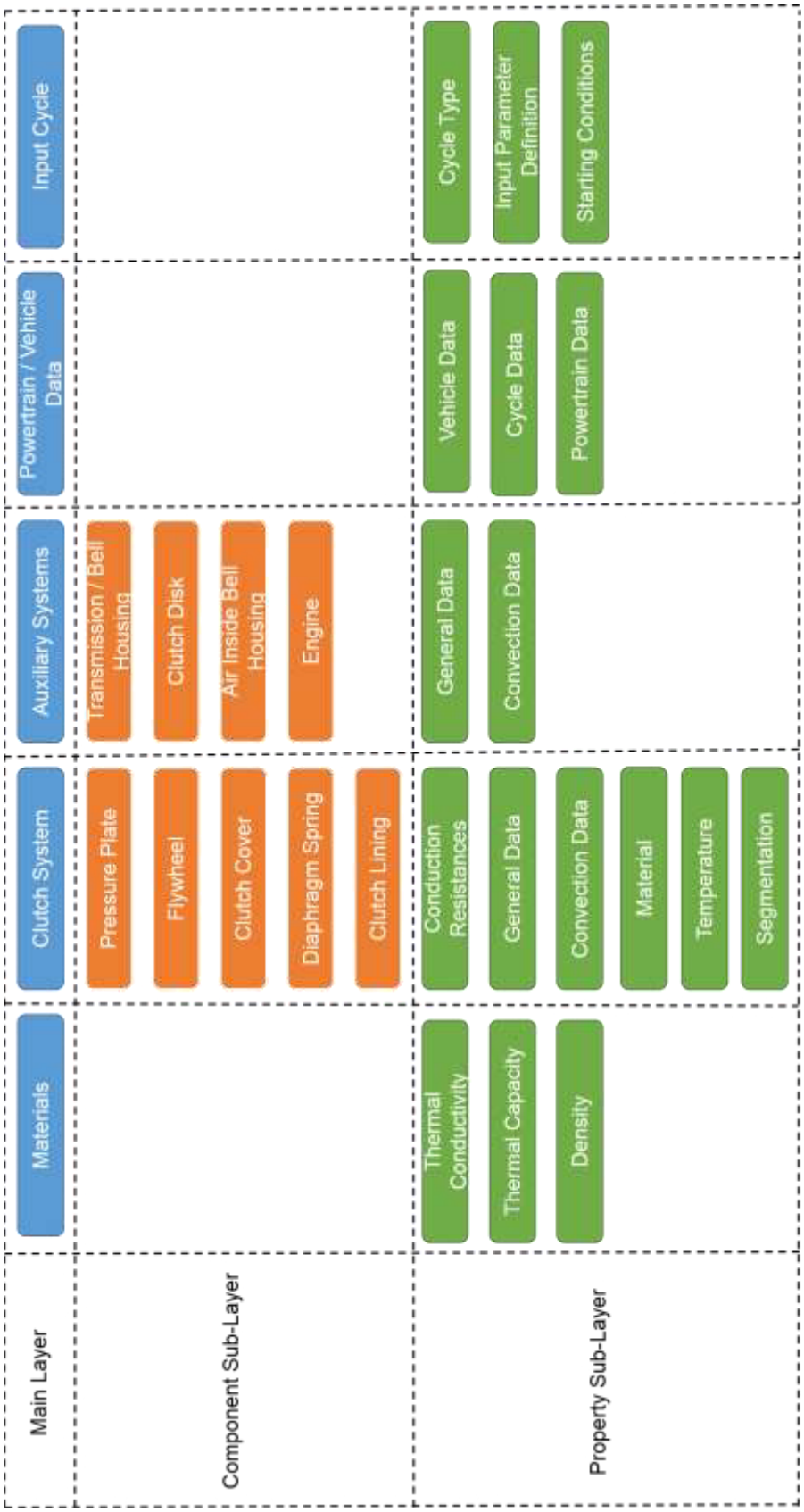

Figure 63: Model Layers

Figure 63 shows the general structure of the model. The model is divided into different layers. In the main layer, the user can choose or define different materials, clutch

systems, auxiliary systems, powertrain / vehicle data and define an input cycle for the model. The material, clutch system and auxiliary systems layer define objects with the properties and objects listed in the component and property sub-layer. A clutch system object consists for example of a pressure plate, flywheel, clutch cover, diaphragm spring and clutch lining object. Each component of the clutch system is an object with the properties listed in the property sub-layer. The applied object oriented programming helped to minimize the programming complexity by using similar code structures for similar objects. Properties like thermal conductivity, thermal capacity, density and convection resistances are implemented temperature, engine speed or vehicle speed dependent via tables.

When the user has defined the clutch system, auxiliary system, powertrain, vehicle data necessary to run the model (including their individual sublayer properties), the last step is to define the input cycle. The user can choose between a frequent launch calculation, a single launch event both with settings defined in the vehicle / powertrain data table or run a temperature calculation with input data from a data file. In the frequent or single launch calculation the frictional power needed as input for the simulation is calculated according to the energy calculation procedure in chapter 2.4.1. The ambient conditions, engine speeds and vehicle speeds are assumed constant for these cycles. Figure 64 shows the flowchart of the frequent launch cycle.

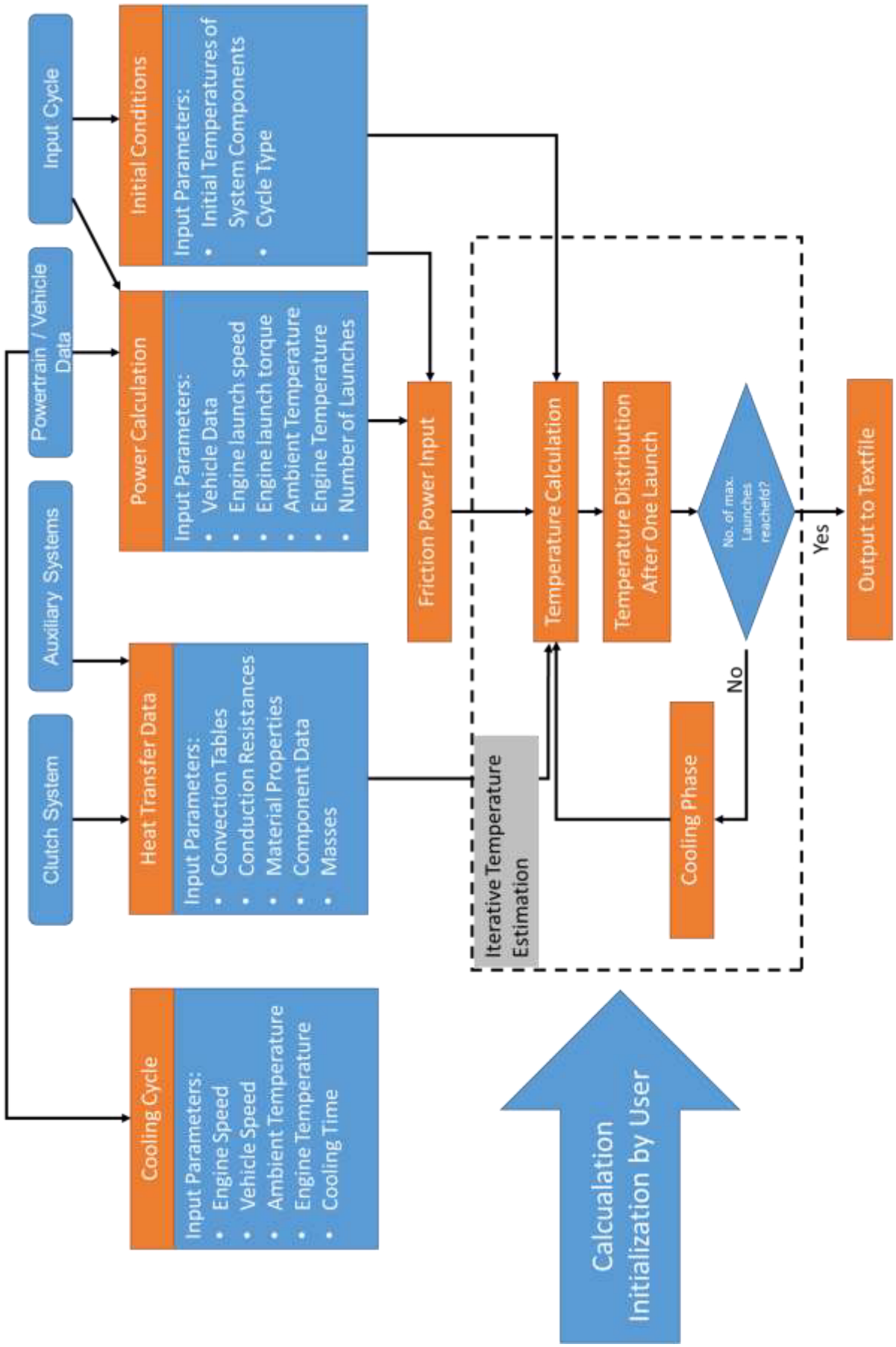

Figure 64: Flow Chart of Frequent Launch Cycle

After launching the temperature calculation, the calculated temperatures are written to an output text-file which can be processed in an external data processing software (e.g. MS EXCEL). It is also planned to implement a life cycle simulation which can be implemented as extension of the frequent launch cycle. The extension can be easily implemented with an additional iteration loop around the iterative temperature estimation block in Figure 64. Different power distributions, ambient temperatures, engine and vehicle speeds could be implemented in a simple way.

The simulation model was programmed in JAVA Eclipse 3.1. A main advantage of said proceeding is, that it can be run on almost any PC operating system, since JAVA uses a virtual machine to execute the desired program code. The software is therefore platform independent and thus assumed to have a bigger life span.

Based on the findings in chapter 2.4.2 it was chosen to use an implicit method as solver to preserve the possibility to implement varying time steps to save simulation time (small time step at power input – large time step at cooling).

$$\frac{T_{PP}^{n+1} - T_{PP}^{n}}{\Delta t} = \frac{1}{m_{PP} \cdot c_p(T_{PP}^{n+1})} \cdot [\lambda_{PP-DS} \cdot \left(T_{DS}^{n+1} - T_{PP}^{n+1}\right) + \lambda_{PP-CC} \cdot \left(T_{CC}^{n+1} - T_{PP}^{n+1}\right) + \lambda_{PP} \cdot \left(T_{PP\,k-1}^{n+1} - T_{PP}^{n+1}\right) + \alpha_{PP} \cdot \left(T_{Air\,BH}^{n+1} - T_{PP}^{n+1}\right)] \tag{4.6}$$

From equation 2.49 (chapter 2.4.2), equation 4.6 can be derived which is shown here as an example of an implicit temperature equation (index n: current state; index n+1 next state in time after the current state). Since the thermal capacities are temperature dependent and the solution of equation 4.6 would therefore lead to extensive mathematical effort, it was chosen to use an iterative scheme according to equation 2.50 to solve the equation.

For the launch energy input calculation, the simplified equations from chapter 2.4.1 for power intake calculations for a manual clutch system where adapted according to equations 4.7 to 4.9 to implement factors describing the driver behavior as outlined in chapter 4.1.

$$M_{clutch} = M_{res} + d_2 \cdot \left(M_{engine} - M_{res} - \frac{J_{Engine} \cdot \omega_{launch} \cdot (d_1 - 1)}{t_s} \right) \tag{4.7}$$

$$M_{clutch} - M_{res} = \frac{J_{red} \cdot \omega(t = t_s)}{t_s} = d_2 \cdot \left(M_{engine} - M_{res} - \frac{J_{Engine} \cdot \omega_{launch} \cdot (d_1 - 1)}{t_s} \right) \tag{4.8}$$

$$t_s = \frac{d_1 \cdot \omega_{launch} + d_2 \cdot \frac{J_{engine}}{J_{red}} \cdot \omega_{launch} \cdot (d_1 - 1)}{\frac{d_2}{J_{red}} \cdot \left(M_{engine} - M_{res}\right)} \tag{4.9}$$

In the equations d_1 represents the engine speed drop factor and d_2 represents the driver factor. They are calculated according to equations 4.10 and 4.11. The transmission or secondary side rotational speed at vehicle start is assumed to be zero. All engine speed changes in this approach are assumed to have a linear character.

$$d_1 = \frac{\omega(t = t_s)}{\omega(t = 0)} \tag{4.10}$$

$$d_2 = \frac{a_{launch}}{a_{available}} \tag{4.11}$$

The engine speed drop factor (4.10) is the relation between the engine speed at the start of the launch and the synchronized engine speed when the clutch is closed. The driver factor (eq. 4.11) is the relation between the launch acceleration and the maximum available acceleration determined from the engine map and the engine launch speed. The transferred clutch torque in equation 4.7 can therefore be interpreted as representing the sum of the powertrain resistances together with the remaining torque used for accelerating the vehicle.

These factors can be used to characterize driver performance and vehicle characteristics. For the precise determination of these factors measurements of the clutch power input are necessary. First measurements of the driver behavior of expert drivers on a test track (chapter 4.1) show, that it is possible to characterize drivers with these formulas. It could be shown, that taking one launch of a driver as basis and extrapolating all other launches from this basis, only a constant factor was between the slopes of the calculated (blue line) and measured (red line) energy intake as displayed in Figure 65.

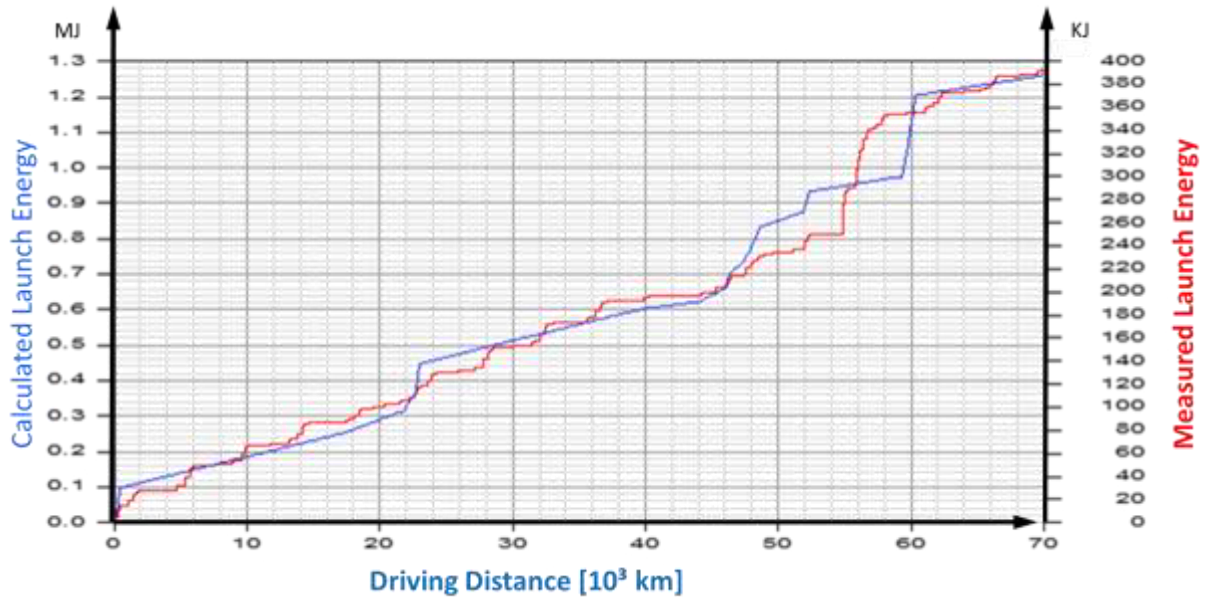

Figure 65: Comparison of Calculated and Measured Launch Energy Input

With equations 4.7 to 4.11 the frictional power input can be evaluated according to equations 4.12 to 4.15.

$$\omega_{engine}(t) = \omega_{launch} \cdot \left(1 + (d_1 - 1) \cdot \frac{t}{t_s}\right) \tag{4.12}$$

$$\omega_{transmission}(t) = \left(M_{engine} - M_{res} - \frac{J_{engine} \cdot \omega_{launch} \cdot (d_1 - 1)}{t_s}\right) \cdot \frac{d_2 \cdot t}{J_{red}} \tag{4.13}$$

$$\omega_{slip}(t) = \omega_{engine}(t) - \omega_{transmission}(t) \tag{4.14}$$

$$P_{friction}(t) = M_{clutch} \cdot \omega_{slip}(t) \tag{4.15}$$

4.4 Heat Transfer Simplification Process

For the simplification of the surface averaged heat transfer coefficients several considerations were taken into account. In a first step it was tried to use similarity analysis to select proper geometrical aspects of the clutch system and relate the heat transfer data to these parameters (see chapter 2.2.3.5). Main driver for this consideration was the idea to find globally valid mathematical descriptions for the heat transfer of the individual parts.

As equations 2.25 and 2.26 indicate, there exists a relation between the surface friction and the heat transfer at the surface of the body of interest. For a clutch system under vehicle mounting conditions this relation can be used if the flow system inside the clutch system and the recirculation flow outside the clutch system could be decoupled. The problem that arises here is that in vehicle powertrains mostly the clutch system size varies and due to cost optimization considerations the bell housing of a transmission does not, so that the clearance between the outer diameter of the clutch system and the bell housing changes. This change then has influence on the recirculation flow and therefore on the surface friction in and outside of the bell housing, making the relations found for the same clutch system for one application not relatable to another application.

With the possibility to have different engines, transmissions, clutch systems and actuation systems, there are simply too many parameters that can be changed. A similarity analysis based description is therefore seen from this standpoint as impractical. It was chosen to neglect the description of the convectional heat transfer by analogy relations and to use a description related only to the powertrain application under consideration. With an increasing number of investigated powertrains it is recommended here to come back to the point of considering the description with analogy relations.

For the simplified model, a heat transfer coefficient based on a global reference temperature is seen as the most promising approach and was therefore implemented, because no additional changes in the model structure are necessary.

A problem that can arise with the use of a heat transfer coefficient based on a global approach is if the temperature difference between the wall and the reference temperature approaches zero, resulting in values close to infinity. To overcome this difficulty, the averaging process was adapted.

$$h_{glob} = \frac{\sum_i \frac{q_{w,i} \cdot A_i}{\left(T_{wall,i} - T_{ref.}\right)}}{\sum_i A_i} \tag{4.16}$$

$$h_{glob} = \frac{\sum_i Q_{w,i}}{\left(\left(T_{wall,av} - T_{ref.}\right) \cdot \sum_i \left(A_i\right)\right)} \tag{4.17}$$

By using equation 4.17 instead of the implemented equation 4.16 to describe the surface averaged heat transfer due to convection, the difficulties of heat transfer coefficients close to infinity are avoided. This step can be seen as additional filtering process necessary to avoid numerical difficulties.

If the temperature difference in equation 4.17 is set as the difference between the average fluid temperature and the average temperature of the solid body under consideration, the additionally necessary modeling of the wall layer of the solid structure in the simplified model can be avoided. This again reduces the overall complexity.

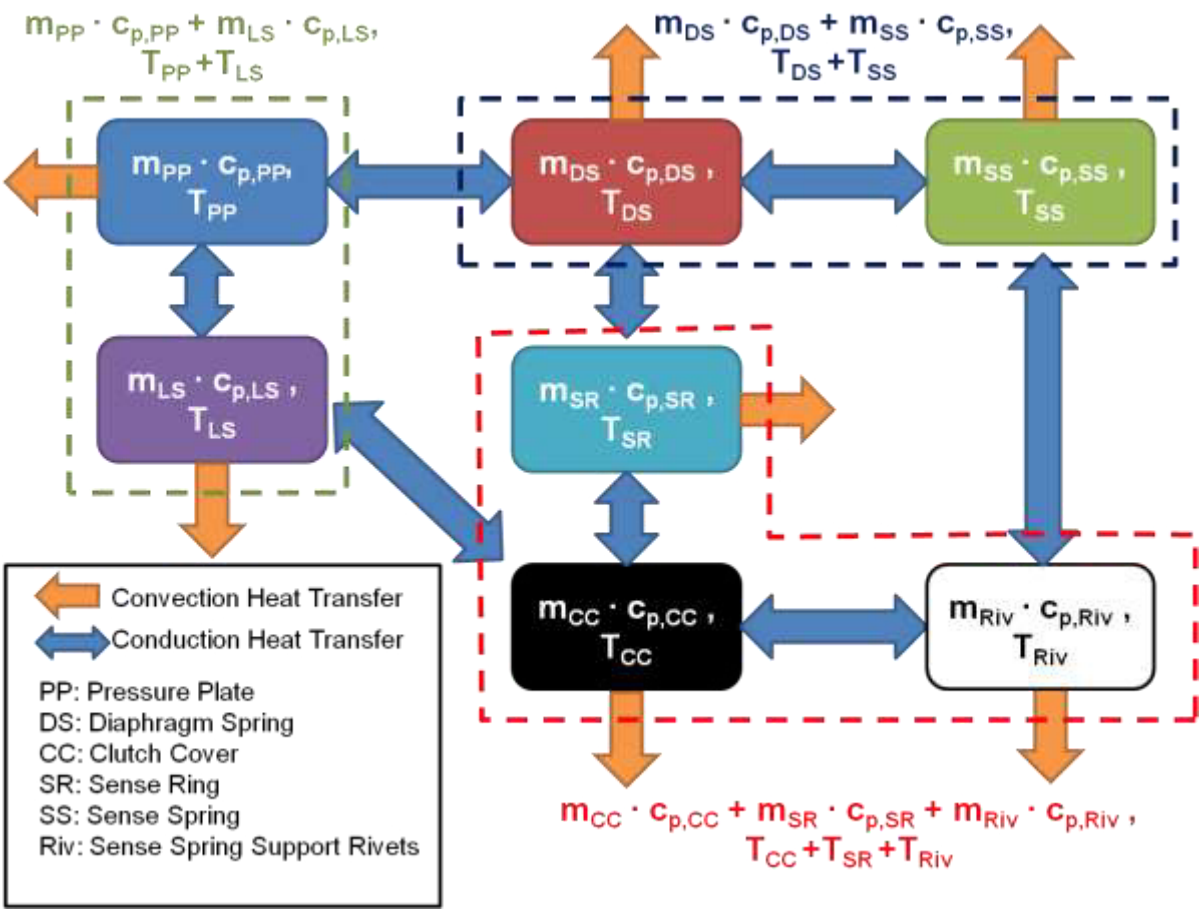

Figure 66: Example of the Heat Transfer Simplification Process for a SAC Clutch System (Figure 5)

After the definition of a heat transfer coefficient to be used for the simplification process, it is necessary to find a way on how to reduce the components of the clutch system to match the structure of the model presented earlier.

For the reduction of the parts inside the clutch system it is necessary to have a close look at the overall energy balance inside the clutch system. In Figure 66 the simplification process is shown for the heat transfer between the pressure plate, diaphragm spring and the clutch cover. The connection of the pressure plate and clutch cover will be used to explain the simplification process.

Heat from the pressure plate is transferred to the clutch cover by heat conduction through the lift springs. The lift springs are not considered in the thermal clutch model, because they have a low thermal mass. Still, the overall heat balance of the thermal system has to be maintained. The heat conducted from the pressure plate is not fully conducted into the clutch cover. Part of the heat is lost via convection to the air inside the bell housing. In order to capture the heat transfer correctly and address it to the right phenomena, the heat loss by convection has to be added to the convectional heat transfer of the pressure plate. The heat transferred by conduction from the “augmented” pressure plate is therefore less than from the component itself (with an

increase in convectional heat transfer). This approach can also be displayed for this connection, when regarding the simplified energy balance between the three components.

$$m_{PP} \cdot c_{p,PP} \cdot \frac{dT_{PP}}{dt} = -\dot{Q}_{conv,PP} - \dot{Q}_{cond,PP-LS} \tag{4.18}$$

$$\overset{=0}{\cancel{m_{LS} \cdot c_{p,LS} \cdot \frac{dT_{LS}}{dt}}} = -\dot{Q}_{conv,LS} + \dot{Q}_{cond,PP-LS} - \dot{Q}_{cond,LS-CC} \tag{4.19}$$

$$\dot{Q}_{cond,PP-LS} = \dot{Q}_{conv,LS} + \dot{Q}_{cond,LS-CC} \tag{4.20}$$

$$m_{CC} \cdot c_{p,CC} \cdot \frac{dT_{CC}}{dt} = -\dot{Q}_{conv,CC} + \dot{Q}_{cond,LS-CC} \tag{4.21}$$

$$m_{PP} \cdot c_{p,PP} \cdot \frac{dT_{PP}}{dt} = -\dot{Q}_{conv,PP} - \dot{Q}_{conv,LS} - \dot{Q}_{cond,LS\text{-}CC} \tag{4.22}$$

From the energy balance of the lift springs (equation 4.18) and the assumption, that the thermal mass of the lift spring can be neglected, equation 4.20 can be directly derived. While nothing changes for the energy balance of the clutch cover (equation 4.21), the energy balance of the pressure plate (equation 4.18) is now replaced by the augmented form (equation 4.22).

For parts, where the thermal mass cannot be neglected as in the simple case for the lift springs, other measures have to be taken. The heat exchange between two thermal masses with additional convection can be described by equation 4.23 and 4.24.

$$m_1 \cdot c_{p,1} \cdot \frac{dT_1}{dt} = -\dot{Q}_{conv,1} - \dot{Q}_{cond,1-2} \tag{4.23}$$

$$m_2 \cdot c_{p,2} \cdot \frac{dT_2}{dt} = -\dot{Q}_{conv,2} + \dot{Q}_{cond,1-2} \tag{4.24}$$

Solving equation 4.24 for the conductional part and substituting the result into equation 4.23 results in equation 4.25.

$$m_1 \cdot c_{p,1} \cdot \frac{dT_1}{dt} + m_2 \cdot c_{p,2} \cdot \frac{dT_2}{dt} = -\dot{Q}_{conv,1} - \dot{Q}_{conv,2} \tag{4.25}$$

$$m_1 \cdot c_{p,1} \cdot \frac{dT_1}{dt} + m_2 \cdot c_{p,2} \cdot \frac{dT_2}{dt} = -\dot{Q}_{conv,12} \tag{4.26}$$

As displayed in equation 4.26 the heat transferred by convection can be summarized into one variable. Target is now to transfer equation 4.26 into equation 4.27.

$$\left(m \cdot c_p\right)_{av} \cdot \frac{dT_{av}}{dt} = -\dot{Q}_{conv,12} \tag{4.27}$$

$$m_1 \cdot c_{p,1} \cdot \frac{dT_1}{dt} + m_2 \cdot c_{p,2} \cdot \frac{dT_2}{dt} = (m \cdot c_p)_{av} \cdot \frac{dT_{av}}{dt} \quad | \cdot dt \tag{4.28}$$

$$m_1 \cdot c_{p,1} \cdot dT_1 + m_2 \cdot c_{p,2} \cdot dT_2 = (m \cdot c_p)_{av} \cdot dT_{av} \tag{4.29}$$

$$(m \cdot c_p)_{av} = m_1 \cdot c_{p,1} + m_2 \cdot c_{p,2} \tag{4.30}$$

$$\frac{m_1 \cdot c_{p,1} \cdot T_1^+ + m_2 \cdot c_{p,2} \cdot T_2^+}{m_1 \cdot c_{p,1} + m_2 \cdot c_{p,2}} - \frac{m_1 \cdot c_{p,1} \cdot T_1^- + m_2 \cdot c_{p,2} \cdot T_2^-}{m_1 \cdot c_{p,1} + m_2 \cdot c_{p,2}} = T_{av}^+ - T_{av}^- \tag{4.31}$$

$$\frac{m_1 \cdot c_{p,1} \cdot T_1 + m_2 \cdot c_{p,2} \cdot T_2}{m_1 \cdot c_{p,1} + m_2 \cdot c_{p,2}} = T_{av} \tag{4.32}$$

By setting equation 4.26 equal to 4.27 and multiplying the result by a time increment dt one obtains equation 4.29. With an average thermal mass described by equation 4.30 and taking the differential between two small time steps (indicated by + and -) one finally obtains equation 4.32, which is the needed definition for the average temperature. In equation 4.30, the thermal capacities are temperature dependent. The simplification can still be performed, since the difference between the individual capacities is small and the temperature difference between the directly coupled parts is rather small.

Since in the simplified model, the convectional heat transfer coefficients will be calculated in dependence of the engine speed, it is important to monitor the heat amount transferred by a component and the component temperature itself in the CFD simulation model. To calculate the augmented heat transfer coefficients (see equation 4.33), the heat amount by convection can be summarized to obtain its final value, but the average temperature has to be calculated according to equation 4.32.

$$h_{av} = \frac{\sum_i Q_{conv,i}}{(T_{av} - T_{av,air}) \cdot \sum_i A_{conv,i}} \tag{4.33}$$

For the heat conduction parameters this process of averaging the temperatures is also necessary. The conductivity between two masses will be evaluated according to equation 4.35.

$$L_{av} = \frac{\dot{Q}_{cond,1-2}}{(T_{av,1} - T_{av,2}) \cdot \sum_i A_{cond,i}} \tag{4.35}$$

For the surfaces in equation 4.35, either the contact surfaces between the two parts will be taken as conduction area, or the smallest cross section in the heat conduction path.

With equations 4.32 to 4.35 all necessary equations to define the simplified heat transfer are available. In the simplification procedure the clutch cover, support rivets of the sense spring and the cover screws will be simplified to represent one thermal mass. The diaphragm spring together with the sense ring and sense spring will also be joined to represent one thermal mass. And finally, the lift springs and the pressure plate will be taken as one part (see Figure 66). The main reason for this choice was the heat transfer path and the contact surface to the neighboring part. The touching surface between the diaphragm spring and the sense spring or sense ring is significantly larger than between the mentioned parts and the clutch cover. The heat between these parts is therefore spread much easier.

5 CFD Based Heat Transfer Determination of a Vehicle Clutch System

The simulation of a clutch system under vehicle mounting conditions is treated in this chapter. The main focus is on how the rotating movement of a clutch system can be modeled, how the temperature is spread inside the clutch system and how the flow field inside the bell housing can be described. As will be shown, a conjugate heat transfer model of a clutch system can aid the identification of optimization potentials.

5.1 CFD Model

For the evaluation of the heat transfer characteristics of a clutch system under vehicle mounting conditions, a CFD model was set up in Star CCM+. The model is primarily based on the initialization calculations of the CFD model presented in [137], which was developed by cd-Adapco for transient simulation of a clutch system during a launch procedure.

During initial discussions with cd-Adapco, a simplification of the overall mesh by only using a section of the geometry was considered. This option was then neglected due to lack of symmetry of the bell housing.

The geometry modeled consisted of a self-adjusting clutch system (composed of the pressure plate assembly, clutch disk with lining and the single mass flywheel), crankshaft, clutch actuation cylinder with release bearing, bell housing of the transmission, rear face of the engine block, and the starter engine from a Ford Fiesta ST MK06 (Figure 67). To optimize the simulation, only the primarily necessary parts were considered. For instance the engine block or the starter motor have been cut off and the rest of the transmission was neglected.

[137] Ford Development Report 371-218552-R1 2012

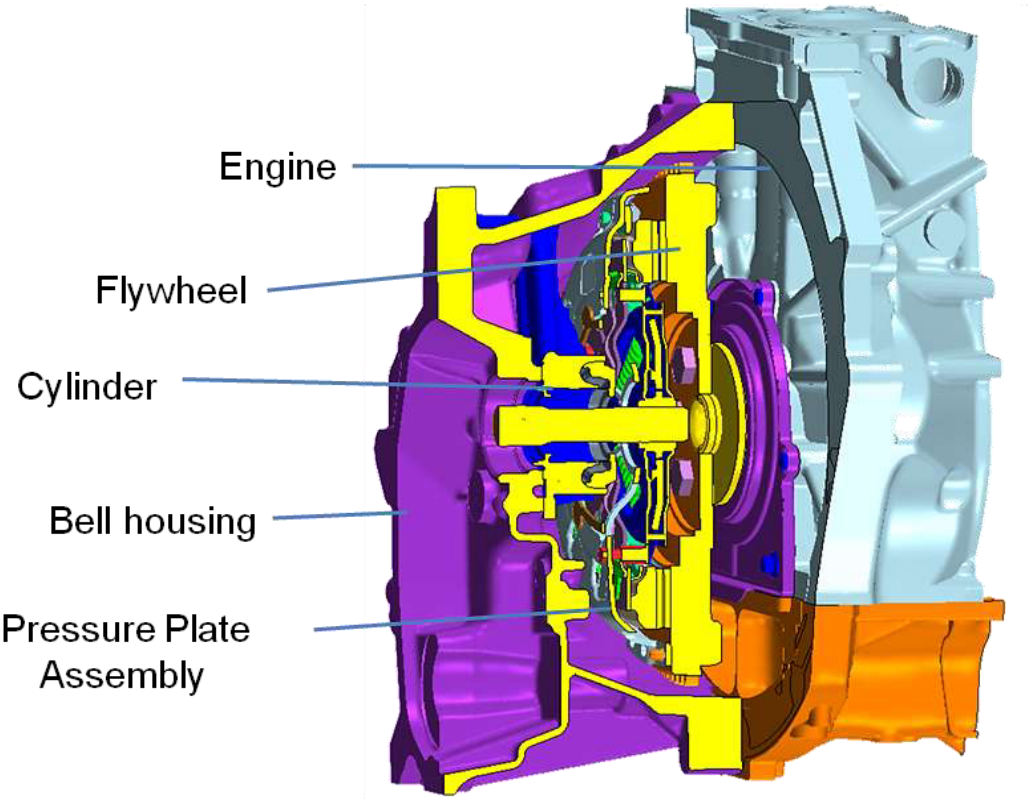

Figure 67: Modeled Geometry

The rotating movement of the clutch system was modeled by a moving reference frame approach (see chapter 2.2.3.11), together with a rotation rate applied to boundary surfaces with suitable orientation (e.g. backside surface of flywheel, crankshaft or transmission input shaft). The air region between the clutch system and the bell housing was divided according to Figure 68.

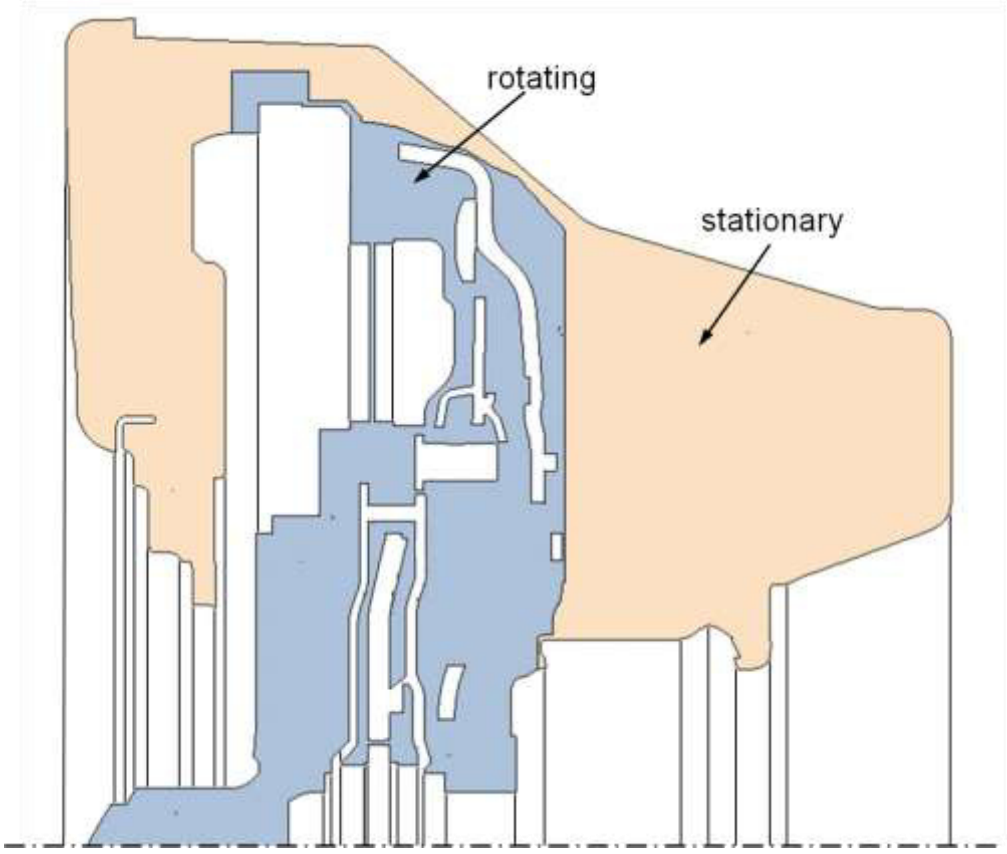

Figure 68: Division of Air inside Bell Housing[138]

Main target of the simulations was the determination of the conduction and convection heat transfer coefficients under different engine speeds. It was therefore chosen to use a conjugate heat transfer modeling approach for the simulations. In this approach both the fluid and solid regions thermal balances are evaluated together, allowing direct interaction between the temperature fields of the air inside the bell housing and the other solid components. An additional advantage of this approach is that only one model has to be run to obtain the results (compared to the hill launch CFD model in [139]).

As boundary conditions for the simulations, a constant specific heat input of 15000 W/m² at the flywheel or pressure plate frictional interface was considered. The engine speed was set constant at 750 / 1500 / 3000 / 4500 / 6000 rpm. It was hereby possible to obtain a heat distribution in the system close to the conditions faced by a clutch system in reality. A relative movement between the clutch disk and the clutch system itself was not considered. The clutch system was considered closed. The temperature of the engine block and the crankshaft was set constant at 87 °C (derived from measurement data). For the outside surface of the bell housing (including the

[138] Ford Development Report 371-218552-R1 2012, P.11
[139] Ford Development Report 371-218552-R1 2012

starter motor) a convection boundary condition with a heat transfer coefficient of 20 W/(m²K) and a reference temperature of 60 °C, which are reflecting the conditions of a vehicle launch. Under driving conditions (gear shift) the outside conditions will change according to the vehicle speed, but the energy input will not be as high as under launch conditions. To represent the heat transfer conditions at the transmission side of the bell housing a convection boundary condition with a heat transfer coefficient of 10 W/(m²K) and a reference temperature of 60°C was set. At the openings to the ambient a pressure outlet boundary condition was chosen with an air temperature of 60 °C. The openings to the ambient air are displayed in Figure 69. One opening is located at the starter engine and one opening results from a misalignment between the engine and the bell housing. The small drainage hole at the bottom (Figure 69) was neglected).

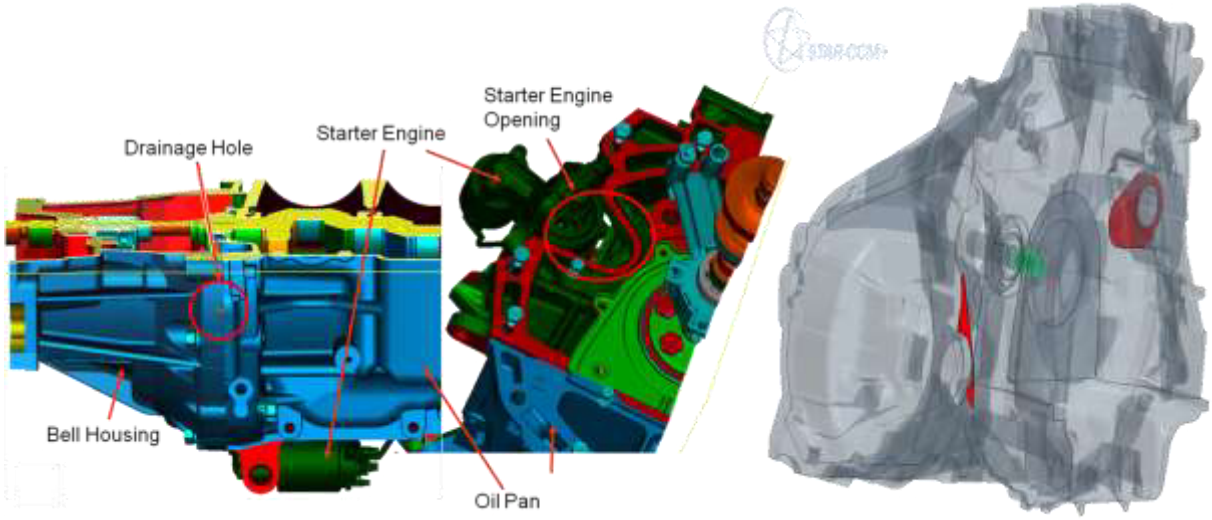

Figure 69: Openings to the Ambient Air (red) (Adapted from [140])

As initial temperature of the bell housing 85 °C was chosen. For all other solid bodies (except the engine block) and the air inside the bell housing 70 °C was chosen as initial temperature.

The air inside the bell housing was considered as ideal gas. In an additional simulation run, it was also treated with the constant density option. This separation between the two models was performed due to the fact, that because of the large outer diameter of the clutch system and the high rotary speeds (above 5500 rpm) a Mach number of above 0.3 would be reached.

The values for the materials of the clutch and peripheral structure where set according to the results of the material measurements (chapter 4.2.3). For the aluminum casting

[140] Ford Development Report 371-218552-R1 2012, P.22

of the bell housing standard values from literature were taken. The data for the clutch actuation cylinder was set according to the lining data.

A mesh on the basis of polyhedral cells was used for the simulation. Polyhedral meshes have the advantage for systems with poorly known velocity vector field, that the cells faces have a high probability to be oriented advantageous to the flow field. For the mesh settings the tight packaging of the clutch assembly and the direct connection of the cell size to the overall simulation steps needed for a converged solution were taken into account. It was decided to model the boundary layer between the solids and the air inside the bell housing with one layer together with a global boundary layer thickness of 0.5 mm. Figure 70 shows the mesh structure inside the pressure plate assembly.

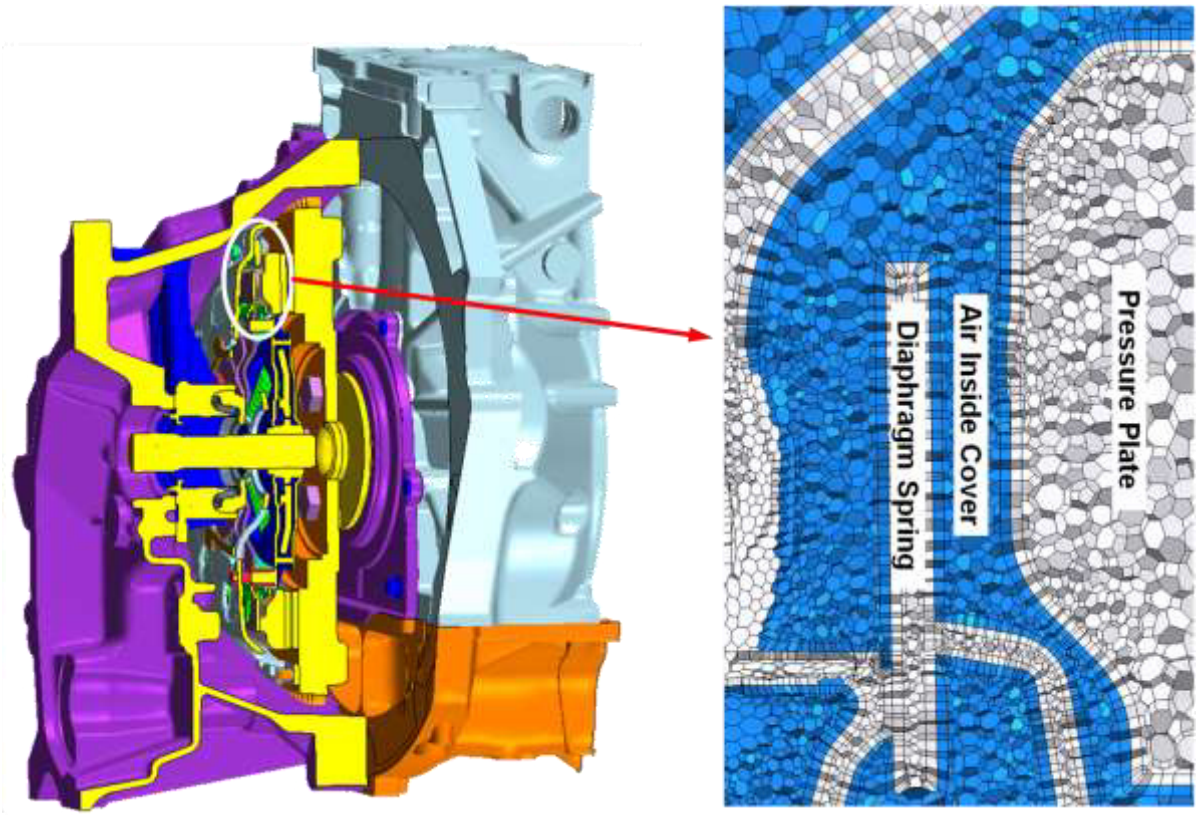

Figure 70: Mesh Structure inside the Pressure Plate Assembly

This definition results in the need to choose the all-wall-y+ treatment for the boundary layer. Since for a pre-defined thickness of the boundary layer, the y+ values will not be in the recommended region, the all-wall-y+ treatment allows the simulation to switch between the wall treatment for a resolved boundary layer and the wall-law treatment. At interfaces between solid parts an additional boundary layer per part was considered. Since high gradients were expected at the interface between the lining and the flywheel / pressure plate, the amount of boundary layers was increased. As quality thresholds the minimum face validity was set to 0.8, the minimum cell quality was set to 10^{-6} and the minimum volume change was set to 10^{-4}. The face validity is a measure of how

faces are oriented towards the cell center. A face validity below 0.5 is an indication for negative volume cells, which can result in poor quality of the obtained volume mesh.[141]

As turbulence model, the reasonable k-ε model was used, which is the standard turbulence model in Star-CCM+. The use of a large eddy or detached eddy turbulence model was not considered, since the transient simulation would cause a significant increase in the discretization effort (time and space). The need to solve seven conservation equations with a Reynolds-Stress-Model would also increase the calculation time and resources.

5.2 Simulation Results

The principle structure of the flow field is shown in the vector field plot of Figure 71. In this figure, the vector length was set constant, so that only the color represents the velocity magnitude. The smaller the vectors are, the larger the velocity component in tangential direction is. The flow field can be divided into two major recirculation regions divided by the flywheel. The developing recirculation flow structures are indicated by the schematic arrows in Figure 71.

The first recirculation flow is located at the pressure plate assembly side of the bell housing. After entering the clutch system through the openings in the cover or the diaphragm spring openings, air is mainly passing through in tangential and radial direction. As indicated there exists very little flow exchange between the air enclosed by the clutch disk and the flywheel and the rest of the air inside the clutch system. After the flow has passed the pressure plate, the flow leaves the pressure plate assembly through the holes in the clutch cover. The flow then impacts on the bell housing and is directed back towards the openings of the clutch system.

[141] Star-CCM+ User Manual 2010

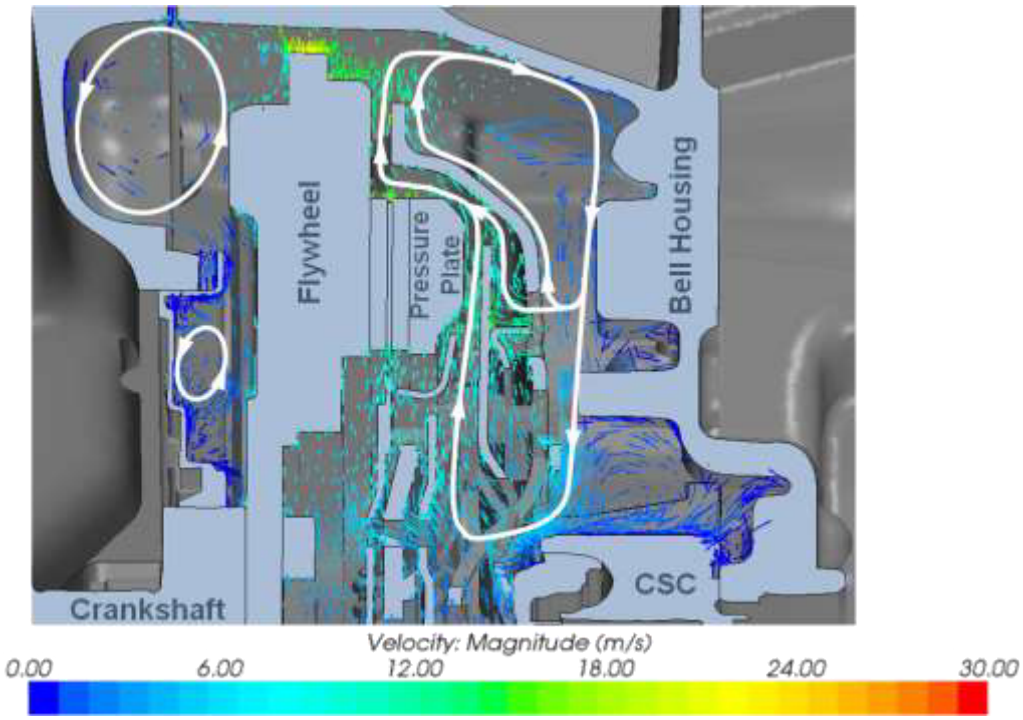

Figure 71: Flow Field Inside the Bell Housing

The first expectation here was, that because of the angle of the bell housing wall there would be a flow exchange happening with the flywheel sided air. The ring gear at the outer diameter of the flywheel and the small clearance to the bell housing wall act here as flow field separators.

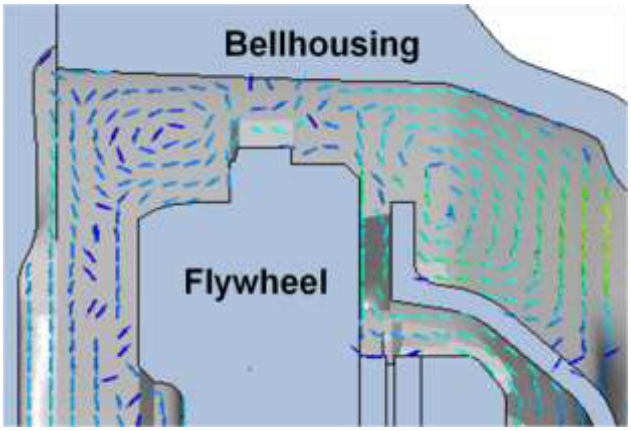

Figure 72: Flow Field Separation Inside the Bell Housing

As shown in Figure 72 the flow at the flywheel side is circulating back towards the engine side of the powertrain and air at the pressure plate assembly side of the flywheel is circulating back towards the transmission side of the powertrain. This phenomenon was monitored at all engine speeds. The separation between the left and right sided air of the flywheel has also effect on the temperature field.

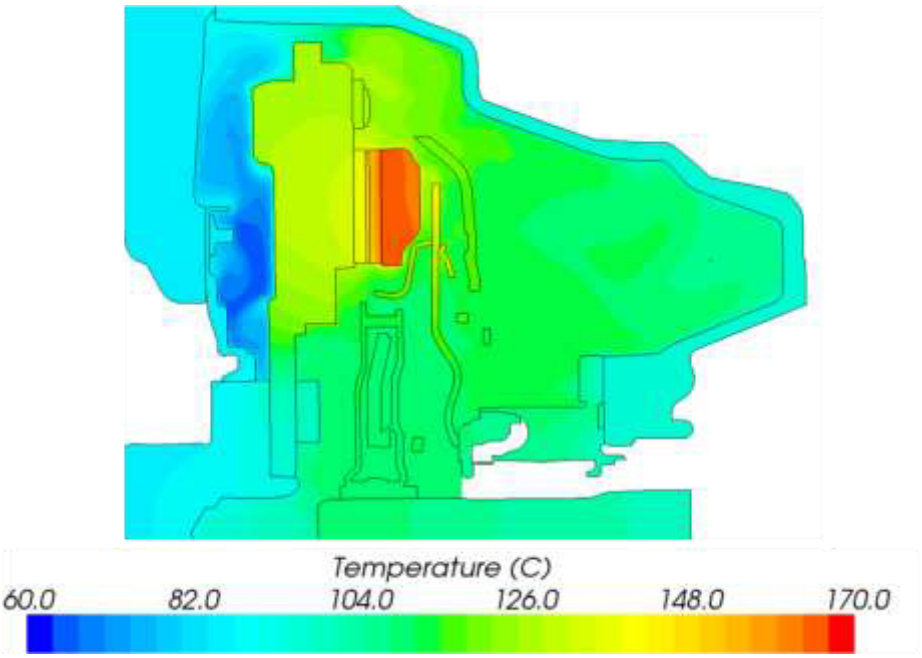

Figure 73: Temperature Field Inside the Bell Housing at 1500 rpm

Figure 73 shows the temperature field at 1500 rpm. It can be seen that there is an obvious temperature difference between the left and the right side of the flywheel. The temperature difference results from the hotter pressure plate, the engine sided openings to the ambient causing cool air being transferred into the bell housing and the low mixing of the air inside the bell housing on the left and right side of the flywheel.

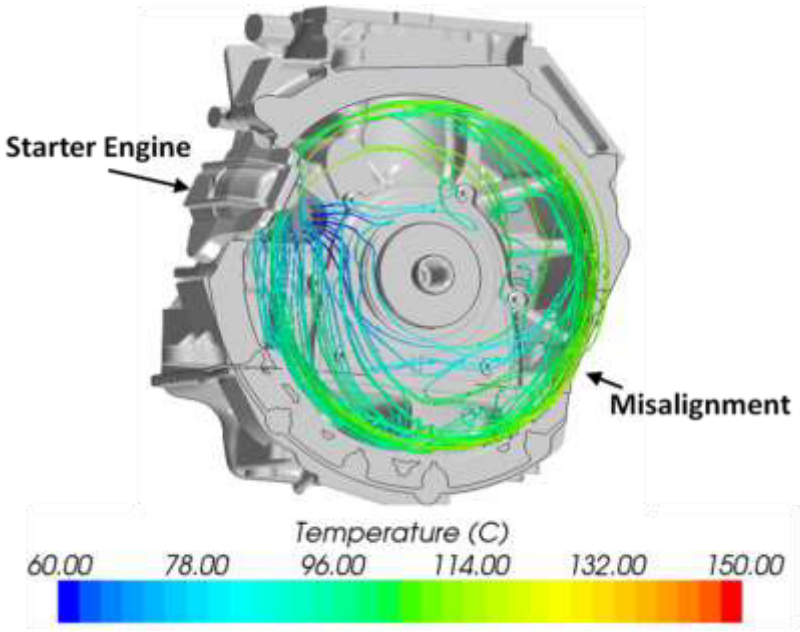

Figure 74: Streamline Plot with Origin at the Starter Engine Opening

To see how the colder air from the outside of the bell housing is distributed inside the bell housing a closer look at the streamlines from the opening of the starter engine was taken.

Figure 74 shows the streamlines with an origin at the starter engine opening. The streamline color represents the temperature of the air flow. It can be seen, that air entering the bell housing domain follows the rotation direction and mixes with the air inside the bell housing. To maintain the mass balance, the same amount of air entering the bell housing leaves the bell housing at the misalignment between the engine and the bell housing located on the right side of Figure 74.

The mentioned flow field separation is also an area of optimization potentials. Looking at the heat transfer coefficient of the engine one discovers, that due to the relatively small clearance between the flywheel and the engine side, the heat transfer to the engine is at a comparable level to the bell housing.

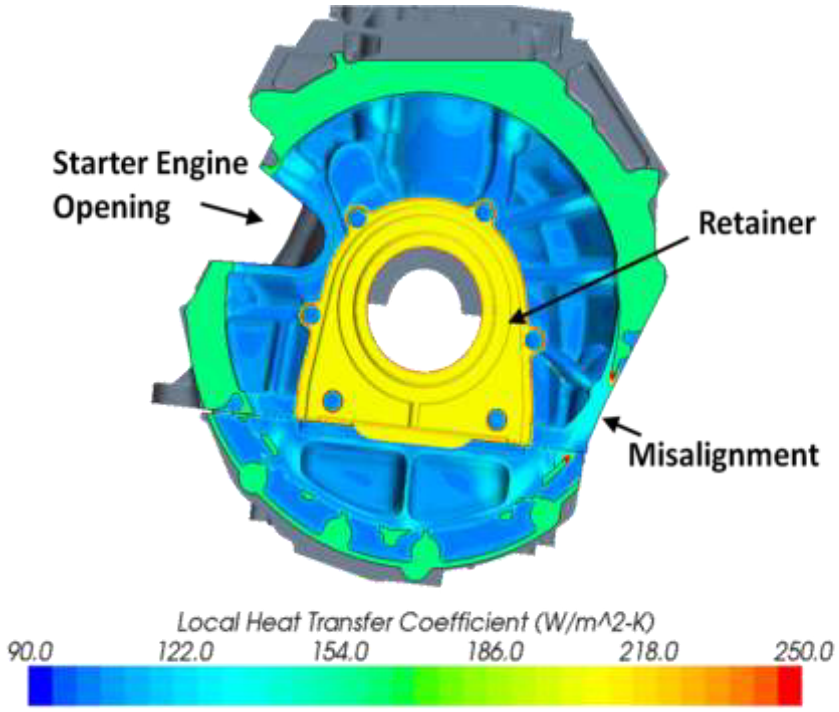

Figure 75: Local Heat Transfer Coefficient at 750 rpm at the Engine Side

In Figure 75 the distribution of the local heat transfer coefficient at the engine side is shown. The higher and approximately constant heat transfer coefficient of the retainer is accounted to the small clearance to the flywheel and the low distance to the rotation axis of this part. If a high energy event occurs, e.g. multiple launches in short period of time, the air inside the bell housing will be hotter than on the engine side. It would therefore be an additional benefit, if the mixing between the left and right sided air of the flywheel would be high. The thermal mass of the engine together with the engine cooling circuit could then be used more efficiently to reduce the bell housing air temperature.

The bell housings of modern vehicles are usually closed (only a drainage hole at the bottom of the bell housing is left open) to reduce water ingress and corrosion. The

displayed flow exchange to the ambient therefore does not exist in most vehicle powertrains. Still, as will be shown in chapter 7, the ambient air exchange is an interesting and efficient way to reduce the air temperature inside the bell housing.

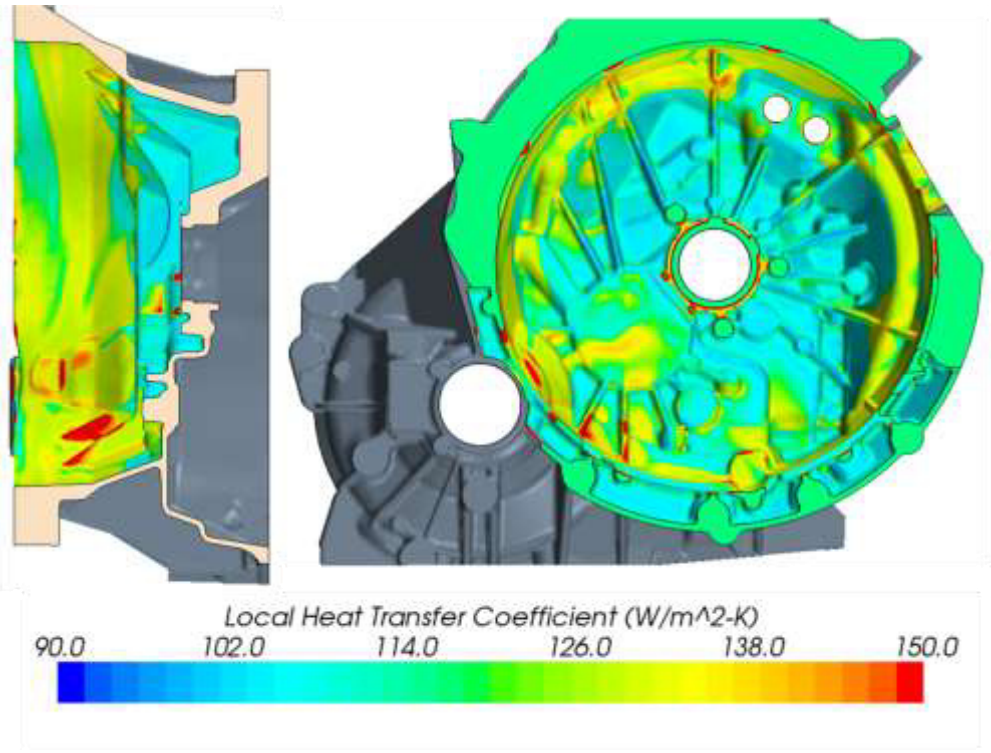

Figure 76: Local Heat Transfer Coefficient at the inside of the Bell Housing at 750 rpm

Figure 76 shows the distribution of the local heat transfer coefficient on the inside surface of the bell housing at 750 rpm. It can be seen, that areas close to the clutch systems outer diameter have a high local heat transfer coefficient. Compared to this, the surface towards the transmission has a lower local heat transfer coefficient. The local heat transfer coefficient is directly related to the wall friction and therefore to the flow field. As shown earlier in Figure 71, the flow velocity at the transmission side of the bell housing is low due to numerous ribs acting as flow resistance. The resulting wall shear stress profile of the inside of the bell housing indicates, that most of the heat generated inside the clutch system is transported directly into the lateral surface of the bell housing, making the assumption of neglecting the rest of the transmission a reasonable choice.

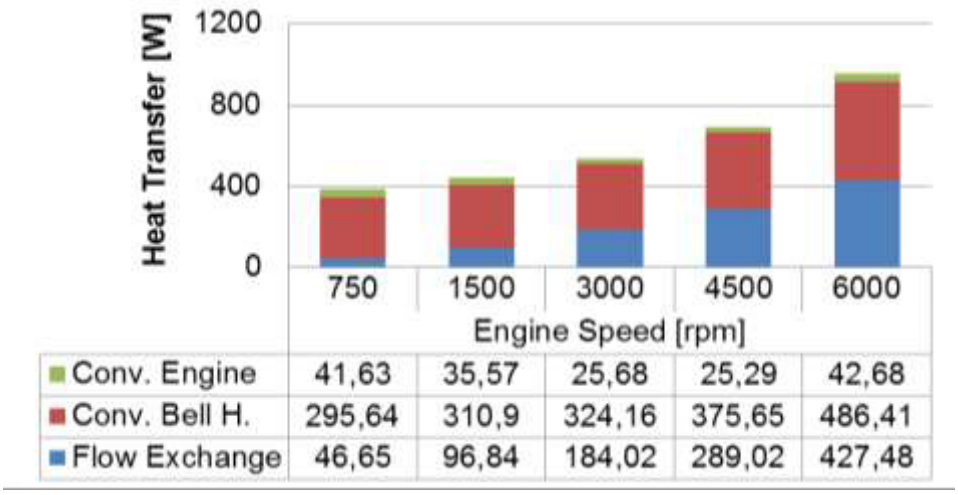

	750	1500	3000	4500	6000
Conv. Engine	41,63	35,57	25,68	25,29	42,68
Conv. Bell H.	295,64	310,9	324,16	375,65	486,41
Flow Exchange	46,65	96,84	184,02	289,02	427,48

Figure 77: Division of Heat Transfer to Ambient

Figure 77 shows the division of the overall heat transfer to ambient. It can be seen, that the convection heat transfer towards the engine can be neglected compared to the amount of heat transferred out of the system by flow exchange and convection towards the bell housing.

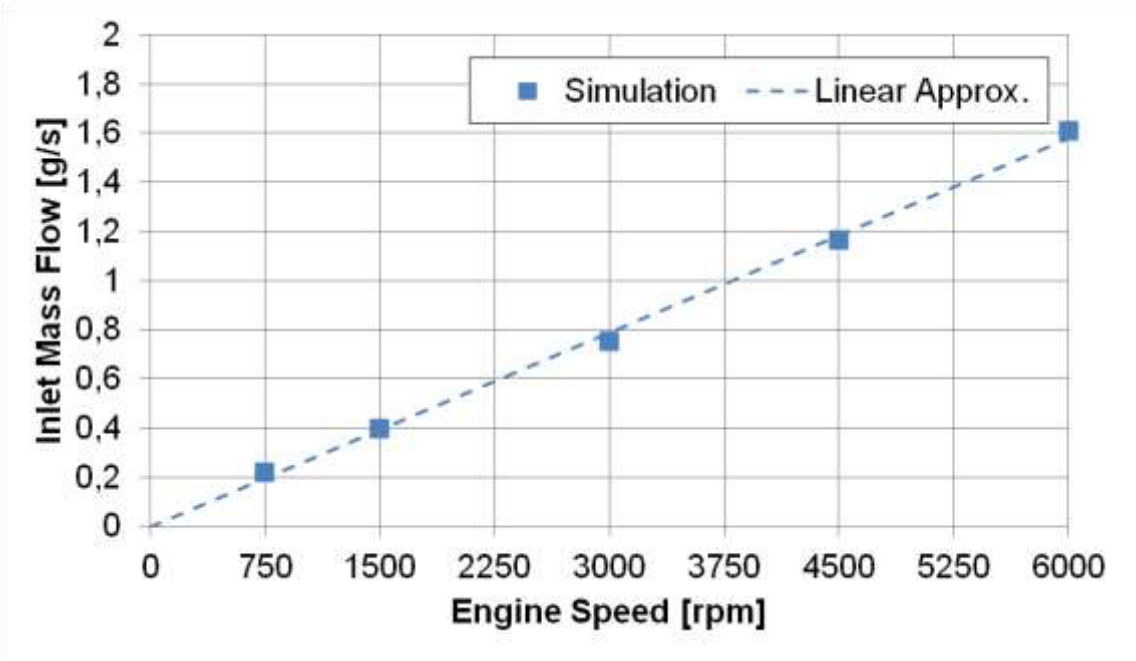

Figure 78: Mass Flow into the Bell Housing

Figure 78 shows the mass flow engine speed dependency. With an increase in engine speed, the air flow into the bell housing is increased. In Figure 79 the overall integrated surface friction of the clutch system is shown in dependency of the engine speed. The diagram shows the same behavior as the last diagram – with increasing engine speed the frictional torque rises. It is also obvious, that the mass flow into the bell housing and the frictional torque on the surface of the clutch system are directly connected.

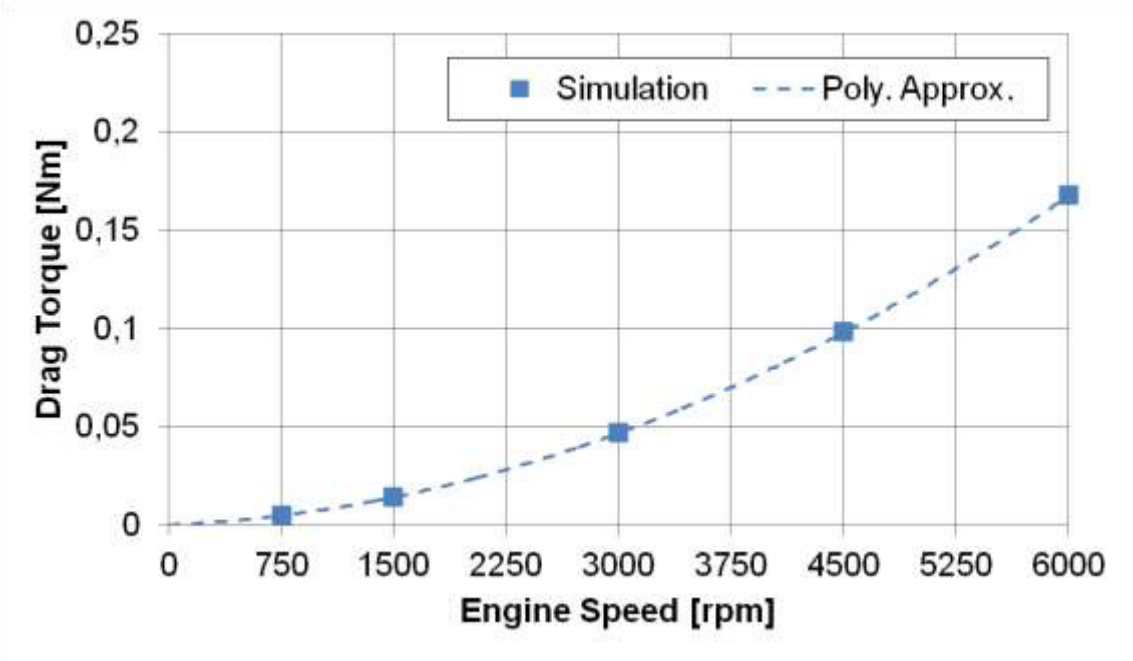

Figure 79: Overall Drag Torque of the Clutch System

In Figure 80 the wall shear stress profile for the flywheel is shown. The grey surfaces in the diagram are interfaces to other parts and have therefore no wall shear stress values. The Backside of the flywheel shows a distribution close to a rotating disk in free air. The wall shear stress values increase from the inner radius to the outer radius.

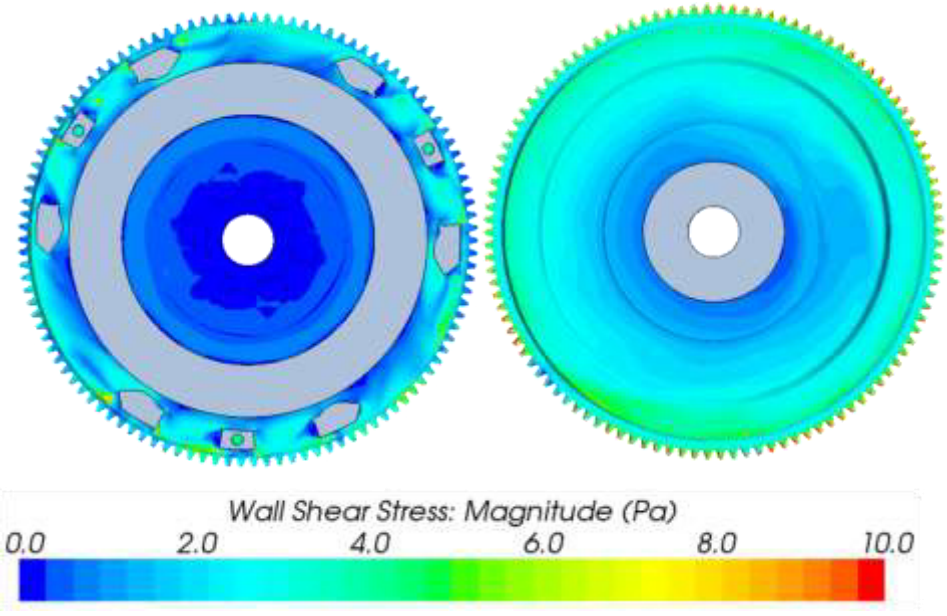

Figure 80: Wall Shear Stress Distribution on Flywheel at 3000 rpm: Frontside (left), Backside (right)

On the front side of the flywheel wall shear stress profile is more disturbed than on the backside, due to flow obstacles. Still, some flow structures, like the slightly outward and tangential dark blue areas, can be identified. These areas are due to the geometry of the clutch system and the radial and tangential outflow of the clutch system

“protected from the wind” and there exists no or very few relative movement between the clutch system and the air.

For the clutch cover similar flow structures as for the flywheel can be identified, as shown in Figure 81. Inside the clutch cover, the dark blue areas again indicate no relative movement between the cover and the air inside the clutch system. On the outside of the clutch cover an increase of the wall shear stress values with the radius can be observed. The most significant difference between the inner and outer surface of the clutch cover can be obtained when comparing the magnitudes of the wall shear stress values.

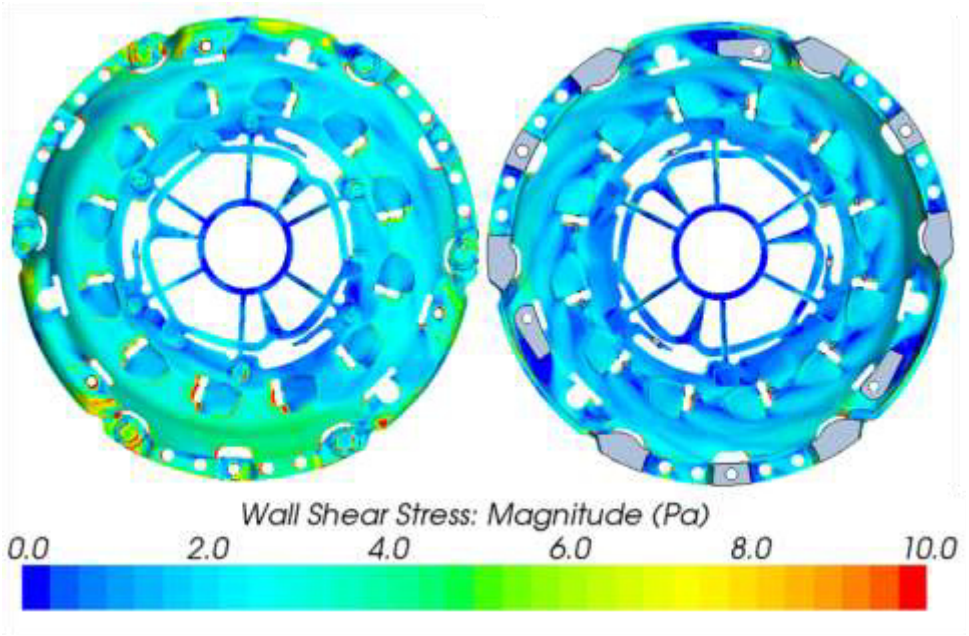

Figure 81: Wall Shear Stress Distribution on Clutch Cover at 3000 rpm: Outside (left), Inside (right)

The values on the outside of the clutch system are approximately two to four times higher than at the inside of the cover. This phenomenon can be explained if the flow field structure inside and outside of the clutch system is taken into consideration. At the inside of the clutch system the air is accelerated in angular direction, causing the air to move towards the outer diameter of the clutch system due to centrifugal forces. This means, that the relative velocity inside the clutch system will be smaller compared to the relative velocity at the outside of the clutch system. The relative velocity at the outside is comparably larger due to the deceleration of air at flow obstacles like ribs or plain surface friction on the inner surface of the bell housing.

Similar structures can also be identified when looking at the wall shear stress profile of the diaphragm spring shown in Figure 82. At the surface towards the clutch disk the wall shear stress values are significantly smaller than on the outer surface. Again this is due to the fact, that the air region restricted by the clutch disk and the flywheel is nearly rotating like a solid body with relatively small velocity difference to the clutch

system itself. This can also be observed at a closer look at Figure 71. At the connection interfaces to the sense spring or the pressure plate areas with low wall shear stress magnitudes due wake effects are visible.

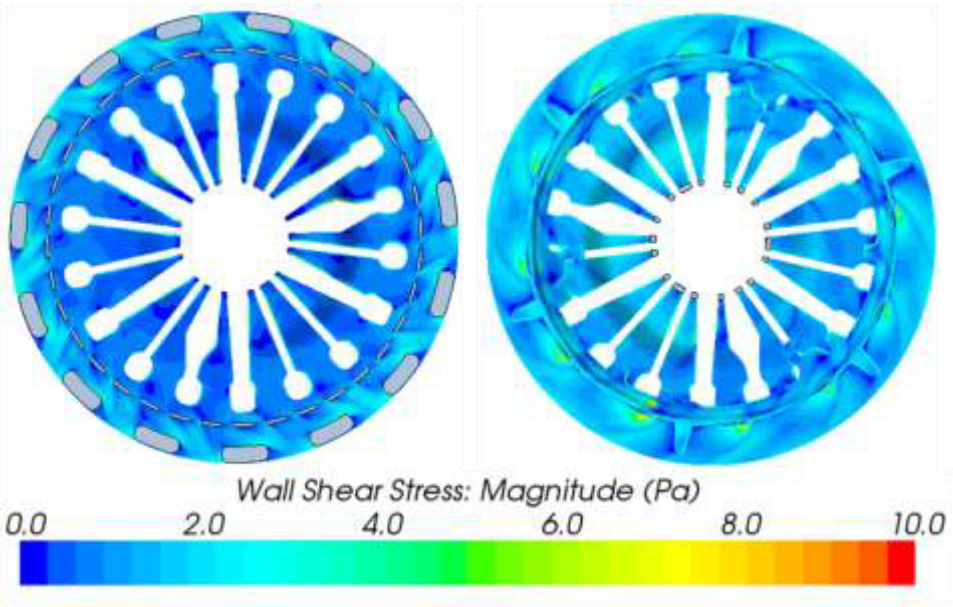

Figure 82: Wall Shear Stress Distribution on Diaphragm Spring at 3000 rpm: Frontside (left), Backside (right)

At the outer side of the diaphragm spring, the magnitude of wall shear stress values is a little more homogenous than on the inside. Compared to the flow structure on the clutch cover or on the backside of the flywheel, the wall shear stress values on the diaphragm spring seem to have no distribution dependent on the radial coordinate. This can be explained by the relative speed difference. The fingers of the diaphragm spring experience a higher relative speed, as they are directly in contact with the air outside of the diaphragm spring. The other surfaces of the diaphragm spring experience similar relative velocities due to the more advanced position towards the outer diameter of the clutch system.

The wall shear stress distribution for the pressure plate is shown in Figure 83. Here, as for the flywheel and the clutch cover, a radial distribution of the wall shear stress magnitudes can be observed. Towards the outer diameter the highest wall shear stress values are present. At the diaphragm spring supports wake effects, indicating low relative speed differences between the pressure plate and the air inside the clutch system, can be observed.

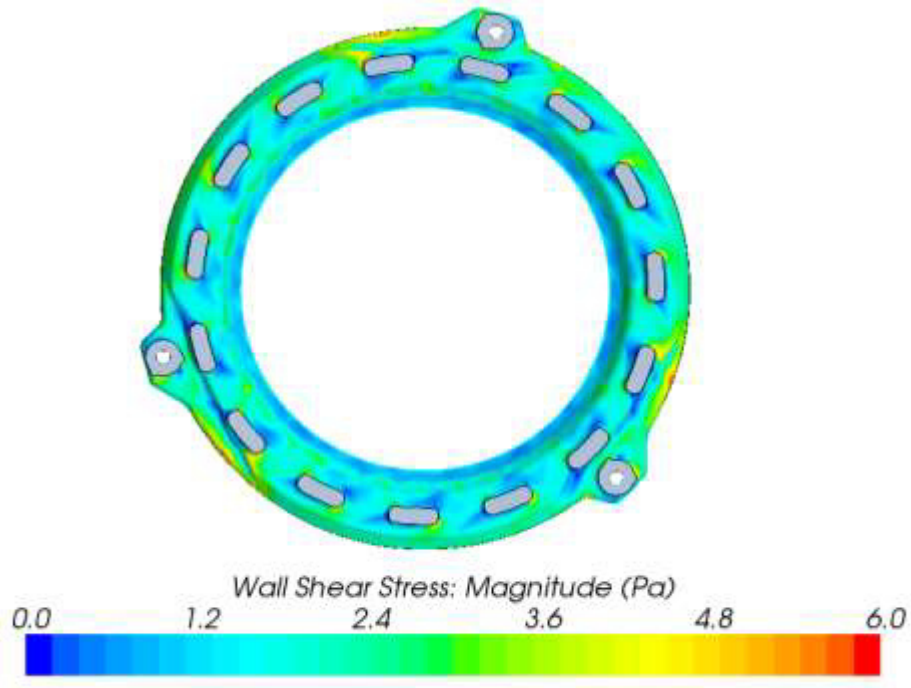

Figure 83: Wall Shear Stress Distribution on Pressure Plate at 3000 rpm

Figure 84 shows exemplarily the influence of how the air inside the bell housing is modeled in the heat transfer coefficient of the pressure plate. It can be seen, that the highest influence is at lower engine speeds.

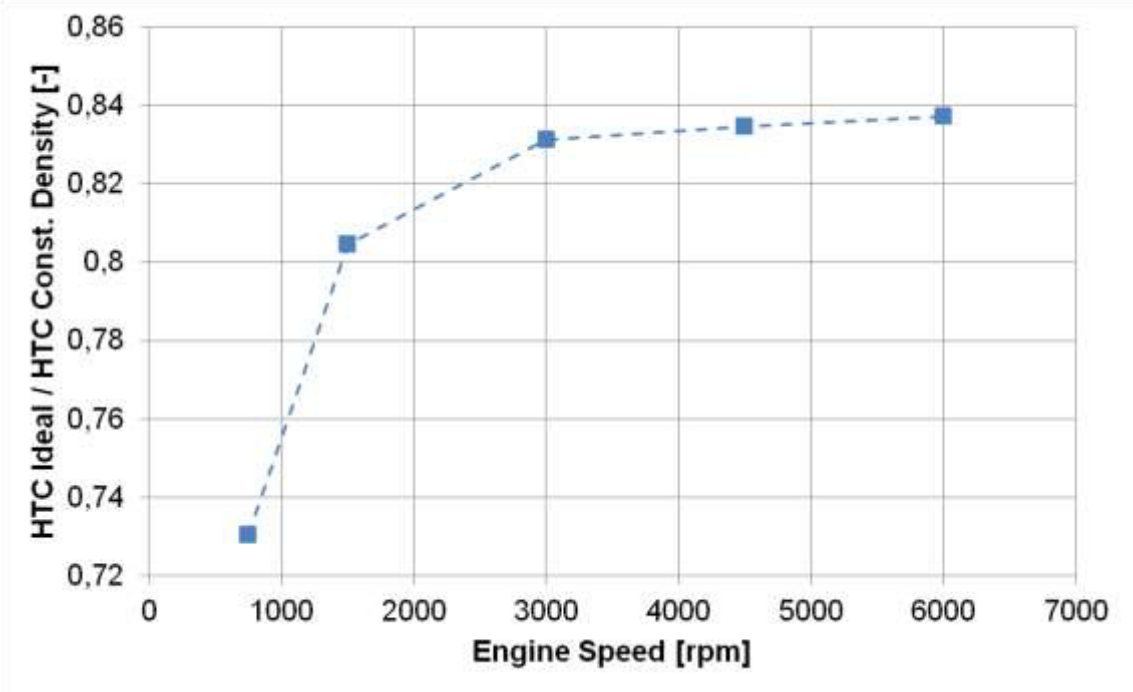

Figure 84: Influence of Modeling Treatment of Air

This is due to the higher temperatures of the air inside the bell housing, which can result from the lower volume flow rates in and out of the simulation domain and the lower heat transfer towards the bellhousing.

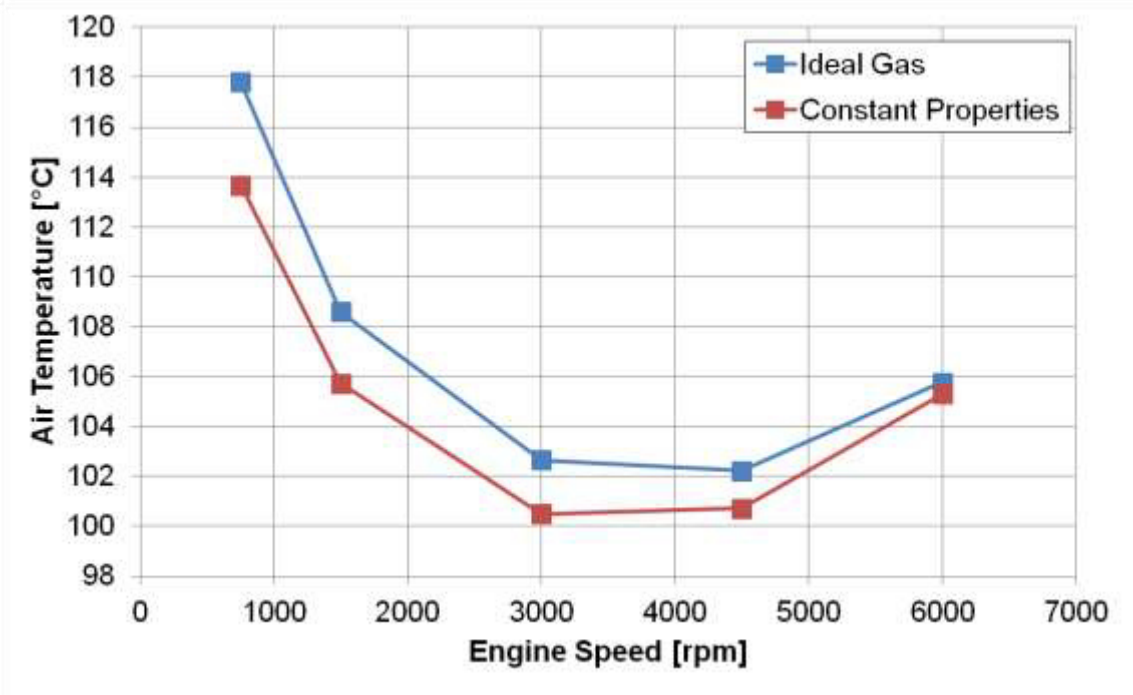

Figure 85: Engine Speed Influence on Air Temperature

The air temperature dependency on the engine speed is shown in Figure 85. As can be seen the air temperature drops for both modeling approaches until an engine speed of about 4500 rpm is reached. The following increase in temperature is suspected to be coupled to the earlier mentioned flow field separation. The highest temperature difference between the two models is approximately 4 °C.

The overall heat transfer coefficients calculated with the simplification procedure for the ideal gas case for the pressure plate, diaphragm spring, clutch cover and flywheel (see chapter 4.4) are shown in Figure 86. While the heat transfer coefficient increases for the pressure plate, flywheel and bell housing, the clutch cover and diaphragm spring heat transfer coefficient also decreases after a certain engine speed.

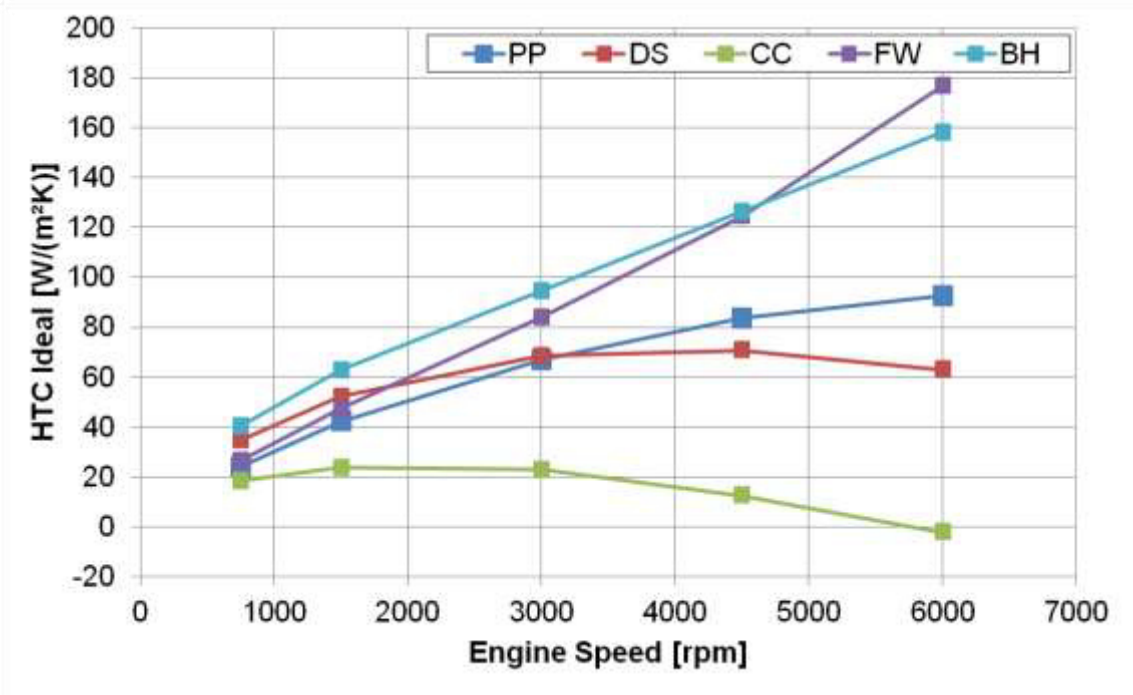

Figure 86: Simplified Overall Heat Transfer Coefficients

This phenomena observed for the clutch cover can be related to almost equal heat transfer to and from the component resulting in an almost leveled heat balance making the heat transfer coefficient approach zero. Other possible reasons for this behavior are the good coupling to the flywheel and the calculation of a heat transfer coefficient based on a global air temperature as reference and the decreasing air temperature behavior with increasing engine speeds. A study of the overall heat balance for the clutch cover revealed, that at 6000 rpm the direction of the heat transfer of the clutch cover changed, resulting in a negative heat transfer coefficient.

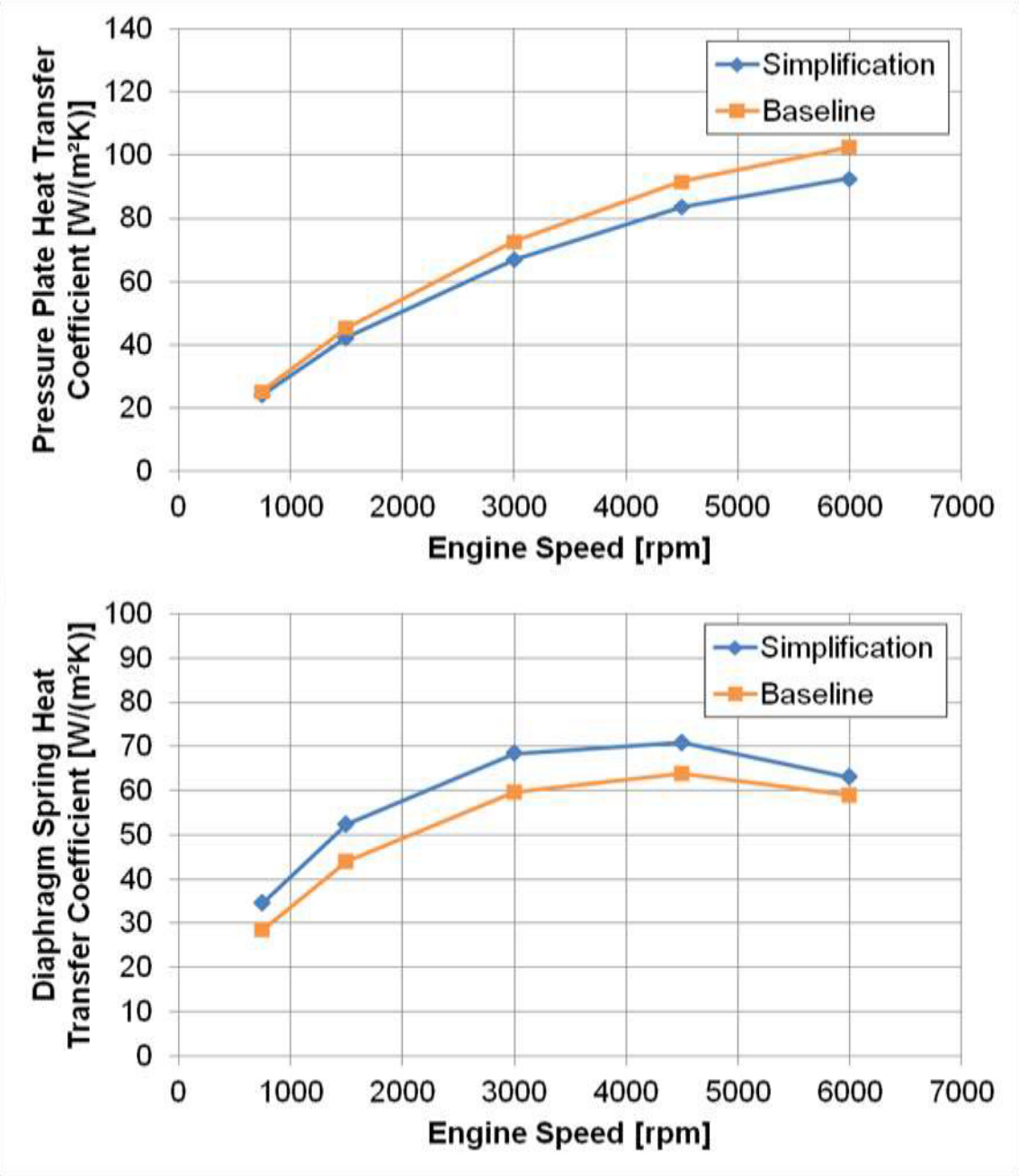

Figure 87: Influence of Simplification Process on HTC Values: Pressure Plate (Top); Diaphragm Spring (Bottom)

Figure 87 shows two examples of the influence of the simplification process on the heat transfer coefficients. The top shows, that for the pressure plate the heat transfer coefficient drops a small amount with rising engine speed. This is due to the increasing amount of heat being transferred over the backside of the pressure plate by convection, while the heat transferred by conduction is reduced and the overall thermal mass is increased. The same can be observed for the diaphragm spring as shown in the bottom part of Figure 87. Here, the distance between the two curves decreased from the starting engine speed to the maximum speed. This is due to an increase in convectional heat transfer of the summarized parts.

5.3 Transferability of Results

After the presentation of the results for one clutch system, the question of transferability of the generated results to other clutch or vehicle system remains. A general problem regarding this topic is that due to increasing restrictions in packaging, resources or functionality the components used for one vehicle application may not be sufficient for another application.

Figure 88: Packaging Conditions in Different Vehicle Applications

Figure 88 shows an example of the variety of packaging conditions of a dry clutch system in different vehicle applications. It can be derived from these conditions that the recirculation flow structure will definitely vary and therefore the heat transfer conditions will too.

To judge and display the influence of different clutch designs on the heat transfer a short study in free air was performed. Target is the analysis of geometrical variations and the impact on the heat transfer. Main focus was on the heat transfer from the pressure plate.

The boundary conditions for the simulations are:

- Steady state simulation in free air
- Closed condition
- Three clutch systems with equivalent outer diameter
- Constant heat input rate at frictional interfaces (15 kW/m²)
- Engine speed range: 750 / 1500 / 3000 / 4500 / 6000 rpm

The free air simulation domain condition was chosen to meet the requirement of equal conditions for all systems. Figure 89 shows the calculation domain. The air space was divided in a rotating region containing the clutch system and a stationary region as ambient.

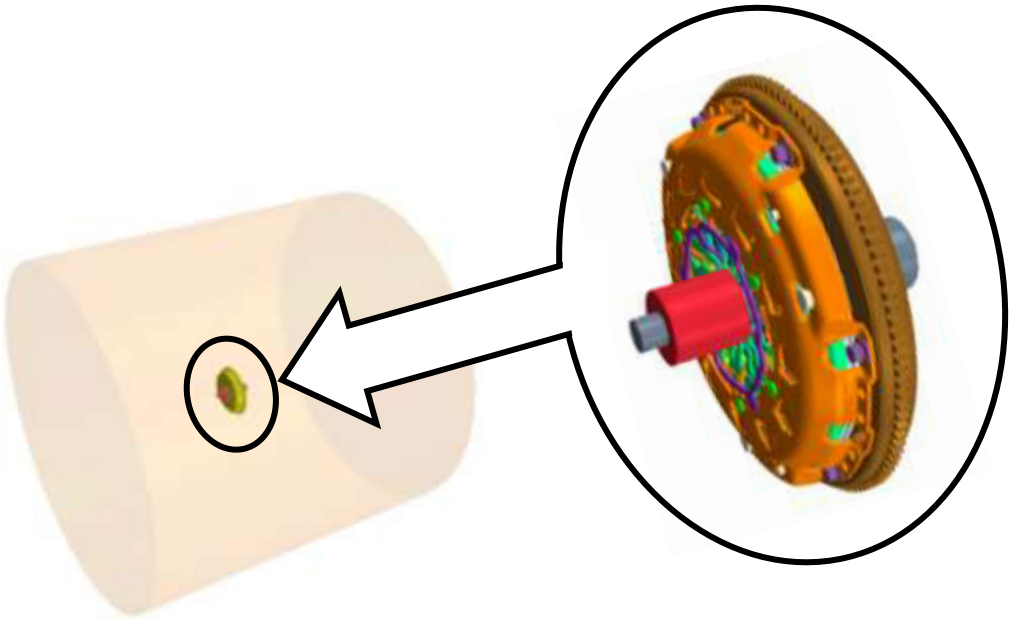

Figure 89: Calculation Domain and Clutch Geometry

Figure 90 shows the results for the pressure plate of the clutch systems. Usually the heat transfer coefficient in rotating systems can be expressed by an exponential function of the rotation rate. If the exponent if close to 0.5 heat transfer is dominated by laminar, if it is close to 0.8 it is dominated by turbulent effects. The exponents of the fitted trend lines show different behaviours.

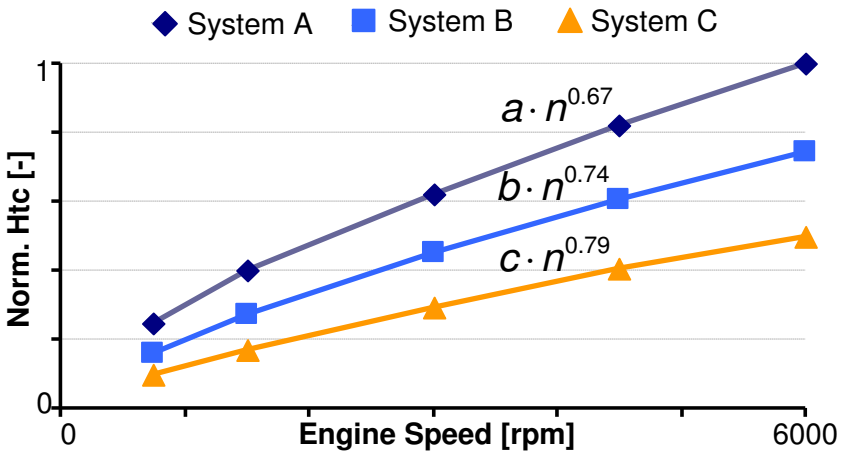

Figure 90: Normalized Heat Transfer Coefficients of Analysed Clutch Systems

Looking at the heat transfer coefficients in combination with the mass flow (Figure 91) through the clutch system, an indication on the origin of these differences can be derived. The mass flow shows linear behaviour with engine speed.

With rising volume flow through the system, the air has a lower residence time inside the clutch system. Figure 92 shows a vector plot of the flow inside two clutch systems.

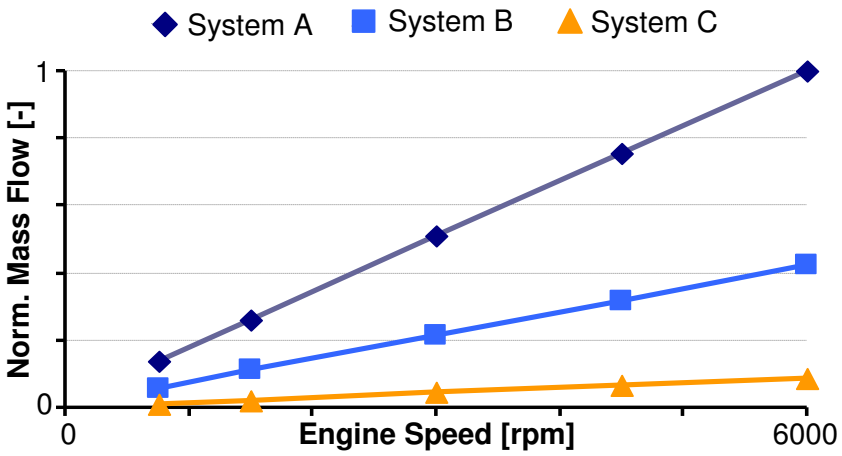

Figure 91: Normalized mass flow through clutch system

For the left system, it can be seen, that after the air passes through the gap between diaphragm spring and pressure plate (Inflow) and remains in the clutch system for a while (Delay Area) before leaving the domain between the cover and the pressure plate (Outflow).

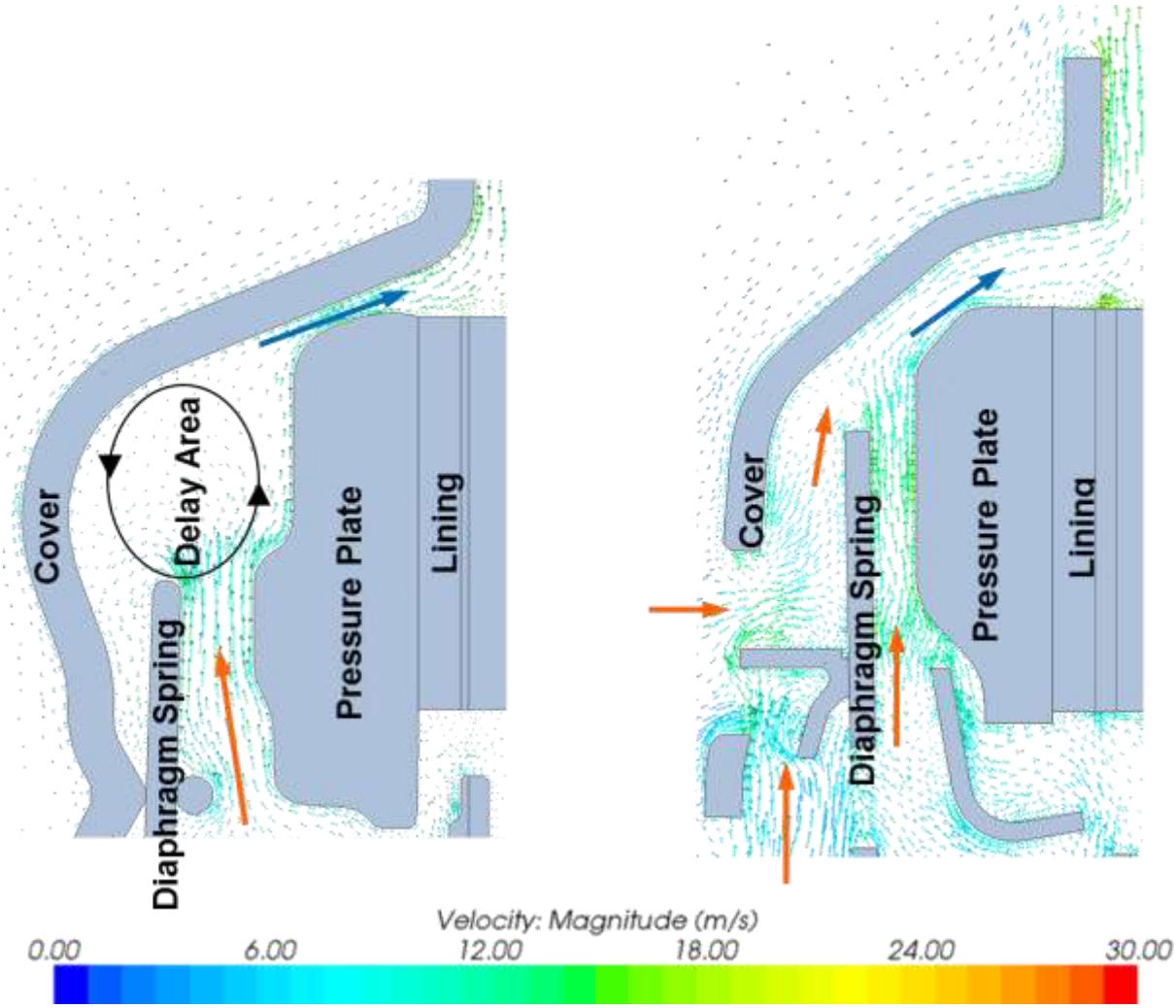

Figure 92: Tangential Projection of the Velocity Vector for two Systems at 1500 rpm

From the heat transfer coefficient and mass flow results, it could be assumed, that the overall performance of system C is reduced compared to system A and B. A judgement of overall system performance needs to consider the entire heat path. The heat division for system C is displayed in Figure 93.

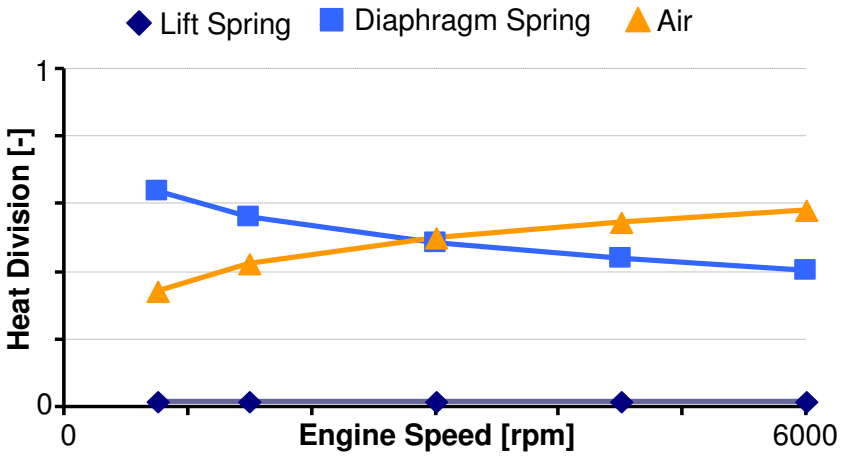

Figure 93: Heat Division in System C

It can be seen on Figure 93 that at lower engine speeds the heat transferred from the pressure plate is dominated by conduction to the diaphragm spring. As the engine speed increases, the amount of conduction decreases because of the rise in mass flow through the system. Due to the geometry of the lift springs (thin strips of sheet metal), the heat transferred from the pressure plate by conduction is very low. This phenomenon could be observed for all clutch systems.

As can be concluded from these results, the transferability of the results from one clutch system to another is very difficult because not only frictional surface effects are influencing the heat transfer. Additionally another variable is the clutch size itself. With larger outer diameter, the flow rates inside the clutch system will definitely rise and therefore the heat transfer coefficients will as well. Under these circumstances and with the overall variability in mind it is seen as most practical to simulate individual clutch and vehicle applications by CFD to obtain the heat transfer related data.

6 Model Verification

The verification of the simulation results of chapter 5 is treated in this chapter. Main focus is on how well the CFD simulation model reproduces the flow and heat transfer conditions. Also important is the validity of the simplified clutch life cycle simulation tool, which will be provided at the end of this chapter. Since the flow field is of high importance the chapter will start with a short review of different flow measurement principles displayed in chapter 2.3 and then detail the overall verification procedure.

6.1 Conclusions on Measurement Principles

In chapter 2.3 various measurement techniques for flow systems are displayed. Dependent on the measurement task, level of information needed on the flow system, packaging space and available resources, these techniques are more or less suitable compared to each other.

Flow field measurements (two and three dimensional) with optical access for example can be efficiently performed by visual / optical measurement techniques (e.g. particle image velocimetry). This technique offers the lowest influence on the flow system and maximizes the amount of information being captured. It can be used for stationary and transient cases. The direct need of a visual access to the area of interest and high resources needed for the equipment can be seen as the only disadvantages. The technique is therefore predestinated for accurate measurement of the flow outside of the clutch system.

All of the other measurement techniques can be seen as point wise techniques, because they only deliver data on a certain point in the flow field. If properly calibrated, the techniques of electro / mechanical and thermal techniques have no advantages or disadvantages compared to each other. As displayed the possible application of foil sensors inside the clutch system extends the field of application of thermal measurement techniques to the rotating system.

6.2 Verification Procedure

Main objective of the verification procedure is to demonstrate that the CFD modeling procedure displayed in chapter 5 and the simplified thermal model outlined in chapter 4 are capable of reproducing flow and heat transfer conditions for a manual dry clutch system under vehicle mounting conditions.

In chapter 5.2 it was demonstrated that heat transfer is tightly coupled to the flow conditions in and outside the clutch system. A split up of the CFD verification procedure into three main segments is therefore considered:

1. Validity of the recirculation flow outside of the clutch system
2. Validity of flow inside the clutch system
3. Validity of the heat transfer from and between the clutch components

The validity of the recirculation flow outside of the clutch system can be performed with various measurement devices. It was selected to measure the absolute velocity at arbitrary chosen points between the clutch system and the transmission bell housing with a thermal anemometer. In addition it was decided to measure the flow field around a clutch system rotating in free air with a particle image velocimetry system to circumvent packaging and application issues.

For the validity of the flow and heat transfer inside the clutch system the validity of the conditions around the pressure plate are of high importance. It was thus decided to validate the flow and heat transfer around this part.

As displayed in chapter 6.1 it is difficult to obtain information from inside the clutch system. The central problems that arise here are on one side due to the rotation of the clutch system and on the other due to minimization of the influence of the measurement device on the flow field (packaging). The only measurement techniques available for the selected measurement task are therefore the application of an optical / visual technique or the use of flush mounted thermal measurement sensors. The possibility of spanning thin wires between the support points of the diaphragm spring on the pressure plate to measure the average velocity was also considered but was neglected due to the lack of information on the flow angle, as well as handling and centrifugal influences on the wire.

To obtain visual access to the surface of the pressure plate severe modifications to the clutch system would be necessary (modification of cover, diaphragm spring, sense spring, sense ring). It was therefore decided to apply a thermal measurement technique to measure flow quantities inside the clutch system.

In order to optimize the measurement effort to validate the heat transfer and flow conditions, it was considered to validate conditions inside the clutch system using a quantity which both phenomena are highly dependent on. As outlined in chapter 2.2.3.3 heat transfer and flow conditions are mainly dependent on surface friction. The correctness of the local wall shear stress was therefore taken as verification measure for the flow and heat transfer inside the clutch system.

As the heat distribution inside the clutch system is dependent on conduction heat transfer between the individual parts, it was decided to take the conductional resistances between the main clutch parts as additional verification parameter on the thermal side.

Finally, temperature measurements from vehicle test track are used to verify the simple model and therefore prove the correctness of the simplification procedure.

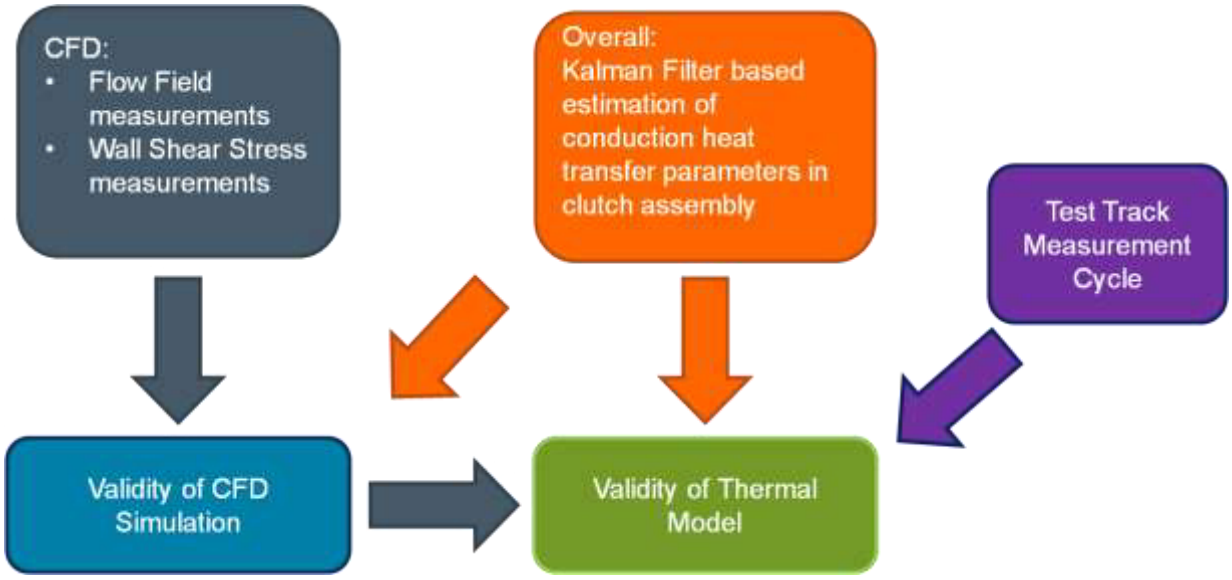

Figure 94: Verification Procedure

In Figure 94 the overall process of verification measurements and their interrelations are shown. It can be seen that all performed measurements have the crucial target of providing enough information to ensure the validity of the simplified thermal model.

6.3 Average Flow Velocity Measurements

For the average flow velocity measurements outside of the clutch system a test rig was prepared. The rig consisted of the clutch system, flywheel, bell housing of a 5-speed manual transmission, clutch actuation cylinder and a cover plate to close the bell housing. The individual components where mounted to a rig, which is normally used to test the burst speed capability of flywheels (Figure 95). The rotational speed could be adjusted manually by a potentiometer. A sensor mount was used to position the sensor manually at the desired points.

Since the complete reproduction of all geometrical features of a vehicle model on a test rig is not always possible and feasible, a simplified version of the overall vehicle model used in the last chapter, was also assembled in the CFD environment. The engine side was replaced by a simple cover plate and in addition the starter engine was neglected to reflect test rig conditions. Initial measurements with a different clutch actuation cylinder showed, that the correct geometry on the test rig and inside the CFD model is highly important and care should be taken at this point.

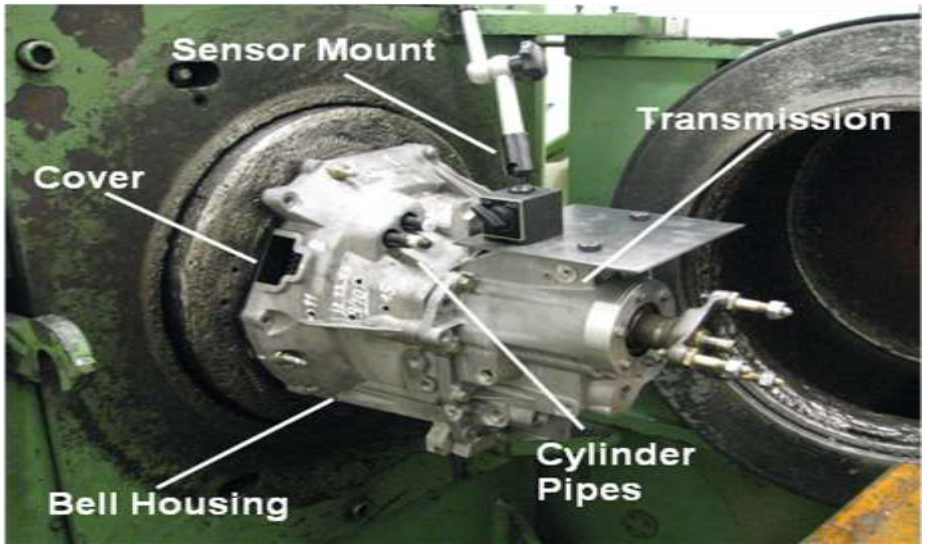

Figure 95: Test Rig Set-Up

A comparison between the CFD rig model and the vehicle model can be seen in Figure 96. It shows a comparison of the flow field in the individual models at 3000 rpm. The flow field on the pressure plate side in the two models has negligible difference compared to the flow field between the flywheel and engine / cover plate. The reduced clearance and missing ribs and crowning of the engine / oil pan surface make the flow in the test rig model more stable and organized compared to the vehicle model.

The flow field on the transmission side of the clutch system is very similar to the flow field in the vehicle environment. This in fact aids the thesis of no (or few) exchange or interference of air between the flywheel sided and transmission sided air.

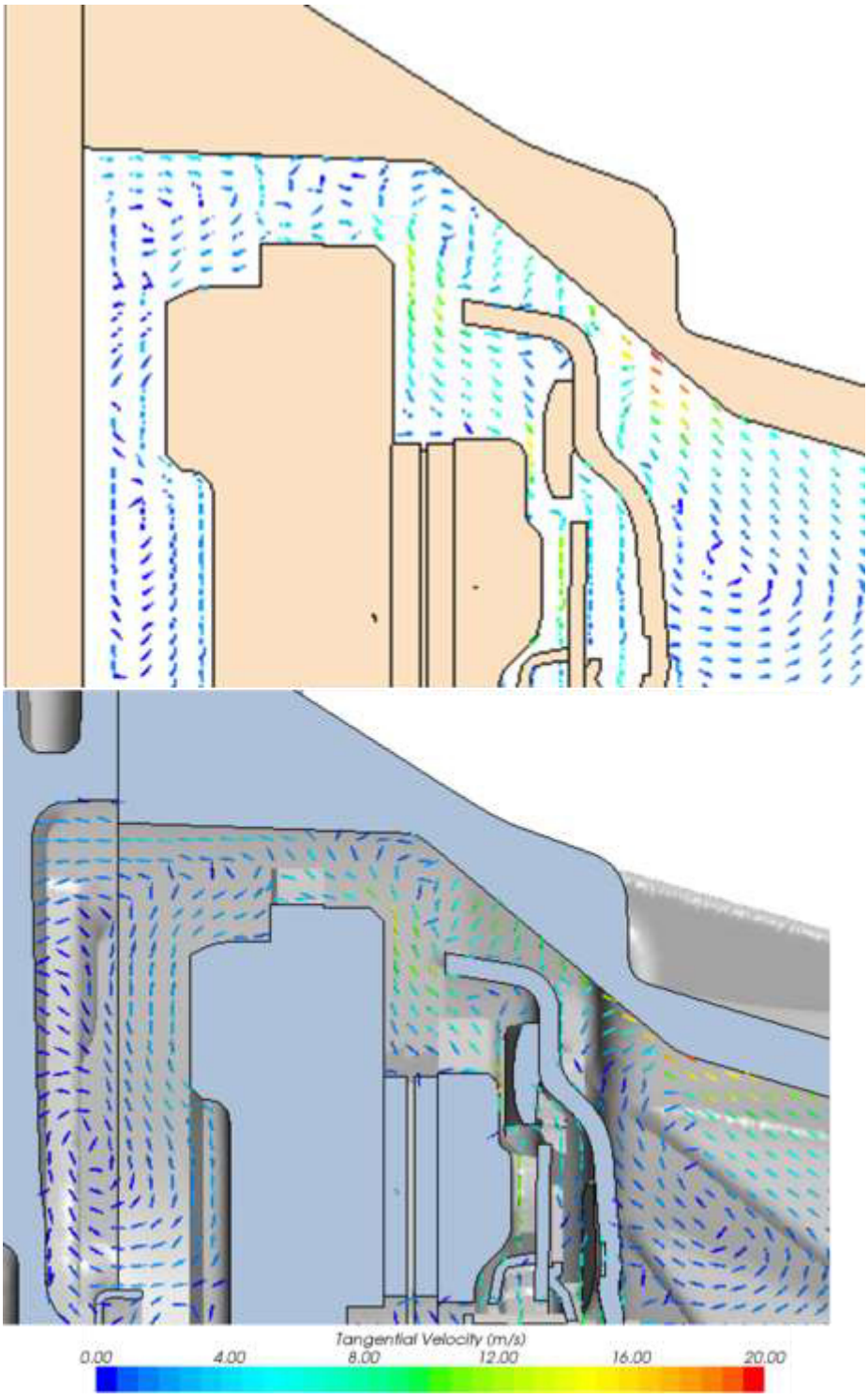

Figure 96: Flow Field Similarity (left: Test rig Configuration; right: Vehicle Configuration)

Figure 97 shows an example of measurement positions in the vertical measurement plane through the assembly.

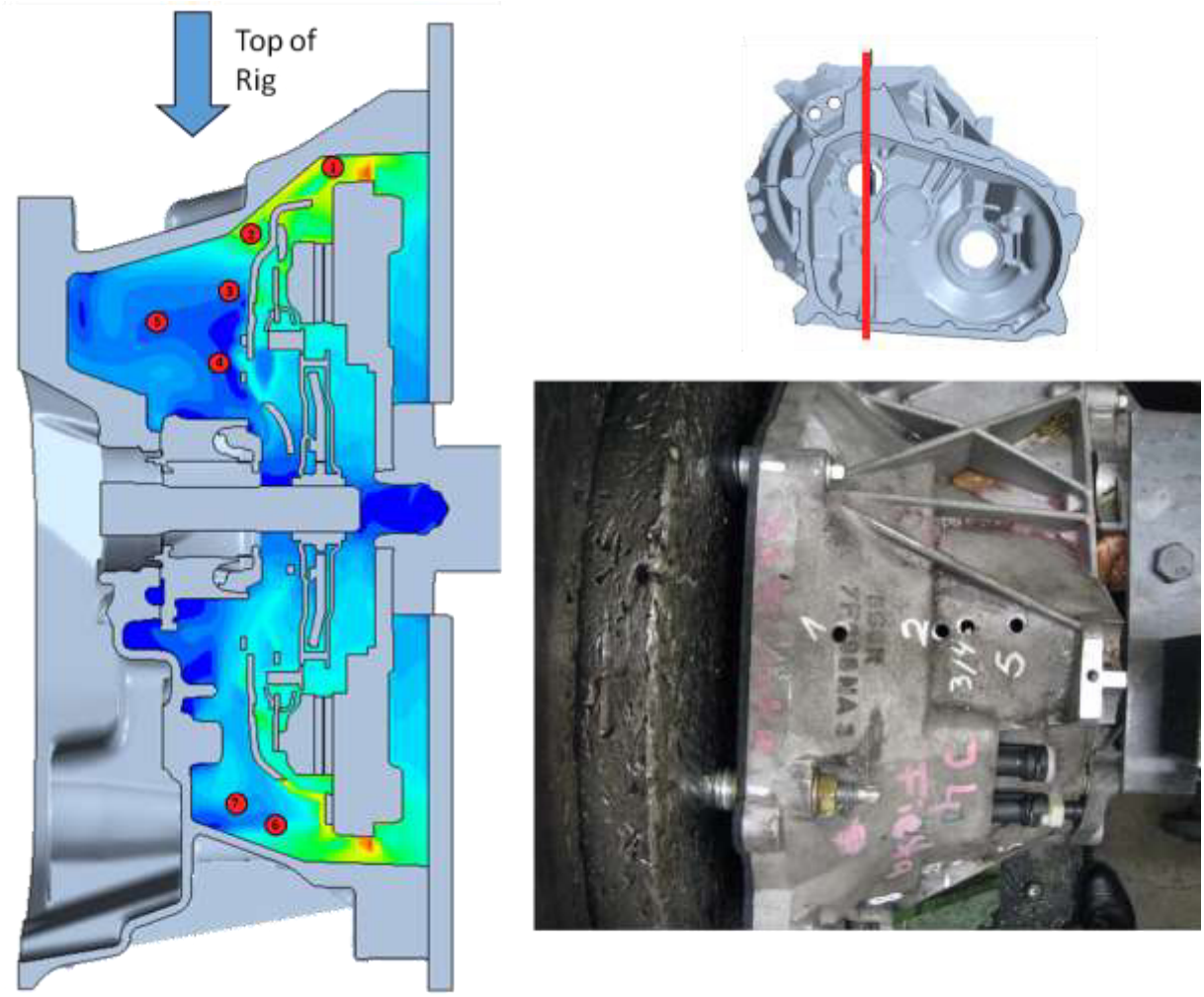

Figure 97: Measurement Positions Vertical Plane Section

For the measurements of the average flow velocities a 54T29 reference velocity probe of Dantec Dynamics was considered. The probe has the advantage of a built in temperature compensation and is known as being highly robust.

In the first tests performed prior to the measurements, the selected sensor head of the 54T29 CTA probe was damaged and could not be repaired. As a replacement for the sensor a locally available testo 425 CTA was taken. With a measurement range of 0-20 m/s, a resolution of 0.01 m/s with an accuracy of ±0.03m/s +5% of measurement value, the sensor was considered capable of performing the measurement task.

An advantage of this device compared to the original device can be seen in Figure 98. The tangential and axial direction of the flow can be measured independently due to the shielding of the sensor head. Disadvantage was, that the flow measurement signal could not be acquired digitally and that due to safety reasons the built in flow velocity averaging function could not be used.

Figure 98: testo 425 Velocity Probe[142]

To circumvent these challenges it was chosen to monitor the measurement device with a camera and to record 15 consecutive values displayed manually to capture some time dependent turbulent properties of the flow. After this, the 15 values were averaged and compared to the values obtained by the simulation.

The rotary speeds where chosen from the range of 1000 rpm to 3000 rpm with a step size of 500 rpm. Since the utilized test rig does not have high requirements on rotary balance and there was no option to adjust any imbalance of the clutch system, the engine speed was limited to 3000 rpm. The ambient temperature in the test rig room was kept constant at 20°C. In addition temperature compensation is implemented in the measurement device.

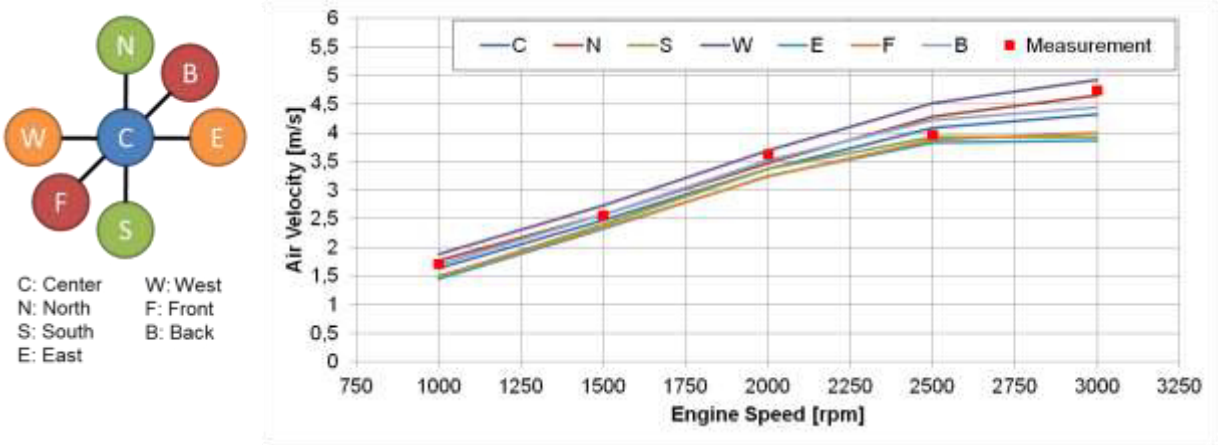

Figure 99: Evaluation Positions with a Measurement Example

Key point to the success of the measurements is to know the correct location of the measurement sensor. As can be observed from Figure 99, a small change in position in all directions in the measurement plane can cause a velocity change.

[142] Testo Homepage www.testo.de

To help overcome these obstacles, the simulated velocities were evaluated at one central position and additional 6 adjacent positions with an offset of 5 mm.

Figure 100 shows a selection of final measurement and simulation results. In the diagrams the line represents the simulation result in the position from the left side of Figure 99 with best fit to the obtained measurement data.

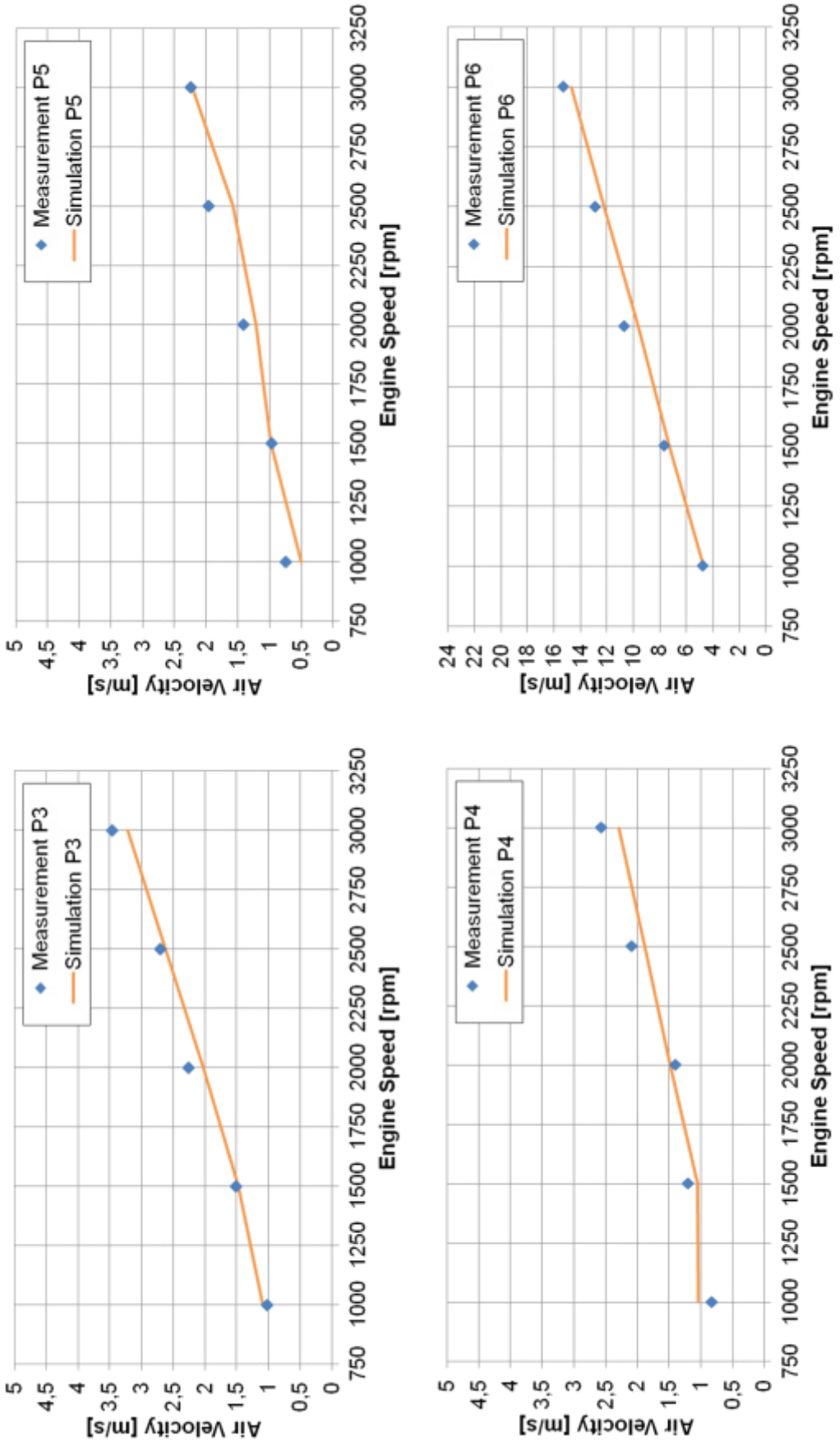

Figure 100: Measured and Simulated Velocity Distributions

6.4 Wall Shear Stress Measurements

For the wall shear stress measurements the overall measurement procedure is divided into four sections:

1. Setup of a test rig for sensor behavior and calibration purposes
2. Calibration of the foil sensors against a reference wall shear stress measurement principle
3. Determination of influencing factors and study of general sensor behavior
4. Application of sensors to the pressure plate of the clutch system and to measure wall shear stress levels under different rotary speeds

6.4.1 Rig Configuration for Reference and Sensor Behavior Testing

The first and most important decision in performing the reference measurements was the selection of a reference measurement technique. As shown in the earlier chapters, all measurement principles have some advantages and disadvantages. The application of a floating element sensor as reference technique was disregarded since the flexibility of its application is poor. If the sensor is applied to different parts of the clutch system, it would have to be mounted on similar positions, which is not always possible due to packaging and material thicknesses. Wall fence techniques were also neglected due to similar reasons.

The Ideal technique would have to be flexible in regards of measurement position on the clutch system, provide repeatable results and have the desired range of measurement value. Techniques like the near wall Pitot-tube measurements would be possible, but the unknown thickness of the momentum layer would also have to be tested to obtain the optimal sensor probe for this specific problem. Due to the local availability of a boundary layer probe, it was decided to use it to measure the velocity distributions in surface normal direction and evaluate the wall shear stress values by curve fitting.

The second assignment in planning the rig setup is selecting a thin foil sensor for the measurements on the surface of the pressure plate. Typically these sensors are custom made for a specific application. During general research the sensor displayed in Figure 32 from Dantec Dynamics was the only industrial available sensor found and therefore was selected for this application.

According to [143] this type of sensor has a high dependence on flow angle, temperature and the support material on which the sensor is mounted. To test and characterize these influences on the sensor, the dependencies were considered as boundary conditions for constructing the test rig. This step is of high importance, because it defines (or even limits) the accuracy of the desired measurements on the pressure plate component. It is therefore beneficial to choose simple flow and ambient conditions for calibration purposes or to study sensor behavior. In preliminary planning the desired ambient conditions for the flow measurements were chosen to be stationary in order to have one dimensional character in sensor area and to have a constant temperature (component and ambient air). The one dimensional character of the flow is important, because also the boundary layer probe does only allow pressure characterizations in one direction.

For the design of the test rig different considerations were taken into account. Primarily it is important to check if mounting conditions of the sensor have an impact on the sensor behavior. The application of the sensors on different materials is regarded as an efficient way to determine the influence caused by mounting conditions. The rig needs to offer the possibility to mount different sensor and material combinations. This can be provided by mounting the sensors on small inlays which can be individually applied to the rest of the rig.

As mentioned before, a highly influencing factor is the angle between the sensing element and the ambient flow. To measure the flow angle influence, the test rig has to contain a rotary functionality with the tough constraint to have the same flow conditions under all possible flow angles.

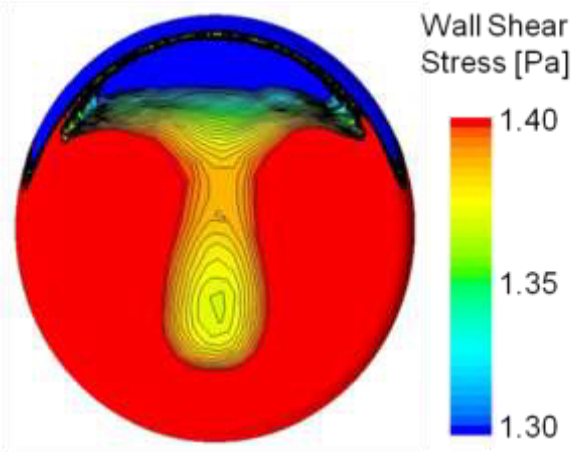

Figure 101: Wall Shear Stress Profile for a Round Disk

In a first attempt it was decided to construct the support plate in shape of a disk with a radius chamfer on the circumference and rotate the entire support plate to test angular

[143] Nitsche & Brunn 2006, P.87ff.

dependence. Simulation results for a wind tunnel outlet velocity of 20 m/s is displayed in Figure 101. For a round disk shape it is indicated that the flow direction and wall shear stress on the surface of the support plate are not one dimensional as required.

It was therefore necessary to redesign the support plate. The resulting rectangular support plate shape can be seen in Figure 102. The rotary functionality was maintained by splitting the support plate into a sensor mounting which can be rotated individually (as indicated in the left diagram of Figure 102) and a support plate.

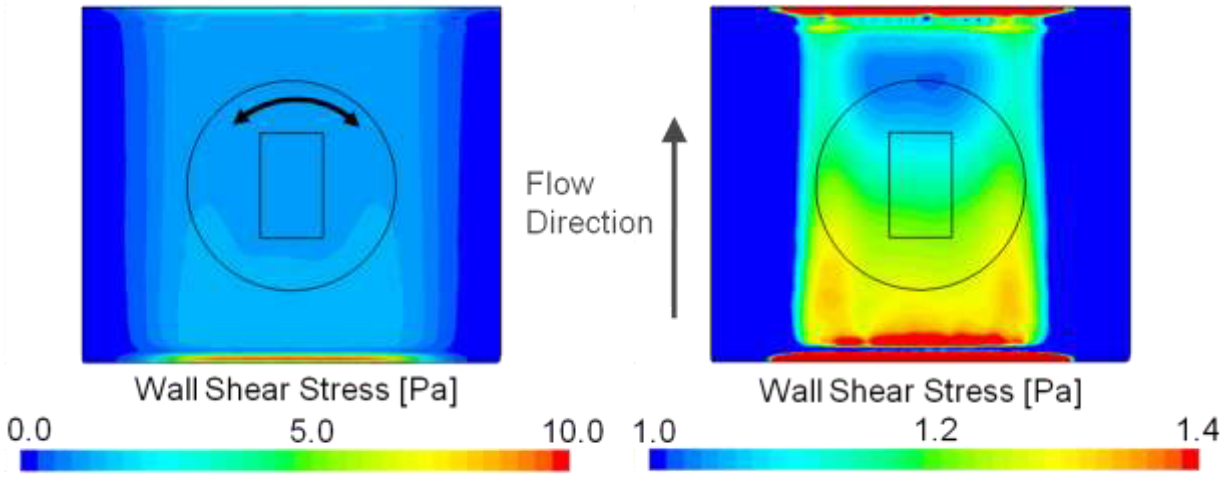

Figure 102: Wall Shear Stress Profile for the Second Plate Configuration

The simulation results in Figure 102 show that the flow and wall shear stress near and on the surface are suitable for the anticipated measurements. The leading edge of the plate was rounded with a radius of 5 mm. To allow the flow to stabilize itself, it was selected to have a length of 100 mm from the leading edge to the center of the sensor.

Compared to the angular dependencies and the mounting conditions of the sensor, the temperature sensitivity does not have a high constraint on the test rig. It can be treated as external boundary condition and varied individually. The study of the temperature sensitivity of the sensor does not have any constraints on test rig geometry.

The final rig configuration is displayed in Figure 103. It was designed based on local available expertise and CFD simulations to obtain ideal conditions for the wall shear stress measurements.

The main components of the rig are a wind tunnel and a support plate. At the end of the wind tunnel a flexible tube was used to connect the wind tunnel to a fan. The support tray can be divided into three main components: support plate, sensor mount and inlay. The sensor mount can hold different inlays to either study the sensor behavior or to measure the wall shear stress in the center of the plate.

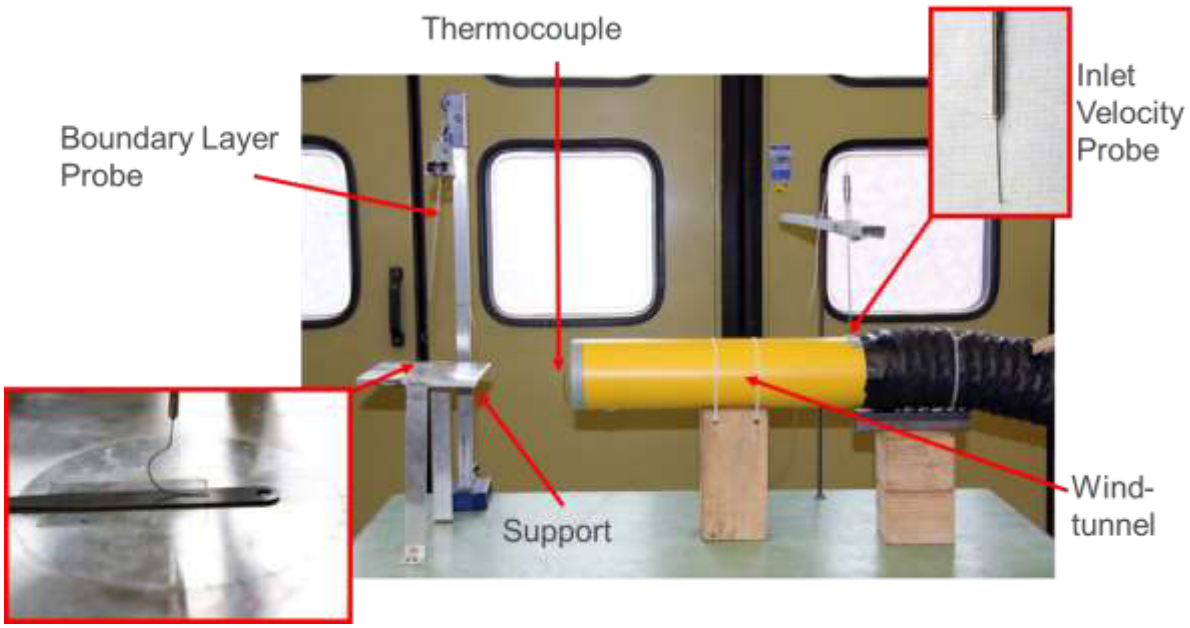

Figure 103: Test Rig Configuration for Reference Wall Shear Stress Measurements

To perform an angular dependency study, the sensor mount in the middle of the support plate can be rotated. Figure 104 displays the main components of the measurement equipment are displayed.

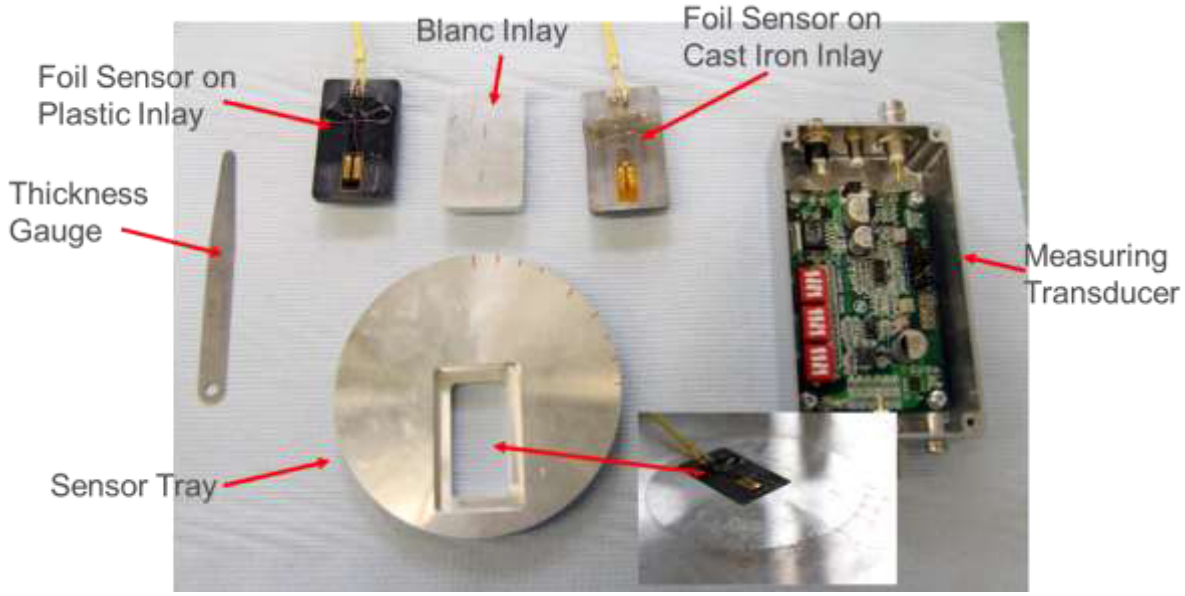

Figure 104: Measurement Equipment for Wall-Shear-Stress Test Rig

At the entrance of the wind tunnel a Pitot tube was put in place to measure the inlet velocity of the air. A temperature sensor (thermocouple type K-1) was placed at the end of the wind tunnel to obtain the air temperature exiting the wind tunnel.

The measurement transducer offers the operator to adjust the wall (or working) temperature of the sensor via a resistor decade. For the calibration and sensor

behavior measurements the resistor decade was set to represent a wall temperature of 120 °C since the temperature limit of the foil sensor is 150 °C. Besides this, it is also possible to adjust the voltage output of the sensor by using two potentiometers (gain and offset adjustment). The before mentioned temperature correction is then no longer applicable.

6.4.2 Reference Wall Shear Stress Measurements

Main objective of these measurements is to obtain the inlet velocity dependent function of the wall shear stress levels in the center of the support plate as enabler for calibration and sensor behavior testing.

As indicated in the general wall laws for turbulent flow, the boundary layer can be separated into a laminar sub layer (eq. 6.1) and a full turbulent layer (eq. 6.2). Between these layers there exists a transition zone (12 < y+ < 30) which connects the two regions. Equations 6.1 and 6.2 point out, that the wall shear stress level at the surface is dependent on the flow velocity profile in surface normal direction and temperature dependent quantities such as density and viscosity.

$$u^+ = y^+ \tag{6.1}$$

$$u^+ = \frac{1}{\kappa}\ln\left(y^+\right) + C \tag{6.2}$$

Assuming that the near-surface laminar sub layer is too small to be measured by the boundary layer probe, the focus has to be on the determination of the velocity profile of the turbulent boundary layer. Taking equation 6.2 and the simplifications in equations 6.3 for boundary layers (chapter 2.2.3.3) leads to equation 6.4.

$$u^+ = \frac{u(y)}{u_\tau} \;;\; y^+ = \frac{y \cdot u_\tau}{\upsilon} \;;\; u_\tau = \sqrt{\frac{\tau_w}{\rho}} \tag{6.3}$$

$$u(y) = \sqrt{\frac{\tau_w}{\rho}} \cdot \left(\frac{1}{\kappa} \cdot \ln\left(\frac{y}{\upsilon} \cdot \sqrt{\frac{\tau_w}{\rho}} \right) + C \right) \tag{6.4}$$

Using this equation together with the result of a curve fitting of the measured velocity profile, one can obtain the wall shear stress by comparing the coefficients. This operation can be done, because in equation 6.4 the unknown wall shear stress value can be treated as constant. The only variable in this equation is the surface normal distance. For the values of density, viscosity and kappa, standard values for air where used in the performed experiments. The constant C in the equations was chosen to match with a smooth surface.

Figure 105 shows a measured velocity profile determined with the boundary layer probe. The probe was connected to a Baratron-Manometer from MKS Instruments.

The manometer offers a pressure measurement accuracy of ±0.5 % of the measurement value. Additionally pressure manometers are usually calibrated at room temperature and therefore have a temperature dependent zero point offset coefficient which has a value of for example 0.02% of the measured value per degree Celsius. The temperature dependent measurement error can be neglected because all measurements will be performed at room temperature.

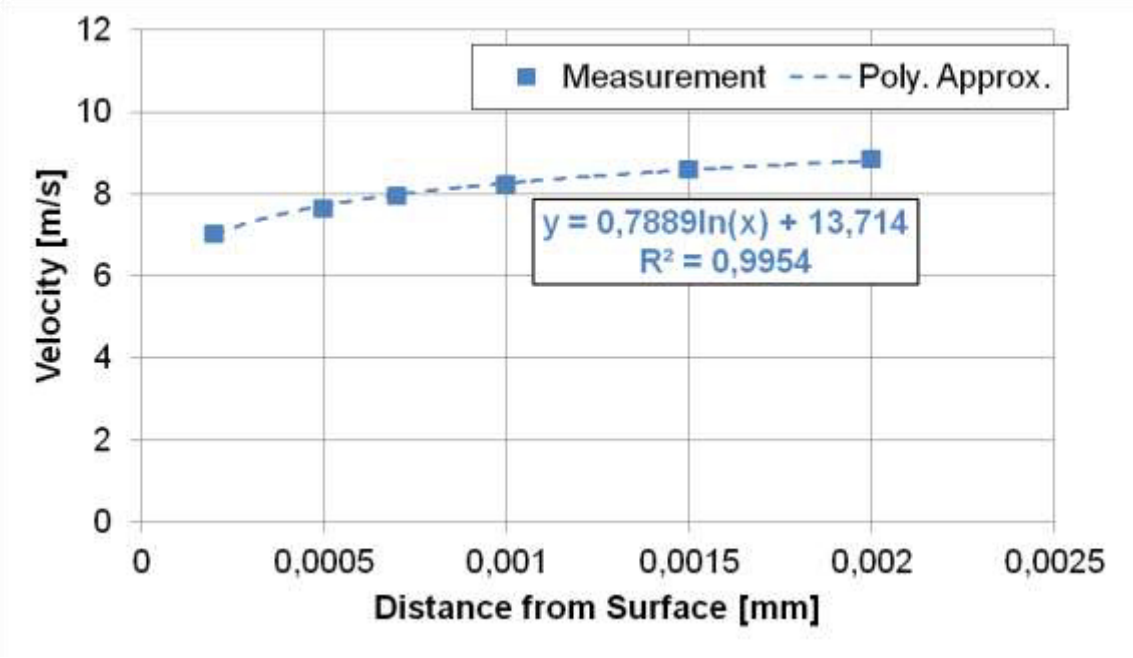

Figure 105: Measured Velocity Profile

The velocity profile in Figure 105 shows a good fit to a logarithmic function. The process of comparing coefficients to obtain the desired wall shear stress values was accompanied by some major challenges. The issue of the curve fitting is that it does not directly consider a measurement error caused by position inaccuracy. As can be derived from equation 6.4 the knowledge of the correct position of the boundary layer probe is of highest importance. The performed curve fitting procedure is not open to measurement errors.

For the solution to this complex of finding the correct wall shear stress values at the surface, the problem was reformulated to incorporate a position measurement error.

$$u(y) = \sqrt{\frac{\tau_w}{\rho}} \cdot \left(\frac{1}{\kappa} \cdot \ln\left(\frac{\bar{y} + \delta y}{\upsilon} \cdot \sqrt{\frac{\tau_w}{\rho}} \right) + C \right) \tag{6.5}$$

Taking equation 6.4 and substituting the position y with an average position, representing the known offset of the probe from the surface adjusted with thickness gauges and an offset error (eq. 6.5). Taking equation 6.5 as initial point for an optimization scheme with variables, one loosens the tight coupling of the position and velocity values and makes it thus more convenient for the proposed wall shear stress

measurements. Since the distance levels from the surface for the individual velocity measurement is known, the remaining unknowns in equation 6.5 are the offset and the wall shear stress level at the surface.

As optimization scheme a Kalman filter (see chapter 2.5) was selected. Main advantage of the Kalman filter algorithm is that it directly incorporates measurement and system noise resulting from inaccuracies from measurements and modeling.

6.4.3 Application of the Kalman Filter to the Measurement Task

The state space formulation needed to evaluate the problem can be obtained by taking the unknown wall shear stress and position offset as state variables, together forming the state vector displayed in eq. (6.6).

$$\vec{x} = \begin{pmatrix} \tau_w \\ \delta y \end{pmatrix} \tag{6.6}$$

The position offset error was assumed equal for all measurements at one wind tunnel velocity. This helps the convergence of the algorithm due to the reduction of variables. The measurement update equation is formed by augmenting all velocity measurements into a single vector (eq. 6.7).

$$\vec{u}_m = \left(u_{m,0} \quad . \quad . \quad . \quad u_{m,n}\right)^T \tag{6.7}$$

$$u_{u,i} = \sqrt{\frac{\tau_w}{\rho}} \cdot \left(\frac{1}{\kappa} \cdot \ln\left(\frac{\bar{y}_i + \delta y_i}{\upsilon} \cdot \sqrt{\frac{\tau_w}{\rho}} \right) + C \right) \tag{6.8}$$

Taking the measurement vector of eq. 6.7 the measurement update can be formulated by eq. 6.8. As can be seen by equation 6.8 the parameter identification task has a non-linear measurement update function. The stated problem can be characterized as stationary non-linear parameter identification task. A nonlinear filtering technique is therefore needed to overcome this hurdle. The Unscented Kalman Filter Algorithm (chapter 2.5.3) was chosen with a parameter definition according to equation 6.6.

To confirm the identified parameters of the calibration test rig an additional simulation model was set up. The model geometry is shown in Figure 106. By using a symmetry plane boundary condition the geometry modeled can be reduced to one half of the test rig.

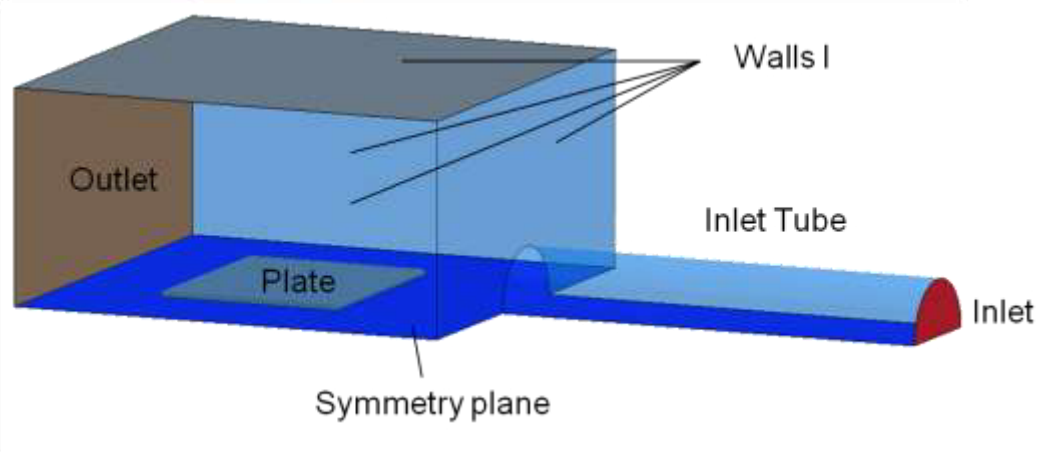

Figure 106: Test Rig Simulation Model

As boundary condition the inlet velocity was set to the desired value. The surface of the inlet tube and the plate were treated as no-slip condition. All other surfaces (except the symmetry plane) were set as pressure outlets.

The parameters were limited by a pre-factor ($p_{i,0}$) for the offset error of 0.5 mm and a shear velocity of 4 m/s. These values were chosen based on the possible air speed of the test rig (max. 24 m/s – 4 m/s ≈ 16%) and the assumed maximum displacement error (assuming that an error of 0.5 mm is obviously detectable by the operator). The scaling factor was chosen close to 1, to be able to use the entire range of positive parameter values. System and measurement noise were assumed constant, additive and of Gaussian type.

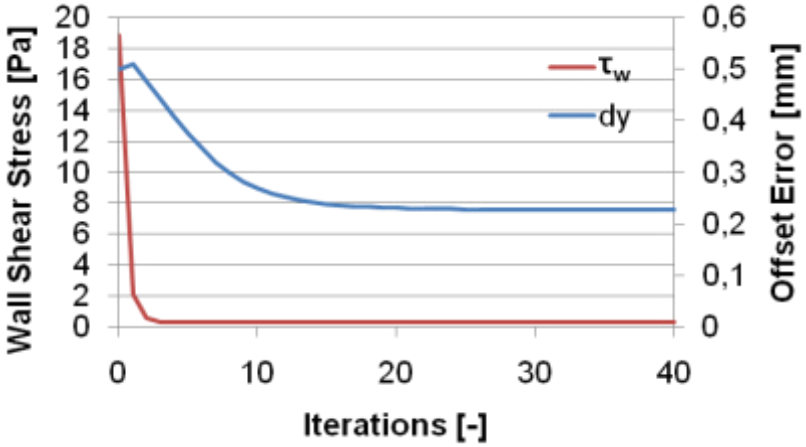

Figure 107: Convergence Behavior Example

The system covariance was set as 2x2 matrix with diagonal entries of 10^{-4} and the system noise covariance was set as 2x2 matrix with diagonal entries of 10^{-3}. The measurement noise matrix was chosen as diagonal 6x6 matrix with entries 10^{-2}. For a

parameter identification task, this matrix can in fact be chosen arbitrary, because it cancels according to [144] out of the algorithm.

In Figure 107 the convergence behavior is shown for one example. It can be observed, that the wall shear stress converges to its final value in the first 10 iterations while the offset error needs 30 iterations to converge. For this example the obtained final parameter x_i inside the hyperbolic function was estimated as $(-0.61, -1.29)^T$. The final system covariance matrix had corresponding diagonal entries of $(0.0032, 7.63*10^{-6})$. The limits, as displayed in Figure 38, were therefore not achieved and the result can be regarded as valid.

[144] Merwe 2004, P.89

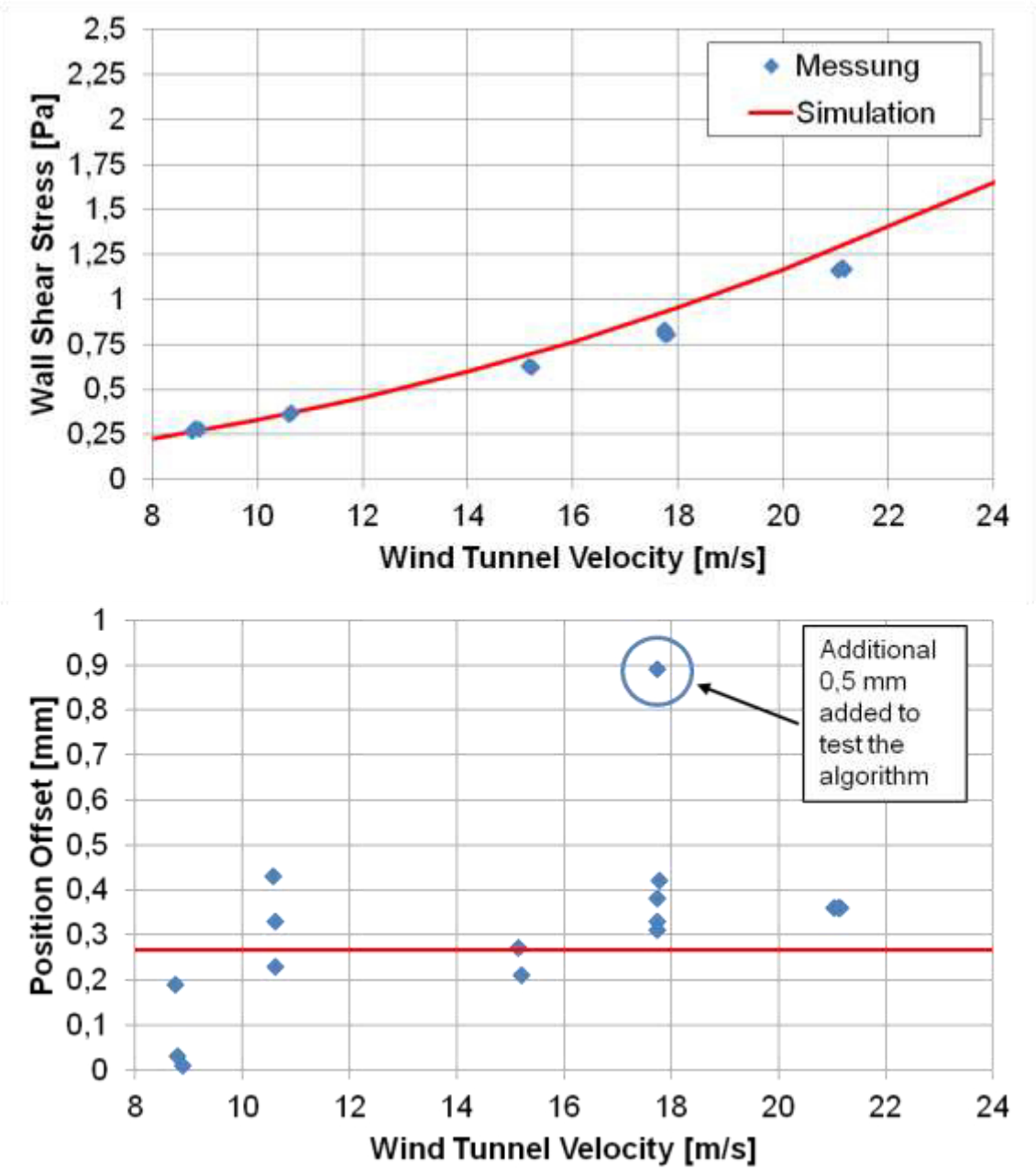

Figure 108: Wall Shear Stress (Top) and Position Offset (Bottom) Results

A comparison of simulated and measured parameters can be seen in Figure 108. The wall shear stress values have a good match to the simulated values (Figure 108 top). The bottom diagram in Figure 108 shows the identified position offset error, which has an average value of 0.27 mm. To test the algorithm additional 0.5 mm was added in one measurement run to the thickness gauges. The result shows that the algorithm works and correctly identifies this additional inaccuracy.

The dependency between the inlet velocity of the wind tunnel and the wall shear stress levels at the center of the plate has therefore been identified and is used as basis for the following tests of sensor behavior.

6.4.4 Influencing Factors and Sensor Behavior

For sensor calibration the coefficients A and B of equations 2.38 and 2.40 of chapter 2.3.3 have to be quantified for temperature, mounting conditions and angular changes between the air flow and the sensing element in order to be able to apply the sensor to the clutch system. To analyze the influencing factors on the sensors the following variation studies were performed:

- Temperature Dependency
- Flow Angle
- Mounting Conditions (Material)

6.4.4.1 Temperature Dependency

Formulas 2.21 to 2.23 show that the heat transfer from a surface is highly dependent on the ambient and wall temperature. The higher the temperature difference (assuming equivalent local heat transfer coefficients) between the wall and the ambient air, the higher the transferred heat will be. To test the temperature dependencies of the sensors, the rig was set up in a climate chamber which allowed setting the ambient temperature at a desired level.

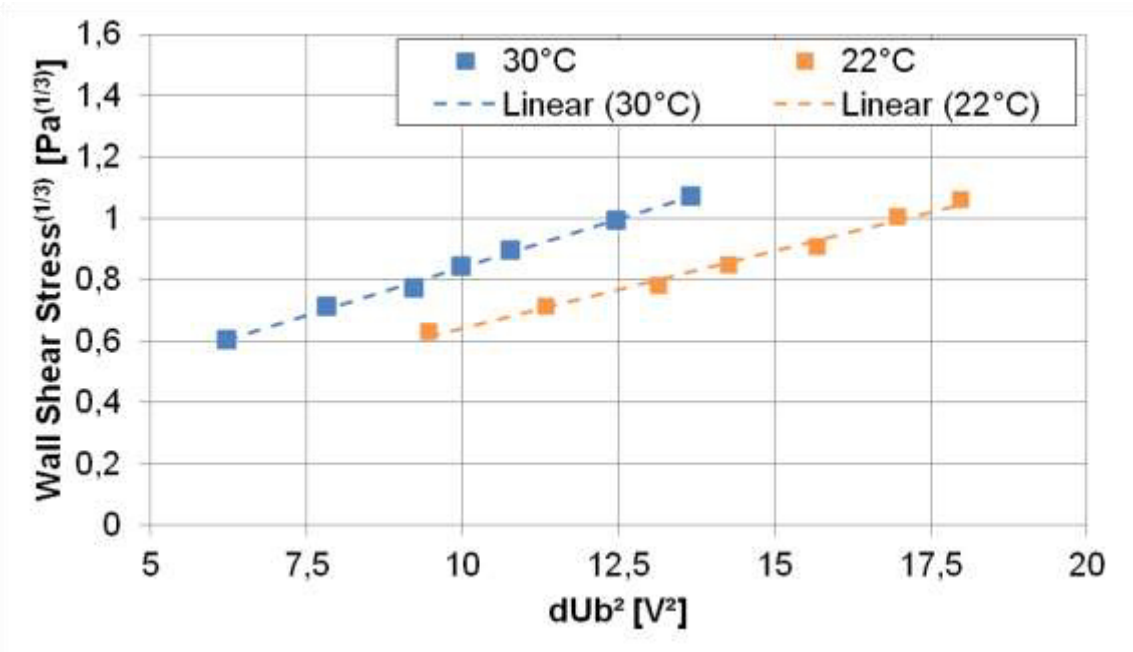

Figure 109: Temperature Dependency of Calibration Curve

Figure 109 shows the temperature dependency for the sensor placed on the plastic inlay. It can be seen, that not only the values change, but also the sensitivity of the sensor (increase in slope) drops with increasing temperature. It is therefore necessary to calibrate the sensors against varying ambient temperatures.

6.4.4.2 Mounting Conditions

The mounting conditions are highly responsible for how the heat is removed from the sensing element. Heat generated by the sensing element is dissipated by conduction into the carrier material, radiation to peripheral components and convection to the ambient. To minimize the conductive heat transfer to the support material, a blind hole was placed under the sensing element. According to [145] this helps to improve the sensor sensitivity.

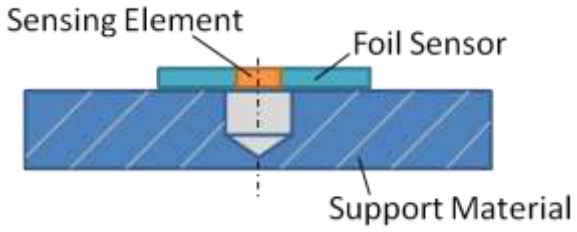

Figure 110: Sensor Positioning Principle

To study the mounting condition influence two sensors where placed onto different support materials. One sensor was placed onto cast iron (pressure plate material – CGI) and the other was placed on plastic material. It can therefore be quickly derived how big the influence of the mounting condition and carrier material is, since one material has nearly insulating properties.

In Figure 111 the results of the tests at ambient temperature of 20°C are displayed. The sensor placed on the metal support has a lower sensitivity than the sensor placed on plastic.

[145] Nitsche & Brunn 2006, P.89

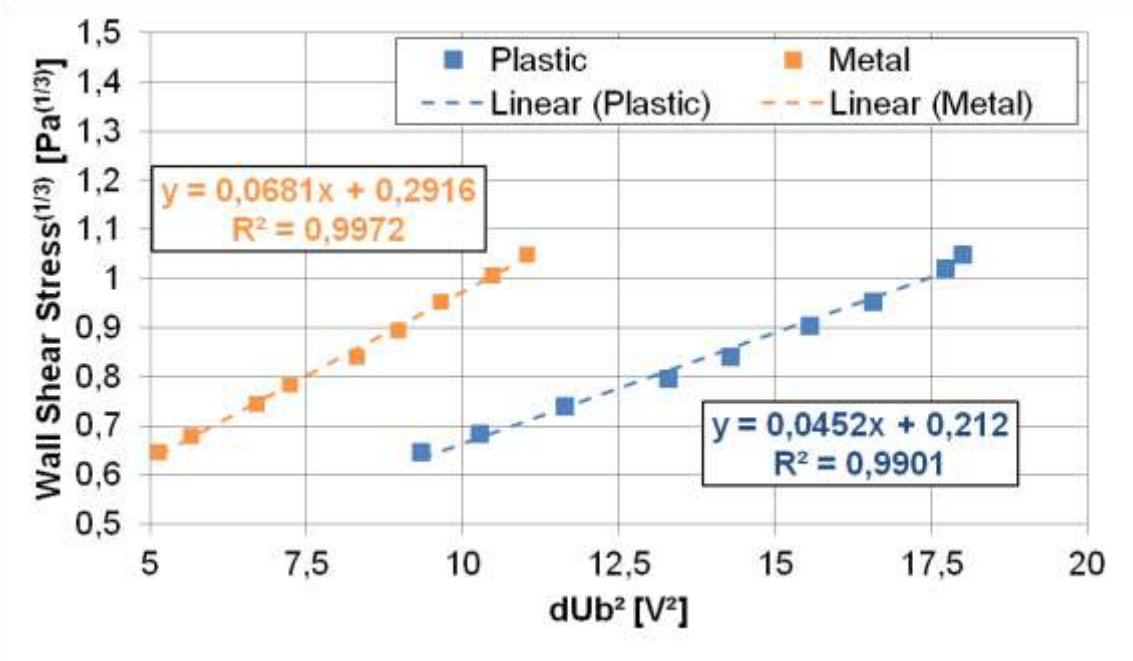

Figure 111: Influence of Mounting Conditions on Sensor Behavior

The behavior is similar to the ambient temperature change experiments conducted earlier. Reason for the similarity is that due to the lower thermal conductivity of the plastic material the heat transferred by conduction is lower and therefore the convective heat flux is higher with unchanged ambient conditions.

6.4.4.3 Flow Angle Dependency

The flow angle has a high impact on the heat transferred from the sensing element to the ambient air by convection. Changing the angle between the air flow and the sensing element results in a change of the overflown length.

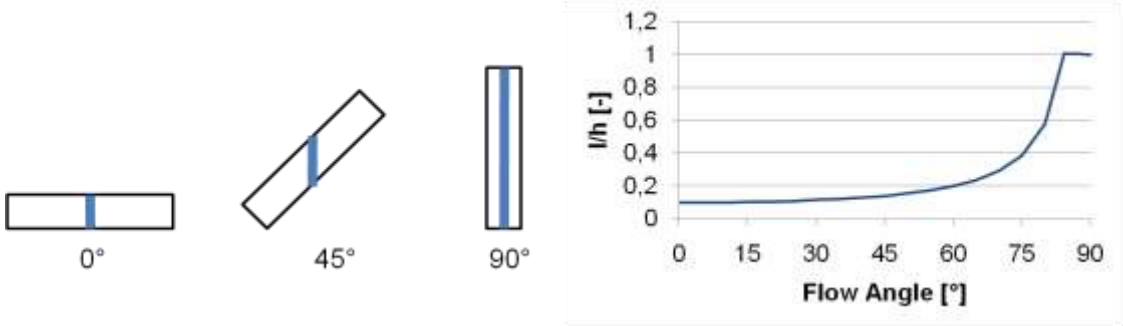

Figure 112: Change of overflown Length with Flow Angle

For a simplified rectangular geometry with a width 10 times as large as its height, Figure 112 shows the change in overflown length. According to Figure 112 the sensor should show a low sensitivity to small changes in flow angle. At an angle of approximately 60° the sensitivity increases dramatically.

In Figure 113 the measured angular dependencies are shown. Both plastic and metal mounted sensors show the same behavior if normalized to the squared bridge voltage difference at a perpendicular flow angle.

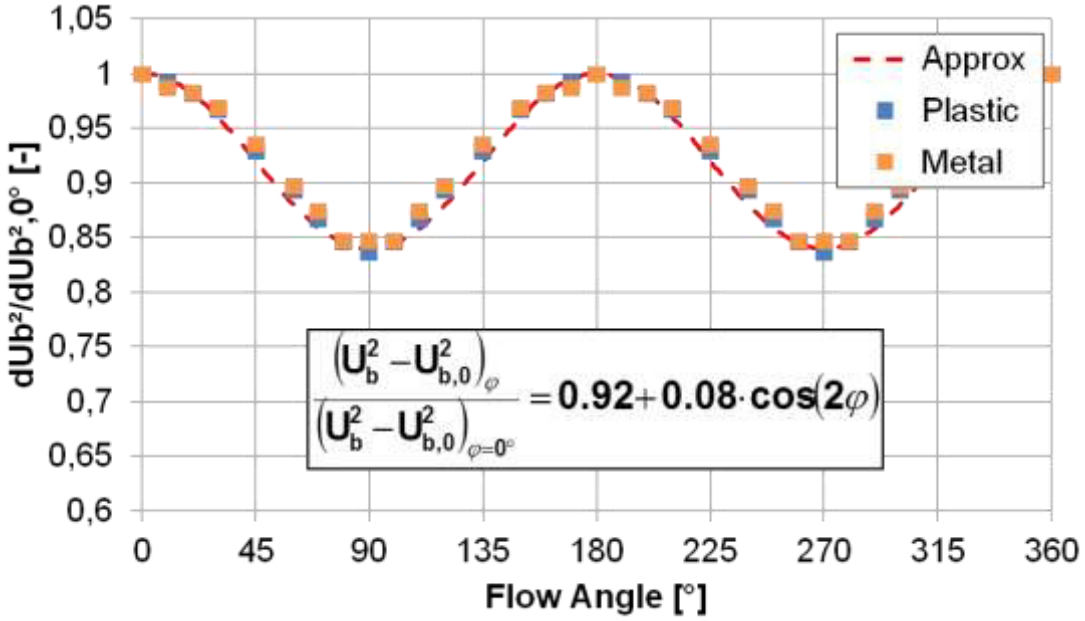

Figure 113: Sensitivity of Sensors to Flow Angle

The above mentioned behavior was not fully obtained by the measurements. Angular changes can be characterized by a trigonometry function, but the stated high drop at angles larger than 60° could not be observed. This phenomenon is related to the small size of the sensing element, reducing this influence. The results indicate that the angle between air flow and sensing element can be characterized by a general function and is not mounting condition or temperature dependent.

6.4.4.4 Conclusions

As shown, foil sensors cannot be applied to different measurement problems with the use of a global calibration formula. Mounting conditions and temperature changes have high impact on the sensor behavior and have to be calibrated individually. An important result of the conducted experiments is that the flow angle dependency obtained in Figure 113 is not dependent on mounting or temperature conditions and can be treated as globally valid law. This simplifies the calibration procedure for the clutch system measurements as will be shown later.

6.4.5 Clutch System Measurements

For the measurements of the wall shear stress inside the clutch system, the test rig used for the average flow velocity measurements was modified. Since the sensor signal had to be transferred from the surface of interest out of the rotating system, a

rotary signal transmitter was used. For this, the input shaft of the transmission was modified to obtain a free end from which the signal could be transferred.

Figure 114: Rotary Transmitter (left) and Maintenance Hatch (right)

For a simplified assembly of the clutch system with surface mounted wall shear stress sensors, a maintenance hatch was cut into the bell housing of the transmission (Figure 114). With this hatch it was possible to mount the entire assembly and to connect the wires of the foil sensors to the rotary transmitter wires with the transmission mounted to the test rig at the end of the procedure.

For the placement of the transducer two options were considered:

1. Placement on the rotating shaft as close as possible to the foil sensors to minimize additional resistances by additional wires and the rotary transmitter

2. Stationary placement and transfer of unamplified signal through transmitter

Both options have advantages and disadvantages. The placement of the transducer on the rotating shaft for instance would make it possible to transfer the amplified voltage through the transmitter but would also cause an imbalance on the through shaft. Placement of the measurement transducer after the rotary transmitter would make the installation simpler but would increase the value of the pre-resistor of the sensor due to additional wires and the inner resistance of the rotating transducer.

To test both options and see the effects of transducer placement on the measurement signal initial tests were performed. During these tests it was discovered that high voltage signal disturbances occur, when the transducer is placed before the rotary transmitter, making precise measurement impossible. By placing the transducer after the rotary transducer, the measurement noise was completely removed. Disadvantage

of the placement of this configuration was an increased total resistance before the transducer. This disadvantage could be overcome by manually adjusting the sensor with the gain and offset voltage potentiometers. The manual adjustment was performed iteratively, so that a maximum sensitivity was obtained in the desired range.

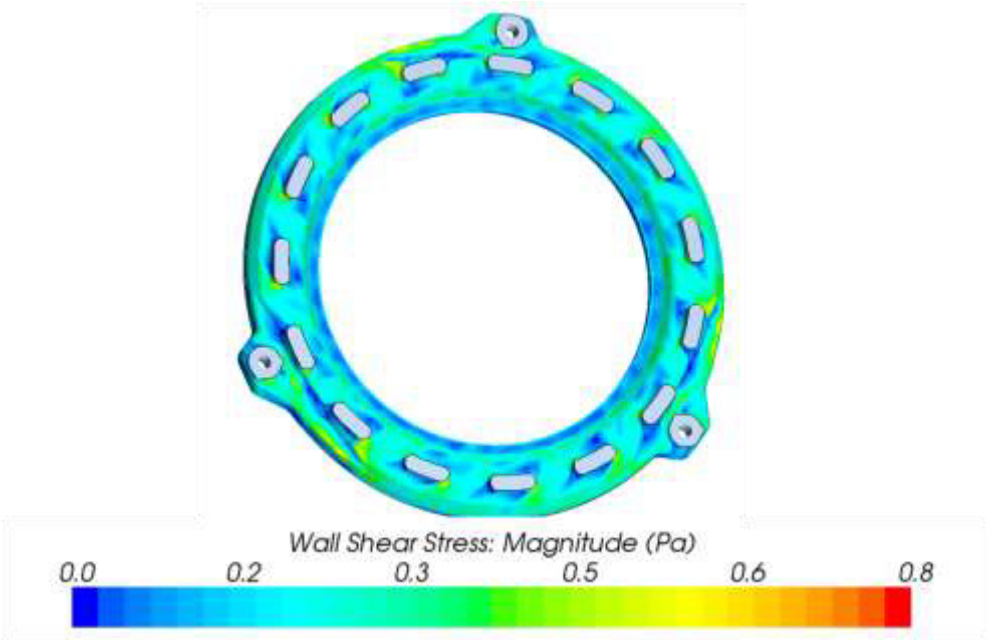

Figure 115: Wall Shear Stress Distribution of the Pressure Plate at 750 rpm

The pressure plate of the clutch system was chosen as suitable object for sensor positioning. Figure 115 shows the wall shear stress distribution on the surface of the pressure plate. Between the diaphragm spring supports the wall shear stress shows low gradients at all engine speeds, making this position a good choice for the measurements. The remaining uncertainty is the sensor orientation on the pressure plate. As shown in the previous section the foil sensor is sensitive to angular changes in flow direction.

Figure 116: Sensor Positions on Pressure Plate

To solve the issue of unknown flow direction, a second sensor was applied to the pressure plate with an angle of 45° to the other sensing element. With this configuration it is possible to obtain the unknown flow direction and wall shear stress level as follows:

With a reformulation of equation 2.40 one can obtain equation 6.9. By substituting equation 6.9 into the flow angle equation from Figure 113, equation 6.10 is obtained

$$\left(U^2 - U_0^2\right)_{\varphi=0°} = \frac{\tau_w^{\frac{1}{3}} - A(T)}{B(T)} \tag{6.9}$$

$$f(\varphi) = \frac{\left(U^2 - U_0^2\right)_{\varphi}}{\tau_w^{\frac{1}{3}} - A(T)} \cdot B(T) \tag{6.10}$$

With equation 6.10, the calibration constants for both sensors and the knowledge that the flow angle at one sensor is the same angle plus 45° at the other sensor, the problem becomes well posed (two equations for two unknowns).

Figure 116 shows the sensor positions on the pressure plate. The sensors where placed between the diaphragm spring supports in the middle of two lift springs (120° between both sensors). To simplify the application of the sensors, the remaining surface roughness was leveled by application of glue. The third position left on the

pressure plate was also prepared for sensor application but left blank for reference measurements (velocity measurements with the boundary layer probe). As can be seen in Figure 116, the riveted connection of the lift spring to the cover was drilled out and replaced by a common thread screw connection.

The remaining tasks are now to identify the wind tunnel velocity / wall shear stress dependence for the pressure plate and to find the temperature dependent calibration constants for both sensors on the pressure plate under mounting conditions. As shown in Figure 117 an additional casing of the pressure plate was necessary to perform the measurements.

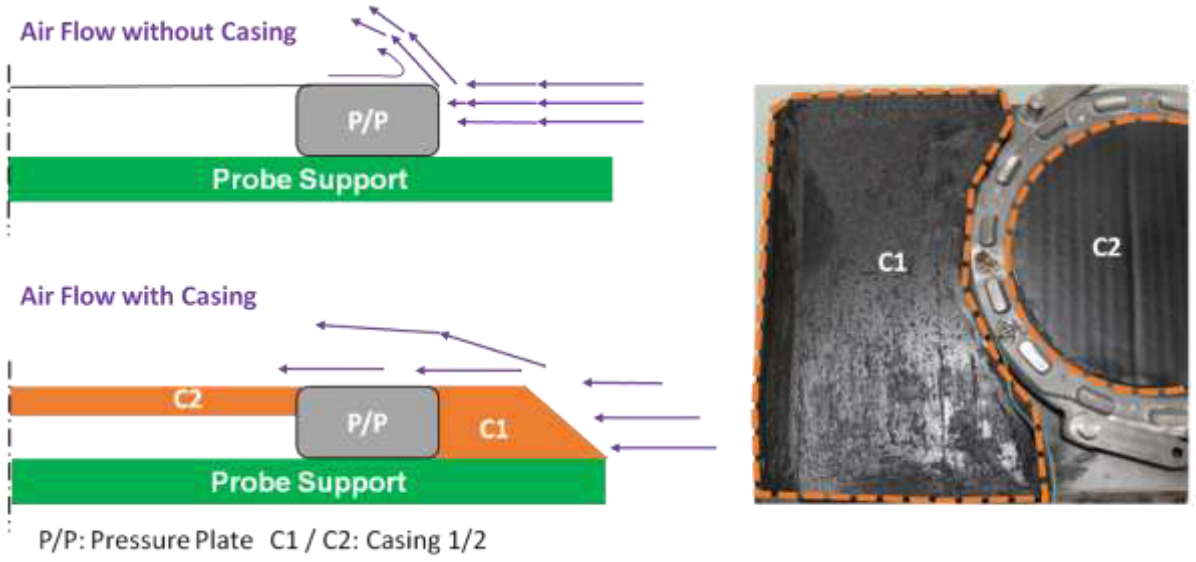

Figure 117: Casing of Pressure Plate

With the application of the casing the flow at the sensor positions became similar to the flow over a flat plate and the reference wall shear stress measurements were therefore possible.

The calibration of the sensors was then performed at different ambient temperatures. In the evaluation of the calibration curves care has to be taken with the sensor which has an orientation of 45° to the flow from the wind tunnel. For this sensor the measured calibration curves at one ambient temperature have to be transformed by the angular dependence equation to obtain the desired calibration coefficients.

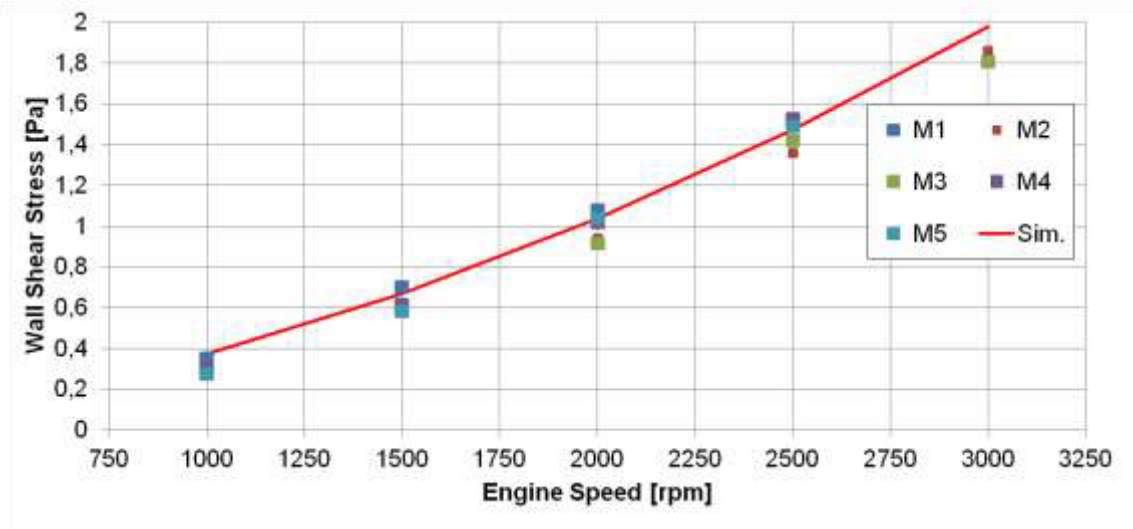

Figure 118: Comparison of Simulated and Measured Wall Shear Stress Profiles

The results of the performed clutch system measurements can be seen in Figure 118. The points M1 represents the first day measurements, M5 the last day. The measured wall shear stress shows good match with the simulation results.

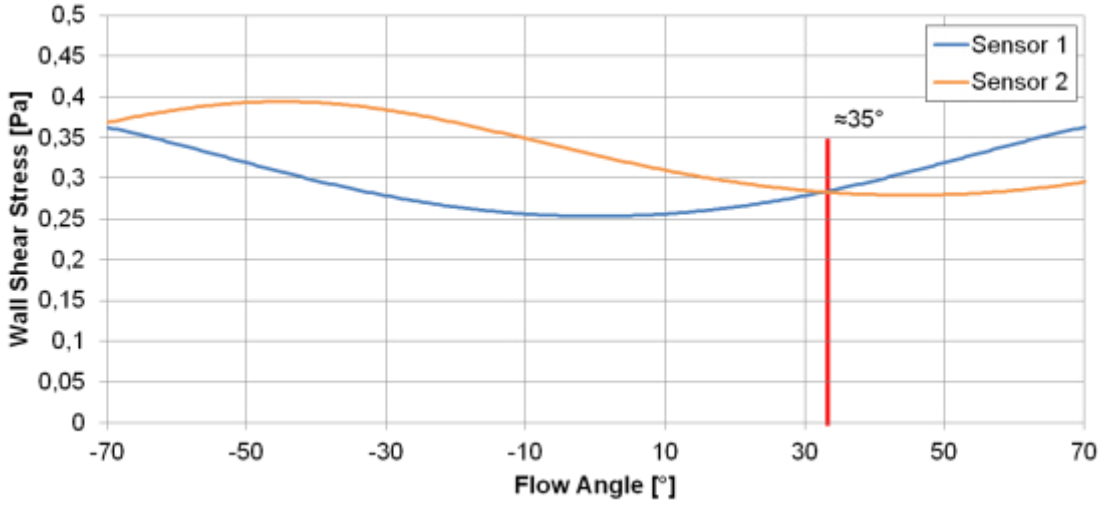

Figure 119: Flow Angle at 1000 rpm

For the solution of equation 6.10 a graphical solution method was chosen. In Figure 119 an example of the graphical evaluation is shown. The angle between the sensor and the flow at 1000 rpm is approximately 35°.

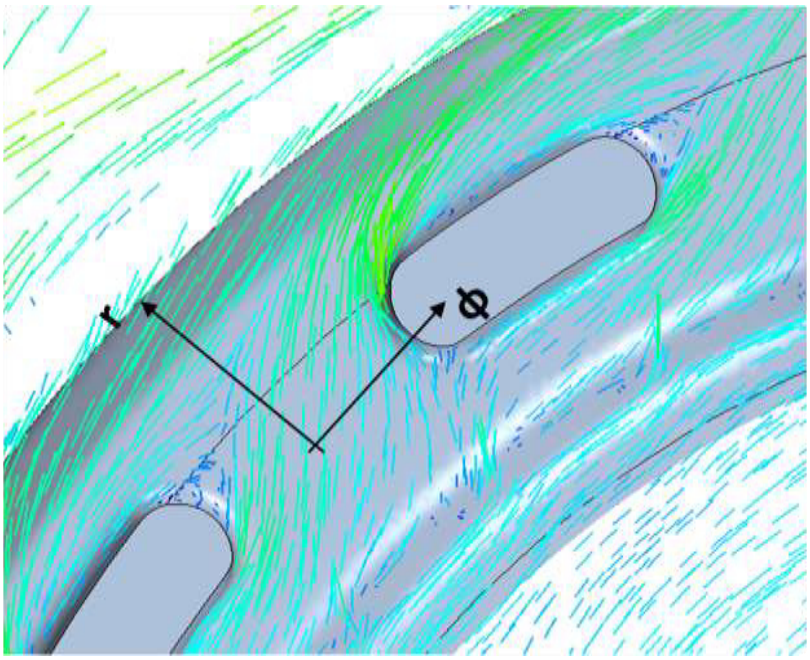

Figure 120: Flow Direction inside the Clutch System

This reflects the flow conditions inside the clutch system quite well. Figure 120 shows the flow direction inside the clutch system around the pressure plate. It can be derived that the simulated flow angle also is about 35° to 40°.

6.5 Flow Field Measurements

The prior measurements all had in common, that validity of the simulation was proven by point wise measurements of flow specific quantities. To gain more confidence in the overall capability of the simulation tool to reflect the flow conditions, additional particle image velocimetry measurements were performed. As outlined earlier, the measurement technique makes it possible to evaluate the velocity vector field and therefore provides the most information on how precise the simulation is compared to the measurements.

Since no literature data could be found on PIV measurements of dry clutch systems, it was decided to measure the outside flow field of a clutch system rotating in free air. The restrictions caused by packaging of the clutch system itself or inside the transmission bell housing could therefore be circumvented. This step can be interpreted as first step towards measurements under vehicle mounting conditions.

6.5.1 Simulation Model

The simulation model used as basis is the same as the simulation model in chapter 5.3. To reflect the free air condition the clutch system was placed in a cylinder with a radius of half a meter and a total height of 1 meter. Figure 89 shows the simulation model domain. Again the air region was split into a stationary and rotating part.

6.5.2 Measurement Preparation

For the preparation of the measurements there are two main areas to be covered:

1. Selection of suitable seeding particles
2. Choice of possible measurement plane positions

For the selection of seeding particles the density and size of the particles are of high importance. The higher the density and the smaller the particles are, the smaller the measurement window has to be for the algorithm to detect the particle groups.

In a first trial, fog from an industrial fog generator was used for particle generation. As can be derived from Figure 121 the fog has a high density and rather small particles. It is therefore not appropriate for the measurements. Tests with water vapor or smoke from coal had equivalent properties. The issue with the seeding material could be resolved after using a PALAS AGF 10.00 particle generator, which was kindly supplied by the “Institut für Thermische Strömungsmaschinen” (ITS) at the Karlsruhe Institute of Technology. The particle generator uses compressed air which flows over a small pipe which has oil inside to generate the desired seeding particles. By adjusting the air pressure and the amount of oil flowing into the small pipe, the size and density of the fog can be tuned.

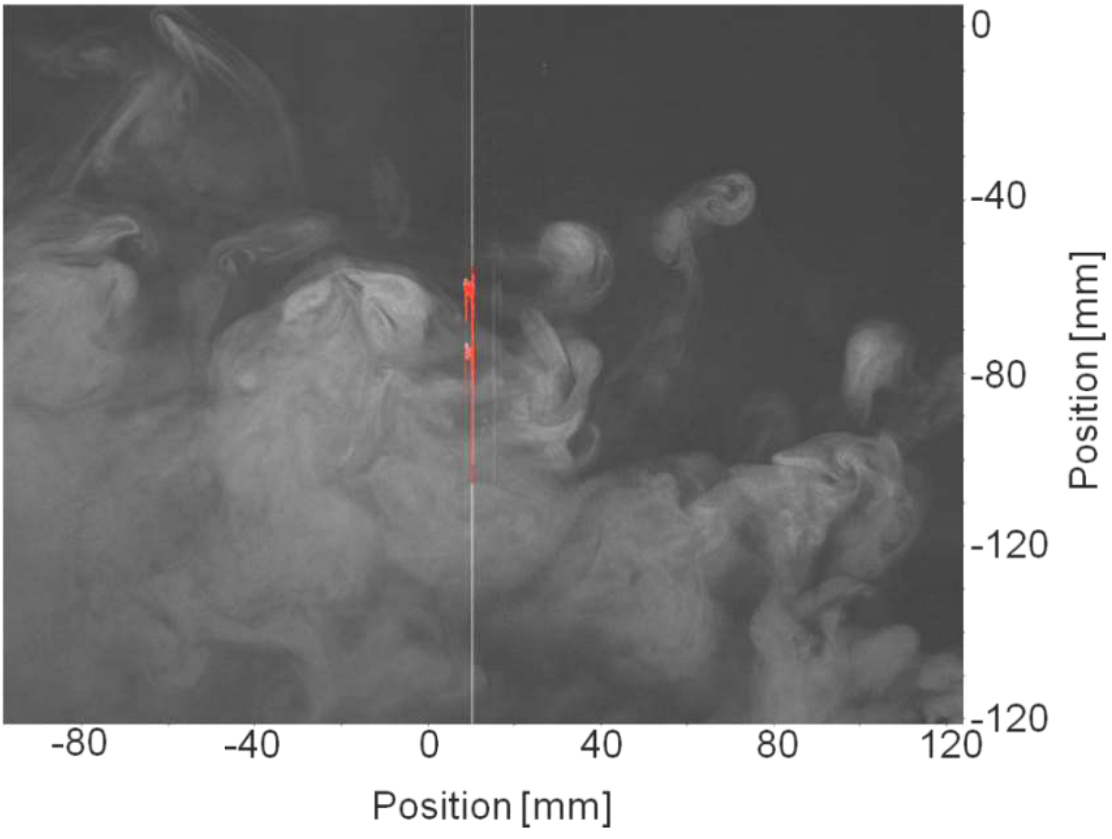

Figure 121: Trial Measurements with Industrial Fog Generator

As pointed out the density of the fog is a very important factor for the success of the measurements. Additionally it is desirable to have the same density of particles in the entire test chamber. Air flowing out of the clutch system has to have the same particle density as air flowing around the clutch system in the ideal case.

To obtain the highest degree in freedom of choice in the measurement plane positioning, it was chosen to surround the test rig with an additional casing (Figure 123). This makes it possible to firstly adjust the particle density in the air inside the casing and to measure under constant seeding conditions in case the casing is properly sealed. The measurement time is then only dependent on how fast the particles sediment on the test rig surfaces. This configuration is also necessary since, due to health considerations, it is not recommended to be subjected to seeding particles over a long period of time.

For the positioning of the measurement planes, the results of the simulation model were taken as guideline. As described in the beginning of this chapter, the particle image velocimetry is a two dimensional measurement principle. The technique can measure three dimensional flow systems in case one component of the velocity vector is relatively small and can be neglected against the other components. Inside a cylindrical coordinate system the radial component is always necessary to span a plane. The decision to be made has therefore to be between the tangential and axial component of the velocity vector. The left part of Figure 122 shows a plot of the relation between the axial and tangential velocity component. In front and in the back of the clutch system the axial velocity is much higher than the tangential velocity.

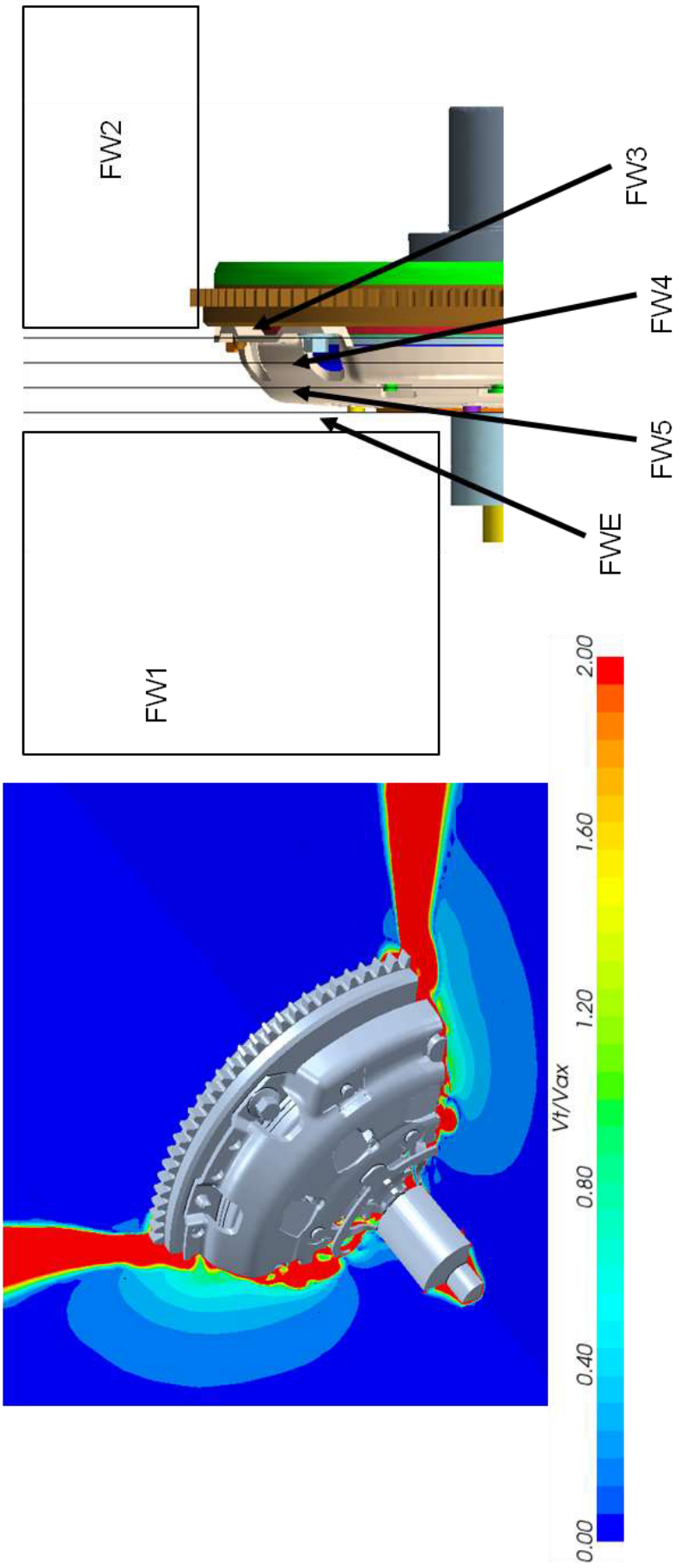

Figure 122: Measurement Plane Positioning

In these areas it would be recommended to span a measurement plane in the radial and axial direction. Above the clutch system the tangential component of the velocity vector has a higher influence. It is therefore advantageous to span the measurement plane in the radial-tangential direction. The selected positioning of the measurement planes is shown in the right part of Figure 122.

6.5.3 Test Rig Setup

Figure 123 and Figure 124 show the test rig setup. The rig basically consists of an electric motor which is connected to a support bearing by a bellow coupling.

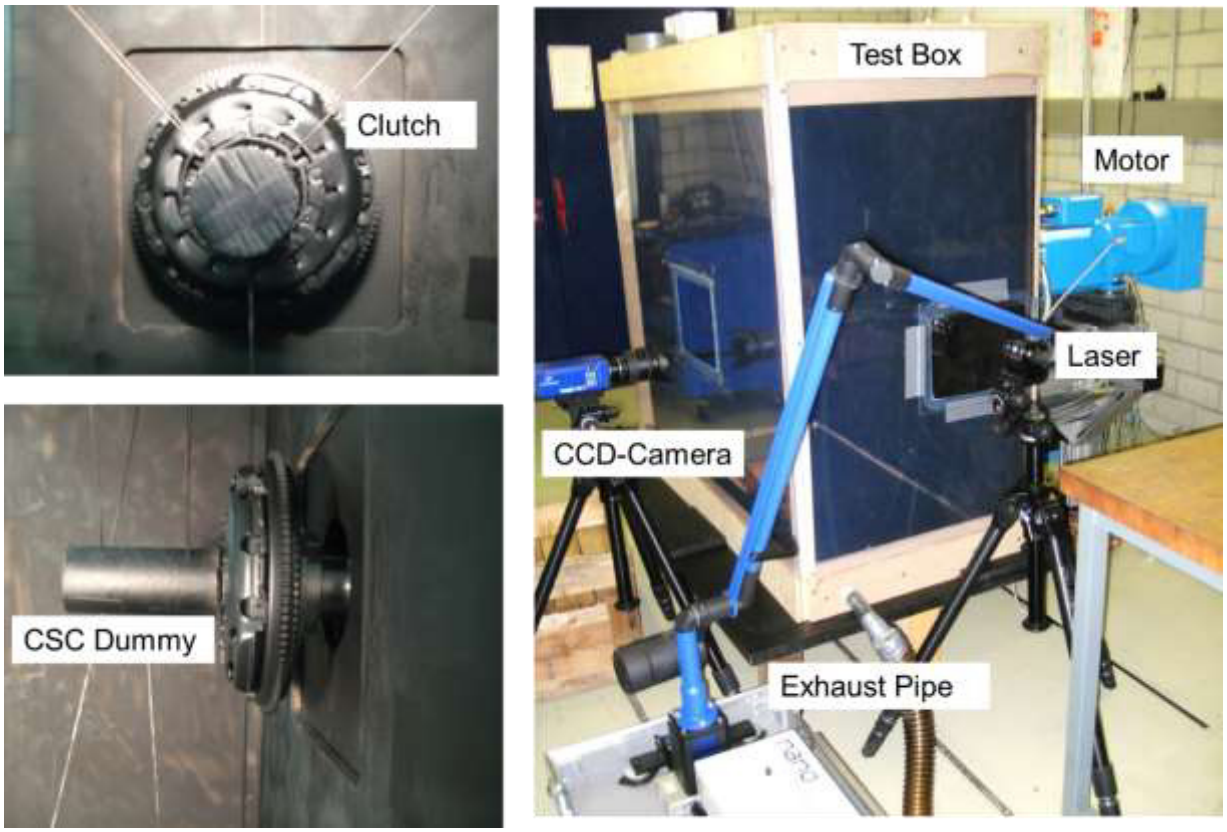

Figure 123: Test Rig Front-Side

The clutch system is directly mounted to the support bearing shaft. It consists according to the simulation model of a pressure plate assembly, a clutch disk and the flywheel. To consider the cylinder dummy, a substitute was build out of cardboard and placed in front of the clutch system. Two ropes attached to the bottom of the cylinder make it possible to adjust the axial position of the cylinder. Translations in radial direction are possible by adjusting the length of the four welding wires attached to the top of the cylinder. To be able to measure radial / axial and radial / tangential planes it is necessary to have at least a visual access in the front and at the side of the test rig. To be able to position the measurement planes freely, the front and the side wall of the casing was at the beginning of the tests made of Plexiglas.

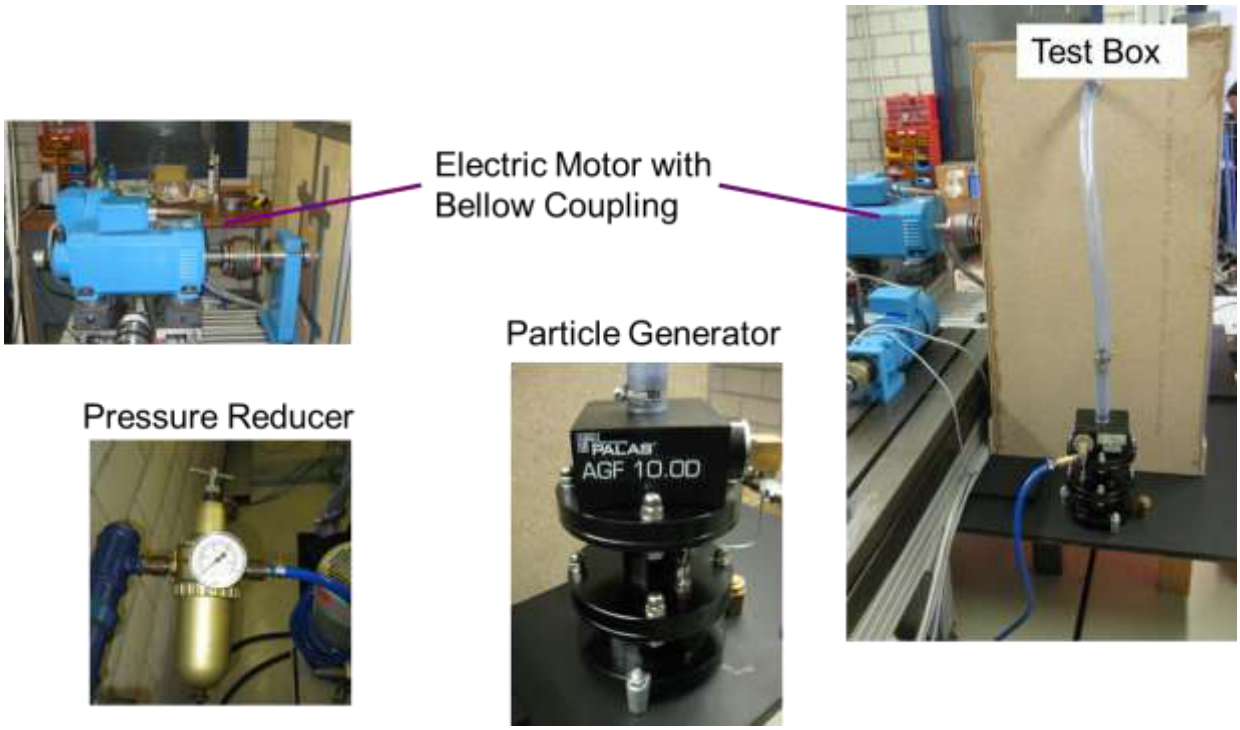

Figure 124: Test Rig Side View

The remaining walls of the casing were made of plywood. Gaps between the plywood sides or between the plywood and the Plexiglas were sealed by silicone. A pressure reducer was placed in the feed line of the particle generator to be able to reduce the air pressure. To be able to dispose the air inside the casing when the testing is done, an exhaust pipe which was attached to an extraction system was connected to one side of the test box. The PIV system itself consists of a CCD-Camera, a laser and a control unit.

During initial tests it was discovered that all camera images had a striped pattern. It was supposed, that the accuracy of the result of the PIV detection algorithm would suffer. As root cause of the striped pattern the Plexiglas window was identified. When passing through the Plexiglas the laser light seems to experience interference effects. After exchanging a small part of the window in the desired measurement position with glass, the striped patterns dissolved. The left side of Figure 125 shows an example of the observed striped pattern.

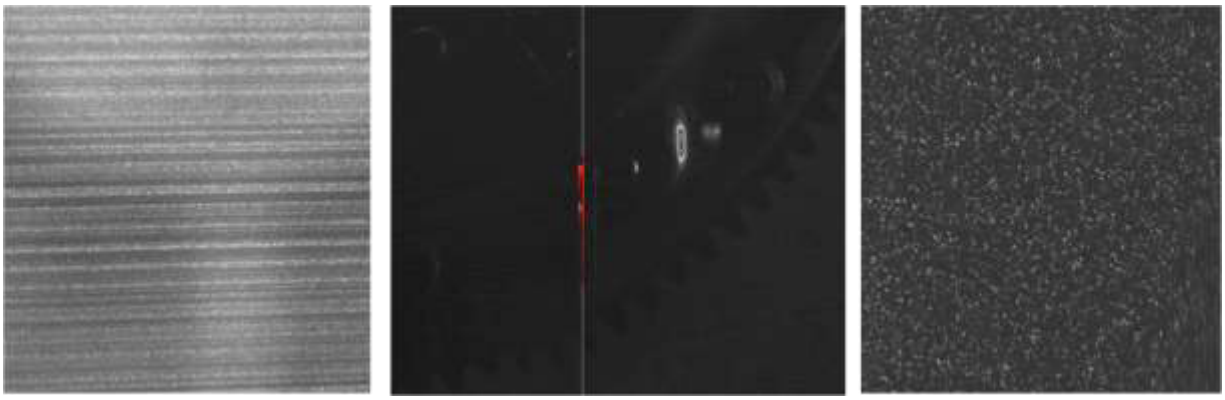

Figure 125: Left: Observed Striped Pattern; Middle: Clutch Reflections; Right: Visible Particles

The center section of Figure 125 shows the experienced laser light reflections on the clutch system. Due to these reflections the aperture had to be closed-in so far that the particles were not visible anymore (black graining of the image). As a first solution to this issue it was decided to spray-paint the clutch system and the background of the casing in black. By this measure the reflections could be reduced, but still not to a satisfactory level. To be able to perform the measurements it was decided to measure the flow field right next to the clutch system. In the right section of Figure 125 an example of the resulting particle images is shown. It can be observed, that the mentioned stripes are not visible and the particles are clearly visible.

The measurements next to the clutch system make it difficult to relate the clutch rotation position to the images taken. To resolve this issue the CCD-Camera was triggered by an incremental rotational position sensor. Since the clutch system has a 120° symmetry, it was decided to monitor the clutch system at 0° / 40° / 80°.

6.5.4 Measurements

The measurements planes were positioned according to Figure 122, with high focus on the flow entering and leaving the clutch system. The axial / radial measurement plane at the flywheel side of the assembly was not measured. The engine speed was limited to 2000 rpm due to safety reasons.

Figure 126 shows the simulation results of the vector field in front of the clutch system. It can be observed, that here the air flows in a rather organized manner towards the clutch system.

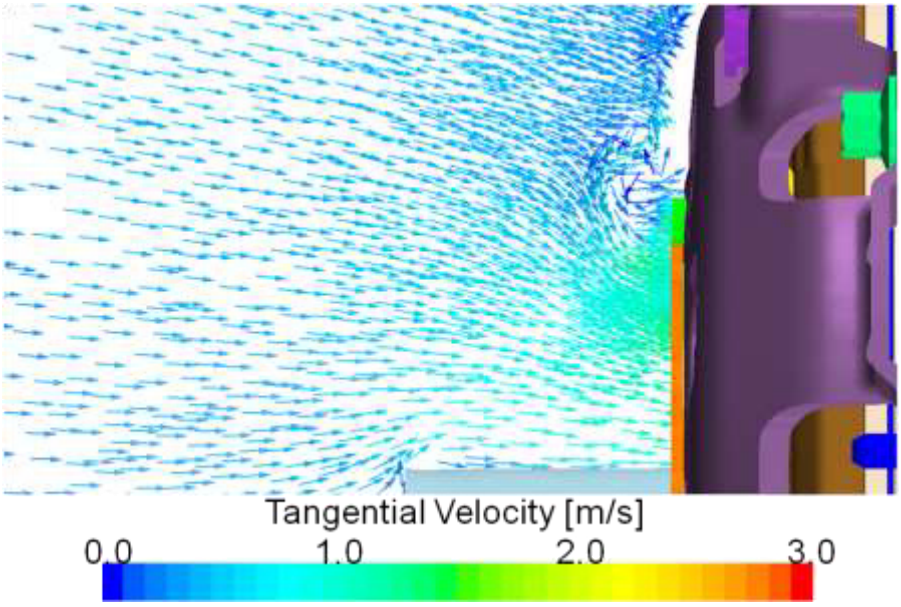

Figure 126: Flow Field In front of Clutch System at 1500 rpm

It can also be observed that the air mainly enters the clutch system at diaphragm spring opening near the rotation axis.

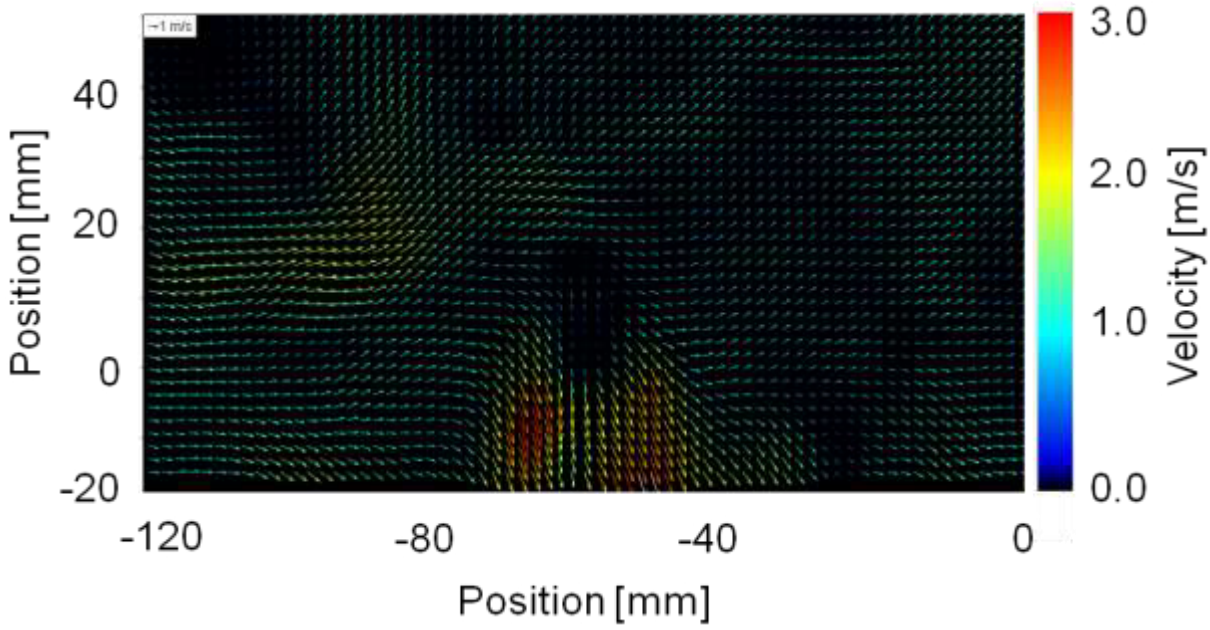

Figure 127: Measured Vector Field In Front of Clutch System

The result from the PIV measurements in front of the clutch system for 1500 rpm is shown in Figure 127, which was recorded as close as possible to the clutch system and to the cylinder dummy without recording any reflections. It can be seen that the flow direction of the obtained vector field is in good accordance to the vector field of the simulation. The average velocity of the measurements and the simulation is according to Figure 126 and Figure 127 in the same range of about 1 – 1.5 m/s. In

total, the performed measurements in front of the clutch system showed good accordance to the simulation at all engine speeds.

In the center section of Figure 127 the correlation of the performed measurements is at a first glance not very good. The reason for this inaccuracy can be found by regarding Figure 128.

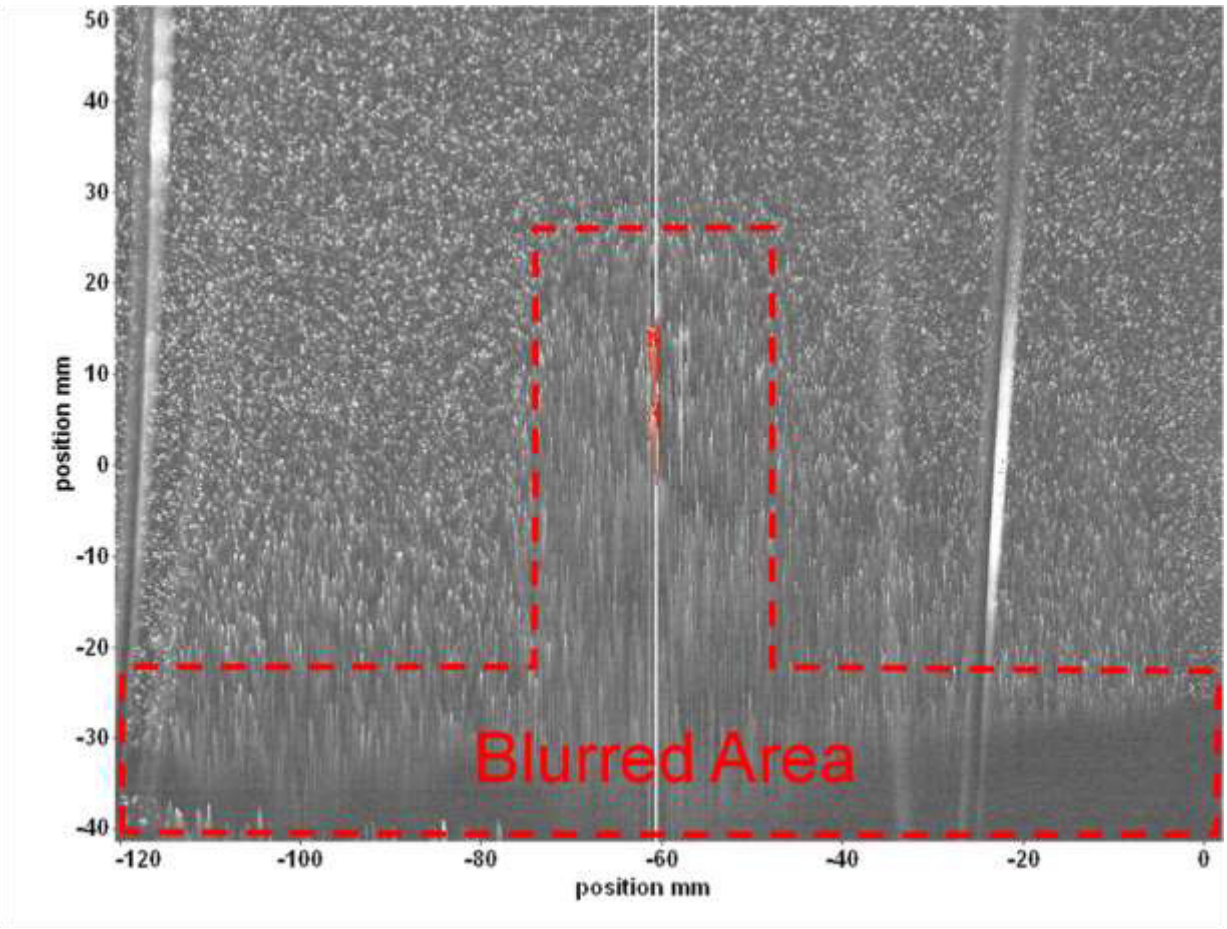

Figure 128: Blurred Area of CCD Camera

The middle and the lower section of the image have a blurred area. In this area, the tracking algorithm produces high errors. During the measurements the cause behind was not found. It is assumed that reflections or the camera itself are the main root causes.

After the measurements in front of the clutch system, the measurements above the clutch system were performed. Figure 129 shows an example of an obtained vector field for a rotary speed of 1500 rpm.

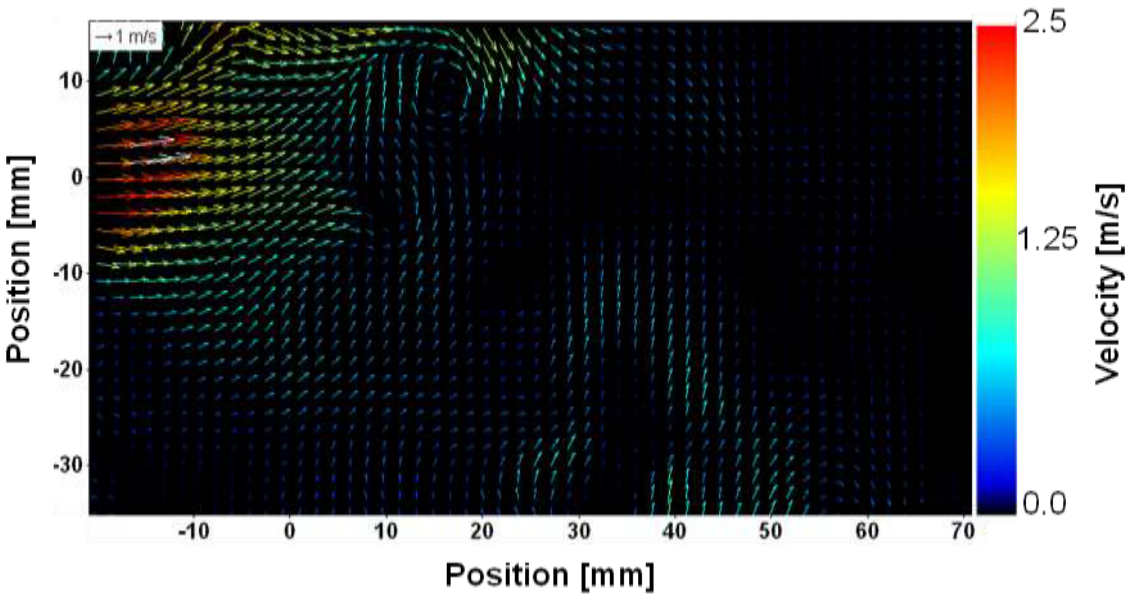

Figure 129: Flow Field above Clutch System at Measurement Plane FW3

Compared to the flow field of the simulation in Figure 130, it is difficult to find similarities apart from the velocity range, which is in very good accordance. At a closer look it is possible to divide the flow field of the simulation into different types of areas.

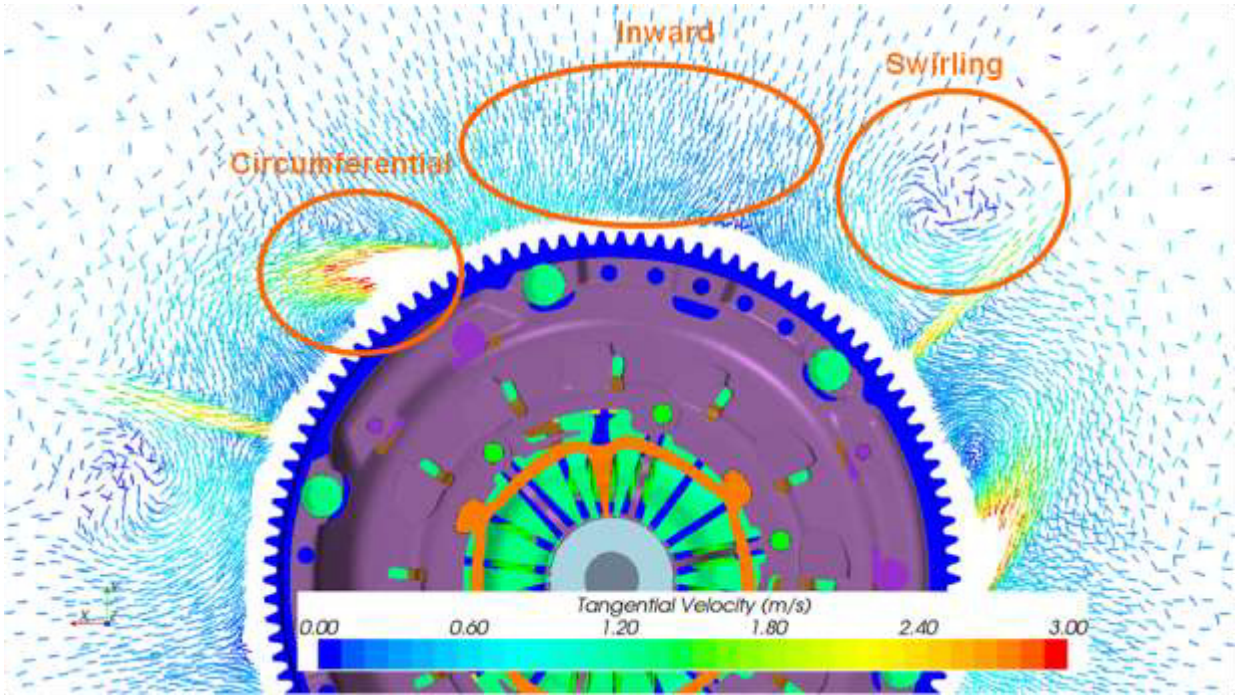

Figure 130: CFD Flow Field Measurement Plane FW3

The air flowing around the clutch system can be segmented in areas where the flow is moving in a circumferential direction, areas where air is flowing towards the center of the rotation axis and swirling areas. Taking this information as background to the post processing of the measurement data, similarities between the measurements and the simulations can be found.

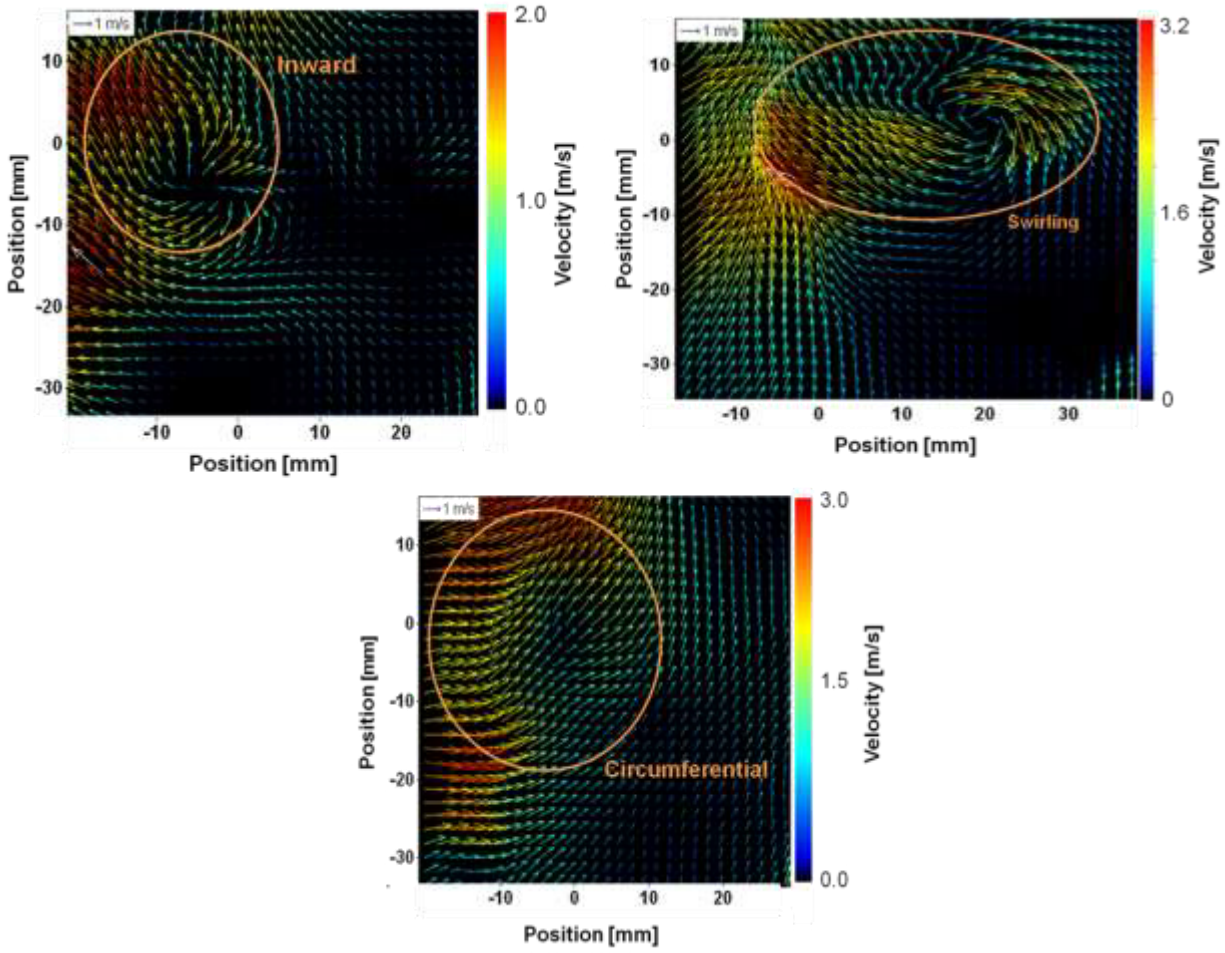

Figure 131: Flow Field above the Clutch System at 1500 rpm

Figure 131 shows examples for all three types of areas. Close to the rotating surfaces, the flow field around the clutch system is compared to the flow in front of the clutch system not stationary and does not have a preferred flow direction. Due to the viscosity based relative movement between the clutch system and the air flowing around the clutch, it was also not possible to obtain stationary vector fields by triggering the camera.

From these observations it could be concluded, that inside the simulation model the choice of stationary flow field is inadequate. This statement can be weakened when looking at the average and maximum velocities, the entire structure of the flow field and the calculation procedure of the CFD software.

As shown in Figure 130 and Figure 131 the maximum and average velocity of the flow field is in good accordance. The overall structure of the flow field in the far field is well reflected by the simulation as can be seen in Figure 130. Close to the clutch system high velocity gradients occur. With increasing distance to the clutch system the absolute velocity and the instationary effects decay which are then again well reflected by the simulation. When using a moving reference frame to simulate rotation in CFD code, the solver only solves the flow field for one position of the clutch system relative

to a fixed coordinate system. Instationary effects like movement of the flow field relatively to the clutch system are not considered. If this specific flow field is then rotated with a relative speed proportional to the total viscosity of air surrounding the clutch system, the same flow field as the obtained measurements would be observed.

6.5.5 Conclusions

Particle image velocimetry measurements for a dry clutch system were performed in the last chapter. It was shown, that the overall flow conditions around a clutch system can be captured by a two dimensional measurement technique. The flow conditions in front of the clutch system are in excellent accordance with the simulations. Turbulent and instationary effects near the clutch system make a direct identification of flow structures difficult, but not impossible. The overall accordance of the simulation model with the reality is rated as being high.

6.6 Conduction Heat Transfer Parameters

For the heat transfer from a clutch system the conduction resistances are of high importance because they determine the way heat input is spread from the frictional interface throughout the clutch system. The affirmation of the obtained conduction heat transfer parameters is therefore a highly important step in the verification of the CFD model.

The first step in measuring the heat conduction resistances is the selection of an identification procedure. For this it is beneficial to divide the clutch system into several groups of interest. These groups are according to the simplified multiple thermal mass model of chapter 4.3.1:

- Pressure Plate
- Flywheel
- Diaphragm Spring
- Clutch Disk (with Lining)
- Clutch Cover

Parts like sense spring, sense ring, rivets, etc. are treated as content of one of the main thermal masses. A simple way of determining the heat conduction parameters between the individual parts could now be performed in two steps:

1. Measure the cooling temperature head of a part heated up to a specified temperature to obtain the convectional resistances of the individual parts

2. Measure the cooling / heat up temperature head between two parts in contact from which only one is heated up to a specified temperature

When the contact conditions and the ambient conditions can be repeated according to the assembled condition, this method supplies the easiest way to determine the heat conduction resistances.

$$m_i \cdot cp_i \cdot \frac{dT_i}{dt} = h_i \cdot A_i \cdot (T_{amb} - T_i) \tag{6.11}$$

$$m_1 \cdot cp_1 \cdot \frac{dT_1}{dt} = h_1 \cdot A_1 \cdot (T_{amb} - T_1) + \frac{1}{R_{1-2}} \cdot (T_2 - T_1) \tag{6.12}$$

$$m_2 \cdot cp_2 \cdot \frac{dT_2}{dt} = h_2 \cdot A_2 \cdot (T_{amb} - T_2) + \frac{1}{R_{1-2}} \cdot (T_1 - T_2) \tag{6.13}$$

As equations 6.11, 6.12 and 6.13 show the system of equations necessary to evaluate the heat conduction resistances is well posed (four equations for two convection resistances and one conduction resistance).

When only regarding the clutch system (mounted to the flywheel) the necessary parameters to be estimated, according to the model of chapter 4.3, are shown in the table below.

Heat Conduction	**Convection**
Pressure Plate – Diaphragms Spring	Pressure Plate
Pressure Plate – Clutch Cover	Diaphragm Spring
Diaphragm Spring – Clutch Cover	Clutch Cover
Flywheel – Clutch Cover	Flywheel
Pressure Plate – Lining	Clutch Disk
Flywheel – Lining	Lining

Table 1: Heat Transfer Parameters for a Clutch System

With a total of one heat balance equation for each considered thermal mass (number equivalent to the number of convectional parameters) it can be concluded, that the system of equations describing the heat transfer of a clutch system is heavily under-determined (six unknown heat conduction parameters plus six unknown convection parameters for six heat transfer equations). A direct solution to this problem is therefore not available. The Joint Central Difference Kalman filter algorithm presented in chapter 2.5.3 was therefore applied to overcome this hurdle.

To aid the algorithm, following simplifications were performed:

1. Use of a global convection coefficient for all parts
2. Thermal capacity of the lining is neglected (conduction resistance only between flywheel and pressure plate)

3. According to the translational behavior of component interfaces, it is assumed, that only the contact conditions between the pressure plate and diaphragm spring change if the pressure plate assembly is mounted to the flywheel

A temperature head close to the conditions faced by the clutch system in a vehicle was obtained with the use of a flywheel thermal shock test rig. The rig is usually used to characterize the thermal shock behavior by inductively heating the flywheel in the frictional area with a certain power. After the heat up cycle is completed, the flywheel is subjected to water causing high cooling rates and therefore thermally induced tension inside the flywheel. For the performed tests the rig was adapted to mount a complete test rig with temperature sensors applied. As stopping condition the surface temperature, measured by a pyrometer, was used. Figure 132 shows the setup.

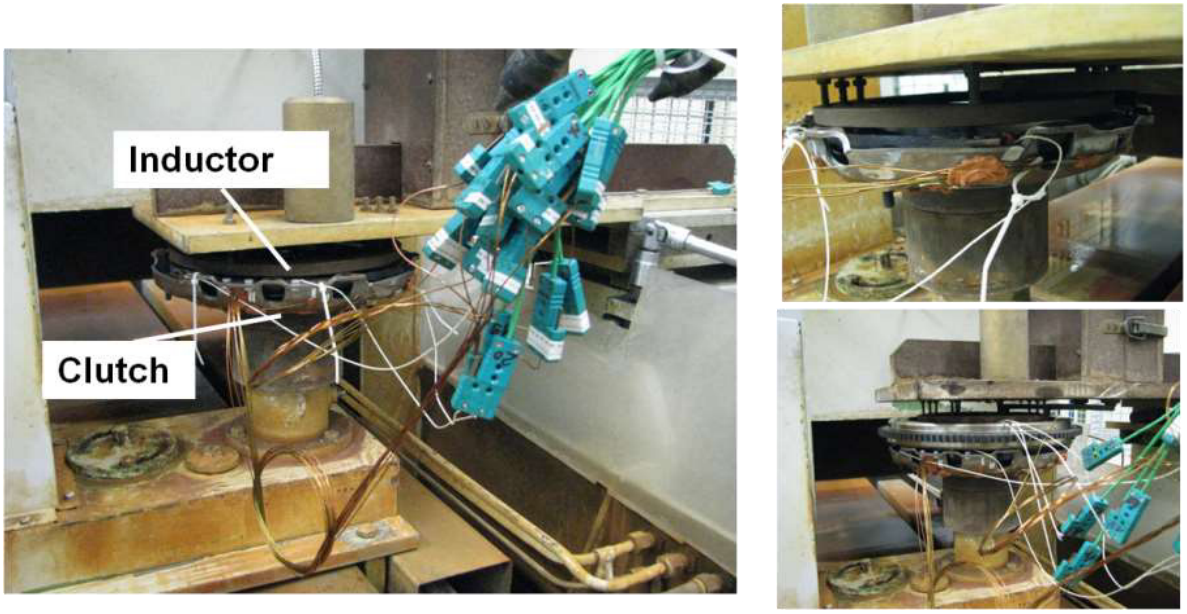

Figure 132: Thermal Shock Rig Configuration

The measurement procedure was split into different stages:

1. Measurement of temperature head for pressure plate assembly only, to determine the heat conduction resistances between the pressure plate and the clutch cover

2. Measurement of the temperature curves for the complete assembly to determine the conduction resistances between flywheel – clutch cover, pressure plate – diaphragm spring and flywheel – pressure plate

The measurement positions on the main thermal masses were selected with the usage of the 120° symmetry condition in a clutch system. Figure 133 shows the measurement positions inside the clutch system.

Figure 133: Temperature Measurement Positions Clutch System

In the frictional area of the pressure plate and flywheel the temperatures were measured 4 mm below the frictional surface. The flywheel temperature was additionally measured at the interface to the crankshaft. For all other measurement points (e.g. clutch cover or diaphragm spring) the surface temperatures were measured. In Figure 134 the boundary conditions and number of measurement cycles is displayed.

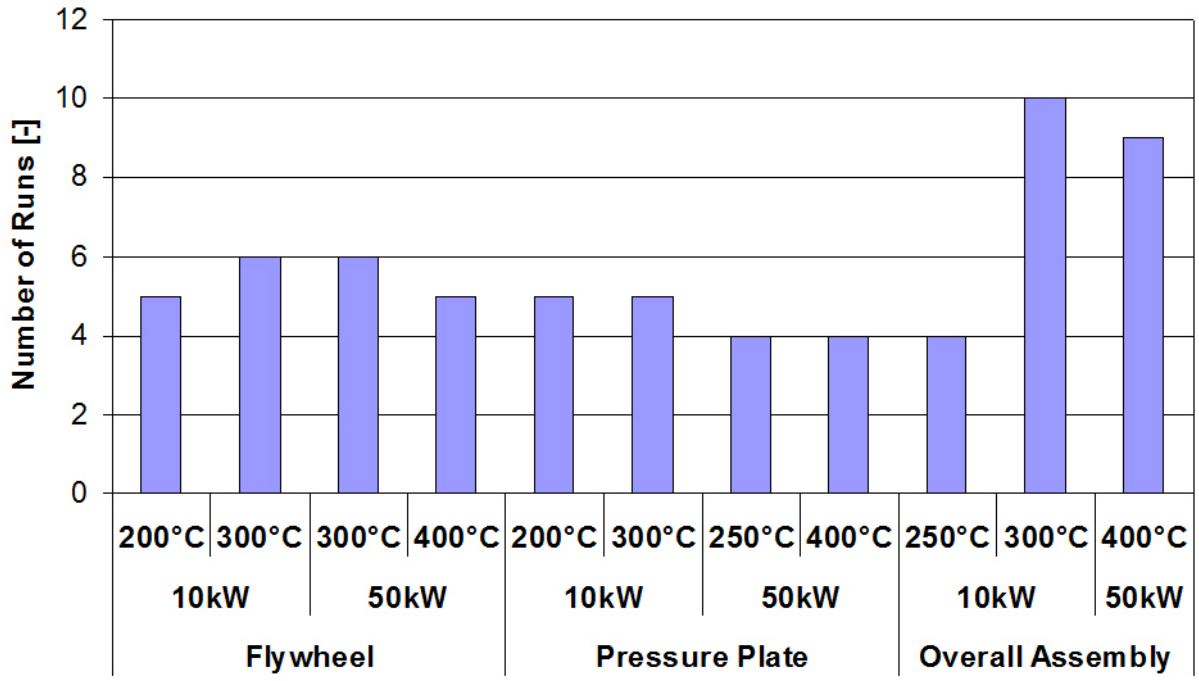

Figure 134: Measured Cycles

During the evaluation of the test-runs, it was defined to use the heat up runs with a power input of 10 kW and a 300 °C surface temperature for the estimation of the heat

transfer parameters to minimize the non-linear effects of temperature spread throughout the assembly.

Different to the algorithm for the wall shear stress reference measurements, the parameters were determined directly. As starting conditions for the temperatures the first values from the measurements were taken. The initial conduction resistances were set according to the results from the CFD simulations. Since the overall cycles were relatively short, the estimation procedure was restarted with the obtained parameters after all measurement data has been processed.

The results of the performed measurements for the pressure plate assembly are shown in Figure 135.

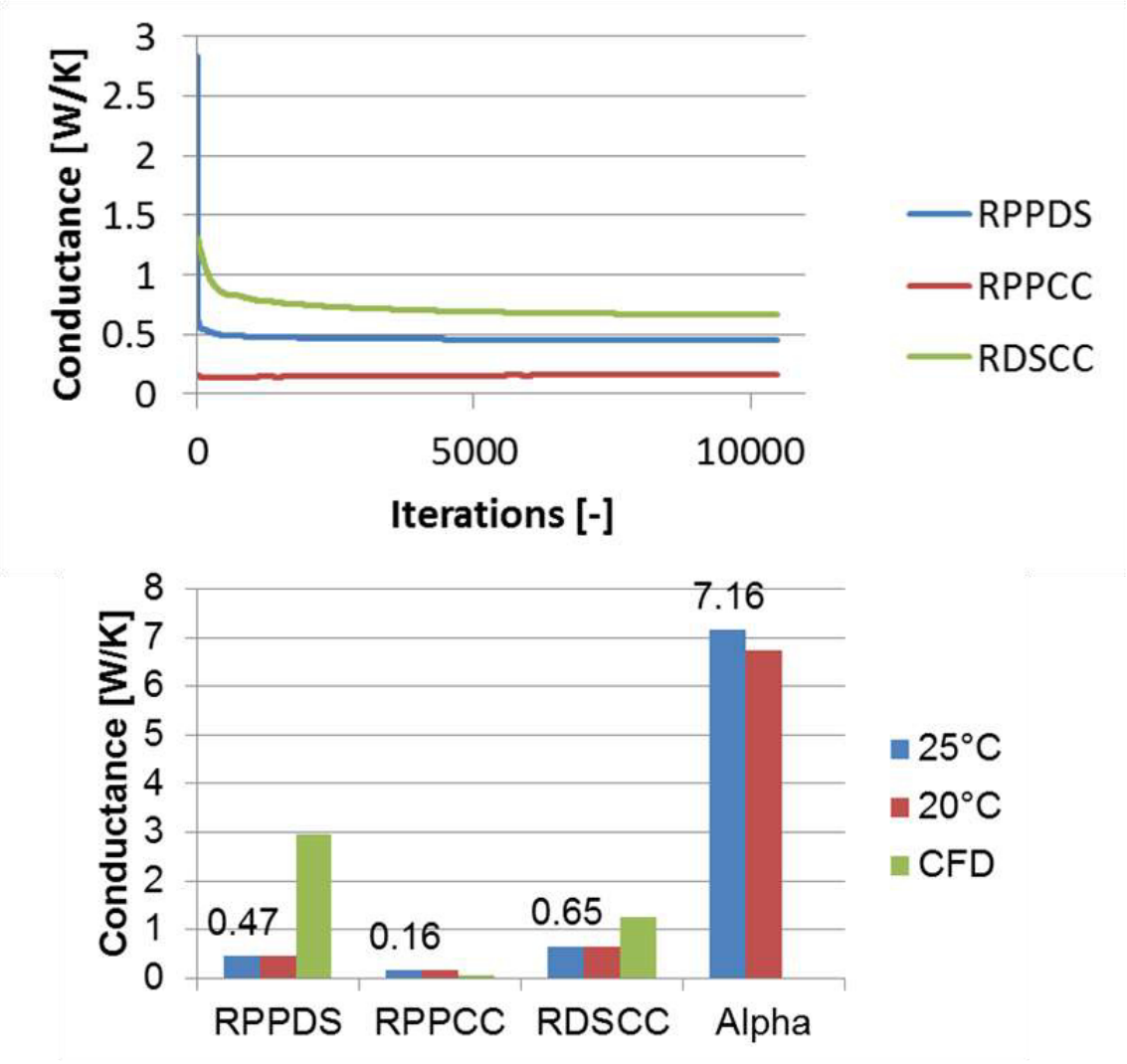

Figure 135: Results of Parameter Estimation for the Pressure Plate Assembly (Conductances: RPPDS: Pressure Plate – Diaphragm Spring; RPPCC: Pressure Plate - Clutch Cover; RDSCC: Diaphragm Spring – Clutch Cover; Alpha: Global Convection Coefficient)

In the top part of Figure 135 the convergence behavior is shown. After the first 2000 iterations (one complete measurement cycle contains 5500 iterations) the parameters

have almost reached a stable level. The bottom part of Figure 135 indicates that the resulting parameters are too low compared to the results of the CFD simulation for the connection between the pressure plate and diaphragm spring and the diaphragm spring and clutch cover. Different ambient conditions were also set for the filter (20 °C and 25 °C) to test the sensitivity to ambient temperature changes.

As explained above, the obtained parameters were taken as constant for the parameter estimations of the clutch assembly. The results are shown in Figure 136.

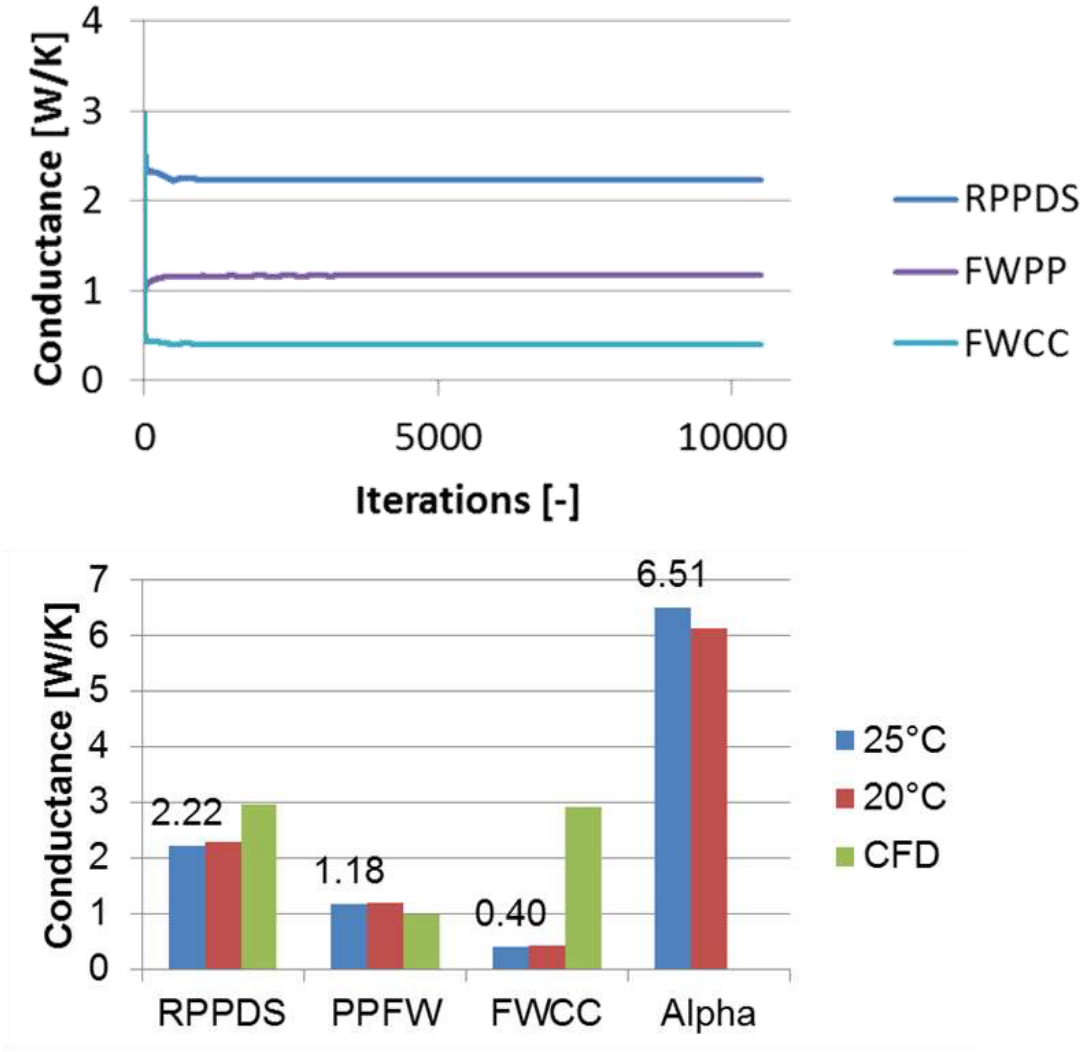

Figure 136: Results of Parameter Estimation for the Pressure Plate Assembly (Conductances: RPPDS: Pressure Plate – Diaphragm Spring; RPPFW: Pressure Plate - Flywheel; RFWCC: Flywheel – Clutch Cover; Alpha: Global Convection Coefficient)

As the top part of Figure 136 indicates, the converged condition is reached after the first 1000 iterations in this case. The heat conduction resistances, as shown in the bottom part of Figure 136, have a better match with the CFD results, except for the connection between the flywheel and clutch cover. The overall convection coefficient is lower than in the pressure plate assembly case. This is caused by the change in the

convectional heat transfer conditions. By mounting the flywheel to the pressure plate assembly, the flow rate through the clutch system is reduced.

From the two performed experiments, it seemed that the heat conduction conductance between the individual parts is either underestimated by the filter algorithm or overestimated by the CFD simulation model. To solve this question, the obtained heat conduction parameters were applied to the simplified model (convection coefficients were set according to the CFD results for both runs). As basis of the simulation, vehicle measurements were performed with the same vehicle as used for the CFD simulations.

The cycle is shown in Figure 137 and Figure 138. It can be divided into a heat up section by multiple launches and a cooling section at the end of the cycle. The measurements were performed on the local proving ground at the John Andrews Development Center at Ford Merkenich.

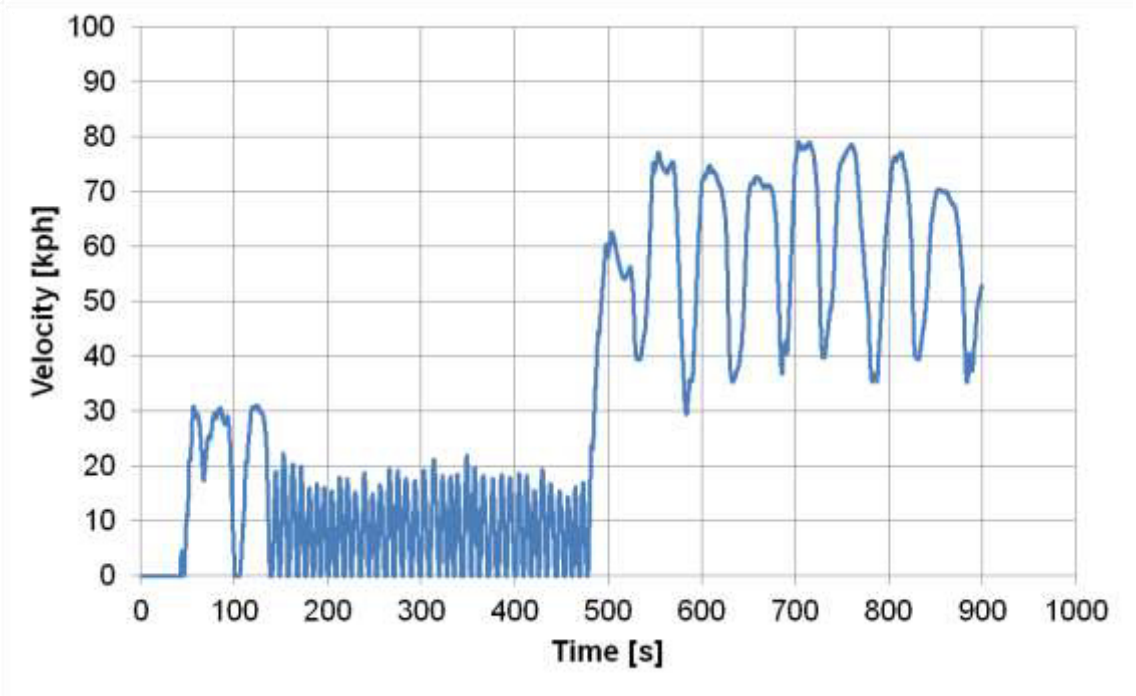

Figure 137: Velocity Profile of the Considered Cycle

In Figure 139 the results for the two parameter sets are indicated. It can be clearly seen, that the fit of the filtered parameters is better than the fit of the CFD values. This is clearly an indication, that the filtered parameters reflect the real conditions more accurately.

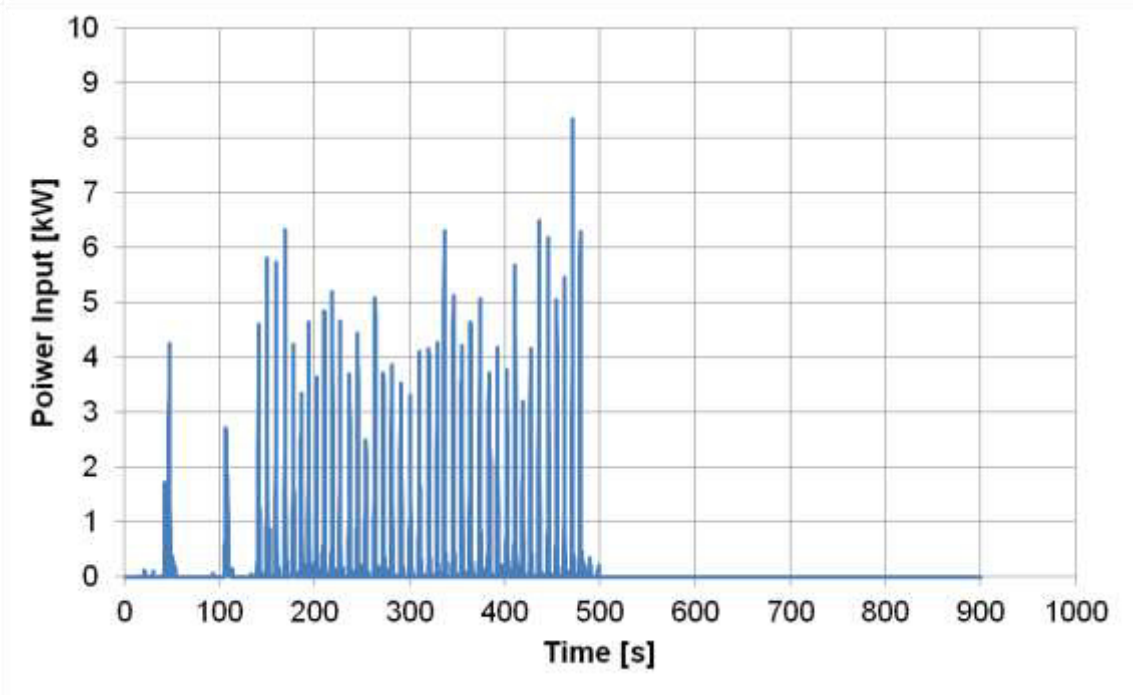

Figure 138: Power Input of Clutch System

The cause for the difference between the CFD parameters and the filtered values was identified after taking a close look at the contact conditions in the CFD model. During the process of reverse engineering (x-ray based reconstruction) and meshing, the contacts between the pressure plate and diaphragm spring or clutch cover and flywheel were modified and therefore not accurately reflected in the model (contact surfaces too large).

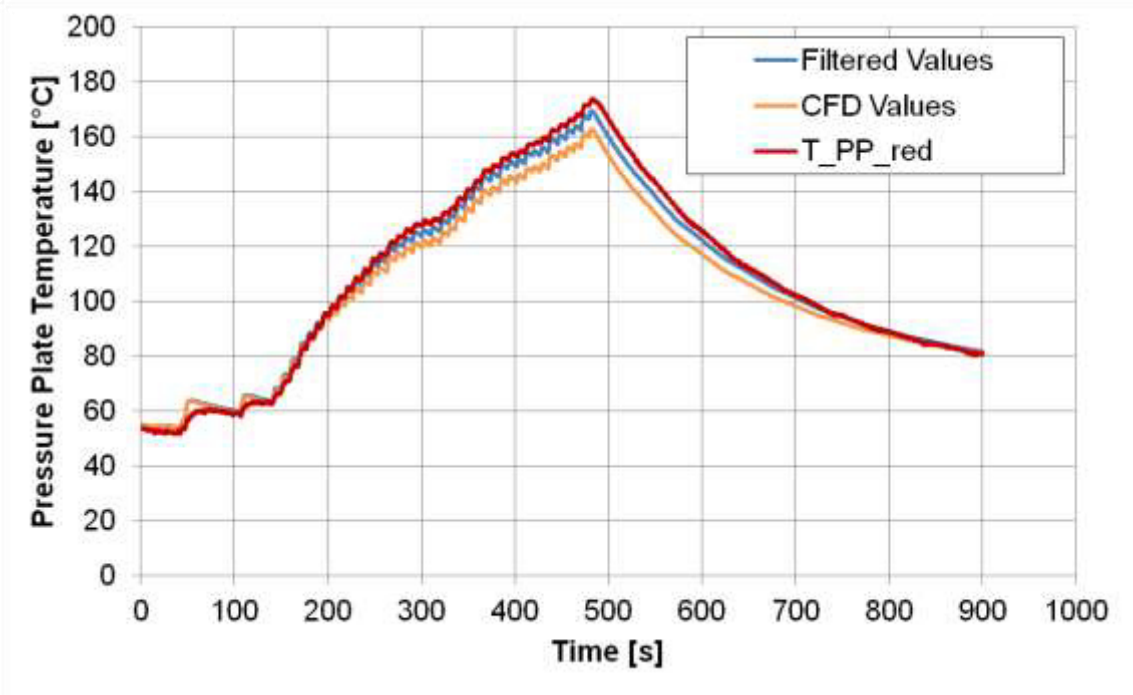

Figure 139: Results of the Simplified Simulation Model for Filtered and CFD Resistances

It can be derived from Figure 139 that the difference between the maximum temperatures is below 6 %, which is according to the defined boundaries still in a reasonable range. Moreover, at the end of the cycle the temperatures all reach the same level. This is an indication, that the overall heat balance is correct.

6.7 Conclusions

In this chapter the overall validity of the CFD and simplified clutch temperature model of chapter 4 and 5 was shown. The flow field measurements indicated that the resulting flow field is in good match with the simulation results. The newly developed wall shear stress measurement method provided excellent results. It could also be shown, that for a three dimensional flow, two dimensional measurements can be performed in case the measurement planes are positioned with care. Overall the identified heat conduction parameters showed better, but not superior, performance compared to the identified CFD parameters. Accurate reproduction of the contact conditions is an important factor for heat transfer in clutch systems.

The presented methods in this chapter can be used to validate any other clutch system in future and enhance the verification environment presented in [146].

[146] Albers 2012 b

7 Integration of CFD Based Analysis in the Product Development Process

The simulation based CFD-analysis of engineering problems can be implemented into the IPeM inside the system of resources (see 2.6). In the most general case it can be seen as addition to the method pool of available approaches for problem solving. It can therefore be a part of all stages of the product development process.

The first example of application can be given when looking at the modelling of principle soluition and embodiment stage of the IPeM and the process of this work. As shown in the previous chapters, a CFD based simulation of a clutch system can give valuable information on heat transfer of a vehicle clutch system. The information from a CFD model can be used as a base for simplified models or efficiently provide valuable input for future designs of a vehicle powertrain. As presented in Figure 140 the information available on a clutch system can be used to define different stages of modelling. The information gained on one stage can again be used to influence other higher or lower stage models. A basic size selection can be performed with stage one models. For a wear analysis the stage two model would be an appropriate choice with regards to simulation time and detail. The clutch temperature simulation model presented in the chapter 4 is an example for such a model. A CFD model is an example for a stage 3 model. It has the highest complexity, but also high accuracy and detail. The process of selecting a clutch system can therefore be seen as an optimization procedure with several models active in a loop-like procedure.

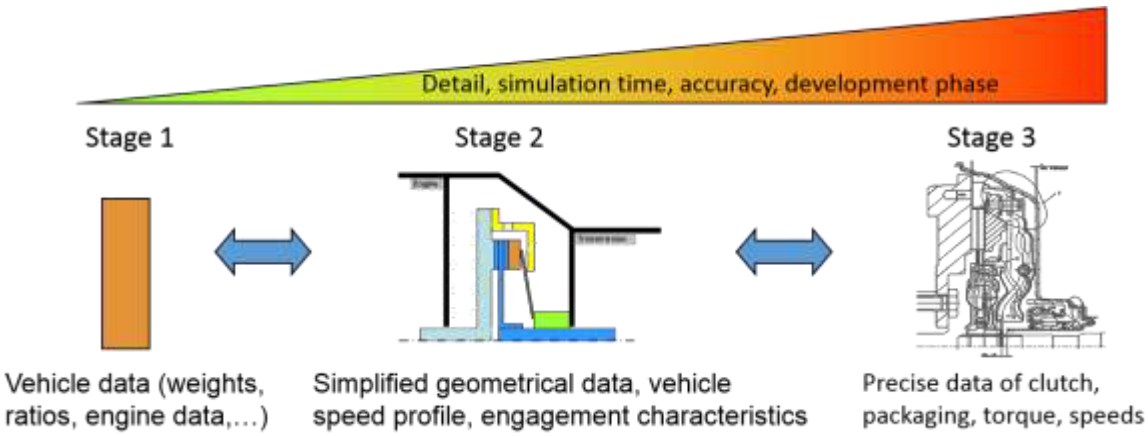

Figure 140: Modeling Stages of a Clutch System in a Development Phases

Inside the idea and profile detection stages of the activities matrix of Figure 39, the CFD based analysis can also provide valuable information to support the product development process. Optimization studies usually help to find a new design for an already developed product in order to optimize the performance or optimize the

resources necessary to manufacture the product. An example of an optimization study can be given when looking at the CFD based initial design considerations of the test rig for the wall shear stress measurements of chapter 6.4.1.

As an example on how physical coherences can be investigated with the help of a CFD model, the study of comparing the heat transfer and flow conditions inside and different clutch systems (see chapter 5.3) can be taken. The results from this CFD based comparison of three different clutch systems can be used to generate optimization potential. By additional venting or flow increase measures, the heat transfer from the clutch system to ambient air can be increased for example.

The CFD based analysis of clutch related development tasks does not necessarily always have to be on stage 3. It can also be used to solve physics based questions regarding flow and cooling problems inside the idea detection phase. To demonstrate the value and effectiveness of a simplified CFD based analysis, a study on the influences on the cooling behavior of a clutch system from a dual-dry clutch transmission will be taken as example. The main target was here to determine whether it is possible to lower the surface temperature by adding a ventilation principle to a dual clutch in a short amount of time.

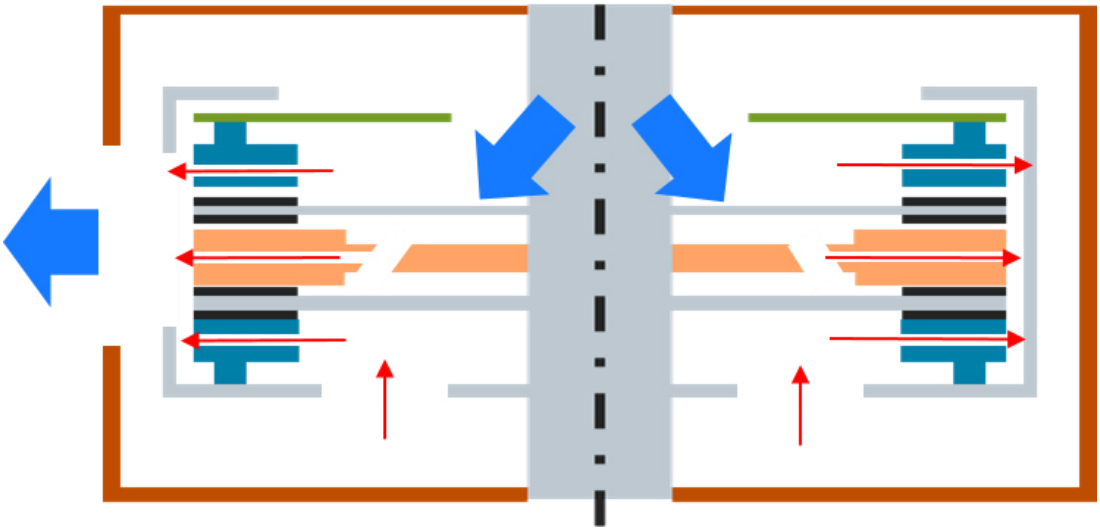

Figure 141: Schematic of Considered Cooling Cases

Figure 141 shows a schematic of the considered cases. The red arrows indicate additional part ventilation by removing material of the pressure plates, center plate or clutch cover. Blue arrows indicate additional air flow exchange with the ambient. The focus in this analysis was mainly on the clutch system. Additionally the effect of external cooling, by ventilation of the bell housing, was considered in the scope of the performed analysis. In a first step an abstracted base geometry of a dual clutch system was generated. Figure 142 shows the abstracted dual clutch model used for the simulations. The geometry consisted of two pressure plates, a clutch cover, a center

plate and a diaphragm spring surrounded by a bell housing. As shown in Figure 142, the model reflects the packaging conditions in a real dual clutch transmission.

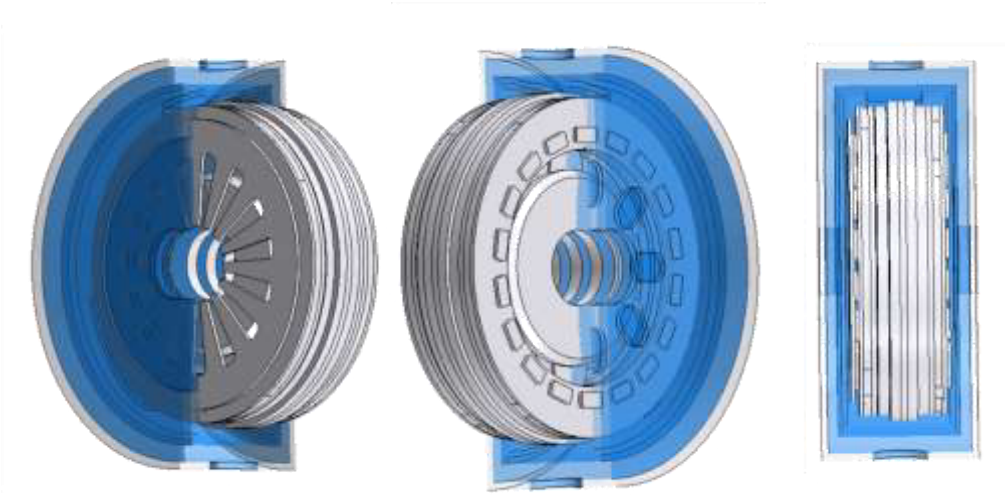

Figure 142: Packaging of Simplified Dual Clutch CFD Model

In Figure 143 the modifications of the center plate and the pressure plate are shown. Both parts were split into a solid part (light and dark gray in Figure 143) and so called ventilation parts (light and dark blue in Figure 143). The same considerations were also applied to the clutch cover and the second pressure plate. Main idea behind the part ventilation was to increase the volume flow through the clutch system and to bring the cool air to hot regions inside the individual parts.

Figure 143: Center Plate (left) and Pressure Plate (right) Modifications

The concept of splitting parts into a ventilation and an always solid part allowed to use a single mesh to perform a series of variation analyses by simply switching the ventilation parts to a solid or fluid region in dependence of the case considered. Between the parts it was chosen to define boundary layers of constant cell size, which

could be used inside the solid as additional cell layer and as boundary layer if the region is simulated as fluid.

It was decided to simulate a constant heat input into the primary side of the dual clutch. This case reflected the worst case scenario, since the primary clutch is packaged inside of the clutch system and the amount of air passing the clutch is low in the standard clutch system.

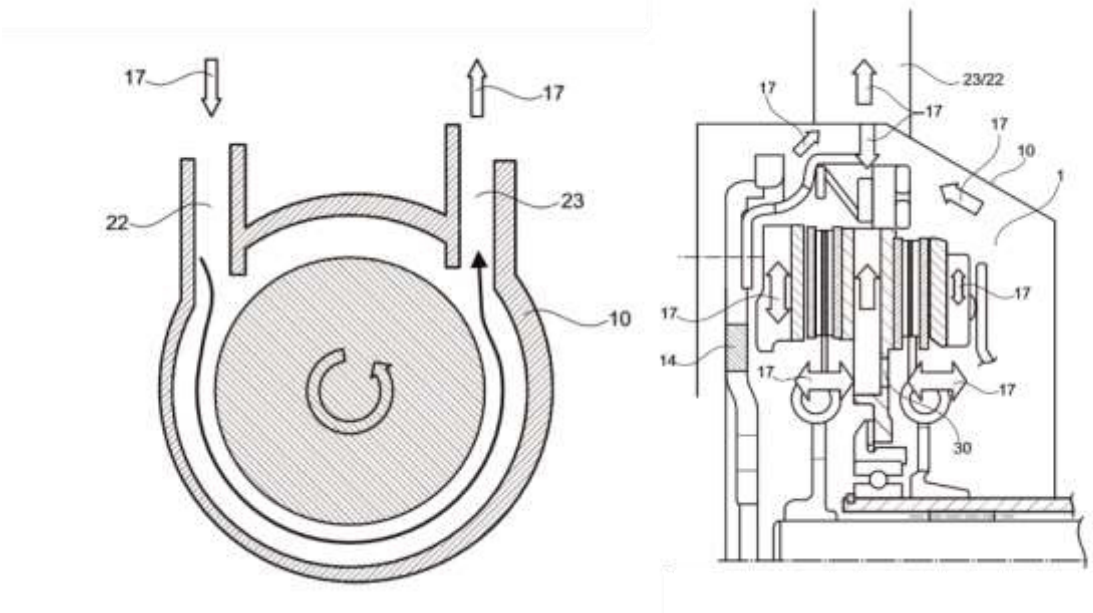

Figure 144: Concepts for Air Exchange with Ambient[147]

It was also considered to use an additional pump or the rotational movement of the clutch system to promote an air exchange with the ambient air. Figure 144 shows a concept of using the rotation of the clutch system to force air in and out of the bell housing.

[147] European Patent 102013215589.1

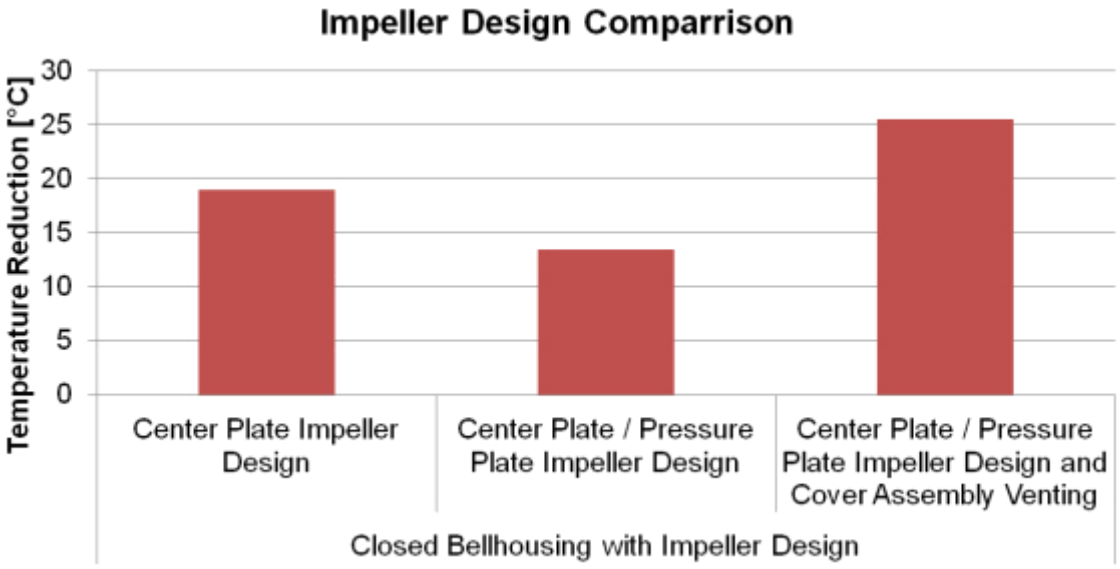

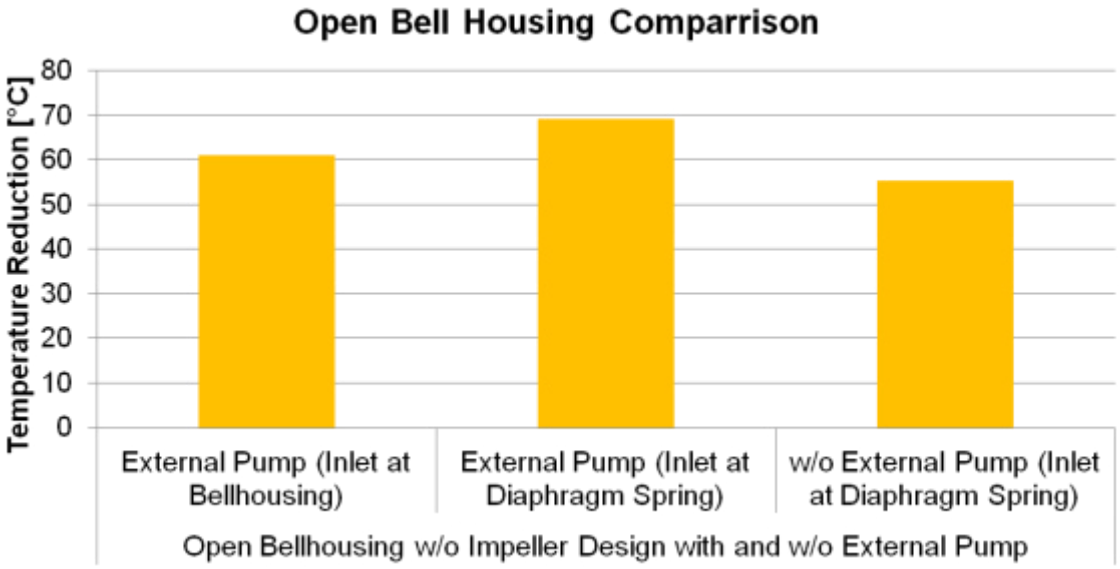

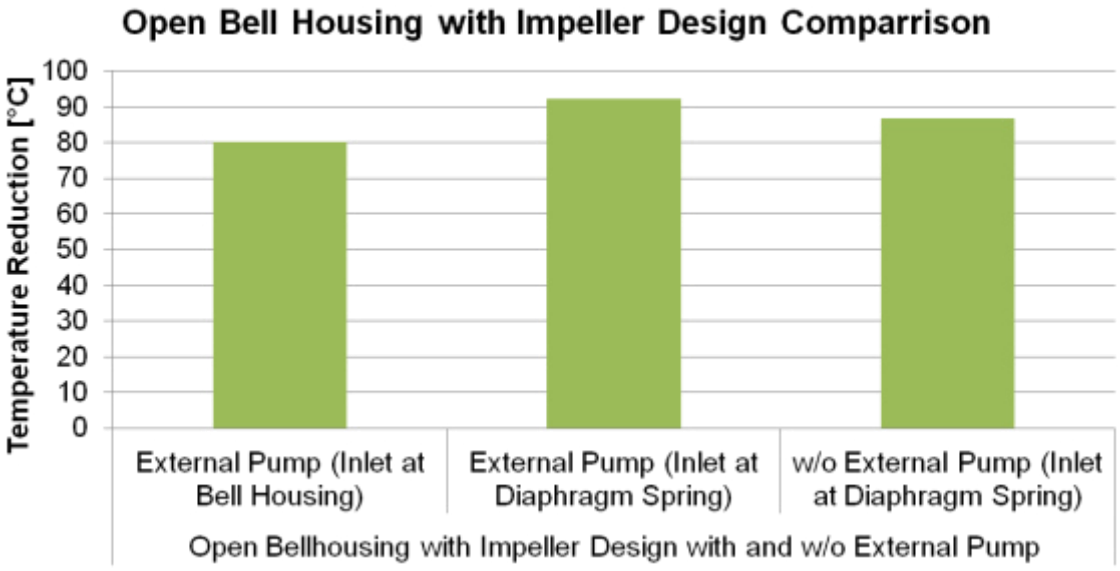

Figure 145: Results of Dual Clutch Cooling Study

The results of this study are displayed in Figure 145. It was concluded, that an intelligent positioning of inlets and outlets to and from ambient air inside the bell housing together with part ventilation of the clutch system can have a positive effect on the temperatures inside the clutch system. With the CFD study as basis, other concepts and solutions were derived.

As shown by these examples the CFD analysis CAE methods in general extend the system of resources of the IPeM model and therefore increase the solution quantity and quality. It can therefore be concluded that CAE methods have a high and valuable position in the product development cycle.

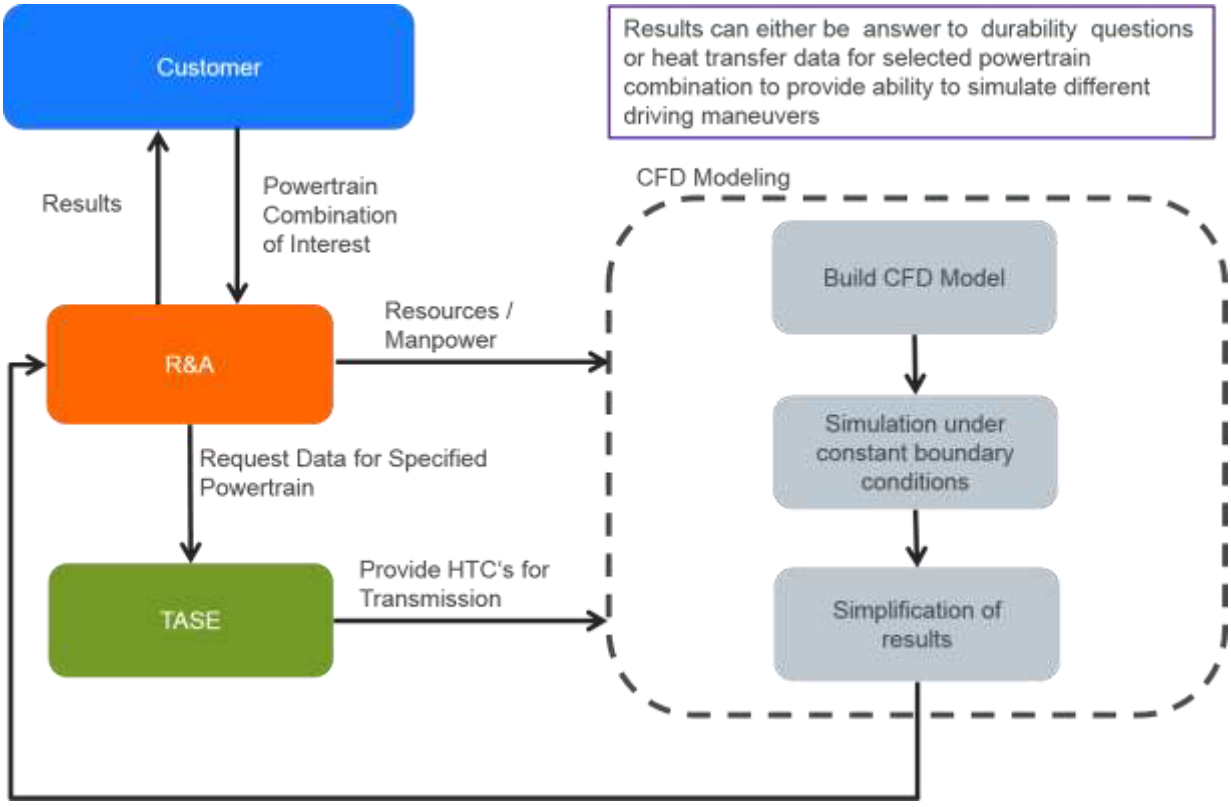

Figure 146: Implementation Example of a CFD Analysis

An example of how a CFD analysis can be implemented in the product development process is shown in Figure 146 from a research and advanced development departments perspective. The process contains many procedures developed in this study. The effectiveness and practicability of the developed methodology supporting the daily development tasks in clutch system development was not evaluated in this study. This is an important section which has to be evaluated in further studies.

8 Conclusion and Outlook

In this study the process of obtaining a temperature determination tool with the help of a CFD based conjugate heat transfer analysis was displayed. After determining the highest influencing factors on heat transfer in regard to a clutch system, the individual heat transfer paths were displayed and analyzed. It was shown, that a conjugate heat transfer analysis is a strong and powerful tool inside the powertrain development.

A process how to treat and simplify clutch systems with different number of components to fit a general model structure was presented in chapter 4 which can and should be used to enhance the powertrain library of the temperature determination model.

The general flow structure and heat transfer of a clutch system was displayed in chapter 5. It could be shown that the flow structure can be divided into recirculation flow systems. Between these systems there exists the possibility of flow field separation. The model presented can be used to determine the conductional and convectional heat transfer coefficient parameters inside a dry clutch system.

In chapter 6 the verification process was developed by rating and categorizing the individual measurement principles by their application and measurement principles in regards to the measurement task (chapter 6.1). Based on this information, the verification of the CFD and temperature determination model was performed. By using different approaches, like wall shear stress measurements (chapter 6.4) and dry clutch system PIV measurements (chapter 6.5), the verification environment presented in [148] could be extended. It was shown, that wall-shear stress measurements inside complex and highly packaged systems are possible with simple means when appropriate methods or measures are applied for the evaluation. The Kalman filter method provided a good method for the determination of unknown nonlinear parameters.

The CFD-based analysis and performed verification proved, that high quality results can be obtained, even by applying a stationary assumption on an obviously instationary flow system.

The implementation of the CFD-analysis into the integrated product development model was shown in chapter 7 together with examples from engineering projects. It could be demonstrated, that this kind of CAE method can produce valuable information and aid the overall problem solution strategy in regards of clutch systems inside the product development process.

[148] Albers et al 2012 b

As a next step, the buildup of a powertrain library containing different clutch, engine and transmission systems should be performed. Once the library contains enough individual systems, the information can then be used as basis for a large scale similarity analysis in order to find simplified approaches for future clutch and powertrain systems.

In order to optimize the simulation time, the effect of using segment models inside the CFD-software should be investigated. By using this simplification together with periodical boundaries, it can be possible to reduce the simulation effort proportional to the resulting mesh size. Together with this analysis the influence of the bell housing shape should also be investigated.

9 Literature

Adair & Tucker 1997
Adair, D; Tucker, P: Efficient modeling or rotating disks and cylinders using cartesian grid; Applied Mathematical Modelling Vol. 21, Elsevier Science Inc., 1997

Albers 2002
Albers, A; Matthiesen, S: Konstruktionsmethodisches Grundmodell zum Zusammenhang von Gestalt und Funktion technischer Systeme – Das Elementmodell "Wirkflächenpaare & Leitstützstrukturen" zur Analyse und Synthese technischer Systeme; Zeitschrift Konstruktion Band 54 7/8; Düsseldorf, 2002

Albers 2005 a
Albers, A; Burkhardt, N; Ohmer, M: How C&CM can help the designer to find the right principles; Proceedings of CIRP Designer Seminar 2005. New trends in engineering design. Pages 232-241, 2005

Albers et al 2006 a
Albers, A.; Deters, L.; Feldhausen, J.; Leidich, E.; Linke, H.; Poll, G.; Sauer, B.; Wallaschek, J.: Konstruktionselemente des Maschinenbaus 2. Berlin, Heidelberg: Springer 2006

Albers et al 2009 a
Albers, A; Babik, A, Ott, S, Späth, C: Einfluss von Werkstoffkenngrößen und Wärmehaushalt auf das tribologische Verhalten trockenlaufender Reibkupplungen; Internationaler VDI-Kongress Getriebe in Fahrzeugen Band 2071, 2009

Albers 2009 b
Albers, A; Braun, A; Clarkson, J; Enkler, H-G; Wynn, D: Contact and Channel Modelling to support early design of technical systems; International conference on engineering design ICED'09, 24 – 27 August 2009, Stanford University, Stanford, CA, USA

Albers et al 2010 a
Albers, A; Meid, M: Advanced Ceramic-Steel Pairings under Permanent Slip for Dry Running Clutch Systems; Mechanical Properties and Performance of Engineering Ceramics and Composites V: Ceramic Engineering and Science Proceedings, Volume 31, 2010

Albers et al 2010 b
Albers, A; Meid, M, Ott, S: Ansätze zur Komfortsteigerung eines trockenlaufenden Kupplungssystems mit ingenieurkeramischen Friktionswerkstoffen; SFB 483, Institut für Produktentwicklung Karlsruhe, 2010

Albers 2010 c
Albers, A: five Hypotheses about Engineering Processes and their Consequences; Proceedings of the TMCE 2010, Ancoana Italy

Albers et al 2011 a
Albers, A; Ott, S, Bernhardt, J: Kupplungssystementwicklung für Fahrzeuge unter der Anwendung ingenieurkeramischer Friktionssysteme zur Steigerung der systemischen Leistungsdichte; Abschlusskolloquium des SFB 483, Institut für Produktentwicklung Karlsruhe, 2011

Albers 2011 b
Albers, A; Braun, A: A generalized framework to compass and to support complex product engineering processes; Interscience Enterprises Ltd, 2011

Albers 2012 a
Albers, A; Braun, A: Towards Handling Complexity – Testing the IPeM Process Modeling Approach; Proceedings of TMCE 2012, Karlsruhe Germany 2012

Albers et al 2012 b
Albers, A; Brezger, F; Koch, C: Development of a new validation environment for CFD simulations on the example of a lubricated clutch. International VDI Congress Transmission in Drivetrains 2012 b

Albers 2013 a
Albers, A: Teil I: Produktentstehnungsprozess für Leichtbaukomponenten und –systeme; Lecture Notes, Institute of Product Development Karlsruhe, Karlsruhe Institute of Technology 2013

Albers 2013 b
Albers, A; Sadowski, E: The Contact and Channel Approach (C&C²-A): relating a system's physical structure to its functionality; An Anthology of Theories and Models of Design: Philosophy, Approaches and Empirical Explorations; Springer, Heidelberg, 2013

Albers 2013 c
Albers, A; Thau, S: Heuristiken zur Analyse und Synthese technischer Systeme mit dem C&C²-Ansatz auf Basis von Entwicklungsprojekten im industriellen Umfeld; IPEK Forschungsberichte Band 66, Dissertation, Institut für Produktentwicklung Karlsruhe, 2013

Albers et al 2015 a
Albers, A; Ott, S; Basiewicz, M: Innovatives Kupplungsscheibendesign mit hoher Leistungsdichte für PKW-Anwendungen, VDI-Berichte 2245, VDI-Verlag Düsseldorf 2015

Baer & Stephan 2010
Baer, Stephan: Wärme und Stoffübertragung; 7. Auflage; Springer Verlag Heidelberg Dordrecht London New York, 2010

Beitler 2008
Beitler, H.: Analysis of the temperature and heat output characteristic of a single-plate dry clutch. KIT Diss., Institute of Product Development Karlsruhe, 2008

Benkeira 1996
Benkreira, H: Fluid Mixing 5; Institution of Chemical Engineers, Warwickshire, UK, 1996

Biering 2001
Biering, B: Identifikation von Wärmeaustauschparametern thermischer Netzwerke durch transient gemessene Knotentemperaturen bei minimierter Meßzeit; Dissertation, Fakultät V-Verkehrs- und Maschinensysteme der technischen Universität Berlin, 2001

Cardone et al 1996
Cardone, G; Astarita, T, Calomagno, G: Infrared heat transfer measurements on a rotating disk; Optical Diagnostics in Engineering Vol. 1(2), 1996

Elkins 1997
Elkins, C: Heat transfer in the rotating disk boundary layer; Dissertation; Mechanical Engineering Stanford University; April 1997

European Patent 102013215589.1
European Patent: Integriertes Kühlsystem für Kupplungsgetriebe mit einer trockenen Einzelkupplung bzw. einer trockenen Doppelkupplung; Ford Global Technologies, LL; Official File Reference 102013215589.1, Deutsches Patent- und Markenamt

Ferrer 2015
Ferrer, E; Montlaur, A: CFD for Wind and Tidal Offshore Turbines; Springer International Publishing Switzerland 2015

Ferzinger & Peric 2008
Ferzinger, J; Peric, M: Numerische Strömungsmechanik; Springer-Verlag Berlin Heidelberg, 2008

Fluent 2001
Fluent Help Documentation, Chapter 9, Fluent Inc. 2001

Ford Development Report 371-218552-R1 2012
Internal Ford Development Report 371-218552-R1: CFD-Simulation of the Heat Distribution in a Clutch, prepared by R. Gaupp, cd-Adapco, 2012

Ford Report REP1485
Ford Report REP1485: Temperature of Clutch Engagement, Loughborough University, 1993

Gauterin & Unrau 2008
Gauterin, F.; Unrau, H.-J.: Grundlagen der Fahrzeugtechnik 1. Vorlesungsskript Institut für Fahrzeugtechnik und mobile Arbeitsmaschinen, Universität Karlsruhe, 2008

Gullberg et al 2009
Gullberg, P; Löfdahl, L; Adelman, S; Nilsson, P: A Correction Method for Stationary FAN CFD MRF Models; SAE Technical Paper 2009-01-0178, SAE International 2009

Hill & Ball 1999
Hill, R; Ball, K: Direct numerical simulations of turbulent forced convection between counter-rotating disks; International Journal of Heat and Fluid Flow 20; 1999

Hopf & Gauch 2000
Hopf, A; Gauch, A: Numerische Simulation der Bremsenkühlung mit CFD und FEM; VDI-Berichte Nr. 1559; VDI Verlag Düsseldorf, 2000

Julier & Uhlmann 1997
Julier, S; Uhlmann, J: A New Extension of the Kalman Filter to Nonlinear Systems; The Robotics Research Group, Department of Engineering Science, University of Oxford; 1997

Kalman 1960
Kalman, R: A New Approach to Linear Filtering and Prediction Problems; Transitions of the ASME-Journal of Basic Engineering, 82 (Series D): 35 – 45; 1960

Kichner 2007
Kirchner, E: Leistungsübertragung in Fahrzeuggetrieben; Springer-Verlag Berlin Heidelberg New York, 2007

Kopitz & Polifke 2009
Kopitz, J; Polifke, W: Wärmeübertragung: Grundlagen, analytische und numerische Methoden; 2., aktualisierte Auflage, Pearson Studium, 2009

Kreith et al 1958
Kreith, F; Taylor J; Chong, P: Heat and mass transfer from a rotating disk; Second National Heat Transfer Conference, Chicago Illinois, 1958

Kubota et al 2003
Kubota, T; Kobayashi, T; Saga, T; Taniguchi, N; Segawa, S; Kajitani, K; Fukunaga, T; Tasaka, T; Kunisaki, Y: Application of PIV measurement of flow field around lock-up clutch of automotive torque converter; JSAE Review 24 (2003) 425 – 430

Kunisaki et al 2001
Kunisaki, Y; Kobayashi, T; Saga, T; Taniguchi, N; Segawa, S; Kajitani, K; Fukunaga, T; Tasaka, T: A study on internal flow of automotive torque converter – three dimensional flow analysis around a stator cascade of automotive converter by using PIV and CT techniques; JSAE Review 22 (2001) 559 – 564

Lavalle & Rahman 2010
Lallave, J; Rahman, M: Numerical simulation of transient thermal transport on a rotating disk under partially confined laminar liquid jet impingement; Journal of Heat Transfer Vol. 132; ASME 2010

Lechner & Naunheimer 2007
Lechner, G; Naunheimer, H: Farhzeuggetriebe, Grundlagen, Auswahl, Auslegung und Konstruktion; Springer-Verlag Berlin Heidelberg New York 1994

Lee & Cho 2006
Lee, B; Cho, C: Numerical Analysis Procedure For Predicting Temperature Field in Design of Automotive Friction Clutch; International Journal of Automotive Technology, 2006 Vol. 7, No. 1, pp 61 – 68; KSAE

Levillian et al 2015
Levillan, A; Brassart, P; Patte-Rouland, B: Impact of the Housing Air Flow and the Thermal Behavior of an Automotive Clutch System; Open Journal of Fluid Dynamics 5, Scientific Research Publishing, 2015

Li, Zhou & Aung 2009
Li, X.C; Zhou, J; Aung, K.: On selection of reference temperature of heat transfer coefficient for complicated flows; International Journal for Heat and Mass Transfer Volume 45; Pages 633-643; 2009

LUK Brochure 2015
LUK Kupplungs-Kurs (PKW): Einführung in die Kupplungstechnik für Personenkraftwagen, Broschüre, 2015

Marek & Nitsche 2007
Marek, R; Nitsche, K: Praxis der Wärmeübertragung; Fachbuchverlag Leipzig im Carl Hanser Verlag, 2007

Merwe 2004
Merwe, R: Sigma-Point Kalman Filters for Probabilistic Inference in Dynamic State-Space Models; Dissertation, Faculty of the OGI School of Science & Engineering at Oregon Health & Science University, 2004

Mocikat & Herwig 2009
Mocikat, H; Herwig, H: Heat Transfer Measurements with Surface Mounted Foil-Sensors in an Active Mode: A comprehensive Review and a New Design; Sensors 2009, ISSN 1424-8220

Moffat 2010
Moffat, RJ: What's new in convective heat transfer? Interational Journal of Heat and Fluid Flow Volume 19 Issue 2, Pages 90 – 101; 1998

Moisy et al 2003
Moisy, F; Pasutto, T; Rabaud, M: Instability patterns between counter-rotating disks; Nonlinear Processes in Geophysics (2003) 10: 281 – 288

Müllges et al 2004
Müllges, G; Niederdrenk, K; Wodicka, R: Numerik-Algorithmen; 9. Auflage; Springer Berlin Heidelberg New York, 2004

Naughton & Sheplak 2002
Naughton, J; Sheplak, M: Modern Developments in Shear Stress Measurement; Progress in Aierospace Sciences February 2002

Neumann & Stürmer 2007
Neumann, K; Stürmer, W: Untersuchungen der Lüftströmung in der Kupplungsglocke von Nutzfahrzeugen von Fahrzeuggetrieben; VDI-Berichte Nr. 1987, VDI Verlag Düsseldorf, 2007

Nitsche & Brunn 2006
Nitsche, W; Brunn, A: Strömungsmesstechnik; 2. Auflage, Springer-Verlag Berlin Heidelberg 2006

Oedekoven 1989
Oedekoven, A: Temperaturverhalten von trockenlaufenden Kupplungen. Fortschrittsberichte VDI Reihe 1, Nr. 181; VDI-Verlag Düsseldorf 1989

Oertel et al 2006
Oertel, H; Böhle, M; Dohrmann, U: Strömungsmechanik; 4. Auflage; Friedr. Vieweg & Sohn Verlag, GWV Fachverlage GmbH, Wiesbaden 2006

Pischinger et al 2009
Pischinger, R; Klell, M; Sams, T: Thermodynamik der Verbrennungskraftmaschine; Springer Verlag Wien, 2009

Prokhorov 1979
Prokhorov, M; Saul'ev, M: The Kalman-Bucy Method of Optimal Filtering and its Generalizations; Matematicheskii Analiz, Vol. 14, pp. 167-207; 1977; Plenum Publishing Corporation 1979

Pryzbilla et al 2011
Pryzbilla, M.; Kunze, C.; Celik, S.; Dongaonkar, S.: Combined simulation approach for dry clutch systems; SAE 2011 World Congress, Detroit Michigan, USA

Rhee 2006
Rhee, J.: The Role of Superposition Techniques in Thermal Management; 11th International Symposium on Advanced Packaging Materials: Processes, Properties and Interface; Pages 163 – 168; 2006, Atlanta, GA

Ribeiro 2004
Ribeiro, M: Kalman and Extended Kalman Filters: Concept, Derivation and Properties; Instituto Superior Tecnioco; 2004

Schlichting & Gertsen 2005
Schlichting, H; Gertsen, K: Grenzschicht-Theorie, Springer Verlag 10. Auflage, 2005

Schütz 2009
Schütz, T: Ein Beitrag zur Berechnung der Bremsenkühlung an Kraftfahrzeugen; Schriftenreihe des Instituts für Verbrennungsmotoren und Kraftfahrwesen der Universität Stuttgart, Band 45, Expert Verlag Renningen 2009

Schwarze 2013
Schwarze, R: CFD-Modellierung, Grundlagen Anwendungen bei Strömungsprozessen, Springer-Verlag Berlin Heidelberg 2013

Shevchuck 2009
Shevchuk, I.: Convective Heat and Mass Transfer in Rotating Disk Systems; Lecture Notes in Applied and Computational Mechanics; Springer-Verlag Berlin Heidelberg 2009

Siekmann & Thamsen, 2008
Siekmann, H; Thamsen, P: Strömungslehre, 2., aktualisierte Auflage, Springer-Verlag Berlin Heidelberg New York, 2008

Soong et al 2003
Soong, C; Wu, C; Liu, T, Liu, T-P: Flow Structure Between two Co-Axial Disks Rotating Independently; Experimental Thermal and Fluid Science 27, 2003

Stan 2005
Stan, C: Alternative Antriebe für Automobile; Springer-Verlag Berlin Heidelberg 2005

Star-CCM+ User Manual 2010
Star-CCM+ User Manual; CD-Adapco: Melville, New York. 2010

Tamm 2002
Tamm, A: Beitrag zur Bestimmung der Wirkungsgrade einer Kreiselpumpe durch theoretische, numerische und experimentelle Untersuchungen; Dissertation, Fachbereich Maschinenbau an der Technischen Universität Darmstadt, 2002

Thuresson 2014
Thuresson, A: CFD and Design Analysis of Brake Disc; Master's Thesis in Automotive Engineering, Department of Vehicle Engineering and Autonomous Systems, Chalmers University of Technology, Gothenburg, Sweden 2014

VDI Wärmeatlas 2006
VDI: VDI Wärmeatlas; Verein Deutscher Ingenieure, VDI-Gesellschaft Verfahrenstechnik und Chemieingenieurswesen (GVC); 10. Auflage; Springerverlag Berlin Heidelberg 2006

Wagner 1948
Wagner, C: Heat transfer from a rotating disk to ambient air; Journal of Applied Physics Volume 19, 1948, IEEE Xplore

Wallentowitz & Reif 2006
Wallentowitz; Reif: Handbuch Kraftfahrzeugelektronik; ATZ/MTZ Fachbuch; Friedrich Vieweg & Sohn Verlag, GWV Fachverlage GmbH, Wiesbaden 2006

Wesseling 2009
Wesseling, P: Principles of Computational Fluid Dynamics; Springer Series in Computational Mathematics 29; Springer-Verlag Berlin Heidelberg, 2009

Wittig et al 1998
Wittig, S; Kim, S; Scherer, T; Weissert, I: Numerical Study for Optimizing Heat Transfer in High Speed Rotating Components; International Journal of Rotating Machinery, 1998 Vol. 4 Nr. 3, pp. 151 – 161; Overseas Publishers Association

Wosetschläger & Göttlich 2008
Wosetschläger, J; Göttlich, E: Recent Applications of Particle Image Velocimetry to Flow Research in Thermal Turbomachinery; Institute for Thermal Turbomachinery and Machine Dynamics, Graz University of Technology, Inffeldgasse 25, A – 8010 Graz, Austria, 2008

Wu 2009
Wu, S: A PIV study of co-rotating disks flow in a fixed cylindrical enclosure; Experimental Thermal and Fluid Science 33 (2009) 875 – 882

Wu et al 2013
Wu, Y; Li, S; Liu, S;Dou, H-S; Qian, Z: Vibration of Hydraulic Machinery; Springer Science+Buisness Media Dordrecht 2013

Zadravec 2007
Zadravec, M: The influence of rotating domain size in a rotating reference approach for simulation of rotating impeller in a mixing vessel; Journal of Engineering Science and Technology Vol. 2, 2007

Zhai, Zhang & Chen 2007
Zhai, Z; Zhang, Z; Zhang,W; Chen, Q: Evaluation of Various Turbulence Models in Predicting Airflow and Turbulence in Enclosed Environments by CFD: Part-1: Summary of Prevalent Turbulence Models; HVAC&R Research, 13,(6), 2007

Zierep & Bühler 1991
Zierep, J; Bühler, K: Strömungsmechanik; Springer Verlag Berlin Heidelberg New York; 1991